A Computational Approach to Studying the Inflammatory Processes Active During *Helicobacter hepaticus*-Induced Intestinal Inflammation

Stephanie Evans

PhD

University of York

Biology

October 2016

Abstract

Inflammatory bowel disease (IBD) is a chronic inflammatory condition of the gastrointestinal tract that usually manifests as either ulcerative colitis or Crohn's disease. *Helicobacter hepaticus* (*Hh*)-induced colitis is a mouse model of intestinal inflammation whereby IL-10 knock out mice are infected with *Hh*, resulting in pathology similar to that seen in Crohn's disease.

Following the Complex Systems Modelling and Simulation (CoSMoS) process, a principled approach to the engineering of simulations of complex systems, we have developed IBDSim, a computational model of the processes active in the intestinal tract during *Hh*-induced colitis. IBDSim is a hybrid agent-based model (ABM) that combines agent-based modelling with systems biology and quantitative systems pharmacology approaches, to capture both cell- and system-level behaviours. In combining these approaches, the Automated Simulation Parameter Alteration and SensItivity Analysis toolkit (ASPASIA) was developed to aid in the calibration and analysis of models written in Systems Biology Mark-up Language (SBML), where the addition of an intervention is required for key behaviours to emerge. SBML models generated using this toolkit could then be incorporated into IBDSim.

IBDSim was calibrated to reproduce behaviours such as the dynamics of *Hh* burdens and increasing cell infiltration seen *in vivo* in the *Hh* colitis model and validatory experiments demonstrated that IBDSim can be used as a predictive tool. We present two examples of explorative *in silico* experimentation using IBDSim. The first experiment examined the effects of blocking lymphocyte egress from the lymph node on intestinal inflammation. The second experiment investigated how altering the composition of the microbial flora can contribute to intestinal inflammation, both in the absence and presence of *Hh*. IBDSim can be used to study the immunological processes involved in the development of intestinal inflammation, predict targets for therapeutic treatments, and examine the effects of drug intervention on disease outcome.

Contents

List of Tables

List of Figures

Acknowledgements

There are a number of people to whom I owe my sincere thanks.

- To my supervisors Marika Kullberg, Jon Timmis, and Lourdes Cucurull-Sanchez for your excellent supervision throughout this project, and for turning a mathematician into an immunologist, computer scientist, systems pharmacologist, and all things in between.
- To my thesis advisory panel members Mark Coles and Susan Stepney for your advice.
- To Denise Kirschner, and your lab, for your help and kindness during my visit to the lab.
- To Shraddha Kamdar for sharing your biological expertise, and for your friendship over the last four years
- To the members of the Timmis lab past and present, especially Kieran Alden, James Butler, Johnny Leonov, and Jason Cosgrove for always being there to troubleshoot, and for creating a sense of camaraderie within the lab.
- To my husband Richard for your patience and understanding.
- To my parents Lynn and Steve for always supporting my decisions, even if you don't always understand them!

Declaration

I declare that the research described in this thesis is original work, which I undertook at the University of York during 2012 - 2016. Except where stated, all of the work contained within this thesis represents the original contribution of the author.

Chapter 1

Introduction

The goal of this thesis was to generate a computational model that will provide novel insight into the inflammatory processes active in the gut during intestinal inflammation. This chapter provides an introduction to both the immunology behind the model, and to mathematical and computational techniques for the modelling of biological systems.

1.1 Background Immunology and an Introduction to the *Helicobacter hepaticus*-Induced Colitis Model

1.1.1 Overview of the Immune System

The immune system is a highly evolved biological system whose function is to identify and eliminate foreign material (Farmer et al., 1986). It is made up of cells, tissues, and organs that work together to defend against pathogens. In mammals, the immune response is generated by white blood cells that originate in the bone marrow, and either circulate in the blood or migrate to lymphoid organs around the body. Lymphoid organs are organised tissues containing large numbers of cells, and can be divided into primary (central) lymphoid organs, and secondary (peripheral) lymphoid organs. Primary lymphoid organs are sites like the thymus where lymphocytes become mature, and secondary lymphoid organs include the many types of lymph nodes, where the adaptive immune response is initiated (Janeway et al., 2001). The mammalian immune response can be divided into two arms known as the innate and the adaptive immune system.

1.1.1.1 Innate Immunity

The innate immune system is the first line of immune defence against an invading pathogen and responds immediately with a non-specific response. When a pathogen penetrates a barrier for the first time it is met by cells of the innate immune system and an innate immune response is mounted. The innate response is mediated by phagocytic cells including dendritic cells (DCs), macrophages and neutrophils, among others. DCs and macrophages become activated by recognising pathogen-associated molecular patterns (PAMP) on the surface of pathogens via germline-encoded pattern-recognition receptors (PRRs) on their surface (Akira et al., 2006). Innate immune responses are non-specific, meaning that there is an immediate, maximal response to a pathogen, regardless of antigen-specificity or whether the host has seen it before

1.1.1.2 Adaptive immunity

Following the initiation of the innate immune response, antigen-presenting cells (APCs) including DCs and macrophages trigger the adaptive immune response. The adaptive immune system is highly specific and requires a sophisticated rearrangement of receptor genes and this means that unlike the innate response that is immediately activated when a pathogen enters the body, the adaptive immune response takes days to develop. Adaptive immune responses are induced by white blood cells called lymphocytes, including B cells that produce antibodies and T cells that produce a cell-mediated response. B-cell secreted antibodies circulate in the blood stream and act by binding to the type of antigen that stimulated their initial production. This binding blocks the ability of that specific antigen to bind to receptors on host cells and marks it for destruction, making it easier for the cells of the innate immune system to identify and ingest it. In the cell-mediated T-cell response, activated T cells react directly with antigen that is presented to them by APCs. Activated T cells produce signalling molecules called cytokines that can activate macrophages in the periphery and cause them to destroy the pathogens they have engulfed (Alberts et al., 2002).

T cells derive from hematopoietic stem cells in the bone marrow and migrate to the thymus where they become mature. They express a unique antigen binding receptor on

their surface known as a T-cell receptor (TCR) that can interact with the peptide-major histocompatibility complex (MHC) complexes on the surface of an APC. There are two types of MHC molecules, class I that are expressed by all nucleated cells, and class II that are found on certain immune cells including DCs, macrophages and B cells, so called professional APCs. When an APC has broken down and processed an antigen, it presents small antigenic fragments called peptides on the MHC molecules on its surface. MHC-I molecules present endogenous peptides while exogenous peptides are presented by MHC-II (Bonilla and Oettgen, 2010; Janeway et al., 2001). In the thymus, peptide-MHC:TCR interactions result in the maturation of immature T cells into either a $CD4^+$ or $CD8^+$ lineage (Bosselut, 2004). $CD8^+$ T cells are known as cytotoxic, and are primarily involved in the destruction of infected cells, whereas $CD4^+$ T cells are T-helper (Th) cells that have no cytotoxic or phagocytic ability and cannot kill infected cells or clear pathogens. $CD4^+$ cells have an important role in establishing and maximising the immune response by secreting chemicals called cytokines that direct other immune cells to become phagocytic or cytotoxic (Warrington et al., 2011). Th cells are activated through interaction of their TCR with a peptide-MHC-II molecule on the surface of an APC in a secondary lymphoid organ. Activated Th cells secrete a different array of cytokines depending on the cytokine stimulation received from their local environment. Activated Th cells can be classified as either Th1, Th2, Th17 or Treg cells by the types of cytokine they produce (Figure 1.1). If an activated $CD4^+$ T cell is in the presence of Interleukin (IL)-12 it will adopt a Th1 phenotype. Th1 cells were first described by Mosmann et al. (1986) and secrete high amounts of Inteferon-γ (IFN-γ) and other inflammatory cytokines including Tumour Necrosis Factor-α (TNF-α). IFN-γ protects against intracellular pathogens by inducing antimicrobial mechanisms of macrophages as well as up-regulating antigen processing and presentation pathways (Schroder et al., 2004). Alternatively, in mice, activated $CD4^+$ T cells in the presence of a combination of Transforming Growth Factor-β (TGF-β) and either IL-6 or IL-21 develop into Th17 cells (Korn et al., 2009). Following polarisation, Th17 cells secrete inflammatory cytokines IL-17 and IL-21 (Wei et al., 2007) and upregulate the IL-23 receptor. IL-23 is required to maintain the Th17 cell population (Stritesky et al., 2008). IL-17 protects against extracellular pathogens by recruiting neutrophils to the site of infection (Griffin et al., 2012). It also promotes the formation of tight junctions

between epithelial cells in the gut (Reynolds et al., 2012). Unlike Th1 cells that maintain a robust phenotype, the Th17 phenotype is plastic with Th17 cells switching from an IL-17 to an IFN-γ producing phenotype in the presence of IFN-γ and IL-12 *in vitro*. *In vivo*, the mechanism driving phenotype switching in yet to be elucidated, but the presence of IL-23 is required as it has been shown that $CD4^+$ T cells lacking the IL-23R fail to switch phenotypes (Ahern et al., 2010; Morrison et al., 2011; O'Shea and Paul, 2010) (Figure 1.1). Th2 cells are induced when activated $CD4^+$ T cells are in the presence of IL-4. They protect against extracellular parasites, including helminths, and play a major role in allergic inflammatory conditions such as asthma by enhancing IgE production by B cells, recruiting and activating eosinophils, and increasing mucus production (Pulendran and Artis, 2012; Deo et al., 2010). The main effector cytokine produced by Th2 cells is IL-4. Treg cells develop in the presence of TGF-β and/or IL-10. They are non-inflammatory cells and secrete anti-inflammatory cytokines IL-10 and TGF-β that reduce inflammation by suppressing the expression of proinflammatory cytokines, chemokines, adhesion molecules, as well as antigen-presenting and costimulatory molecules on macrophages, neutrophils, and T cells (Moore et al., 2001). In addition to their protective functions, $CD4^+$ T cells have been implicated in causing inflammatory bowel disease (IBD), as well as autoimmune diseases including experimental autoimmune encephalomyelitis (EAE), type 1 diabetes, and rheumatoid arthritis (Fletcher et al., 2010; Phillips et al., 2009; Cope et al., 2007; Zenewicz et al., 2009). A balance between regulatory and effector subsets is essential to avoid inappropriate immune responses to self antigens, (Belkaid et al., 2013) but a breakdown of this balance can lead to conditions such as IBD (Powrie, 2004).

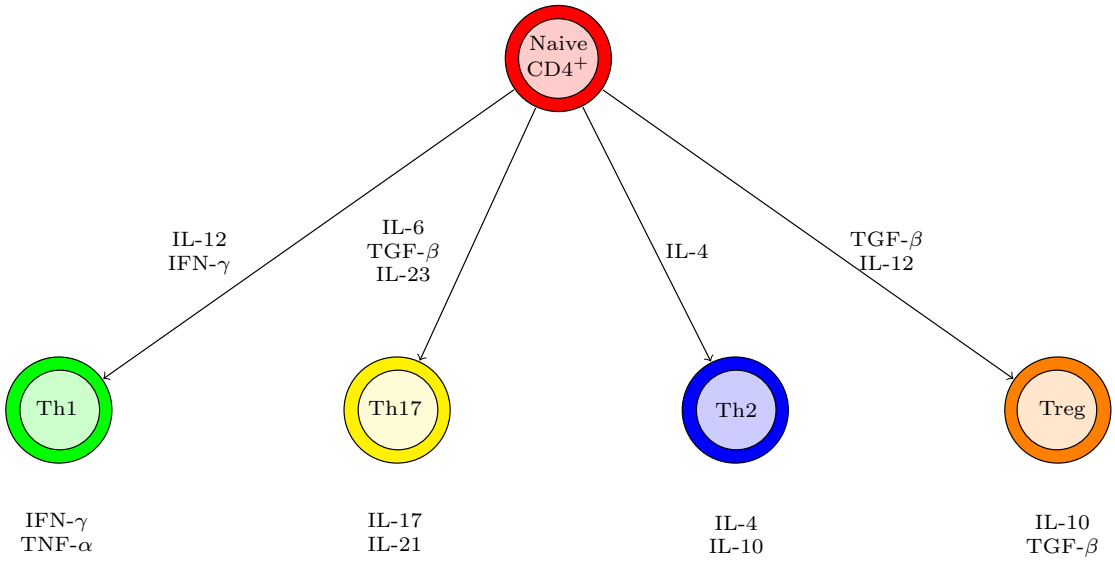

Figure 1.1: CD4$^+$ T cells differentiate into unique subsets following stimulation with different cytokines. Cartoon shows the different effector subsets that a CD4$^+$ T cell can differentiate into following activation. The cytokines driving polarisation are shown on the arrows and the cytokines produced by each subset are shown below each cell.

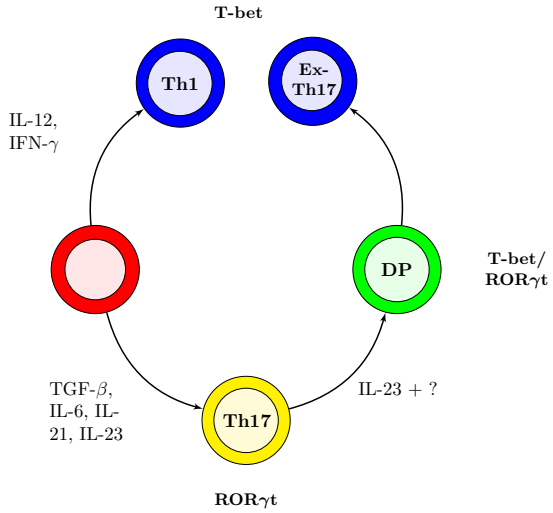

Figure 1.2: Factors controlling CD4$^+$ T-cell phenotype switching*in vivo*. Upon activation, an unpolarised CD4$^+$ T cell (red) can differentiate into a Th1 (blue) or a Th17 (yellow) cell dependent on the cytokine millieu. Th17 cells can subsequently transition through a double-positive (DP) (green) cell to an ex-Th17 cell (blue). Labels on each arrow indicate cytokines involved in this process *in vivo*. Yellow cells secrete IL-17 and IL-21, blue cells secrete IFN-γ, and green cells secrete a combination of IL-17, IL-21 and IFN-γ.

1.2 Inflammatory Bowel Disease (IBD)

In humans, IBD refers to a group of inflammatory conditions that target the gastrointestinal tract, the main forms being Crohn's disease and ulcerative colitis. Both Crohn's

disease and ulcerative colitis are relapsing conditions, meaning patients may experience long periods of remission followed by relapses where the symptoms become more active. The symptoms of these diseases include abdominal pain, recurring diarrhoea, weight loss, and extreme tiredness. The exact cause of IBD is unknown but it is caused in part by an abnormal immune response to intestinal flora, micro-organisms such as bacteria that live in the digestive tract (Podolsky, 2002; Xavier and Podolsky, 2007). During IBD shifts are seen in the microbiota composition; a decrease in anaerobes such as firmicutes and bacteroidetes and an increase in proteobacteria is observed in both animal models of the disease and in patients (Elson and Cong, 2012; Frank et al., 2011). Is is not known if these shifts in microbiota are a cause or effect of IBD; however, it is thought that the microbiota plays a key role in IBD pathogenesis (Sartor and Mazmanian, 2012). Metabolic and genetic studies have been used to shed light on the role of microbiota in IBD (Guinane and Cotter, 2013; Davenport et al., 2015), but animal and computational models can also play a key part in understanding how the microbiota effects the immune response (Suerbaum et al., 2003; Martin et al., 2007).

1.3 Mouse Models of Mucosal Inflammation

Several mouse models have been used to investigate the pathogenesis of intestinal inflammation. These include chemically induced inflammation by dextran sulfate sodium (DSS) or 2,4,6-trinitrobenz- enesulfonic acid (TBNS) as well as several different gene knock out (KO) mouse models of colitis, including the IL-10 KO model, and the CD45RB transfer model where $CD45RB^{hi}$ T cells are transferred into severe combined immunodeficiency (SCID) or recombination activating gene (RAG) KO mice model (Jurjus et al., 2004). The various colitis models are discussed at length by (Strober et al., 2002) and summarised in Table 1.1.

1.3.1 *Hh*-Induced Colitis

Helicobacter hepaticus (*Hh*) is a Gram-negative bacteria the colonises the gastrointestinal tract of mice. *Hh* has been found to be associated with the development of intestinal inflammation in both IL-10 KO mice and wild type mice treated with a blocking antibody to

Table 1.1: Experimental colitis models. Taken from (Kamdar, 2015).

Type	Description	Reference
Spontaneous Models		
C3H-HeJBir mouse	Restricted to ileocecal lesions. Inflammation is similar to Crohn's disease in that it involves a Th1 response.	Cong et al. (1998)
SAMP1/Yit mouse	Develop severe inflammation similar to CD in the colon and ileum.	Matsumoto et al. (1998)
Chemically-Induced Models		
TBNS	TBNS is a hapten administered rectally in ethanol as an enema. There is disruption of the mucosal barrier and intestinal inflammation is similar to both ulcerative colitis and Crohn's disease.	Morris et al. (1989)
DSS	DSS is given in drinking water to disrupt the epithelial barrier and induce acute colitis resembling ulcerative colitis.	Okayasu et al. (1990)
Transgenic or Knock-out Models		
IL-2 KO	Mice develop chronic inflammation similar to ulcerative colitis. Display increased T- and B-cell activation, secretion of anti-colon antibodies and dysregulated MHC II expression.	Sadlack et al. (1993)
IL-10 KO	Develop enterocolitis similar to CD, characterised by a Th1 response. Loss of IL-10 results in loss of regulation of normal immune responses to enteric antigens leading to overproduction of TNF-α and IFN-γ.	Khn et al. (1993)
STAT4 transgenic	Mice develop chronic inflammation characterised by overproduction of TNF-α and IFN-γ	Wirtz et al. (1999)
SCID Models		
CD45RBhigh $CD4^+$ T cells to RAG KO or SCID mice	Transfer of naive $CD4^+$ T cells into lymphopenic mice results in chronic colitis and wasting disease characterised by elevated levels of IFN-γ.	Powrie et al. (1993); Morrissey et al. (1993)
C3H/HeJBir $CD4^+$ T cells to C3H/HeSnJ SCID mice	C3H/HeJBir $CD4^+$ T cells are inherently reactive to microflora-derived antigens and drive the development of chronic colitis when transfered into SCID mice.	Cong et al. (1998); Elson et al. (2000)

the IL-10R, but wild type mice infected with *Hh* alone do not develop intestinal inflammation, demonstrating that there is a requirement for the absence of IL-10, IL-10R signalling in disease establishment (Kullberg et al., 1998). Commensal flora has also been shown to play a role in *Hh*-induced colitis since IL-10 KO mice housed in germ free (GF) conditions do not develop inflammation (Sellon et al., 1998). Further, studies by Nagalingam et al. (2013) and Yang et al. (2013) that show that the microbiota changes over *Hh*-infection, and that there are differences in the microbiota between IL-10 KO mice that are susceptible or non-susceptible to inflammation, that the authors hypothesise are responsible for causing pathogenesis following infection with *Hh*.

$CD4^+$ T cells have also been shown to be essential for the development of *Hh*-induced colitis as *Hh*-infected RAG KO mice do not develop intestinal inflammation unless they are given $CD4^+$ T cells by adoptive transfer (Kullberg et al., 2002).

It has also been shown that mice that lack IL12-p40, a subunit shared between cytokines IL12 and IL23, do not develop intestinal inflammation following infection with *Hh*, but that IL-12p35 KO mice (that only lack IL12, not IL23) still develop inflammation (Kullberg et al., 2006), thus IL-23 is an important cytokine in disease development. Kullberg et al. (2001) showed that administration of an anti-IFN-γ antibody, concurrent with *Hh*, blocks the development of *Hh*-induced intestinal inflammation, but that administration of an anti-IFN-γ antibody at 28 days post infection could not resolve established inflammation. This suggests that IFN-γ plays a key role in disease establishment, but not in disease maintenance. Finally, Brucklacher-Waldert et al. (2016) showed that unlike in EAE, the presence of ex-Th17 cells is not required for the development of pathology in *Hh*-induced colitis.

1.4 Modelling Biological Systems

Models have been used to inform biology through *in silico* experimentation for decades, a famous example being Watson and Cricks model that defined the structure of DNA (Watson and Crick, 1953). Modelling and simulation techniques provide novel biological insight by facilitating experimentation that is impractical to perform *in vivo* either due to cost, ethical constraints or gaps in the availability of experimental tools (Efroni

et al., 2003). Recently a combination of wet lab experimentation and modelling have been used to provide fundamental understanding in the field of immunology (Chakraborty et al., 2003; Leonov, 2015). The use of computational modelling and simulation in biology builds on the concepts of the mathematical and statistical models that have previously been developed by allowing for the creation of hybrid models that incorporate several modelling techniques. Compared with real-world experimentation, modelling is time and cost-effective. Most laboratory experiments are expensive and have to be in agreement with ethical specification. Furthermore, in a simulation environment, it is possible to systematically generate different scenarios, conduct and replicate experiments. Although computational models can take a reasonable length of time to develop, as long as the data behind the model already exists, computational modelling is an ethical, efficient way of generating insight into biological systems.

1.4.1 Mathematical models

Mathematical modelling has been used in the context of biological research for many decades (Wooley, 2005). Mathematical models can be divided into two classifications, deterministic and stochastic. In a deterministic model, every variable alters according to a mathematical function with no random fluctuations. This means that given the same input, a deterministic model will always produce the same results. Deterministic models are commonly used in immunology in the form of ordinary differential equations (ODEs) and, less commonly as partial differential equations (PDEs).

ODE models have been used to describe a variety of immunological systems at a highly abstracted level by capturing interactions between populations of entities that are represented as real numbered variables. Such models are widely used in immunology and have found applications in tuberculosis (Marino et al., 2010), influenza (Lee et al., 2009) and cancer immunology (Kuznetsov, 2004), as well as many other systems. The following example uses a simple model of human immunodeficiency virus (HIV) infection where only the key players in infection are considered Perelson and Ribeiro (2013). The model is an extension of the basic susceptible, infected, recoved (SIR) model that is commonly used to describe the spread of disease in the field of epidemiology.

The model includes uninfected target cells, T, infected cells I and free virus V and can

be represented by the following system of ODEs;

$$\frac{dT}{dt} = \lambda - d_T T - \beta V T, \tag{1.1}$$
$$\frac{dI}{dt} = \beta V T - \delta I, \tag{1.2}$$
$$\frac{dV}{dt} = pI - cV. \tag{1.3}$$

In this model, target cells are assumed to be produced at a constant rate λ, die with rate δ_T, and become infected at a rate that is dependent on the amount of free virus, βV. Infected cells die at rate δ and produce new virus cells with rate p. The virus is cleared from the system at rate c. This model can be solved to find when the number of cells in each population remains constant, called a steady state, by setting the ODEs equal to 0 and solving to reveal the steady states of the system.

$$\begin{aligned} \lambda - d_T T - \beta V T = 0 \quad &\Longrightarrow \quad \beta V T = \lambda - \delta_T T, \\ &\Longrightarrow \quad V = \frac{\lambda - \delta_T T}{\beta T}. \end{aligned}$$

$$\begin{aligned} \beta V T - \delta I = 0 \quad &\Longrightarrow \quad \delta I = \beta V T, \\ &\Longrightarrow \quad I = \frac{\lambda - \delta_T T}{\delta}. \end{aligned}$$

$$\begin{aligned} pI - cV = 0 \quad &\Longrightarrow \quad 0 = p\left(\frac{\lambda - \delta_T T}{\beta T}\right) - c\left(\frac{\lambda - \delta_T T}{\delta}\right), \\ &\Longrightarrow \quad 0 = p\left(\lambda - \delta_T T\right)\delta - c\left(\lambda - \delta_T T\right)\beta T, \\ &\Longrightarrow \quad 0 = \left(\lambda - \delta_T T\right)\left(p\delta - c\beta T\right), \\ &\Longrightarrow \quad T = \frac{\lambda}{\delta_T} \quad \text{or} \quad T = \frac{p\delta}{c\beta}, \end{aligned}$$

so the steady states $S(T, I, V)$ are

$$S_1 = (\frac{\lambda}{\delta_T}, 0, 0),$$

and

$$S_2 = (\frac{p\delta}{c\beta}, \frac{\lambda c\beta - \delta_T p\delta}{\delta c\beta}, \frac{\lambda c\beta - \delta_T p\delta}{\beta p\delta}).$$

S_1 is a state where there are no infected cells and no virus present. Linear stability analysis reveals that this state is stable if and only if $\frac{\beta v \delta c}{\delta_T} > 0$. S_2 is the infected state and is stable when $\frac{(\lambda c\beta - \delta_T p\delta)c}{p^3\delta} > 0$. Finding biological parameters for this model would identify whether there is a chance of recovery from the infected state and bifurcation theory can be used to predict the effect of different parameter values on virus dynamics during HIV infection (Kuznetsov, 2004). This model demonstrates a way in which ODE models can be used to gain insight in immunology.

PDE models extend ODEs by adding a spatial component. PDEs, like ODEs treat populations of cells as homogeneous, and as they are also deterministic, will produce the same output every time given an identical input. PDE models have been used in immunology to model antigen-independent proliferation of $CD8^+$ T cells (Antia et al., 2003) and neutrophil gradient sensing and polarisation (Onsum and Rao, 2007).

Stochastic models incorporate a degree of randomness. Allen (2003) defines a stochastic process as a collection of random variables $\{\boldsymbol{X}_t : t \in \mathbb{T}, s \in \mathbb{S}\}$, where $\mathbb{T}$ is some index set, usually time, and $\mathbb{S}$ is the sample space of the random variables. For each $t \in \mathbb{T}, \boldsymbol{X}_t(s)$ is a single random variable defined on $\mathbb{S}$. An example of a stochastic model that has been used in an immunological setting is a continuous-time Markov chain. Markov chains are state based models where the transition from state n at time t to $(n+1)$ at time $t + \Delta t$ only depends on the previous state and not on the history of the model and Δt is sufficiently small that only one event can occur in the time interval. The following example demonstrates a simple application of Markov chains in an immunological setting. The example used here considers a simplified version of the model presented by Stirk et al. (2010) and is a model of two T-cell clonotypes competing for a survival signal from an APC. At each time step, the model considers five possible transitions between states;

- The population of clonotype 1 can increase by 1.
- The population of clonotype 1 can decrease by 1.
- The population of clonotype 2 can increase by 1.

- The population of clonotype 2 can decrease by 1.
- Both populations remain the same.

The probabilities of these transitions are defined as

$$p_{\boldsymbol{n},\boldsymbol{m}}(\Delta t) = \begin{cases} \lambda^{(1)}_{n_1,n_2} + o(\Delta t) & \boldsymbol{m} = (n_1+1, n_2), \\ \lambda^{(2)}_{n_1,n_2} + o(\Delta t) & \boldsymbol{m} = (n_1, n_2+1), \\ \mu^{(1)}_{n_1,n_2} + o(\Delta t) & \boldsymbol{m} = (n_1-1, n_2), \\ \mu^{(2)}_{n_1,n_2} + o(\Delta t) & \boldsymbol{m} = (n_1, n_2-1), \\ o(\Delta t) & \text{otherwise.} \end{cases}$$

Here $\lambda^{(1)}_{(n_1,n_2)}$ is the birth rate of T cells of clonotype 1. It is the transition rate from state (n_1, n_2) to (n_1+1, n_2). Similarly, $\lambda^{(2)}_{(n_1,n_2)}$ is the birth rate of T cells of clonotype 2 and represents the rate of transitions from state (n_1, n_2) to (n_1, n_2+1), $\mu^{(1)}_{(n_1,n_2)}$ is the death rate of T cells of clonotype 1 and represents the rate of transitions from state (n_1, n_2) to (n_1-1, n_2) and $\mu^{(2)}_{(n_1,n_2)}$ is the death rate of T cells of clonotype 2 and represents the rate of transitions from state (n_1, n_2) to (n_1, n_2-1). In this model $o(\Delta t)$ represents a small error term that is proportional to the size of the time step, Δt. When a population is equal to 0, the probability of death or division of that population is also 0. This means that $\lambda^{(1)}_{(0,j)} = \lambda^{(2)}_{(0,j)} = \mu^{(1)}_{(0,j)} = \mu^{(2)}_{(0,j)} = 0, \quad \forall j$ and $(0,0)$ is an absorbing state meaning that if the process enters that state it cannot leave. This process is represented by a diagramatically in Figure 1.3. Unlike an ODE model, running this model with the same initial conditions does not result in the same output because the model is probabilistic. To combat this, multiple runs should be performed and average results taken. An application of this kind of model would be to determine if and when extinction of a clonotype will occur, and if there can be a homeostatic balance between the populations, and a similar model was used by Lythe et al. (2016) to predict the maximum number of clonotypes that the human body can maintain.

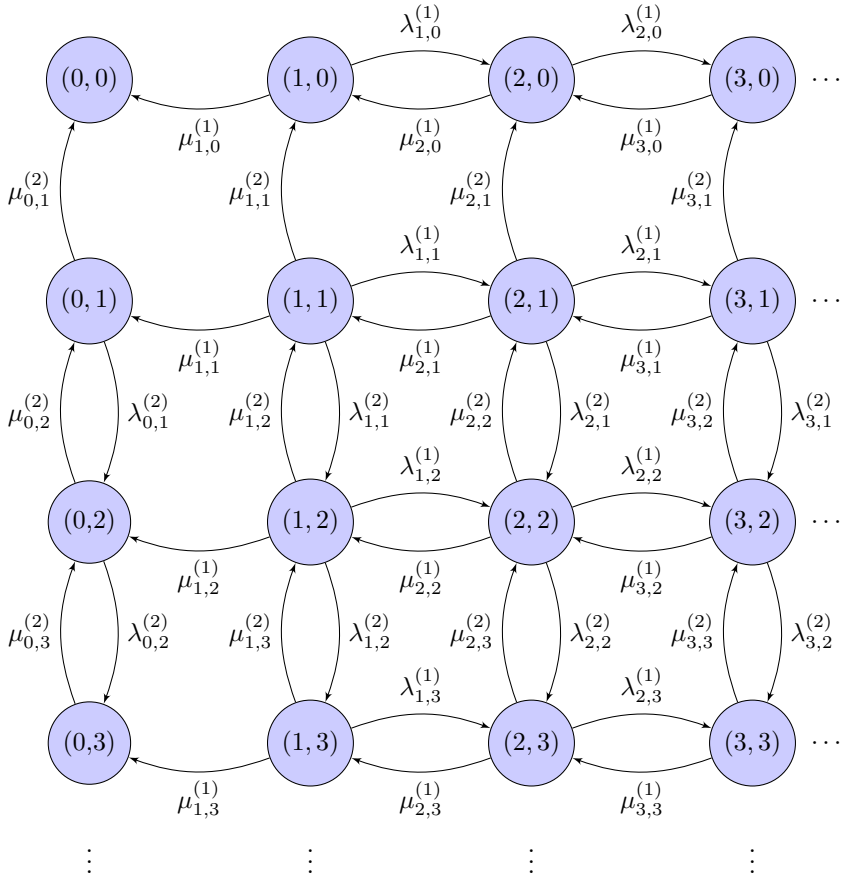

Figure 1.3: Possible transitions of two clonotypes competing for survival signals from a signal APC. The labels on each arrow represent the rates of transitions between states. In the diagram $\lambda^{(1)}_{(n_1,n_2)}$ is the birth rate of T cells of clonotype 1. $\lambda^{(2)}_{(n_1,n_2)}$ is the birth rate of T cells of clonotype 2 $\mu^{(1)}_{(n_1,n_2)}$ is the death rate of T cells of clonotype 1and $\mu^{(2)}_{(n_1,n_2)}$ is the death rate of T cells of clonotype 2.

1.4.2 Agent-based Models

Mathematical models have an underlying assumption that every cell in the population is identical. Sometimes this approach is not appropriate, and each entity in a population requires its own discrete representation. Where this is the case, the agent-based modelling paradigm can be used to allow for the emergence of heterogeneity in a population (Germain et al., 2011; An et al., 2009). In an agent-based model (ABM), the behaviour of each entity is described by a set of rules that determine how the entity can interact with other agents in the system and with its environment, and the overall system behaviour emerges as a result of each agents individual dynamics and interactions (Bauer et al., 2009). ABMs permit for the explicit modelling of space and thus allow for the exploration of hypotheses

that cannot be modelled using ODEs, for example modelling of systems with complex spatial or temporal patterns (Bauer et al., 2009). Explicit spatial modelling opens up the opportunity for developing models where the spatial distribution of environmental factors effect system behaviour such as simulating the structure within lymphoid organs (Alden, 2012) or granuloma formation in the lung during Tuberculosis (Linderman and Kirschner, 2015). Further, modelling at an individual rather than a population level allows the modeller to detect additional features of the system that may be missed with an ODE model (Figueredo et al., 2013). ABMs have successfully been used to model the onset of EAE (Read, 2011), lower respiratory tract infections with *Aspergillus fumigatus* (Pollmcher and Figge, 2014) and infection with the human gut pathogen *Helicobacter pylori* (Carbo et al., 2013).

1.4.3 Hybrid Models

The modelling techniques previously discussed can be combined to create models called hybrids. Hybrid models in immunology combine any number of modelling methodologies including ODEs, PDEs and agent-based modelling techniques. Such models have been used in wound healing (Ziraldo et al., 2013), neuron signalling (Grein et al., 2014), and for modelling cell-cycle dynamics (Eriksson et al., 2011).

1.4.4 Comparing Modelling Techniques

ODE models are an efficient way of capturing system dynamics. There are many advantages to using ODE models. These models can represent large numbers of cells or molecules very efficiently, they require fewer parameters than ABMs so there is less uncertainty, and techniques for analysing system behaviour are well defined (Bauer et al., 2009). If the system under consideration is not spatially resolved and cellular homogeneity can be assumed as is often the case when modelling metabolic networks (Francke et al., 2005) then ODE models are the sensible choice. However, many biological systems are naturally multi-scale and often to fully capture their behaviour the interaction of a number of processes that may occur on diverse temporal and spatial scales must be understood (Twycross et al., 2010). If cellular homogeneity can be assumed but the distribution of entities across the environment affects system behaviour then a PDE approach is more

appropriate (Onsum and Rao, 2007). PDEs can deal with both spatial and temporal dependencies but a disadvantage of these models is that they can be computationally intensive and thus slow. State-based models are useful for modelling heterogeneity in cell populations but do not incorporate spatial representation. Finally ABMs are very useful for representing spatial and temporal aspects of biological systems but there are challenges associated with studying the interconnectivity between the agent rules and the dynamics of the biological system (Mc Auley et al., 2015). The appropriateness of each modelling methodology is summarised in Table 1.2.

		Spatially Resolved	
		NO	YES
Cellular Hetrogeneity	NO	ODE	PDE
	YES	State-Based Model	ABM Hybrid-ABM

Table 1.2: Areas of application of different modelling methodologies. Taken from (Cosgrove et al., 2015).

1.5 Modelling Tools and Protocols

In the field of computational modelling protocols allow models to be shared and extended by clearly laying out the details of a model in a way that can be easily understood. A number of frameworks and toolkits have been created to aid model development, and to bridge the gap between a real world complex system and a model being used to study it. This section reviews the techniques and tools that are currently available to assist with the modelling of complex systems.

There are three frameworks for building a computational model reviewed here. These are overview, design concepts, and details (ODD) protocol for building ABMs, the Complex Systems Modelling and Simulation (CoSMoS) process for developing computational models of complex systems, and Systems Biology Mark-up Language (SBML) for devel-

oping ODE models to describe processes in biology and biochemistry.

1.5.0.1 The ODD Protocol

The ODD protocol is a standard protocol specifically for describing ABMs, that was developed for the field of ecology by Grimm et al. (2006) and has since been applied to several ABMs (Schreinemachers and Berger, 2011; Franz and Nunn, 2009; Larsen et al., 2010). The idea of the protocol is to always structure the information about a model in the same way. As the name suggests, the protocol focusses around three blocks, overview, design concepts, and details.

Overview: The overview block is broken down into submodels of purpose, state variables and scales, and process overview and scheduling. The aim of this section is to provide an outline of the purpose and high level structure of the model.

Design Concepts: The design concepts block describes the thoughts underlying the design of the model and its purpose is to link model design to general concepts identified in the complex system under study.

Details: The details block includes three further elements, initialization, input and submodels. This section extends the overview to give a more comprehensive description of how the model was implemented and should be able to act as a blueprint to the model.

Table 1.3: Framework for ODD

Overview	Purpose State variables and scales Process overview and scheduling
Design Concepts	Design concepts
Details	Initialisation Input Submodels

Each block is divided into elements that are designed to define a structure to be used when describing an ABM (Table 1.3). The elements all contain information relating to specific parts of the model. These elements are:

Purpose This is the first element that needs to be defined because it is essential in identifying the simplifications that can be made. It is here that information about why the model has been developed, and what the model is going to be used for are defined.

State variables and scales The full set of state variables should be defined with this element. That is, the variables that characterise the entities and environments of the model for example an environment might be characterised by location, size, chemical composition, and multiple other factors. Information gathered at this stage in the protocol is low-level, and are elementary properties of the model, so detailed descriptions of entities are not initially required here. Once this information has been collected for all entities in the model higher-level relationships should be described. Finally scales and dimensions of time and space must be defined for all entities.

Process overview and scheduling This element is concerned with defining the processes that are built into the model without defining the way in which these processes will be represented. Orders of processes are also defined and the schedule for updating the state of an agent is recorded.

Design concepts The design concepts provide a common framework for designing and communicating ABMs. Grimm et al. (2006) gives a check list of questions that might be asked during this phase of model development that cover the topics of emergence, adaptation, fitness, prediction, sensing, interaction, stochasticity and collectives.

Initialisation This is where the initial conditions are defined and it is an important feature in making ABMs reproducible.

Input Changes in environmental conditions over time or space are defined under the input element. Output of a model gives the response of the model to a specified input.

Submodels Here, submodels representing the processes listed in the process overview and scheduling element are developed. The models should be explained in detail and all parameters should be defined. It is proposed that two versions of the detailed model description be written. The first is the mathematical description of the model that consists of the equations, rules and parameters with their dimensions, that describe

the entities in them model. The second is a full model description that has the same structure as the mathematical skeleton given in the previous question that is, the same equation number and subtitles are used. This submodel can be very long and complex.

An example of ODD being used in practice is demonstrated by Grimm et al. (2006). ODD was designed specifically for the field of ecology but there is no reason it cannot be applied to any other field where an ABM is being developed. An example of ODD being used outside of the field of ecology is given by Franz and Nunn (2009) who uses the tool to describe a model that used network-based diffusion analyses to detect social learning.

1.5.0.2 The CoSMoS Process

The CoSMoS process (Andrews et al., 2010) provides a framework for developing computational models of complex systems. It was not designed for any specific field but has found many applications in biological systems (Garnett et al., 2008; Read, 2011), as well as in ecological and social systems (Polack et al., 2010). The framework proposed by the CoSMoS process has three key stages;

Discovery Phase: The discovery phase establishes the scientific basis of the model. The overall research context is established, and then the domain of interest, is identified and modelled, and scientific questions are determined that give the model a specific purpose. These questions are important to have in mind when building the model to ensure that it is fit for purpose. The discovery phase focusses on science and questions rather than simulation, and involves a lot of reading around the subject area to develop a solid understanding of the complex processes involved in the system.

Development Phase: Once the discovery stage has been completed, the next stage is to use the conceptual models developed in the discovery phase to develop a simulation platform.

Exploration Phase: After the simulation platform has been developed, it can be used to explore the scientific questions established during the discovery phase.

Building an executable model using the CoSMoS process requires the development of a

series of non-executable models that need to be modified iteratively throughout the development process (Figure 1.4). These non-executable models underpin the understanding of the system that is to be modelled and provide a description of what has been included in the model. Developed in collaboration with experimentalists, the models contain system and implementation specific details including justifications on any abstractions or assumptions that have been made.The models developed under the CoSMoS process are:

Research Context: that asks what the motivation is for creating such a model, formulates the questions to be addressed by the simulation platform and the requirements for validation and evaluation. It is here that the research domain is identified.

Domain Model: that brings together the important aspects of the domain focussing on scientific understanding with no simulation implementation details considered.

Platform Model: that focusses on how aspects of the domain model will be implemented in the simulation and how the questions defined in the research context will be answered. This stage may require further simplification of the model details if implementation is not possible due to a lack of data or a gap in modelling functionality.

Simulation Platform: that requires the platform model to be encoded into a software from which simulations can be performed.

Results Model: that contains the answers to the questions determined in the exploration phase. It is where ideas that need to be verified *in vivo* are generated.

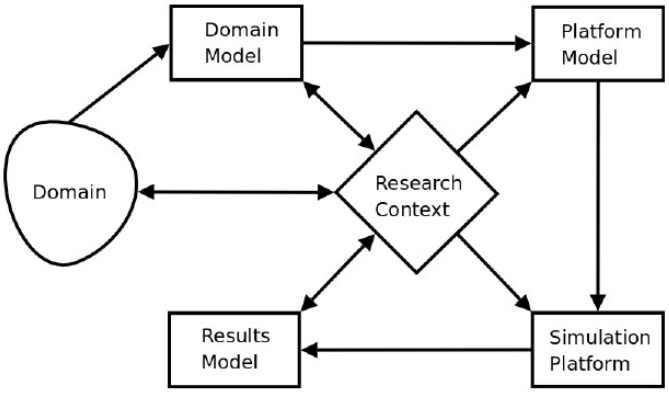

Figure 1.4: Stages of model development under the CoSMoS process. Models created under the CoSMoS process are linked to the domain of interest through the research context. Figure taken from Andrews et al. (2010)

An example of CoSMoS being used in practice is demonstrated by Read et al. (2012); Alden (2012); Moyo (2014).

1.5.1 Systems Biology Mark-up Language (SBML)

SBML was developed in 2002 to provide a methodology that would allow models of biological processes to be evaluated, developed and exchanged(Hucka et al., 2003). SBML is represented in the eXtensible Markup Language (XML) (Bray, 1998), a language that is accepted as a standard data language in bioinformatics (Achard et al., 2001). Computational models of a range of processes, including cell signalling and metabolic pathways (Dias et al., 2015), biochemical reactions (Bois, 2010), and gene regulation (Feist et al., 2007), have been described via SBML. A model definition in SBML consists of lists of one or more components from the following list (Hucka et al., 2003);

Compartment A container of finite volume where reactions take place. The distribution of substances across a compartment is assumed to be homogeneous.

Species A chemical substance or entity that takes part in a reaction.

Reaction An equation describing the interaction that occurs between species, described using rate laws.

Parameter The numbers governing reaction rates. These can be global, that is they apply to the whole model, or local, applying to one specific reaction.

Unit Definition The name for a unit used to express the quantities of a model.

Rule A mathematical expression to model effects that are not represented as reactions.

The usage of a standardised markup language facilitates the deposition of models in repositories in repositories, such as BioModels (Li et al., 2010), and numerous software tools have been released to aid design and implementation. These tools allow SBML models to be simulated over time. As the name suggests SBML was developed specifically for biological and biochemical models and has found little application outside of those fields.

1.6 The Automated Simulation Parameter Alteration and SensItivity Analysis (ASPASIA) Toolkit

Automated Simulation Paramater Alteration and SensItivity Analysis toolkit (ASPASIA) was developed as a tool for parameter alteration and sensitivity analysis of SBML models (Evans, submitted) but has also been useful for parameter estimation. To estimate model parameters using ASPASIA parameter values are varied over a range that is based on data from the literature and a number of SBML models are created with different parameter sets. These models are solved for a specific length of time after which ASPASIA can be used to add any required interventions. Sensitivity analyses can be performed on the results of these simulations to determine the important parameters and models that match specific biological criteria can be identified by plotting the results against known data. These plots can then be used to determine more accurate ranges for sensitive parameters or to select a single model on which a local sensitivity analysis can be performed to determine how robust the model is to small changes in parameter values.

1.6.1 Immune System Simulation Platforms

The frameworks mentioned above aid in the specification of a model but do not specify how the model should be implemented. A number of platforms have been developed to enable the interactions between cells to be specified and responses to these interactions to be simulated. The objective behind the creation of such tools is to allow biologists to develop ODE or ABM simulations without needing an in depth knowledge of the mathematics or computer programming involved in generating the model. There are a number of these platforms have been developed for ODEs and ABMs (Table 1.4), but here we discuss CellDesigner (Funahashi et al., 2008) and Biocellion (Kang et al., 2014).

CellDesigner is a process diagram editor for gene-regulatory and biochemical networks (Funahashi et al., 2008). It facilitates the development of SBML diagrams from process diagrams that are developed using the user interface. Genes, receptors, RNAs and proteins are created and interactions are symbolised by arrows between the interacting species and the parameters governing each interaction label the arrows. Once created, these diagrams can be saved in the format of an SBML model that can be simulated using COmplex

PAthway SImulator (COPASI) (Hoops et al., 2006) resulting in a time course of the levels of each species in the model over time and find a steady state as well as multiple other analyses. The advantage to this approach is that it is much easier for a biologist with no modelling experience to design a diagram detailing interactions, than for them to develop a model in SBML. A disadvantage to using this approach only works for ODE models so no spatial aspects can be considered in such a model.

Biocellion is a platform for developing agent-based models of biological systems. It has three computational modules to i) update individual discrete agent states, ii) evaluate direct physico-mechanical interactions between discrete agent pairs in close proximity and iii) track changes in extracellular space to model indirect interactions among cells via diffusible molecules and interactions between cells and their environment (Kang et al., 2014). It has been used to reproduce models several biological scenarios including cell sorting, microbial patterning in communities of different yeast strains engaging in metabolic interactions and a bacterial system in complex soil structures (Kang et al., 2014). Models developed in Biocellion are restricted to predefined local behavioral rules. Global processes such as blood flow can not be modelled using biocellion. Further it does not include a full range of ODE solvers, and a mathematical background would be required to implement such methods. This makes it more difficult for a biologist to adapt models using such platforms.

1.6.2 Simulation Toolkits

The simulation platforms listed above are very useful for developing models that do not require spatial representations (CellDesigner, Simmune), or for grid-based ABMs that do not require the inclusion of global processes, or multi-agent representations of cells (ImmunoGrid, IMMSIM, Reactive Animation, Biocellion). However, often these platforms fall short of the functionality required to model specific systems in detail and, in this case a bespoke simulation platform must be developed. Several toolkits have been developed to aid model development. In the case where an ABM is most appropriate to capture system dynamics, a range of simulation toolkits are publicly available (Table 1.5). All of the toolkits listed provide a basic functionality upon which complex simulatons can be built. This includes tools to create environments and agents as well as a framework for

Table 1.4: Examples of computational modelling toolkits.

Platform	Reference	Models	Applications
CellDesigner	Funahashi et al. (2008)	ODE	Molecular interactions in Rheumatoid Arthritis (Dampier and Tozeren, 2007)
Simmune	Meier-Schellersheim et al. (2006)	ODE	Signalling networks for eukaryotic chemosensing (Meier-Schellersheim et al., 2006) Signalling network in G-protein coupled-receptors (Zhang et al., 2013) Circadian rhythms in Drosophilia (Xie and Kulasiri, 2007)
ImmunoGrid	Pappalardo et al. (2009)	ABM	Vaccine administration (Pappalardo et al., 2009)
IMMSIM	Celada and Seiden (1992)	ABM	Immunological memory generation Celada and Seiden (1992) Hypermutation (Celada and Seiden, 1996) S1P chemosensing by macrophages (Manes et al., 2015)
Reactive Animation	Efroni et al. (2005)	ABM	Development of T cells in the thymus (Efroni et al., 2005) Neural simulations (Lytton et al., 2008)
Biocellion	Kang et al. (2014)	ABM	Pouch Metaplasia (Cockrell et al., 2015)

specifying rules that agents can follow but the modeller is required to actually specify what the rules are, and thus the user must have some level of knowledge of the language the tool is written in. Simulations of models created in this toolkit are executed in discrete time steps during which every agent in the system performs the behaviours specified by its rules. All of the toolkits listed have found application in modelling biological scenarios in a range of areas. Examples include modelling Payers Patch development using Multi-Agent Simulation Of Neighbourhoods (MASON) (Alden, 2012), modelling immune defence against spores of pathogenic fungi using NetLogo (Tokarski et al., 2012), investigating the function of a group of non coding RNAs, microRNAs, that regulate gene expression at a

Table 1.5: Examples of simulation toolkits available for developing ABMs

Toolkit	Reference	Description
MASON	Luke et al. (2005)	A discrete-event multi-agent simulation library written in Java, designed to be the foundation for large custom-built Java simulations
NetLogo	Tisue and Wilensky (2004)	A multi-agent programming language and modelling environment for simulating natural and social phenomena.
Repast	North et al. (2013)	A widely used, free, and open source environment for agent-based modeling of complex adaptive systems.
FLAME	D'Souza (2008)	A very general system for building detailed agent-based models that generates highly efficient simulation software that can run on any computing platform, in particular it can be run directly on High Performance parallel supercomputers

post-transcriptional level using Repast (Leonov, 2015), and modelling the nuclear factor-kappa B (NF-$_{\mathrm{K}}$B) signalling pathway using Flexible Large-scale Agent-based Modelling Environment (FLAME)(Williams et al., 2014).

1.7 Existing Computational Models of Intestinal Inflammation

This thesis focusses on the design and utility of a computational model of the processes active in the gut following infection of IL-10 KO mice with *Hh*. The aim of this study is to gain insight into the factors contributing to human IBD. Several mathematical models of intestinal inflammation have been developed (Arciero et al., 2010; Leber et al., 2015; Marchuk, 2013) but few consider autoimmunity and specifically IBD. Lo et al. (2013) developed an ODE model describing the roles of T cells in IBD, focussing on the balance between Th1, Th2 and T-reg cells in the pathology of IBD. The model was developed to provide a conceptual framework as a basis for future investigations and as such was

not used for experimentation. The other available model of IBD was developed by Wendelsdorf et al. (2010) and focussed on immune modulatory mechanisms in inflammatory bowel disease. This complex mathematical model describes several different populations of cells in the gut during IBD but considers cytokines as only "activating" or "deactivating". ENteric Immunity SImulator (ENISI) is an ABM simulator for modelling gastrointestinal immune infections caused by immune responses to an invading microbe including commensal bacteria and pathogens (Wendelsdorf et al., 2012). In this system, bacteria and immune cells are represented as agents that move around and interact with their environment. ENISI does not contain a framework for explicit representation of cytokine and gene regulation networks, nor does it allow for dynamic addition or removal of agents meaning that all cells in the system must be specified at the initial starting time.

1.8 Model Validation

Experimental systems are an abstraction of the real-world biology that can be used to study a specific part of a bigger problem. Implementing a computational model of a biological system, e.g. of an animal model of human disease, adds further uncertainty as the end result is a model of a model and is therefore even further removed from the original biological system than the animal model. This does not mean that computational models of experimental systems are not useful as models do not need to be a full representation of a system to generate understanding into how interactions between factors lead to an overall emergent behaviour (Germain et al., 2011). When generating mathematical and computational models, it is important that the assumptions and abstractions are well documented and are taken into account when analysing model results in the context of their impact on the wider biological system that the model is contributing to the understanding of. Read (2011) developed several methods that can be employed to increase confidence in computational results from models of biological systems including aleatory and sensitivity analysis, and model validation.

1.8.0.1 Ensuring a Model Adequately Represents Biology

For a computational model to be useful, the modeller must be able to prove that the results of simulations adequately represent biology. Computational models of biological systems often contain large numbers of parameters and calibration is required to establish a set of parameter values that produce an expected system behaviour. Sensitivity analysis around these parameter values can be used to determine which parameters have the greatest effect on simulated behaviours. Parameters that are deemed to be important should be the most strongly grounded in biology. In addition, performing uncertainty analysis on a model can help to quantify implementation-based error.

1.8.0.2 Aleatory Uncertainty

Aleatory uncertainty is the effect of implementation-induced stochasticity on the results of the simulation. It is critical that the effect of inherent simulation stochasticity on results be understood for modelling and simulation techniques give meaningful biological output (Helton, 2008). In agent-based simulations the use of a pseudo-random number generators to dictate agent behaviour can produce different simulation results despite use of identical parameter values (Alden et al., 2013). To mitigate the effects of this uncertainty, several runs of the simulation must be performed and average results taken. There are many techniques for determining the number of runs that should be performed (Robinson, 2014), that have been implemented in the Simulation Parameter Analysis R Toolkit ApplicatioN (Spartan) toolkit (Alden et al., 2013).

Law and McComas (1991) advocate a rule of thumb approach where they reccomend that at least three to five replications are performed. This approach does not take into account the characteristics of a model's output and in reality many more replications need to be performed to reduce variability of highly stochastic data.

Another approach is the graphical method described by Robinson (2014). This method requires the modeller to plot the cumulative mean of results increasing the number of runs until the mean becomes relatively stable. Figure 1.5 shows an example of how a plot like this might look. In the example, 50 is deemed to be a sufficient number of replicates, since performing additional replicates after this point does not further reduce variability.

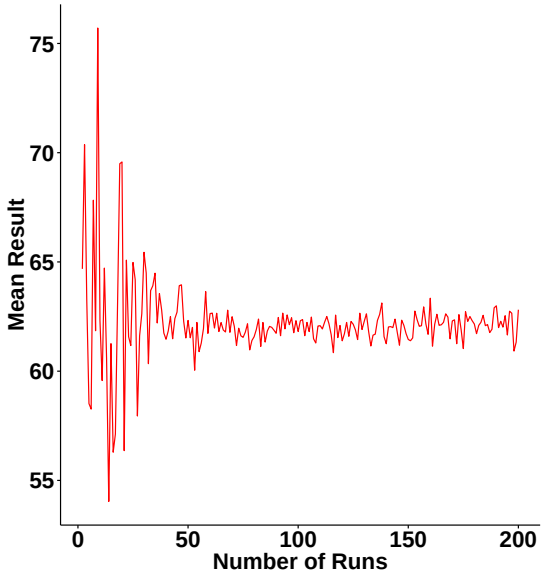

Figure 1.5: Using a graphical approach to determine the number of replicates. The mean value of a simulated measure was calculated increasing the number of replicates from 1 to 200.

This final method discussed by (Robinson, 2014) is the confidence interval method. Using this method, a confidence interval (CI) is developed to show how accurately the mean result is being estimated (Equation (1.4)). A narrower interval means the result is more accurate, a wider interval less so. The formula for the confidence interval is calculated as follows:

$$CI = \bar{X} \pm t_{n-1,\alpha/2} \frac{s}{\sqrt{n}}, \tag{1.4}$$

where $\bar{X}$ is the mean output from the replicated runs, $t_{n-1,\alpha/2}$ is the value for the significance level of $\alpha/2$ from a Student's t-distribution with $n-1$ degrees of freedom, S is the standard deviation, and n is the number of replications. The adequate number of runs can be determined by finding the percentage by which the width of the confidence interval deviates from the mean and choosing the value where this reaches an appropriate level, 5% say. In the results shown in Figure 1.6, an adequate number of runs would be 10, chosen by finding when the deviation of confidence interval from the mean result is less than 5%.

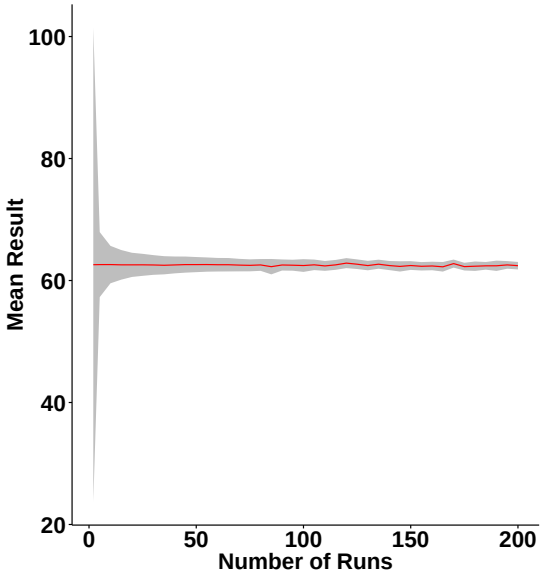

Figure 1.6: Using the confidence interval method to determine the number of replicates. The confidence interval (grey) and mean (red) of the data value was calculated increasing the number of replicates from 1 to 200.

1.8.0.3 Sensitivity Analysis

Sensitivity analysis is a method for quantifying uncertainty in a complex model by determining how input factors such as parameters or initial conditions impacts model outcome (Marino et al., 2008). Local sensitivity analysis determines how a small perturbation of input parameters influences model behaviour. It is a one at a time technique meaning that it looks at the effect of varying each parameter in turn. Performing an effect size magnitude test, such as the A-test or Cohens D test, on results from executing models with each parameter set reveals how robust the model outcomes are to this variation of each parameter.

The effect that one parameter has on a simulated measure can be highly dependent on values of other parameters in the system. In this case a global sensitivity analysis is a more appropriate measure of uncertainty (Read et al., 2012). Global sensitivity analysis examines the relative effect of a each parameter on the simulated measures when multiple parameters are varied simultaneously. To quantify the effect that uncertainty around the parameters in the model affects the output from a simulation, partial-rank correlation coefficient (PRCC) are calculated. Partial correlation characterise a linear relationship between input x_i and output y after the linear effects of $x_j,\ j \neq i$ on y have been discounted. Performing partial correlation on rank-transformed data, that is data

where the inputs are sorted by magnitude, results in a set of PRCCs that can be used to determine the parameters that have the greatest effect on the simulated output (Marino et al., 2008).

Parameter generation for both of the sensitivity analysis techniques is done using a sampling-based approach. For the local, one at a time analysis, the parameters values are sampled at uniformly spaced increments between the maximum and minimum values (Alden et al., 2013) and for global sensitivity analysis, the sampling method used is Latin-hypercube sampling (McKay et al., 1979; Helton, 2008).

The Spartan toolkit aids generation and analysis of the parameter sets for performing sensitivity analysis (Alden et al., 2013) of ABMs and ASPASIA has been developed to allow similar analysis to be performed on SBML models Evans et al. (submitted)

1.8.1 Calibration and Establishment of Baseline Behaviour

Calibrating computational models of biological systems, assigning parameter values to ensure the model reflects behaviours observed biologically, can greatly impact the strength of hypotheses the model generates. A calibrated model provides baseline behaviour upon which sensitivity analysis techniques can be used to analyse potential pathways impacting model response. However, the stochastic nature of biological systems results in significant uncertainty and variance in data (Read et al., 2012). The calibration process of IBDSim involves the simulation being executed with a set of "best guess" parameters that are set either from data in the literature or by estimating sensible values from responses observed when parameter scans were performed on individual pathways within the model. After these parameters were set, average results from a series of simulations were collected to mitigate aleatory uncertainty, and the modeller and domain expert examine by eye how the simulated data compares to that from biology. Once a suitable set of parameters had been determined, the model was validated by simulating the effect of biological problems for which the outcome was already known. This approach increases confidence that the model can be used to perform experimentation into situations where the outcome is yet to be determined.

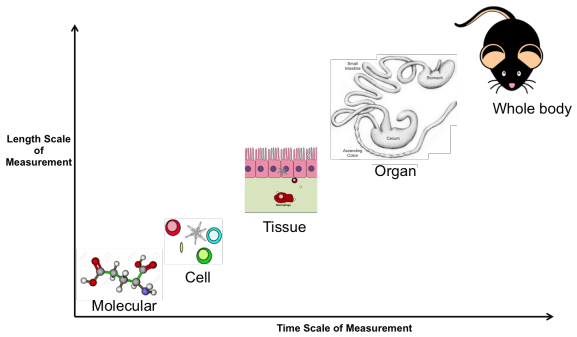

Figure 1.7: Examples of spatial and temporal scales in biology. Arrows represent decreasing granularity

1.9 Dynamic Tuneable Resolution

During the course of a biological experiment, data is often collected different scales. In the *Hh*-induced colitis model for example, data collected includes body weight of mice (whole body scale), length of cecum or colon (organ scale), concentration of cytokine in the cecum or colon (tissue level) and phenotype of $CD4^+$ T cells in cecum or colon (cell level). Although different wet-lab techniques are required to collect the data relevant to each scale, the overall model used to generate the data is the same. Kirschner et al. (2014) argues that a computational model should have the same capabilities. The tuneable resolution approach proposes that multi-scale models should be built with multiple levels of granularity so that a fine or course-grained version of the model can be employed at the users discretion. This allows the resolution to be adjusted in order to answer a specific question or to replicate a specific biological experiment without becoming unsustainable and expands options for model validation and increases model usability.

In addition to providing the flexibility to span varying aspects and scales of interest, tuneable resolution enables a more comprehensive model validation by increasing the variety of ways that *in silico* experiments can be validated against biological data. Further, fine-graining a model can result in an improved course-grained model by providing the opportunity to re-implement the way that abstracted aspects were coded during the first iteration. Tuneable resolution can help identify model flaws through detailed exploration of aspects of the model.

Dynamic tuneable resolution allows different parts of a model to be switched on or off depending on their state. Dynamic tuneable resolution in complex model development

has two main uses, modify the frequency at which parts of a model are run, known as an adaptive time steps and modify or remove parts of the model that are in steady state and temporarily replace them with an abstracted version that results in the same effects. Adaptive time steps are commonly used when solving systems of differential equations numerically to reduce running time and there are several algorithms for determining how large the time step should be at a particular point in the simulation (Minkoff and Kridler, 2006). A similar approach can be used in agent-based modelling to switch between spatially resolved and simplified model compartments using agent behaviours as a trigger for switching compartments on and off.

1.10 Summary

The basic immunology that needs to be understood before developing a model of *Hh*-induced intestinal inflammation has been introduced in this chapter. A variety of modelling techniques that could be used to capture the dynamics of cells and cytokines in the model have also been discussed. Further, previous *in silico* models of intestinal inflammation have bee examined, and it has been determined that neither of these models capture the multi-scale and spatial aspects of inflammation, or allow for the addition of *Hh*, or the recalibration to data from the Kullberg lab. Finally, methods for grounding simulations in biology, and for model validation have been discussed as well as a technique for reducing the computational burden of large multi-scale computational models.

1.11 Thesis Aims

This thesis details the development and utility of a computational model of *Hh*-induced intestinal inflammation and focusses on three main aims:

Aim 1: Develop a computational model that captures the processes active in the gut during *Hh*-induced intestinal inflammation.

Aim 2: Explore the therapeutic effects of a lymphocyte blocking antibody on *Hh*-induced colitis

Aim 3: Determine whether alterations in microbiota alone are sufficient to cause alterations in the phenotypes of disease in intestinal inflammation.

Chapter 2

A Computational Model of Intestinal Inflammation

IBD affects over million people in the developed world and usually manifests as either ulcerative colitis or Crohns disease (Kaplan, 2015). Although the exact cause of IBD is unknown, a dysregulated immune response to the intestinal flora is thought to play a role in disease pathogenesis and genome wide association studies have recognised 71 susceptibility loci for Crohns disease. Genetic factors including defects in IL10 production have also been identified as contributory factors. Several mouse models have been used to investigate the pathogenesis of IBD (Table 1.1). These include chemically induced inflammation by DSS or TBNS as well as KO models (DeVoss and Diehl, 2014). Mice that are deficient in IL10, an anti-inflammatory cytokine, spontaneously develop inflammation of the lower intestinal tract (Khn et al., 1993) (Section 1.3.1).

As defined in Chapter 1, the aim of this project is to develop a computational model of intestinal inflammation based on the *in vivo* *Hh*-induced colitis model. This chapter details the development of such a model that captures the processes active in the gut during the induction of intestinal inflammation in IL-10 KO mice infected with *Hh*. In this thesis, the model has been used for exploring the effects of potential therapeutic targets and identify the best time course for treatment, and also to explore the factors driving intestinal inflammation in the *Hh*-induced colitis model to drive *in vivo* experimentation (Chapters 3,4).

The model was developed following the CoSMoS process (Andrews et al., 2010) that

provides a framework for developing computational models of complex systems. Within the CoSMoS process, the research context must be defined prior to model development. The research context identifies the questions that the model is being built to address and establishes the aspects of intestinal inflammation, and health, that are important in answering these questions. Once the research context has been established, a series of models are developed that are modified iteratively throughout the modelling process to aid production of an executable model that adequately reflects the biological system. The models created following this process form several modules, also referred to as models, that are detailed in Section 1.5.0.2. These modules underpin the understanding of the research domain that is to be modelled in relation to the research context and provide a blueprint from which an executable model can be built. Developed in collaboration with experimental immunologists the modules, or models, of the CoSMoS process contain biological- and implementation-specific details including justifications of any abstractions or assumptions that have been made.

Unified Modelling Language (UML) notation is widely used in software engineering for specifying what is required of a system and how it may be implemented, as well as providing a guide during the software development process. Where the CoSMoS framework has been applied in similar biological applications (Read et al., 2012; Alden, 2012; Moyo, 2014), the use of a series of diagrams developed using a subset of UML diagrams (Fowler, 2003) has proven advantageous for describing the biological background of the model, as well as for identifying model-specific details. The advantage of using UML in this context is that it has a predefined structure that can be learned and understood by users from all disciplines, and that it provides a framework for describing interactions and behavioural changes that is clear, concise and consistent between models.

This chapter describes the non-executable domain and platform models, details of the simulation platform that describes how the model has been built, and the results model in which simulation output is compared with *in vivo* data collected in the Kullberg lab. The techniques used to develop, calibrate, and validate the model ensuring it is fit for the purpose of this study, are also discussed here.

2.1 Research Context

The aim of defining a research context is to set the scope and purpose of the model. The domain of study for this model is the large intestine before and after infection of IL-10 KO mice with *Hh*. As discussed in Section 1.3.1, the organs involved in the development of *Hh*-induced colitis are the cecum, colon and mesenteric lymph node (MLN) and inflammation within these compartments is dependent on the presence of both innate cells and lymphocytes. Innate cell and lymphocyte subsets and their roles in contributing to inflammation are discussed in Section 1.1.1.1 and it can be concluded that the cells of interest from the research domain can be reduced to $CD4^+$ T cells, DCs, macrophages and the cecum, colon and T-cell zone of the MLN.

2.2 A Domain Model for *Hh*-Induced Colitis

As previously stated in Section 1.5.0.2, the domain model is a non-executable model detailing what is known, or hypothesised, to occur in a biological or experimental system of interest. This model focusses on scientific understanding of the biological system and on the research questions that need to be addressed At this stage of the modelling process, no thought is given to how an executable model will be implemented. Previous studies, for example those by Bersini (2006); Read et al. (2009) and Alden (2012), have used three types of diagram to model the biological domain:

Expected behaviours diagram: This diagram is indicates how interactions between the entities identified in the research context contribute to system-level behaviours. The phenomena expected to emerge from any model of the biological system of interest, and the time scales on which these phenomena occur, are stated, and hypotheses of how the phenomena manifest are developed. Each phenomena is joined to a hypothesis that is then linked to the cell types whose interactions are thought to cause the phenomena to develop, if this information is known. This type of diagram helps to set the scope of what entities need to be in the model and what can be excluded and ties the scope of the model to observations and data collected *in vivo*. This type of diagram is not a UML diagram.

Activity diagram: These diagrams are used to represent work flows, and are written in UML. In this context, they describe actions and interactions between cellular components in biology. A guide to understanding UML in the context of activity diagrams is shown in Figure 2.1. Activity diagrams elaborate on the interactions defined in the expected behaviours diagram by defining the conditions under which these interactions to take place. Further, activity diagrams highlight any other events that occur as a result of this interaction happening, or as a result of the interaction not happening.

State diagram: These diagrams define the physical behavioural changes an entity can be in and identify the factors governing the emergence of these behaviours. Like the activity diagrams, the state diagrams are also written using UML, and a guide to understanding additional UML notation in the context of state diagrams is shown in Figure 2.2. State diagrams give more detail about the behaviours an entity can exhibit and are useful for explaining behaviour at an individual rather than a population level. These diagrams help a modeller to fully understand the types of behaviour each entity can exhibit *in vivo*.

The diagrams presented in this chapter were developed following a detailed literature search and in close collaboration with experimental immunologists. Through creating the domain model, biological parameters were identified and where they existed values for known biological parameters such as life spans and velocities of cell types, were recorded. These parameters are listed in Appendix A.

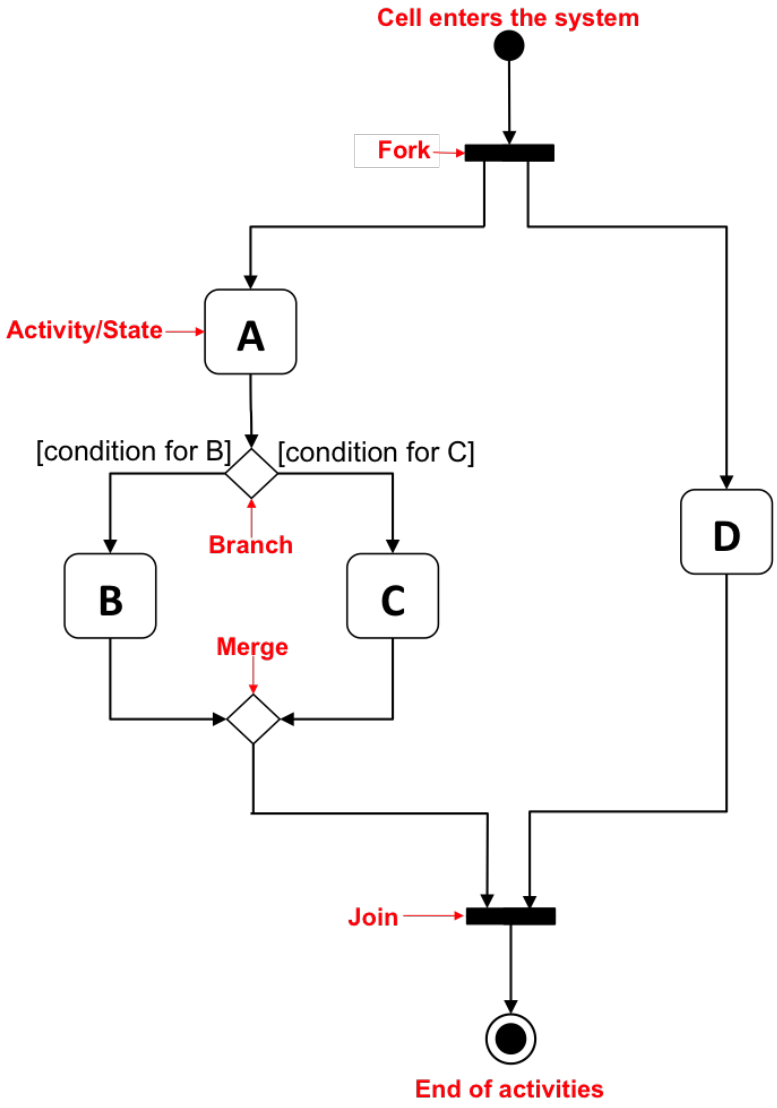

Figure 2.1: UML notation for an activity diagram. The syntax used to describe biological processes as activity diagrams in both the domain and platform models: Rounded rectangles represent actions or activities, diamonds represent decisions, forks and joins represent the start and end, respectively, of acitivities that occur concurrently, a black circle represents the start of the processes for that system while a double circle represents the final state after which no further activities can occur. Expressions in square brackets ([]) define conditions that must be satisfied for the next activity to occur.

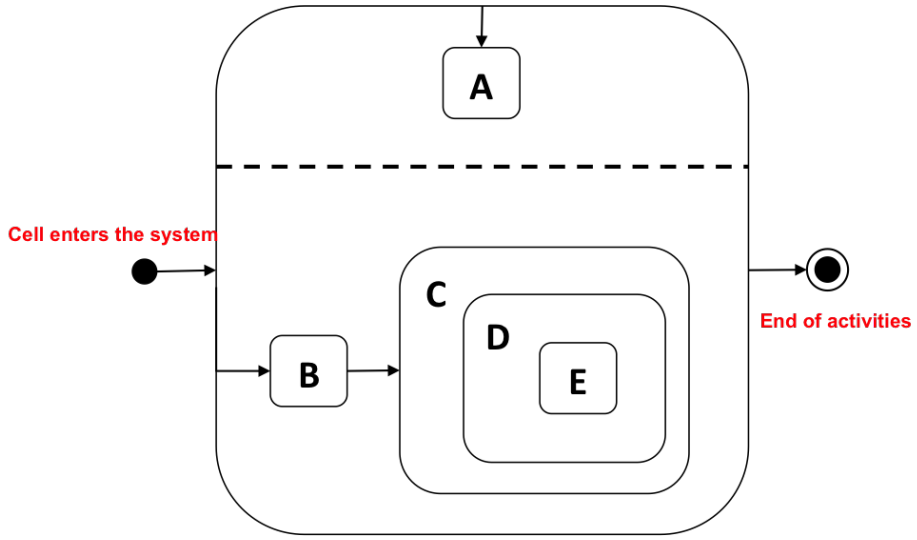

Figure 2.2: UML notation for a state diagram. The syntax used to describe biological properties in a state diagram in both the domain and platform models. Rounded rectangles represent states. A rounded rectangle inside of another one is a substate and means that if the object is in the state of the outer rectange then it can also be in the inner state. A black circle represents the initial state of the object while a double circle represents the final state. As in the domain model expressions in square brackets can be used to define conditions that must be satisfied for an object to proceed into that particular state. A dashed line represents concurrent states.

2.2.1 Expected Behaviours Diagram

The first task in developing the domain model for *Hh*-induced colitis was to identify the key observable phenomena that the model should capture, and determine how these phenomena emerge as a result of entities, such as cells, cytokines and any other factors, in the system interacting with each other and with their environment. Meaningful links between the phenomena observed and the entities in the system, along with hypotheses of how these behaviours manifest *in vivo* were captured in an expected behaviours diagram (Figure 2.3). In the *Hh*-induced colitis model, there are two key observable biological phenomena:

1. **The bacterial load in the cecal lumen is undetectable before *Hh* inoculation, peaks at around 4 days post infection, is low by day 14, and remains low at all further time points (Morrison et al., 2013).** It is hypothesised that there are different biological processes responsible for causing this trend. For a new bacterial species to colonise the gut, the bacterium must find an appropriate niche and multiply (Meurant, 2012). Thus, it is expected that a bacterial growth phase between 2 and 4 days post infection is a result of *Hh* finding its niche in the lumen. Following this growth phase there is a decline in the population of *Hh* in the cecal lumen. It is thought that it is due to the the adaptive immune response that causing a reduction in *Hh* burdens between 4 and 14 days post infection. This is consistent with the knowledge that it takes around 4 days for the adaptive response to be initiated following an infection (Janeway et al., 2001), and with the fact that RAG KO mice that do not have any adaptive immune cells have higher bacterial burdens when infected with *Hh* than conventional IL10 KO mice (Kullberg et al., 2002). After 14 days post infection, it is thought that the levels of *Hh* remain steady due to competition for resources with commensal bacteria.

2. **The level of inflammation in the large intestine is moderate by 7 days post *Hh* infection, severe by day 14.** Between 0 and 7 days post infection, there is a 10-fold increase in the number of $CD4^+$ T cells in the cecum and colon, and 5-fold increase in the total number of immune cells in the cecum and colon. By day 14 there is a 25-fold increase in $CD4^+$T cells compared to day 0, and a 10-fold increase

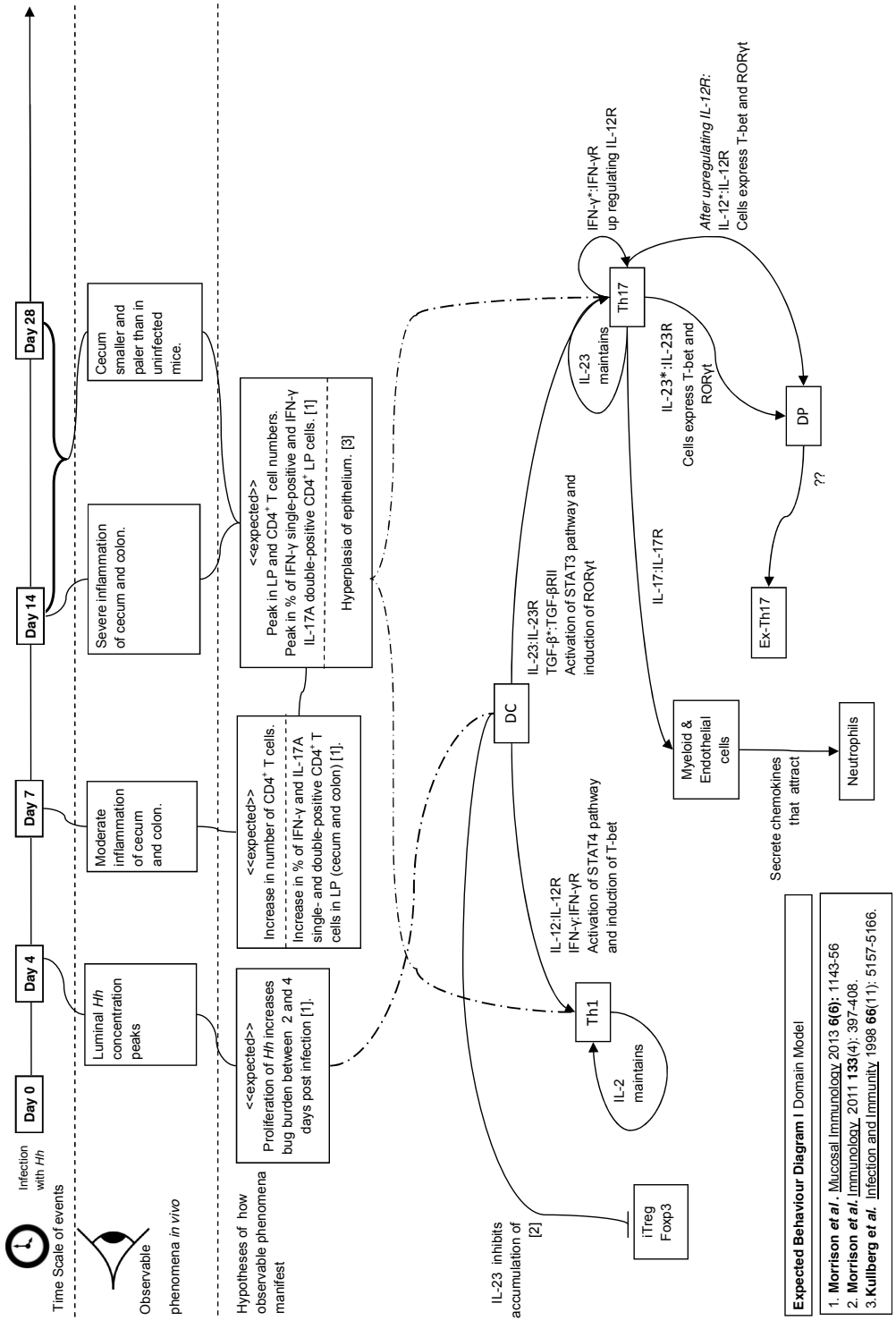

Figure 2.3: Expected behaviors diagram for *Hh*-induced colitis. The observable phenomena from the biological domain have been linked to the time that they occur, and to hypotheses of how each behavior manifests *in vivo*. A dashed line is used where there are multiple hypothesised causes of an observable phenomena.

in the total immune cells (Morrison et al., 2013). This increase in immune cells is accompanied by an increase in inflammatory cytokines, and both of these factors are hypothesised to cause disease pathology including, features of severe inflammation such as goblet cell depletion and crypt abscesses.

2.2.2 Activity Diagrams

The cellular components and the interactions between them that are hypothesised to cause intestinal inflammation in *Hh*-infected IL10-KO mice have now been defined by the expected behaviours diagram (Figure 2.3). To determine the way in which each interaction contributes to inflammation, activity diagrams have been developed. These diagrams describe the interactions that can occur between cells both in the gut and in the MLN (Figure 2.4). To aid description of the activity diagram in Figure 2.4, activities involving *Hh*, APCs, T cells, epithelial cells and neutrophils have been denoted A1-5 respectively.

Activites involving *Hh* (A1)

The first event in the development in *Hh*-induced colitis is intragastric inoculation of IL10-KO mice with *Hh* (A1a). *Hh* colonises the cecal and colonic lumen by binding to its mucus layer and proliferating a a rate determined by its local environment (A1b,c,), (Fox et al., 1994; Belzer et al., 2005). Following colonisation, epithelial cells recognise *Hh* and begin to secrete antimicrobial peptides (AMPs) and cytokines (A4a) (Ostaff et al., 2013; Sterzenbach et al., 2007). This leads to APCs migrating the epithelial barrier to sample *Hh* in the lumen (A2ai) (Nicoletti et al., 2010).

Activities involving APCs (A2)

In steady state, the majority of APCs are resident macrophages but there is a small population of migratory APCs present at the epithelial barrier in the intestine that patrol the epithelium for commensal antigens (Farache et al., 2013). Following a bacterial challenge, more of these DCs are recruited to the barrier to phagocytose and process bacteria using intraepithelial dendrites (Farache et al., 2013). These cells were thought to be DCs until it was shown that these cells are likely to be CX_3CR1^+ macrophages sampling bacteria in the intestinal lumen by extending transepithelial dendrites through tight junctions in the

epithelial layer (Rescigno, 2002; Niess et al., 2005). These macrophages are non-migratory and it is thought that they transfer antigen to DCs to process and present on MHC-II molecules on their surface. APCs that have taken up antigen also begin to secrete cytokine in response to the bacteria they have phagocytosed. In the activity diagram (Figure 2.4), APCs refer to both DCs and macrophages in the gut. These cells are responsible for sampling commensal bacteria at the epithelial barrier and can extend dendrites into the intestinal lumen for bacterial uptake (Farache et al., 2013; Niess et al., 2005; Rescigno, 2002) (A2ai,ii). While both types of APC share many features including phagocytosis (A2b), antigen presentation (A2ci) and cytokine secretion (A2cii), only DCs can migrate to the lymph node to activate and polarise naive T cells (A2d,e).

Activities involving T cells (A3)

In the diagram, the term "T cells" refers to $CD4^+$ and their involvement in the inflammatory process begins in the MLN. T cells scan the MLN for DCs presenting a peptide of the protein for which the TCR is specific for. If a T cell recognises the antigen presented on the MHC-II molecule on the surface of a DC then it will bind (A3a), and if the T cell receives sufficient costimulatory signals then it will become activated and undergo several rounds of proliferation (A3b) (Bousso, 2008). While in an activated state, T cells respond to cytokine secreted by APCs or by other T cells. If the stimulation is strong enough, Janus kinase-signal tranducer and activator of transcription (JAK-STAT) pathways are activated and T cells undergo polarisation into one of several subsets (Figure 1.1) and begin to secrete effector cytokines (A3c). Upon activation T cells downregulate the S1p1 receptor leaving them unable to respond to CCL19 and CCL21, therefore sequestering them in the lymph nodes (Graeler et al., 2002). Sphingosine 1-phosphate (S1P)1 receptor expression is gradually restored in effector cells (Rivera et al., 2008) and these cells can leave the lymph node via the efferent lymph vessels and home to the gut (A3d) (Koboziev et al., 2010). In the gut, T cells can be restimulated by APCs, restarting proliferation and causing the T cell to recommence cytokine secretion (A3e-g) (Mann and Li, 2014).

Activities involving epithelial cells (A4)

Epithelial cells are the first line of defence against mucosal commensal bacteria and

pathogens, forming a barrier between bacteria in the lumen and APCs in the lamina propria. They contribute to inflammation by secreting an array of cytokines and antimicrobial peptides in response to a bacterial challenge (A4a) (Haller et al., 2000; Bona and Revillard, 2001). Cytokines in the gut such as IFN-γ and TNF-α have been shown to alter the proliferation and induce apoptosis of epithelial cells (Yan et al., 2004; Kaiser and Polk, 1997; Peterson and Artis, 2014). This causes damage to the epithelial barrier (A4b), allowing bacteria to enter the lamina propria underneath the barrier (A4b) and activate APCs, increasing the level of cytokine and amplifying this barrier damaging loop (Belkaid and Hand, 2014).

Activities involving neutrophils (A5)

In the absence of *Hh*, and inflammation, only a small number of neutrophils are present in the gut but the number increases rapidly during inflammation (Bain, Unpublished). Neutrophils are attracted to the gut by IL17-induced chemokines (A5a) and promote pathogenic immune responses by phagocytosing and presenting bacteria (A5b,c) (Kolaczkowska and Kubes, 2013).

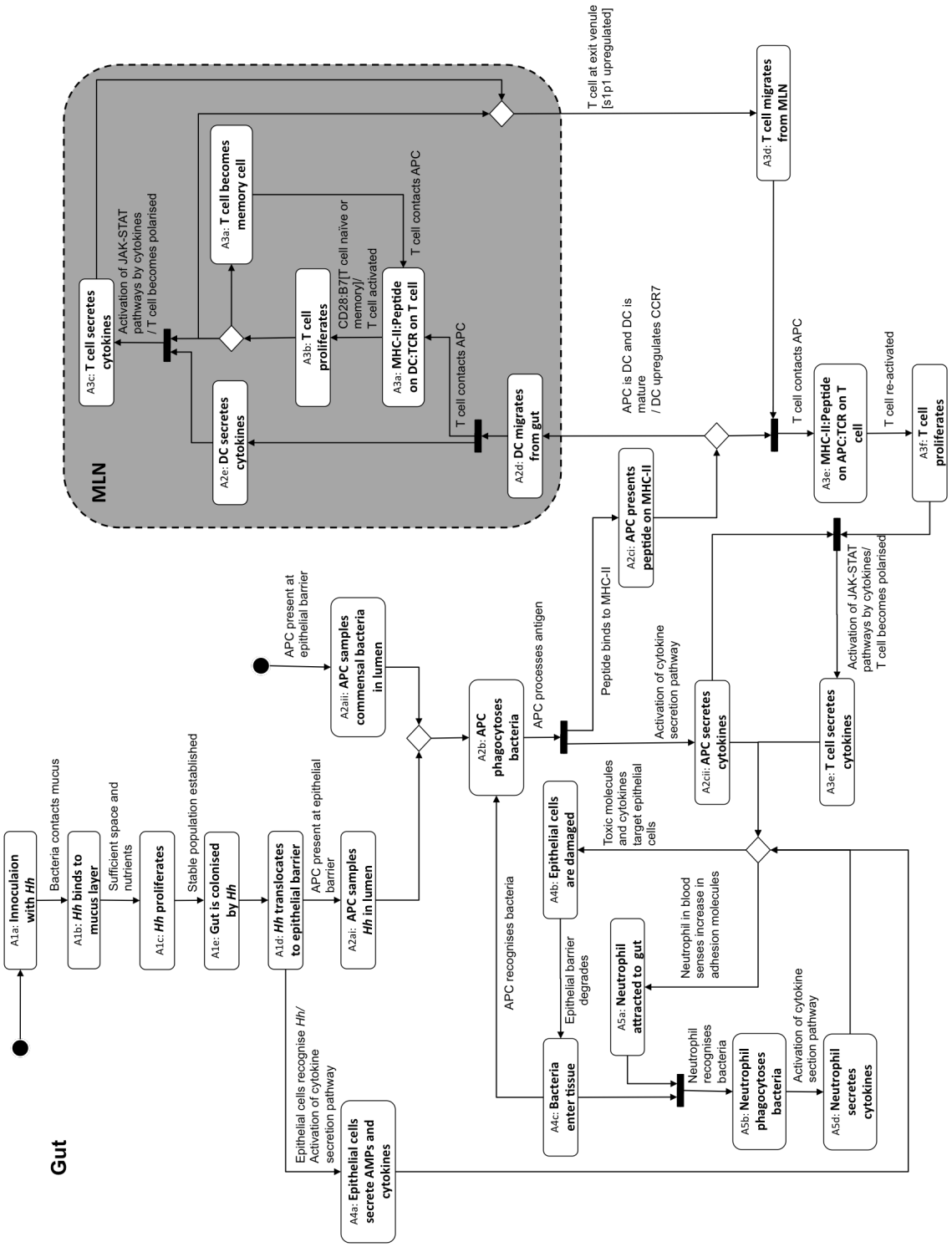

Figure 2.4: Activity diagram describing interactions in the gut during *Hh*-induced intestinal inflammation. APCs are considered to be DCs and macrophages, bacteria refers to both commensal bacteria and *Hh*, and T cells are considered to be $CD4^+$. Guards are placed below horizontal arrows and right of vertical arrows.

2.2.3 State Diagrams

Following on from the activity diagrams, state diagrams were developed to define the different states a cell can be in and to identify the factors governing transitions between these states. Diagrams have been developed for every cell type that is directly involved in the inflammatory process as identified by the expected behaviours and activity diagrams (Figure 2.3, Figure 2.4) and are described below. To aid description of the state diagrams, bacteria, APCs, T cells and epithelial cells have been denoted B, A, T, and E respectively.

2.2.3.1 Bacteria

Figure 2.5 describes the properties that a single bacterium can have. Under the defined research context there are just two initial states for a bacterium, *Hh* (B1a) or commensal (B1b). If a bacterium is of type *Hh*, then it enters the system through the intragastric route (Kullberg et al., 1998) and is therefore initially uncolonised (B2bi), but becomes colonised by binding to the mucus layer as it reaches the gastrointestinal tract (B2bii). Any bacteria that is of type *Hh* that does not become colonised is removed in the faecal matter (B4a). Commensal bacteria are always considered to be colonised (B2bii) as they are first introduced to the mouse at birth (Belkaid and Hand, 2014), and as the experimental model considers adult mice. All bacteria regardless of the type are initially luminal (B2a), that is they are located on or above the mucus layer or epithelial barrier rather than in the lamina propria. Colonised bacteria (B2bii) alternate between being proliferative and non-proliferative depending on space and nutrients in the environment (B2ci,ii). A colonised bacterium can leave the lumen to become tissue resident (B3), entering the lamina propria through gaps in the epithelial barrier created by apoptosis of epithelial cells (Schulzke et al., 2006), or be removed from the system following phagocytosis by an APC (B4d). Both, tissue resident and luminal bacteria can die due to lack of nutrients (B4c).

2.2.3.2 Antigen-presenting cells (APCs)

Section 2.2.3.2 describes the properties that APCs can have. APCs enter the gut lamina propria from the blood (A1) as either DCs (A2a) or macrophages (A3a). DCs are initially immature (A2bi) and phagocytic (A2ci). Immature DCs are also non-migratory (A2cii),

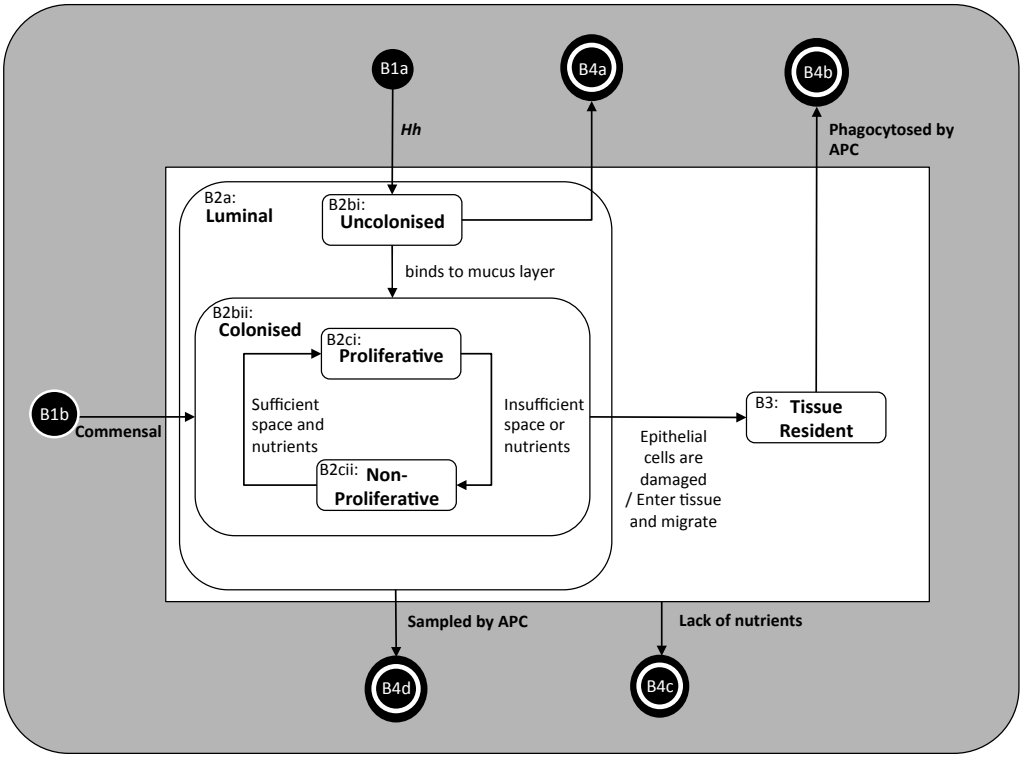

Figure 2.5: Domain model state diagram for bacteria.

that is, while they express chemokine receptors such as CCR2, CCR5, CCR6, CXCR1, and CXCR2 that allow them to respond to inflammatory signals and traffic within the tissue of which they are resident, they do not express CCR7 that allows them leave the tissue and migrate to the lymph node (Cravens and Lipsky, 2002; Riol-Blanco et al., 2005). Following exposure to antigen, DCs become mature (A2bii) (Janeway et al., 2001) and lose the expression of phagocytic receptors (Platt et al., 2010), making them non-phagocytic (A2ciii). Mature DCs also downregulate chemokine receptors responsible for keeping them in the gut and upregulate CCR7. DCs that express CCR7 can respond to CCL19 and CCL21 that are expressed by the T-cell stroma in the lymph node and to CCL21 produced by endothelial cells of afferent lymphatic vessels and high endothelial veins (Gunn et al., 1998; Stein et al., 2000; Warnock et al., 2000), and are therefore in a migratory state (A2civ). Mature DCs present antigen to T cells by upregulation of the MHC-II:peptide complex along with costimulatory molecules B7 (A2cv), and can also secrete an array of

cytokines in response to the antigen that have acquired (A2cvi).

Macrophages begin in a precursor state (A3bi). Once they have taken up and processed antigen they become conditioned to their environment (A3bii) adopting either an inflammatory (A3biii) or regulatory (A3biv) phenotype. Both types of macrophages secrete cytokines, with inflammatory macrophages secreting an array of pro-inflammatory cytokines including IL12, IFN-γ and IL6 and regulatory macrophages secreting anti-inflammatory cytokines such as TGF-β and IL10. They also both express MHC-II molecules to present antigen (A3bv) but only inflammatory macrophages also express co-stimulatory molecules (Bain et al., 2013). Both types of APCs are removed from the system by apoptosis.

2.2.3.3 T Cells

T cells in the model refer to $CD4^+$ T cells. They enter the lymph node from the blood (T1) and are initially in a naive state (T2). T cells scan the lymph node looking for DCs and become partially activated (T3) following the binding of the TCR MHC-II:peptide complex on a DC. Partially activated T cells that do not receive costimulatory signals become unresponsive to further stimulation and this ultimately results in cell death (T6) (Schwartz, 2003). However if a partially activated T cell receives costimulation via CD28:B7 interaction, it will become activated (T4a) and enter a proliferative state (T4bii). An activated cell can enter an effector state (T4bi) following multiple rounds of proliferation (Jelley-Gibbs et al., 2000), and once in an effector state it can become polarised into one of several subsets depending on the cytokine millieu. In *Hh*-induced colitis, effector cells become either a Th1, Treg, or Th17 cell depending on their environment (T4ci-iii, Figure 1.1). Subsequently Th17 cell can switch phenotypes entering either a double positive (T4civ) or an ex-Th17 state (T4cv, Figure 1.1) (Morrison et al., 2013). During proliferation, an activated T cell may also enter a memory state (T5). A memory T cell can return to an activated state following restimulation by an APC expressing MHC-II. In the absence of stimulation T cells will undergo apoptosis or die from activarion-induced cell death (AICD) (T6) (Bertolino et al., 1999).

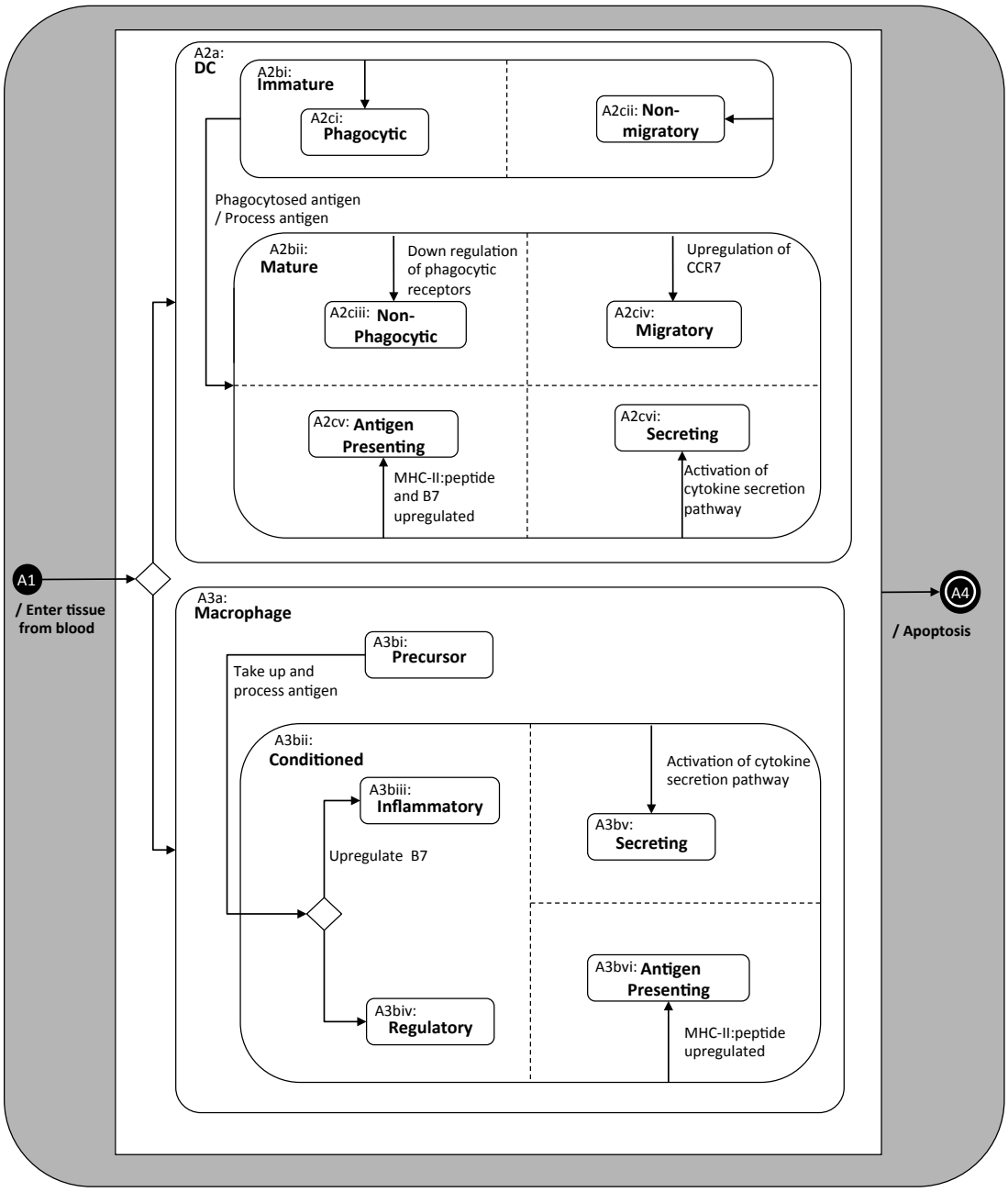

Figure 2.6: Domain model state diagram for APCs (DC or macrophage) in the model.

2.2.3.4 Epithelial Cells

Intestinal epithelial cells constitute a barrier surface that separates commensal and pathogenic bacteria from cells in the lamina propria (Peterson and Artis, 2014). At steady state, the majority of epithelial cells are in a resting state (E2) meaning that they are non-secreting (Figure 2.8). Epithelial cells use PRRs to identify bacterial PAMPs in the intestine. If an

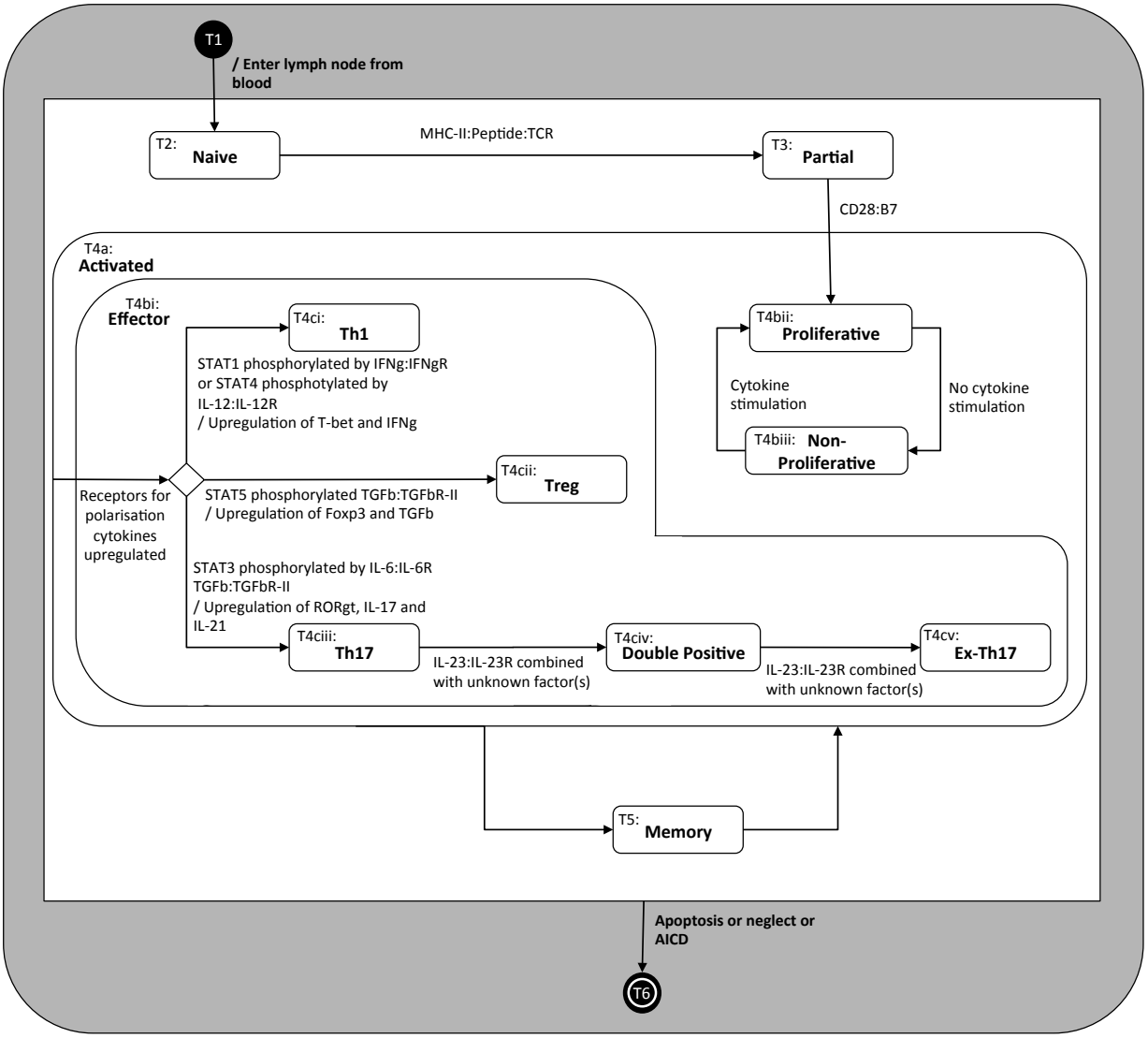

Figure 2.7: Domain model state diagrams for T cells in the model.

epithelial cell identifies a commensal species it will not elicit a strong immune response, but on recognising foreign antigen, it will secrete cytokines and AMPs that can cause distruption of bacteria (Mukherjee et al., 2014; Muniz et al., 2012; Gallo and Hooper, 2012). In the presence of inflammatory cytokines, epithelial cells become damaged (E4), inducing apoptosis (E5), and resulting in the epithelial barrier becoming compromised (Brown et al., 1999; Zolotarevsky et al., 2002; Mankertz et al., 2000).

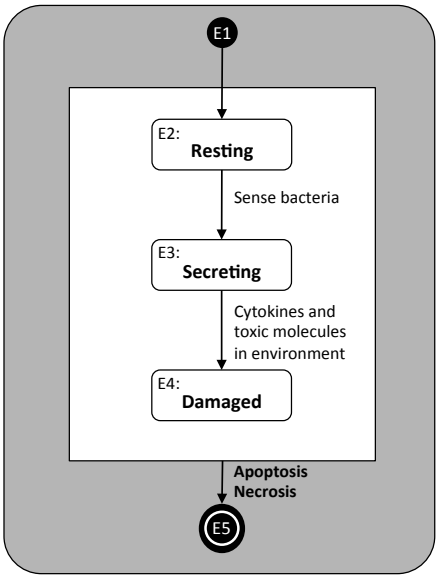

Figure 2.8: Domain model state diagrams for epithelial cells in the model.

2.3 A Platform Model for *Hh*-Induced Colitis

Within the CoSMoS process, the second stage of model development is to establish how an executable model of the biological domain will be developed and implemented. The modelling methodology must first be determined, before simulation specific details including methods and functions that will be used for model implementation can be developed. Cellular interactions are represented here as activity diagram, and state machine diagrams describing individual cell-level behaviours have also been developed. Cellular behaviours will be encoded into the model on the basis of these state machine diagrams, but the interactions from the activity diagrams will not be hard coded, as they are expected to emerge as a result of cellular behaviours being correctly captured. If the activities were

coded into the model, the result would be a an over-fitted model that adequately described the biological system but that could not be used for *in silico* experimentation.

2.3.1 Modelling Methodology

The advantages of different techniques for modelling biological systems have been examined in Chapter 1. Cells in the gut are highly autonomous, and each individual cell responds to its environment in a different way depending on the previous interactions with other cells and with the environment. A key example of this phenomena is the phenotype switching of Th17 cells into double positive and then ex-Th17 cells (Morrison et al., 2013) (Figure 1.1). The exact cause of this switch *in vivo* is unknown but as not all Th17 cells switch phenotype, the history of a cell is potentially important in determining its fate. Further, it has been observed that inflammation in the *Hh*-induced colitis model does not develop uniformly across the gut and so it is important that a model of inflammation is spatially resolved. With this in mind, the most suitable methodology for a computational model to capture the dynamics of cells in the gut is a hybrid ABM that is able to incorporate systems of ODEs to model processes that are not represented at a spatial level (Table 1.2). Using such a model allows ODEs to be incorporated into the system as well as allowing cells to be represented at an individual level rather than as a uniform population allowing for stochasticity. This is an advantage over a full ODE model where there is no spatial resolution or a PDE model where populations are considered to be homogeneous. When developing an ABM, or hybrid ABM, both spatial and temporal considerations must be taken into account.

2.3.2 Spatial Considerations for the *Hh*-Induced Colitis Model

ABMs allow cells to exist in environments consisting of a series of grids that can be either continuous or discrete. In two dimensions, discrete grids are divided into spaces and agents can be in any location (x, y), $x, y \in \mathbb{N}$. A grid space can take the form of any tessellating shape (Figure 2.9), but using squares makes the location system more intuitive. For continuous spaces, $x, y \in \mathbb{R}^+$.

In 3D environment, a z coordinate is added so the locations become (x, y, z) where $x, y, z \in \mathbb{N}$ for discrete spaces, and $x, y, z \in \mathbb{R}^+$ for continuous. In this model the compart-

ments will be created by the layering of different grids of equal size, to allow for multiple cell types.

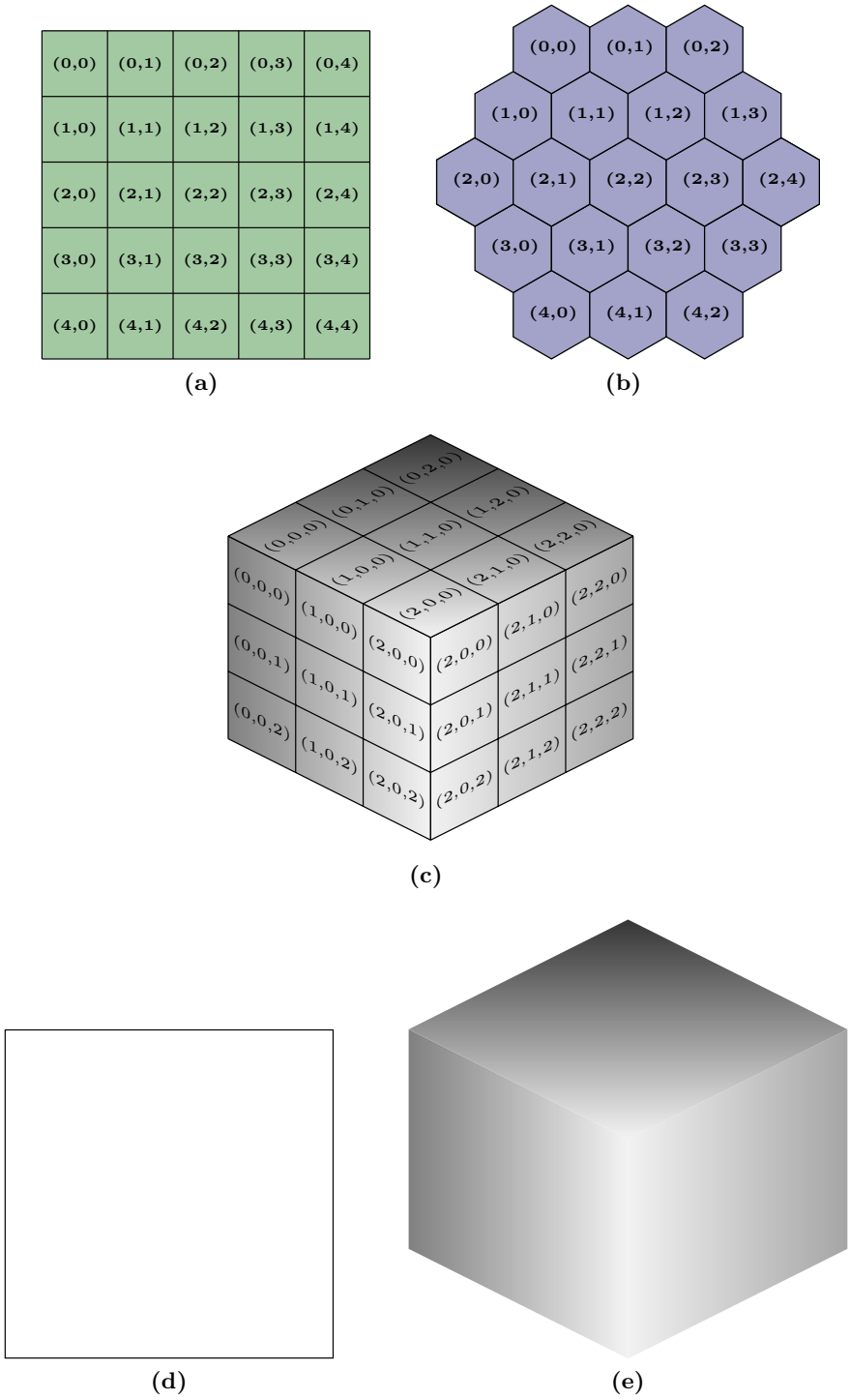

Figure 2.9: Different grids that can be used in an ABM. Examples of discrete grids in 2D (a,b) and 3D (c), and continuous grids in 2D (d) and 3D (e)

The environment identified in the research context for this model is the gastrointestinal

tract, in particular the cecum and colon, and the gut associated lymph node, the MLN (Figure 2.10). To determine the best way to model each organ, the types of cells and cytokines that will be located there must be considered (Table 2.1).

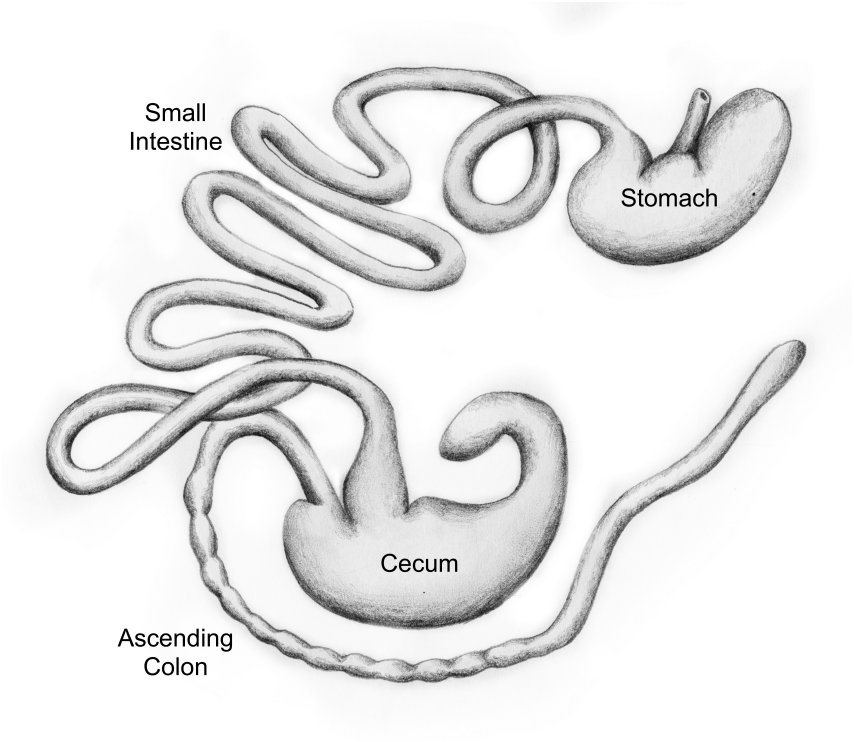

Figure 2.10: Cartoon of the mouse intestinal tract. Diagram shows small and large intestine, comprising on the cecum and ascending colon, that is the focus of the computational model.

Entity / Compartments	**T Cells**	**DCs**	**Macrophages**	***Hh***	**Commensal Bacteria**	**IL6/TGF-β**	**IL12**	**IFN-γ**	**IL21**
Cecum	✓	✓	✓	✓	✓	✓	✓	✓	✓
Colon	✓	✓	✓	✓	✓	✓	✓	✓	✓
MLN	✓	✓							
Cecal Lumen				✓					
Colonic Lumen				✓					
Lymph		✓							

Table 2.1: Cells and cytokines by compartment. The cells and cytokines that reside in each compartment are listed in the table.

2.3.2.1 Mesenteric Lymph Node (MLN)

Several models have been developed to predict the cellular dynamics in lymph nodes. Some of these models use a 2D representation (Beltman et al., 2007; Riggs et al., 2008) and others 3D (Zheng et al., 2008; Kislitsyn et al., 2015). Gong et al. (2013) compared 2D and 3D representation in a model that predicts output efficiency of a lymph node and concluded that the efficiency of cognate T-cell searching is highly dependent on model dimensionality, with the 3D model being more efficient. Despite this, 2D modelling has proved useful in characterising the priming of $CD4^+$ T cells in the lymph node (Linderman et al., 2010). In the current domain of study, the purpose of the MLN is to act as the site for T-cell activation by DCs (Figure 2.13) and this means that a 2D representation similar to that used by Linderman et al. (2010) is sufficient for the requirements of this model. The dimensions of the lymph node in the model will be comparable to those in biology (measured in Figure 2.11a). In the model the MLN will be represented in 2D as a rectangle where the cells are allowed to pass over each other rather than collide, creating a pseudo 3D space.

2.3.2.2 Cecum and Colon

The murine cecum and colon are 3D structures with a luminal space that contains the faecal matter. The lumen contains bacteria, including *Hh* in an infected mouse, and is separated from the lamina propria by a mucus layer and a single layer of epithelial cells. In the computational model, the luminal and lamina propria compartments will be abstracted into two overlaying compartments of the same dimensions. Like the MLN, the cecum and colon compartments will be represented in 2D with dimensions comparable to those in biology (measured in Figure 2.11b). The cecal and colonic luminal compartments are the sites of *Hh* colonisation and bacteria are passed from the lumen into the lamina propria compartments with a probability that depends on the amount of damage to the epithelial barrier (Figure 2.12). In order for the 2D section of the cecum and colon to be spatially representative of the lamina propria, the lumen and lamina propria compartments must sit perpendicular to each other, meaning that the epithelial barrier must be one dimensional, i.e. a line. This organ will be modelled in 2D as a rectangle where the cells are allowed to

pass over each other rather than collide creating a pseudo 3D space.

(a) (b)

Figure 2.11: Dimensions of the MLN, cecum and colon. The MLN (a), cecum and colon (b) were removed from five 24 day old uninfected IL10 KO mice and the height and the width were measured and averaged. Figure shows one representative set of tissues.

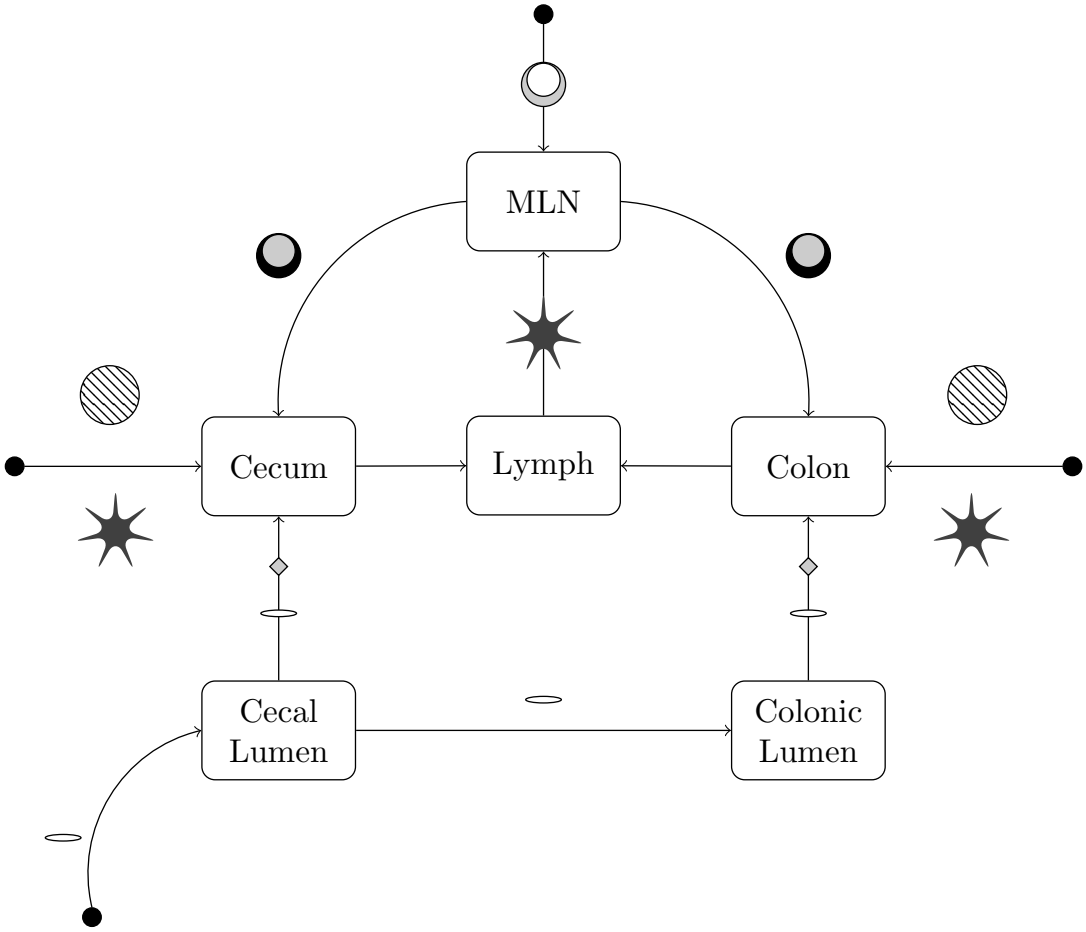

Figure 2.12: Compartments of the model and transitions of cells between them. Legend: ○: Naive T cells , ●: Activated T cells, ✸: DCs, ▨: Macrophages, ◇: Commensal Bacteria, ⬭: *Hh*.

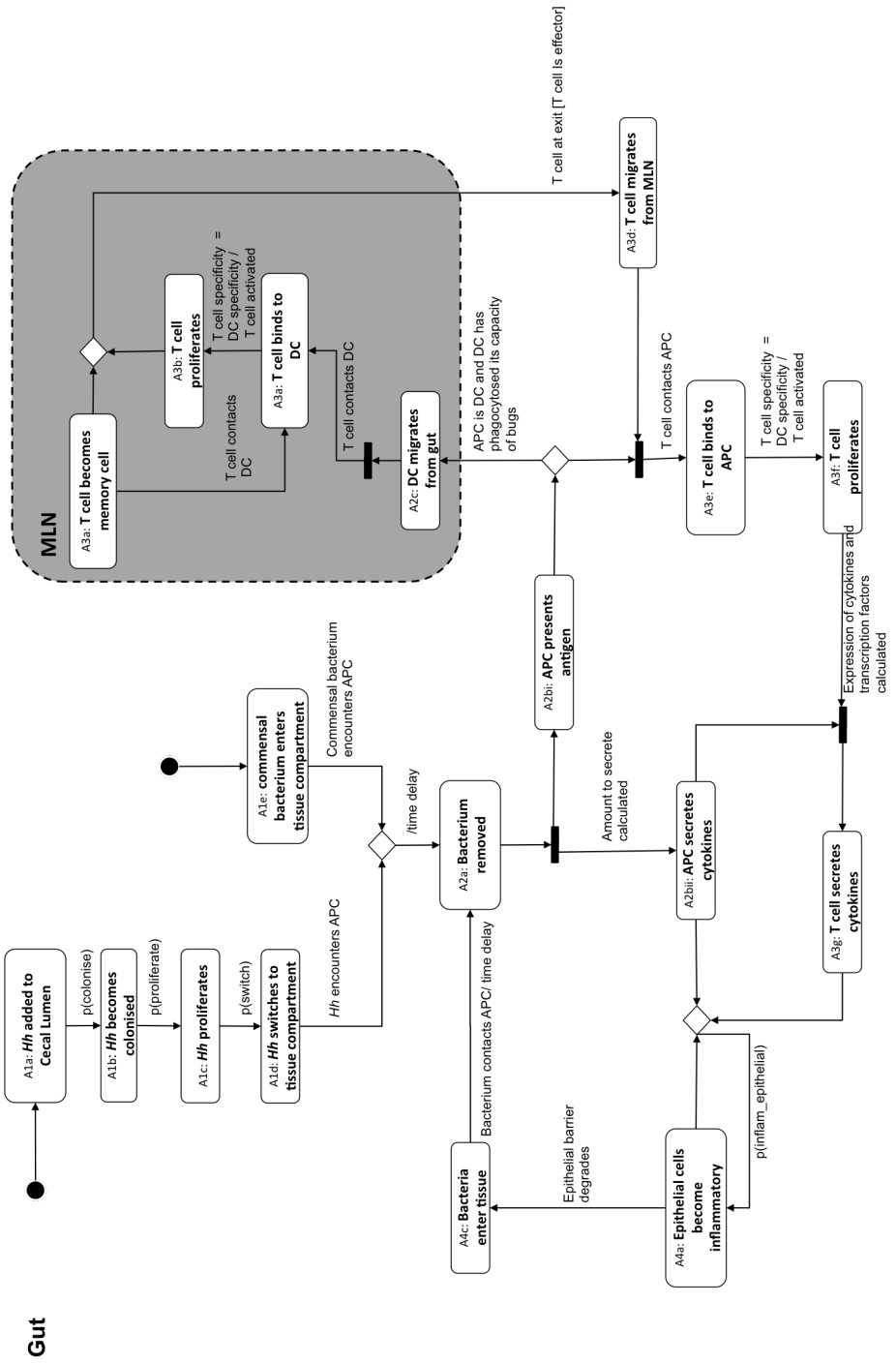

Figure 2.13: Activity diagram describing interactions between entities in the model during *Hh*-induced intestinal inflammation. APCs are considered to be DCs and macrophages and bacteria refers to both commensal bacteria and *Hh*. Guards are placed below horizontal arrows and right of vertical arrows.

2.3.3 Activity Diagrams

Figure 2.13 shows the activity diagram for the platform model. The activities for *Hh*, APCs, T cells, epithelial cells and neutrophils are depicted as A1-5 respectively.

Activities Involving *Hh* and Commensal Bacteria (A1)

Inflammation *in vivo* is initiated by infection with *Hh*. This initiation step is modelled in the ABM by the addition of *Hh*-type bacteria to the cecal lumen compartment (A1a). These bacteria become colonised at a constant rate with probability $p(colonise)$ (A1b) and proliferate with probability $p(prolif)$ (A1c). This leads to some of the bacteria entering the lamina propria compartment with probability $p(switch)$ (A4d). Simultaneously, commensal bacteria enter the lumen with probability $p(comm)$ (A1e). An abstraction has been made that commensal bacteria will not be represented in the lumen, but will enter the lamina propria directly. Consequently, APCs cannot directly sample bacteria in the lumen so all bacteria:APC interactions will be in the lamina propria. The rational for this abstraction is that it would be difficult to develop and calibrate a model of the commensal bacteria in the lumen as little is known about specific species present under this particular experimental set up or the interactions between them. Tissue resident bacteria move randomly around the cecum and colon until they contact an APC when they become stationary and, following a short time delay, are removed (A2a). This activity induces two simultaneous state changes in the APC with it becoming both antigen presenting (A2bi) and cytokine secreting (A2bii).

Activities Involving APCs (A2)

A DC that is in an antigen-presenting state and has removed its maximum number of bacteria that it is allowed to from the lamina propria will migrate to the MLN (A2c, Figure 2.12). Unpublished data from the Kullberg lab show that at peak inflammation, less than 5% of T cells in the MLN secrete IFN-γ or IL17, compared to 50% of T cells in the cecum (Morrison et al., 2013). Further more cytokine levels in the MLN are low compared to those of the cecum and colon, so it is sensible that the cecum and colon serve as the main site of T-cell polarisation while the MLN functions as the site for T-cell activation. Thus an abstraction has been made that DCs will not secrete cytokines in the MLN.

Activities Involving T Cells (A3)

T cells become activated by contacting and then binding to a DC that is presenting the

antigen that the T cell is specific for (A3a). Activated T cells proliferate with a rate of $1/p(prolif)$ where $p(prolif)$ is the probability that a single T cell spawns a single daughter cell per minute (A3b). During proliferation a T cell develops into a memory cell with probability $p(mem)$. When a T cell has undergone a number of proliferations it becomes an effector cell and exits the MLN to the gut (A3d). Here a T cell commences its scanning behaviour looking for APCs presenting its cognate antigen so that it can resume its proliferative state (A3e,f). T cells in the gut can respond to cytokines to become polarised.

Activities Involving Epithelial Cells (A4)

Since the lamina propria and lumen compartments in the gut are separated for the cecum and colon compartments, the epithelial barrier does not explicitly exist between the compartments. However, the level of cytokine in the tissue acts to drive the switch of epithelial cells from resting to inflammatory (A4a, $p(inflam_{epithelial})$). This allows more bacteria to enter the lamina propria (A4b), therefore exacerbating the inflammatory process.

Activities Involving Neutrophils (A5)

A major abstraction from the domain to the platform model is that neutrophils will not be modelled. This is because they mainly act by removing bacteria and dead cells from the environment, something can be incorporated into the death rate of bacteria in the lamina propria compartments.

Summary of Activities

The processes described in the activity diagrams contain a small set of distinct activities, some of which are common between cell types. Here we define what these activities represent for agents in the model and how they will be implemented.

Contact: Two cells at locations (x_1, y_1) and (x_2, y_2), with radii r_1 and r_2 respectively, are defined as being in contact with each other if the inequality $(r_2 - r_1)^2 <= (x_2 - x_1)^2 + (y2 - y1)^2 <= (r_2 + r_1)^2$ is satisfied. This means that all cells in the model require a radius parameter.

Move: There are three ways in which a cell in the model can move from point A (x_a, y_a) to point B (x_b, y_b), all of which are described in Figure 2.14. Under any of these methods, the average distance travelled per time step can be calculated using the equation $d = \sqrt{(x_b - x_a)^2 + (y_b - y_a)^2}$. For a cell to move, it must have a parameter representing average step size, and for directed random movement, the standard deviation of the angle travelled at each step.

Proliferate: When a cell in the model proliferates it will create an identical copy of itself within a small radius of its current location. The new cell must inherit all states from the parent cell, as well as its age and lifespan. The only exception to this rule is when a T cell proliferates and its daughter cell becomes a memory cell but the parent cell stays activated, resulting in the lifespans and activation status being different between parent and daughter cells.

Colonise: When a bacterium is colonised, it remains stationary in the lumen and interacts with the nutrients in the environment.

Phagocytose: Phagocytosis in the model is performed by APCs when they are being contacted by a bacterium. The APC causes the bacterium to become stationary for a time delay, and then remove the bacterium from the model. If the APC dies while contacting a bacterium then the bacterium will be released and recommence migratory behaviour.

Present antigen: To model antigen presentation by APCs, each bacterium will have a numerical "type" variable and upon being phagocytosed, this number is added to a list of antigens to be presented on the APC. When a T cell contacts the APC it searches the list of presented antigen for a number that matches its own numeric specificity (Figure 2.15).

Secrete: In the model, secretion means increasing the number representing the concentration of cytokine in a discrete grid square by a value calculated by a function that is distinct for each cell type.

Die: When a cell dies, it is removed from the simulation. All cells in the model must die eventually, either probabilistically or by exceeding a specified lifespan.

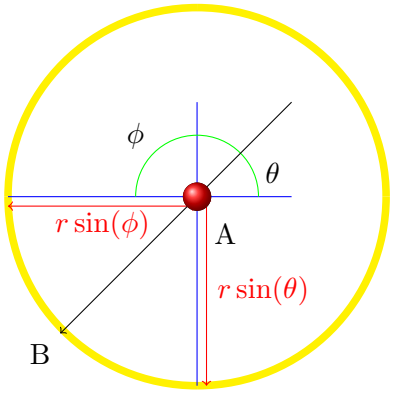

(a) Random Motion

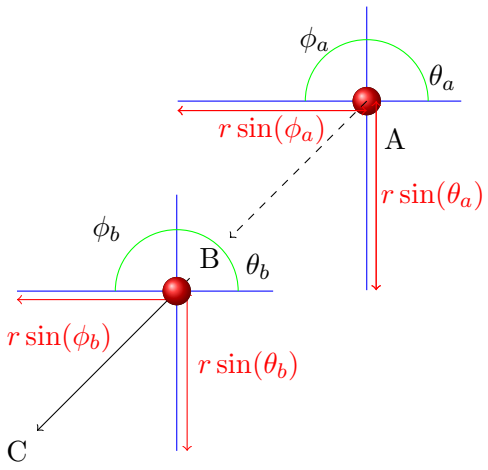

(b) Directed Random Motion

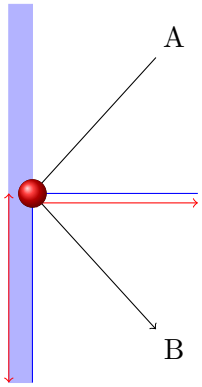

If a cell bounces off the wall there are 4 scenarios;

- If $y = 0$, $\pi \leq \theta \leq 2\pi$, $0 \leq \phi \leq 2\pi$
- If $y =$GridHeight, $0 \leq \theta \leq 2\pi$, $0 \leq \phi \leq 2\pi$
- If $x = 0$, $0 \leq \theta \leq 2\pi$, $0 \leq \phi \leq \pi$
- If $x =$GridWidth, $0 \leq \theta \leq 2\pi$, $\pi 0 \leq \phi \leq 2\pi$

and the new location is $x' = x + r\sin(\phi)$, $y' = y + r\sin(\theta)$.

(c) Bounce

Figure 2.14: Representation of cell movement *in silico*. (a) True random motion, where a cell may travel in any direction at the next step regardless of its previous direction, (b) Directed random motion, where a cell moves in the same direction for a period of time with some stochasticity, (c) Cells that reach a wall will bounce back into the compartment.

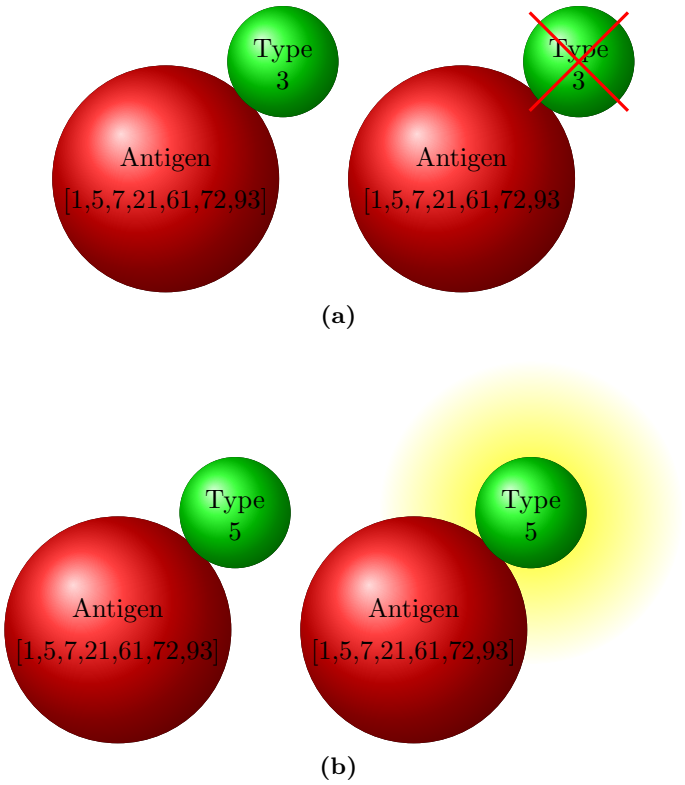

Figure 2.15: How T cell:DC interactions lead to T cell activation. If a naive T cell (green) binds to a DC (red) that is not presenting that antigen that the T cell is specific for, that T cell binds transiently and is not activated (a). If the T cell binds to a DC that is presenting the right antigen for its specificity, the T cell can become activated (b)

2.3.4 State Diagrams

As in the domain model, platform model state diagrams were developed to define the different states a cell can be in and to identify the factors governing transitions between these states. Diagrams have been developed for every cell type that is included in the model and are described below. To aid description of the state diagrams, bacteria, APCs, T cells and epithelial cells have been denoted B, A, T, and E respectively.

2.3.4.1 Bacteria

Hh enters the model in the cecal lumen (B1a). In the transition from the domain to the platform model an abstraction has been made that only *Hh*, and not commensal bacteria, will be modelled in the lumen (B2a). *Hh* is initially in a non-colonised state (B2bi) meaning that it travels with direction random motion (Figure 2.14). A bacterium that remains uncolonised will travel through the cecal lumen and into the colonic lumen. As described in the previous section, for a cell to move, the average step size must be determined. In biology, *Hh* is contained in the faecal matter and not free flowing, so the velocity at which it traverses the cecal and colonic lumen is not known. However, the velocity can be estimated based on the dimensions of the cecum and colon (Figure 2.11b) and the rate of gastric emptying, that is assumed to be 60 mins (Bennink et al., 2003). Under these assumptions the velocity of *Hh* in the lumen is modelled as $15\mu m/\text{min}$.

The probability of *Hh* colonisation in biology has been estimated from levels of *Hh* in cecal contents that has previously been quantified by Morrison et al. (2013), who measured the *Hh* burdens in IL10 KO mice using the concentration of *Hh* DNA. For comparison between *in vivo* and *in silico* data, the bacterial burdens have been transformed into bacterial counts (Figure 2.17), assuming that 20 fg of *Hh* DNA is equivalent to approximately 14 copies of the *Hh* genome, i.e. 14 *Hh* bacteria, as described by Ge et al. (2001). Comparing the number of *Hh* bacteria given on day 0 to the number of bacteria present at 2 days post infection gives an estimated value of $p(colonise) \approx 0.01$. *Hh* that is colonised (B2bii), alternates between a proliferative and non-proliferative state (B2ci,ii) and proliferates according to the space and nutrients in the environment. Doubling times of approximately 12 hours have been abstracted from live bacterial counts of *in vitro Hh* cultures from

unpublished observations in the Kullberg lab. The data shows that plating 10^3 bacteria on agar plates results in approximately 2.2×10^6 live *Hh* after 24hrs and 4.0×10^6 live *Hh* after 48hrs. Hence *in silico*, the proliferation time of a single bacterium should follow a Gaussian distribution with a mean of 12hrs (=720 mins), resulting in the proliferation probability $p(prolif)$ being 0.00138 per minute.

Following colonisation, *Hh* in the lumen is modelled using a grid-based approach. The cecal and colonic lumen compartments each contain two grids, one containing the number of *Hh* bacteria in each square, and another containing the corresponding concentration of nutrients. Using this approach, nutrients will be added to the grid at a set rate that will be calibrated using the simulation platform. If the concentration of nutrients is above a certain level then each bacterium in the square can proliferate and increase the number in either its current square, or any surrounding square, by 1. Alternatively, when the nutrient level is below a certain threshold, also to be calibrated using the simulation platform, each *Hh* bacterium can be removed from the lumen causing the number in that specific grid square to be decreased by 1. Before colonisation *Hh* can be removed from the lumen by exiting the gut when it reaches the end of the colonic lumen compartment (B4a). The removal of colonised bacteria from the lumen could be by a bacterium switching compartments to become tissue resident (B3), or dying due to either the lack of nutrients or the immune response (B4b). The parameters involved in the grid-based representation are listed in Table 2.2.

As specified in the activity diagram (Figure 2.13), the arm of the immune response that reduces the number of *Hh* in the lumen is generated by the epithelial barrier in response to inflammatory cytokines. In the model, the rate of immune response-induced *Hh* death will depend linearly on the amount of secreting epithelial cells, as suggested by Wendelsdorf et al. (2010), who linked the removal of bacteria in the lumen to both secreting epithelial cells and also to the number of so-called luminal DCs, an APC subset that is not present in this model. The relationship between the death rate of *Hh* and the number of secreting epithelial cells E_p will be modelled as:

$$p(death) = -d_c + d_{b_1} E_p, \tag{2.1}$$

where, d_c and d_{b_1} are parameters to be identified through model calibration. Similar to the death probability, the probability that a *Hh* bacterium will switch compartments from the cecal or colonic lumen

$$s(E_p) = s_c + s_{b_1} E_p, \tag{2.2}$$

where, s_c and s_{b_1} are parameters to be determined in the model calibration stage (Section 2.4.1.1).

A similar relationship is required to bring in commensal bacteria (B1b). Commensal bacteria enters the system in either the cecal or colonic lamina propria compartment directly as it enters the system in a tissue resident, migratory state (B3ai).

Bacteria, both *Hh* and commensal, that are in a tissue resident migratory state become stationary upon contacting an APC (B3bii), thus a radius for binding with other cells is required. As bacteria are less than $1\mu m$ in size, the radius is abstracted to be 0. From a stationary state, bacteria can leave the system by being phagocytosed by an APC, if the two cells bind for a sufficient time for removal to occur (B4c). Tissue resident bacteria that remain migratory can die due to a lack of nutrients (B4d) and as this is not a biological parameter, the probability of this death occurring will need to be determined in the model calibration stage.

Table 2.2: Parameters in the grid-based representation of *Hh* in the cecal and colonic lumen. Values for these parameters will be determined in the cailbration phase.

Parameter	**Description**
prolifProb	Probability of a single *Hh* bacterium in the lumen proliferating (min^{-1})
nutLowDeathProb	Probability that a single *Hh* bacterium will die when the level of nutrients in the environment is low (min^{-1}).
nutLow	Level of nutrients below which *Hh* bacteria will die at with probability *nutLowDeathProb* (dimensionless).
removeNut	Amount of nutrients removed by a single *Hh* bacteria ($cell^{-1}$ min^{-1})
addNut	Amount of nutrient added every *addNutTime* (min)
addNutTime	Time at which every grid square is increased by *addNut* (dimensionless)
nutLowProlifThresh	The threshold above which *Hh* will proliferate with probability *prolifProb* (dimensionless)
incNut	Amount of nutrients added to the nutrient grid square corresponding to that of the *Hh* bacterium when it dies (dimensionless)

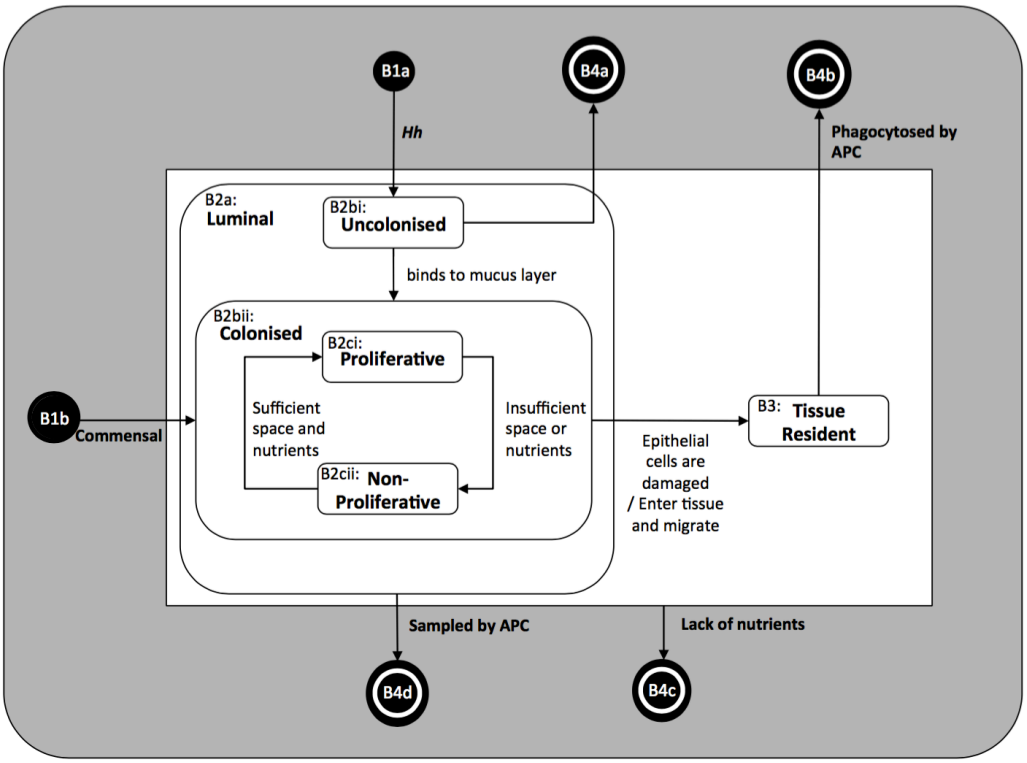

Figure 2.16: Platform model state diagram for bacteria.

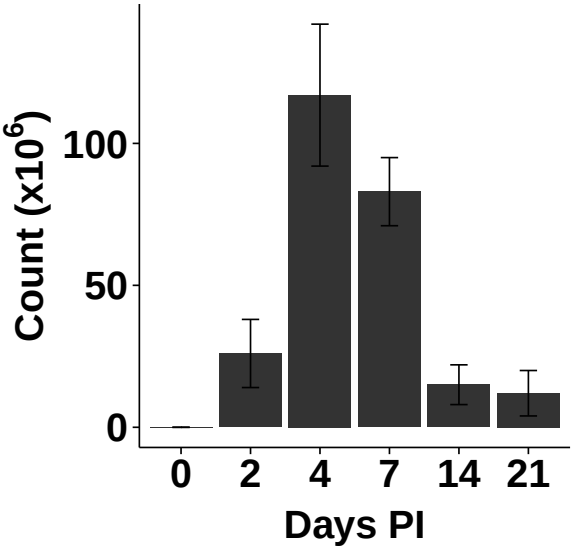

Figure 2.17: Quantification of Hh colonisation levels from cecal washes. Approximate Hh counts assuming 20 fg of Hh DNA is equivalent to 14 *Hh* bacteria calculated using the data on pg/mg of *Hh* DNA/total DNA, combined with total DNA amounts recovered from cecal washes, collected by Morrison et al. (2013)

2.3.4.2 Antigen-Presenting Cells

APCs enter the system as either DCs (A2a) or macrophages (A3a) (Figure 2.18). For ease of understand this section discusses the behaviours of these two cell types separately although in practice there are a lot of shared methods between them.

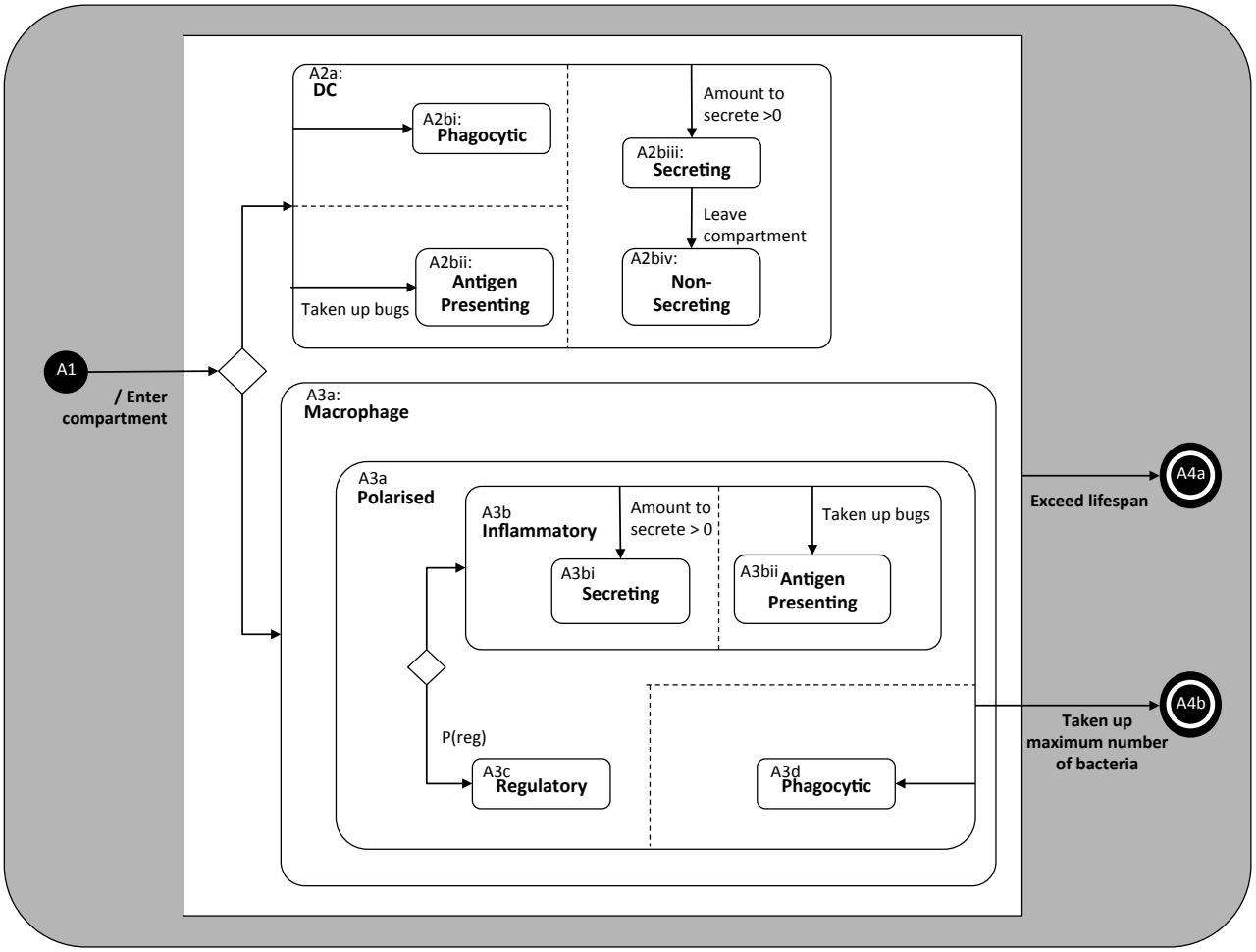

Figure 2.18: Platform model state diagram for DCs. Diagrams represent the states that a cell in the DC subset state of the APC type.

DCs

Figure 2.18 shows the state diagram for the DC subset of the APCs type. In the platform model DCs have been simplified to be phagocytic (A2bi), antigen-presenting (A2bii) cells that have the ability to secrete cytokines (A2biii). Abstractions have been made that assume that DCs are stationary cells because *in vivo* they move slowly with speeds of 2-5 μm/min (Bousso, 2008). It is also a necessary abstraction that DCs only phagocytose

tissue resident bacteria because commensal bacteria in the lumen will not be included in the model. For phagocytosis to take place, a contact between the DC and a bacterium must occur and this requires DCs in the model to have a radius parameter. *In vivo*, DCs have a radius of $7\mu m$ with long dendrites that can reach up to 20 μm when searching for antigen (Miller et al., 2004). With this in mind, DCs in the model will be considered to be circular, with a radius of $25\mu m$. For a DC to become cytokine secreting it must have taken up antigen. In the model, DCs will decide which type of cytokine they are going to secrete based on the type variable of bacteria that they have taken up. Kranzer et al. (2004) looked at the amount of IL12 secreted over time *in vitro* by human DCs in response to either lipopolysaccharide (LPS) or bacterium *Helicobacter pylori*. Using this data, a model that represents the rate at which DCs secrete cytokines in response to different stimulations has been developed. The model uses non-linear regression, with time in minutes and amount of stimulation as independent variables. It has been assumed that the amount of stimulation can be quantified from low to high using a scale of 0-1. The model is

$$il12 = (-5384 + 1.298t - 2235t^2) * stimulation, \tag{2.3}$$

and the results from the model when compared to biology are shown in Figure 2.19. A kolmogorov-smirnov test reveals no difference in the distribution of cytokines over time *in vitro* and *in silico* (p=0.7714).

The model shown in (2.3) will be used to estimate the contribution of IL12 from a single DC in the simulation. It can be generalised to other cytokines by multiplying by different scaling factors that will be calibrated using the simulation platform, once it has been developed. In the ABM, DCs will secrete a combination of IL12, IL6 and TGF-β depending on the type of bacteria they phagocytose. Enzyme-linked immunosorbent assay (ELISA) results suggest that there is little difference in the levels of IL12 and IL6 secreted by DCs following stimulation with LPS (Tada et al., 2004) so it can be assumed that the maximum secretion rate of IL12 and IL6 is the same. Similarly, it has been shown that DCs are able to produce approximately 1.5 times more TGF-β produced than IL12 (Abdi et al., 2012) so the secretion rate can be calibrated using the simulation platform, once it has been developed.

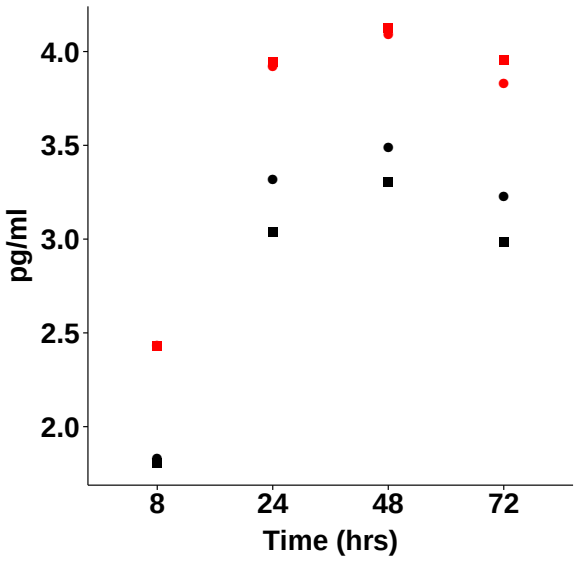

Figure 2.19: Linear regression model of total IL12 produced by 5×10^5 DCs. Concentrations of IL12 produced by 5×10^5 DCs in response to LPS (black) or *Helicobacter pylori* (red) were measured *in vitro* (circles) by Kranzer et al. (2004) and using Equation (2.3) *in silico* (squares).

When a DC has taken up a specified number of bacteria in the model, it will leave the cecum or colon compartments and enter the lymph compartment where it will wait for a time period of 8hrs before migrating to the MLN, appearing at a random location. In the MLN DCs are non-secreting (Figure 2.18, A2biv). The time spent in the lymph compartment is representative of the time taken for DCs to reach the lymph node under CCR7-mediated DC trafficking *in vivo* (Randolph et al., 2005). DCs are removed from the simulation when they exceed their lifespan of 3 days (Kamath et al., 2002).

Macrophages

The state diagram for the macrophage subset of the APC type is shown in Figure 2.18. The model only considers polarised macrophages (A3a) that are inflammatory (A3b) or regulatory (A3c) according to the environment at the time they enter the cecum or colon compartment. On entering the cecum or colon compartment, a macrophage decides whether it will become inflammatory with a probability that depends on the amount of IFN-γ in the compartment (Figure 2.20). If it does not become inflammatory, the macrophage will automatically adopt a regulatory phenotype. Inflammatory macrophages present antigen (Figure 2.18, A3bi) and secrete cytokines (A3bii) following contact with bacteria. Inflammatory macrophages secrete cytokines IL12, IFN-γ, IL6 and TGF-β with secretion rates

that are enhanced by IFN-γ (Marzio et al., 1994) A macrophage calculates the amount of cytokine to secrete at each time step by using a non-linear regression model that has been fitted to data from Marzio et al. (1994). Equation (2.4) represents the amount of IFN-γ produced by 10^6 macrophages *in vivo*;

$$ifng = (-0.7831 + 0.0012805t - 0.0000003706t^2 + 0.00005205i) \times m_c. \qquad (2.4)$$

The independent variables in the model are: t, the time since a macrophage started secreting the cytokine, i, the concentration of IFN-γ in the environment, and as with cytokine production by DCs, a modifier m_c, will be added to set the rate for each specific cytokine. All macrophages in the model are phagocytic (A3c) and the maximum number of bacteria that can be taken up by a macrophage will need to be determined in the calibration stage.

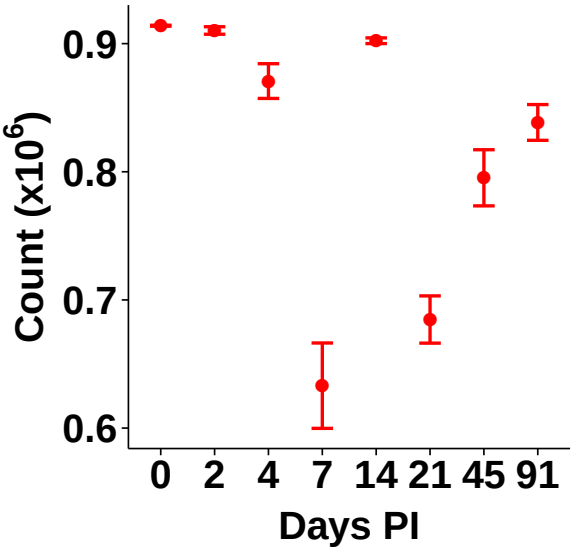

Figure 2.20: Probability that a macrophage will be regulatory depends on the amount of IFN-γ in the tissue. The probability of a macrophahe being regulatory at a single time point was calculated using the amount of IFN-γ in the tissue *in vivo* measured by Morrison et al. (2013)

.

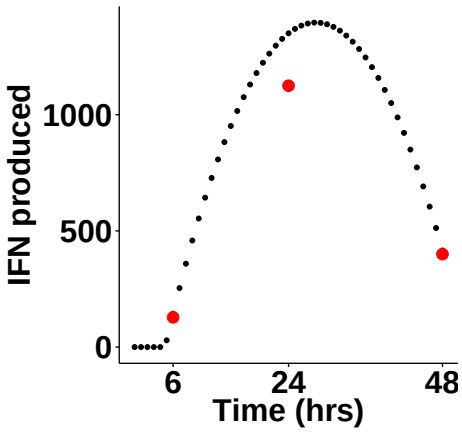

Figure 2.21: Calculation of the amount of IFN-γ to secrete per time step by a macrophage. Where t is the length of time that the macrophage has been secreting IFN-γ, i is the local concentration of IFN-γ. Graph shows *in silico* (black dots) calculated using Equation (2.4) to biological data (red dots) when $5 * 10^6$ macrophages have been pre-stimulated with 100 U/ml of IFN-γ and cultured with LPS *in vitro* (Marzio et al., 1994).

2.3.4.3 T Cells

T-cell state changes are defined in Figure 2.22. On entering the model, T cells are naive (T2), scanning the MLN for DCs at speeds of 11 μm/min (Miller et al., 2004). Previous models of T-cell migration in lymph nodes have represented T-cell motility as a true random walk (Molina-Pars and Lythe, 2011; Beauchemin et al., 2007; Mirsky et al., 2011) or a directed random walk (Linderman et al., 2010). Riggs et al. (2008) compared simulated random motion and with *in vivo* chemotaxis and showed that using random motion to determine T-cell motility adequately captures the dynamics of T-cell priming in the lymph node. Further, Mandl et al. (2012) measured the time taken for $CD4^+$ T cells to traverse the MLN as 9.6hrs (=576mins). This can be used to calibrate the dynamics of T-cell migration. T cells become activated after binding to a DC that is presenting antigen (T3a).

A T cell that has entered an activated state can be proliferating (T3bi) or non-proliferating (T3bii) depending on the length of time that has elapsed since it was last stimulated. The proliferation time for each cell is approximately 11hrs (=660 mins) (De Boer et al., 2003) and during proliferation, a T cell can become a memory cell (T5). Following the rules described by Gong et al. (2013), a T cell that has divided four times becomes an effector cell (T4a) and can leave the lymph node. Effector T cells enter the gut and secrete

cytokines (T4b). The type of cytokine they secrete depends on the polarisation of the T cell. In the model T cells can only adopt a polarisation as either a Th1 or a Th17 cell, and Th17 cells can switch phenotypes to become double positive cells, and then again to become ex-Th17 cells that have a Th1-like phenotype (Figure 2.23). Other T cell phenotypes are ignored as they are not prevalent during inflammation in*Hh* infected IL10 KO mice. The polarisation of T cells into either a Th1 or Th17 phenotype, as well as phenotype switching, will be represented by a set of ODEs 2.24. The model was developed using the COPASI software tool (Hoops et al., 2006), and builds on work by Yates et al. (2004) and Schulz et al. (2009) to capture the dynamics of transcription factors T-box transcription factor T (T-bet) and Retinoic-acid Related Orphan Receptor-γt (ROR-γt) in a single $CD4^+$ T cell undergoing polarisation and phenotype switching following stimulation with exogenous cytokines (Figure 2.24). The dynamics between transcription factors in the model can be understood as follows;

The rate of change in T-bet or ROR-γt

$$\frac{dTbet}{dt} \qquad \frac{dRORgt}{dt} \tag{2.5}$$

The rate of increase in T-bet or ROR-γt expression through external stimulation

$$\left(\frac{s_1 \cdot C_1}{(k_1 + C_1)) \cdot \left(1 + \frac{ROR_{\gamma t}}{g_2}\right)}\right) \qquad \left(\frac{s_2 \cdot C_{17}}{(k_2 + C_{17})) \cdot \left(1 + \frac{Tbet}{g_1}\right)}\right) \tag{2.6}$$

The rate of increase of T-bet or ROR-γt through autoactivation

$$\left(\frac{a_1 \cdot Tbet^n}{(k_3^n + Tbet^n) \cdot \left(1 + \frac{ROR_{\gamma t}}{g_2}\right)}\right) \qquad \left(\frac{a_2 \cdot ROR_{\gamma t}^n}{\left(k_3^n + ROR_{\gamma t}^n\right) \cdot \left(1 + \frac{Tbet}{g_1}\right)}\right) \tag{2.7}$$

The rate of baseline transcription or T-bet or ROR-γt

$$\beta_1 \qquad \beta_2 \tag{2.8}$$

The rate of removal of T-bet or ROR-γt through natural decay or degradation

$$\mu_1 Tbet \qquad \mu_2 ROR_{\gamma t} \tag{2.9}$$

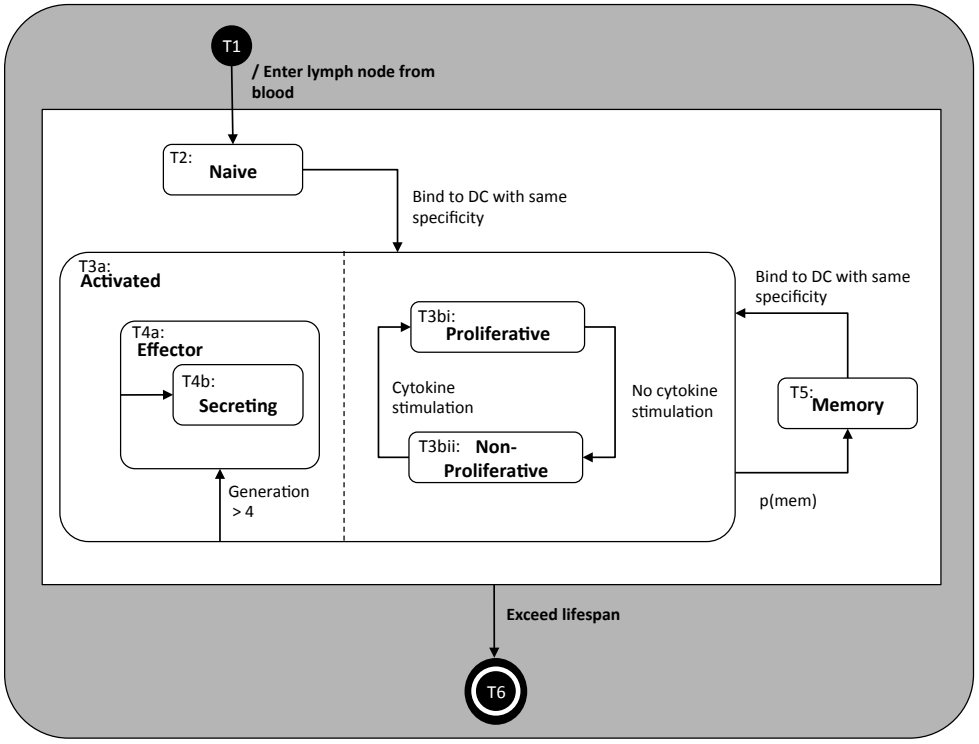

Figure 2.22: T cell state diagram platform model

Previous models of T-cell polarisation have considered the Th1/Th2 axis, focussing on transcription factors T-bet (for Th1) and GATA-3 (for Th2) Yates et al. (2004); Schulz et al. (2009). We utilised ASPASIA to reparameterise these models to capture the dynamics of Th17 polarisation and phenotype switching, using ROR-γt and T-bet as markers of a particular phenotype (Figure 2.23b). A cell in the model is considered to be polarised if one of the transcription factors is stably expressed above baseline level. A cell that expresses both transcription factors at a higher level than at baseline is considered to be a double-positive cell.

As many of the parameters relating to polarisation of Th17 cells were unknown, ASPASIA was used to generate 200 unique SBML models using Latin-hypercube sampling over ranges defined in Appendix D. The models were solved using an SBML solver imple-

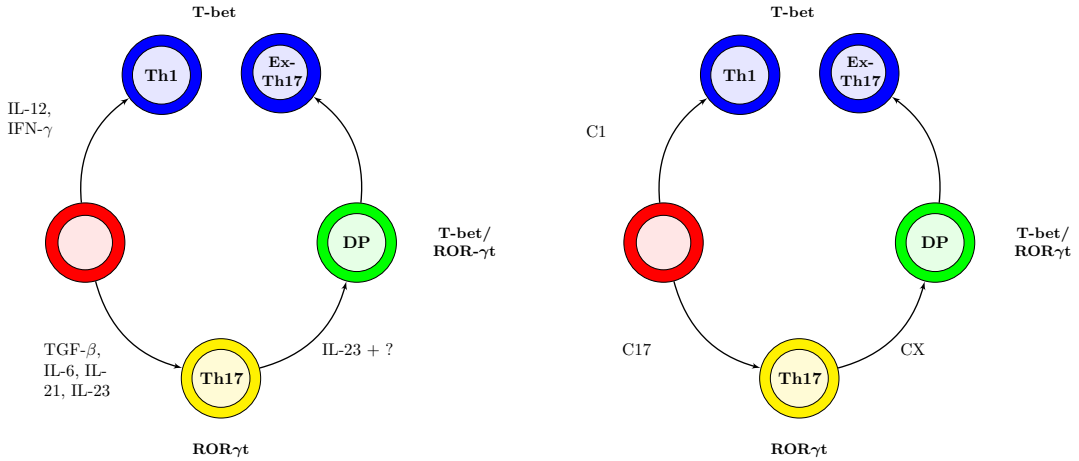

Figure 2.23: Factors controlling CD4$^+$ T-cell differentiation *in vivo* and *in silico*. Upon activation, an unpolarised CD4$^+$ T cell (red) can differentiate into a Th1 or a Th17 cell dependent on the cytokine milleu. Th17 cells can subsequently transition through a double-positive (DP) cell to an ex-Th17 cell. Labels on each arrow indicate cytokines involved in this process *in vivo* (a) and the model species that correspond to these cytokines *in silico* (b). In both cartoons yellow cells secrete IL17 and IL21, blue cells secrete IFN-γ, and green cells secrete a combination of IL17, IL21 and IFN-γ.

menting libSBMLSim Takizawa et al. (2013), with a step size of 0.12 for sufficient time until stable baseline levels of T-bet and ROR-γt were reached. ASPASIA was then used to generate an SBML model with parameters and species concentrations set to baseline values, and interventions introduced representing stimulation with either type 17 (C_{17}) or type 1-polarising cytokine (C_1) (Figure 2.23b). From the 200 models generated we identified the one that best captured the behaviours observed in a CD4$^+$ T cell undergoing Th17 polarisation, i.e. i) no expression of either T-bet or ROR-γt in the absence of polarising cytokines (Figures 2.25a,2.26a), ii) stable expression of ROR-γt following stimulation with type 17 polarising cytokines (Figure 2.25b), and iii) stability of the Th17 phenotype when introduced to type 1 polarising cytokine after initial polarisation has taken place (Figure 2.25c). This same model also met the criteria for a CD4$^+$ T cell adopting a Th1 polarisation (Figure 2.26).

$$\frac{dC_1}{dt} = \left(\frac{s_1 \cdot C_1}{(k_1 + C_1)) \cdot \left(1 + \frac{ROR_{\gamma t}}{g_2}\right)} \right) + d_1 \cdot IFN_\gamma - \mu_3 \cdot C_1 \tag{2.10}$$

$$\frac{dC_{17}}{dt} = \left(\frac{s_2 \cdot C_{17}}{(k_2 + C_{17})) \cdot \left(1 + \frac{ROR_{\gamma t}}{g_1}\right)} \right) + d_2 \cdot IFN_\gamma - \mu_4 \cdot C_1 \tag{2.11}$$

$$\frac{dTbet}{dt} = \left(\frac{s_1 \cdot C_1}{(k_1 + C_1)) \cdot \left(1 + \frac{ROR_{\gamma t}}{g_2}\right)} \right) + b_1 - \mu_1 \cdot Tbet + \left(\frac{a_1 \cdot Tbet^n}{(k_3^n + Tbet^n) \cdot \left(1 + \frac{ROR_{\gamma t}}{g_2}\right)} \right) \tag{2.12}$$

$$\frac{dROR_{\gamma t}}{dt} = \left(\frac{s_2 \cdot C_{17}}{(k_2 + C_{17})) \cdot \left(1 + \frac{Tbet}{g_1}\right)} \right) + b_2 - \mu_2 \cdot ROR_{\gamma t} + \left(\frac{a_2 \cdot ROR_{\gamma t}^n}{\left(k_3^n + ROR_{\gamma t}^n\right) \cdot \left(1 + \frac{Tbet}{g_1}\right)} \right) \tag{2.13}$$

$$\frac{dIFN_\gamma}{dt} = \left(\frac{a_3 \cdot Tbet}{(k_5 + Tbet)) \cdot \left(1 + \frac{ROR_{\gamma t}}{g_3}\right)} \right) - \mu_5 \cdot IFN_\gamma \tag{2.14}$$

$$\frac{dIL21}{dt} = \left(\frac{a_4 \cdot ROR_{\gamma t}}{(k_5 + ROR_{\gamma t})) \cdot \left(1 + \frac{Tbet}{g_3}\right)} \right) - \mu_6 \cdot IL21 \tag{2.15}$$

Figure 2.24: ODE model of T cell polarisation and phenotype switching. Transcription factors T-bet and ROR-γt, indogenous cytokines IFN-γ and IL21 and exogenous cytokines C_1 and C_{17} have been modelled to adequately represent the dynamics of T-cell polarisation. a_i is the autostimulation rate for transcription factors and cytokines, b_i is the basal transcription rate for transcription factors, d_i is the cytokine-induced stimulation of transcription factors, g_i is the level of inhibition of transcription factors and cytokines by opposing transcription factors, μ_i is the decay rate for transcription factors and cytokines, n is the hill-coefficinet, and k_i is the inhibition constant for transcription factors and cytokines.

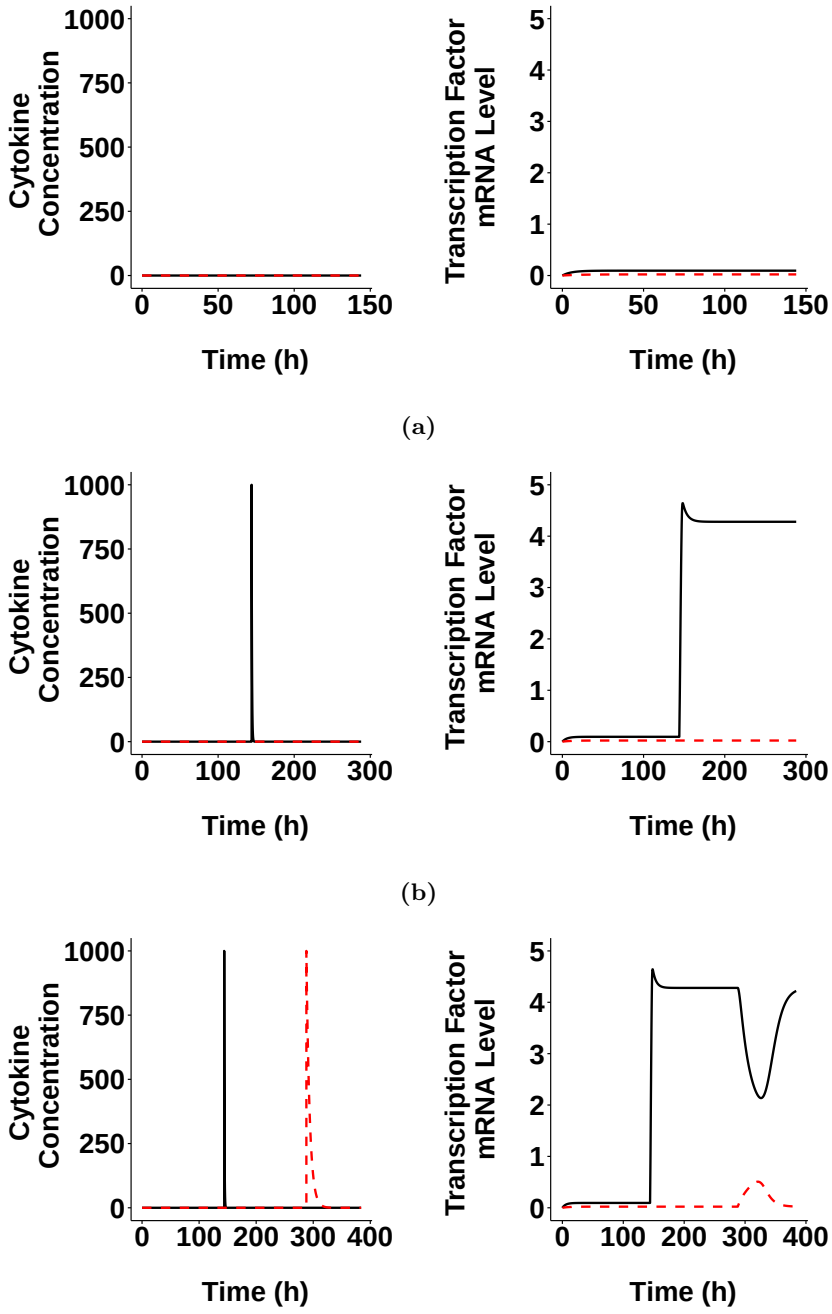

Figure 2.25: ASPASIA-generated model reflects observed biological behaviours of Th17-polarised CD4$^+$ T cells. From 200 ASPASIA-generated models, a single model was selected that best captured biological behaviours. Shown are concentration of polarisating cytokines (left panels) and levels of transcription factor mRNA (right panels) in (a) the absence of type-1 polarising cytokines (C_1) and type-17 polarising cytokines (C_{17}), (b) following stimulation with C_{17}, and (c) following subsequent restimulation with a C_1. Black lines represent C_{17} (left panels) and ROR-γt (right panels), red dashed lines represent C_1 (left panels) and T-bet (right panels).

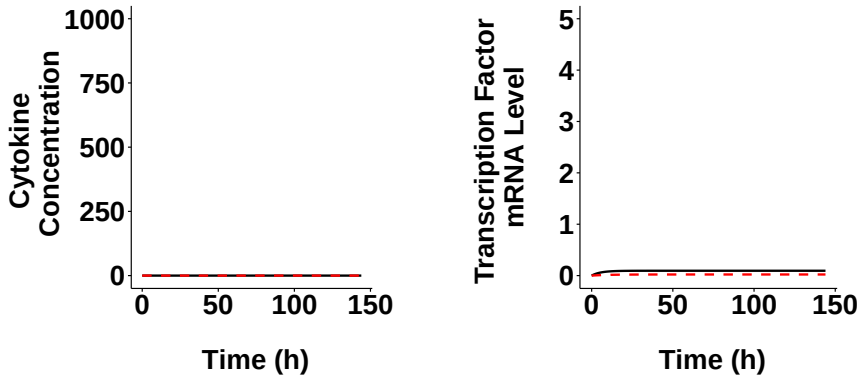

(a)

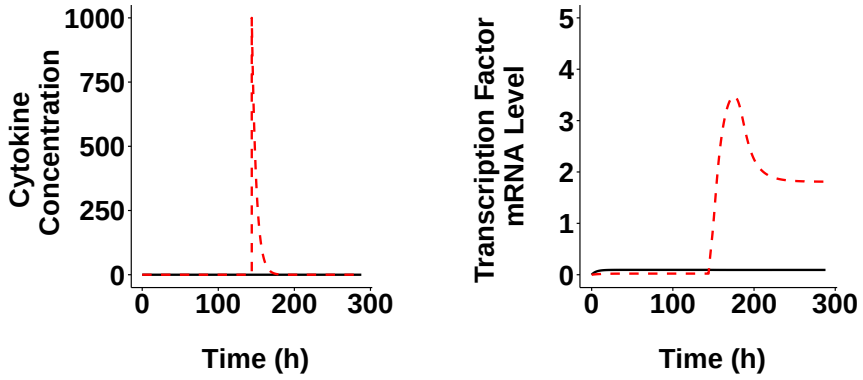

(b)

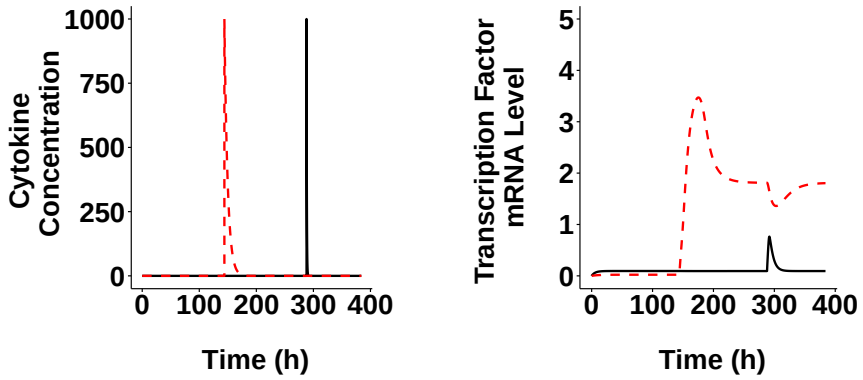

(c)

Figure 2.26: ASPASIA-generated model reflects observed biological behaviors of Th1-polarised CD4$^+$ T cells. The model shown in Figure 3 was examined under Th1-polarising conditions. Shown are concentration of polarisating cytokines and levels of transcription factor mRNA in the absence of type-1 polarising cytokines (C_1) and type-17 polarising cytokines (C_{17})(a), following stimulation with C_1 (b), and following subsequent restimulation with a C_{17} (c). Black lines represent C_{17} (left panels) and ROR-γt (right panels), red dashed lines represent C_1 (left panels) and T-bet (right panels)

2.3.4.4 Epithelial Cells

Epithelial cells will be modelled using a subset of differential equations from a mathematical model of immune modulatory mechanisms in IBD by Wendelsdorf et al. (2010). These authors model the dynamics of 12 populations of cells and two cytokines in the gut during intestinal inflammation. The equations for two of these cell types, epithelial cells and pro-inflammatory epithelial cells, that is epithelial cells that secrete inflammatory cytokines, have been abstracted from this set of equations and will be included in the model of *Hh*-induced colitis (Equations (2.16) to (2.18)). The rate of change per 6 hrs of C_a^E, E, and E_p are given by

$$\frac{d\ C_a^E}{dt} = \lambda_c\ (\ (\ T_h^E\ + M_1^E)\ + D_e^E\ +\ E_p\ ) - \mu_c\ C_a^E, \tag{2.16}$$

$$\frac{d\ E}{dt} = E\ (\lambda_E - \phi_E\ (E\ +\ E_p\ - \mu_E\ -\ \nu_{EC}\ C_a^E\ )\ ) + \mu_E\ E_p, \tag{2.17}$$

$$\frac{d\ E_p}{dt}\ = \eta_{EC}\ E\ C_a^E\ -\ E_p\ (\mu_E + \mu_{ce}\ C_a^E\ ), \tag{2.18}$$

where C_a^E is the concentration of activating cytokine, E is the number of regular epithelial cells, E_p is the number of secreting epithelial cells, and all other model parameters are as defined in Table 2.3. Stability analysis was performed and a time step of 1 minute was deemed to be adequate when simulating this model using the Runge-Kutta algorithm with a step size of 0.012.

Table 2.3: Parameters in epithelial barrier model. Values for paramters Equations (2.16) to (2.18) taken from Wendelsdorf et al. (2010). Values denoted by * will be calculated in the calibration stage.

Parameter	Measure	Value	Units
λ_E	Birth rate of epithelial cells	2	E^{-1}
ϕ_E	Crowding coefficient, epithelial cells	0.00015	Dimensionless
ν_{EC}	Rate of cell switching from epithelial to pro-inflammatory epithelial cell	5×10^{-9}	$C_a^{-1}t^{-1}$
μ_{ce}	Death rate of epithelial cells due to inflammatory factors	5×10^{-10}	$C_a^{-1}t^{-1}$
λ_c	Rate of cytokine production	0.25	$cells^{-1}t^{-1}$
μ_c	Rate of cytokine degradation	0.075	t^{-1}
T_h^E	Number of T cells	*	Dimensionless
D_c^E	Number of T cells	*	Dimensionless
M_1^E	Number of T cells	*	Dimensionless

2.3.4.5 Cytokines

Cytokines are secreted by DCs and macrophages in response to bacteria, and by activated T cells in the cecum and colon compartment. They exist on discrete grids, one for each type of cytokine in each compartment, and the compartments in the model consist of several layers of these grids. In continuous space, chemical diffusion can be modelled using the heat equation (Barnes and Fulford, 2011).

$$\frac{\partial \phi_{(x,y,t)}}{\partial t} = D\left(\frac{\partial^2 \phi_{(x,y,t)}}{\partial x^2} + \frac{\partial^2 \phi_{(x,y,t)}}{\partial y^2}\right) \tag{2.19}$$

To model cytokine diffusion in discrete space, a discretised version of the heat equation

has been developed (Equation (2.23)).

$$\frac{\phi_{(x,y,t)} - \phi_{(x,y,t-\Delta t)}}{\Delta t} \approx \frac{\partial\left(\frac{\phi_{(x,y,t)}-\phi_{(x-\Delta x,y,t)}}{\Delta x}\right)}{\partial x} + \frac{\partial\left(\frac{\phi_{(x,y,t)}-\phi_{(x,y-\Delta y,t)}}{\Delta y}\right)}{\partial y}, \tag{2.20}$$

$$\approx \frac{\frac{\phi_{(x+\Delta x,y,t)}-\phi_{(x,y,t)}}{\Delta x} - \frac{\phi_{(x,y,t)}-\phi_{(x-\Delta x,y,t)}}{\Delta x}}{\Delta x} + \frac{\frac{\phi_{(x,y+\Delta y,t)}-\phi_{(x,y,t)}}{\Delta y} - \frac{\phi_{(x,y,t)}-\phi_{(x,y-\Delta y,t)}}{\Delta y}}{\Delta y}, \tag{2.21}$$

$$= \frac{\phi_{(x+\Delta x,y,t)} - 2\phi_{(x,y,t)} + \phi_{(x-\Delta x,y,t)}}{\Delta x^2} + \frac{\phi_{(x,y+\Delta y,t)} - 2\phi_{(x,y,t)} + \phi_{(x,y-\Delta y,t)}}{\Delta y^2}, \tag{2.22}$$

$$= \frac{\phi_{(x+\Delta x,y,t)} + \phi_{(x-\Delta x,y,t)} + \phi_{(x,y+\Delta y,t)} + \phi_{(x,y-\Delta y,t)} - 4\phi_{(x,y,t)}}{\Delta L^2}, \tag{2.23}$$

where ΔL is the length of an edge of a square in the discretised grid. Cells in the model interact with each other and with cytokines by constantly checking their location on related grids to identify and cells or cytokines present.

2.3.5 Mapping Simulation Output to Biology

To determine if the model adequately reflects biology, simulation output will need to be compared to data from the Kullberg lab. There are two comparisons that can be made, firstly cell counts can be compared to *in vivo* raw data, and secondly a score can be developed that quantifies the level of inflammation in the system at each time point that can be compared to *in vivo* histology scores.

2.3.5.1 Comparing *In silico* and *In vivo*Data

To determine the kind of data that should be output from the simulation at each time point, relevant biological data collected in the Kullberg lab has been collated (Table 2.4). This data can be used to determine what kind of data should be recorded in the simulation. Agreement between simulation output and raw data from biology would confirm that the model adequately captures what is known in biology. From Table 2.4, there are 15 simulation measures per time point that should be collected for direct comparison with *in vivo* data, corresponding to the measures listed.

Data		**Time point (days post *Hh* innoculation**					
		0	**2**	**4**	**7**	**14**	**21**
Cecum							
CD4 $^+$ T cells	Total	0.1	0.1	0.2	1.0	2.8	2.7
($\times 10^6$)	Th1	0.003	0.004	0.007	0.134	0.535	0.486
	Th17	0.003	0.004	0.007	0.091	0.290	0.201
	Double-Positive	0.001	0.000	0.000	0.066	0.549	0.471
Hh	pg/ng total DNA	0.00	3.35	20.83	17.16	4.26	2.41
Colon							
CD4 $^+$ T cells	Total	0.1	0.1	0.1	1.0	3.5	3.7
($\times 10^6$)	Th1	0.003	0.003	0.008	0.177	0.786	0.792
	Th17	0.003	0.003	0.007	0.114	0.312	0.271
	Double-Positive	0.001	0.000	0.001	0.062	0.776	0.697
Macrophage ($\times 10^4$)	Inflammatory	5				8	
	Regulatory	10				65	
Cytokines	IFN-γ	1187	5430	50542	322186	14566	263178
(pg/ml)	IL17	37	0	630	12030	7392	8682
MLN							
CD4 $^+$ T cells ($\times 10^6$)	Total	0.1	0.1	0.2	1.0	2.8	2.7
(% of CD4$^+$)	CD44$^{\text{hi}}$	4.8	5.4	8.5	15.4	12.4	9.5

Table 2.4: Biological data used to inform and validate the model. Data was taken from Morrison et al. (2013), and Bain and Kullberg, unpublished. Days 0 and 14 were used for information and remaining timepoints for validation.

2.3.5.2 Development of a Scoring System to Measure Inflammation *in silico*

The level of inflammation in a tissue *in vivo* is determined by a histology score. Tissues are fixed in buffered 10% formalin, embedded in paraffin and stained with hematoxylin and eosin. Samples are then scored blindly from 0–3 for each of hyperplasia of the epithelium, and lamina propria infiltrating cells, and 0–1 for markers of severe inflammation (submucosal inflammation, goblet cell depletion, crypt abscesses, ulcers). The total score is calculated by adding up the individual scores for each marker of inflammation with a maximum score of 11.

To generate meaningful output from the model, inflammation in the model should be quantified in a similar way to biology. To do this, a scoring system similar to the histology

score has been developed to determine the level of inflammation in a simulation at any time point. As the epithelial barrier in the model is represented by an ODE, hyperplasia cannot be observed. Hyperplasia of the epithelium *in silico*, will be graded from 0–3 based on the number of secreting epithelial cells that are expected to increase with increasing levels of inflammation in the tissue. Mapping the infiltrating immune cells to the simulation is straight forward, as for this part of the score the total number of immune cells (both regulatory and inflammatory) can be counted and scored in the range 0–3. Finally, as the model does not contain every cell type in biology, the severe markers of inflammation will not be observed; however, it is known that goblet cell depletion is caused by IFN-γ (Chan et al., 2013), and that crypt abscesses are caused by IL17 (Fournier and Parkos, 2012). These severe markers of inflammation will each be graded from 0–1 based on total amount of IFN-γ and the amount of IL17 in the compartment, respectively (Table 2.5). This scoring system will need to be properly calibrated once the simulation platform has been developed to ensure that the score qualitatively reflects what is happening in the simulation with respect to the features that would be observed in biology. Using this method to quantify inflammation requires the collection of several additional measures in the simulation than those required for comparison with the data in Table 2.4. The additional measures are: the number of inflammatory epithelial cells in the cecum and colon, the number of macrophages and DCs in the cecum, and the concentrations of cytokine in the cecum.

Biological Measure	**Score**	**Simulation Measure**
Lamina Propria infiltration	0-3	Total number of immune cells in compartment
Epithelial Hyperplasia	0-3	Number of inflammatory epithelial cells
Goblet cell depletion	0-1	Amount of IFN-γ in compartment
Crypt abscesses	0-1	Amount of IL17 in compartment

Table 2.5: *In silico* inflammation scoring system. Scoring system used to compare output from *in silico* experiments to *in vivo* histology score.

2.3.5.3 Platform Model Summary

In the model, all compartments will be represented in 2D. There will be one grid for every cell type in each compartment with the exception of the cecal and colonic lumen where the *Hh* is modelled by integers on a discrete grid with a further grid containing nutrient concentrations that control the proliferation and death of the bacteria (Figure 2.27c). Each cell in the model will be considered to be representative of 5000 cells in biology, but the compartments in the model will be full scale. The scale was chosen to allow adequate cell numbers to achieve statistical significance when comparing between experimental scenarios while reducing computational burden. There is a danger that the scaling down of cell counts in a computational model could lead to some rare events been over or under represented. Although untested, it is believed that a 1:5000 scale is sufficient to observe all possible cellular behaviours in the population, given that no events with a probability below 0.05 are defined in IBDSim. Each grid square will be representative of 50 μm, the diameter of a single DC, to ease calculations of distances; thus, a compartment with length 1cm in biology would be 200 grid squares (10000 μm) long in the model. Figure 2.28 shows the types of grid that make up the environment in each compartment in the model, as well as the cells that are located on each grid, and the equivalent biological dimensions. In the cecum Figure 2.28a, the first grid is a continuous space that contains APCs (DCs and macrophages), the second grid is a continuous space that contains T cells, the third

is a continuous space that contains bacteria, and the final four grids are discrete grids that each contain one of the cytokines IFN-γ, IL12, IL6 + TGF-β, and IL12. IL17 is not modelled using the explicit grid-based representation and is instead contained inside each compartment as a number representing the total concentration of IL17 in the compartment. Time in the model will be represented in discrete steps, each one representing 1 minute in biology. This means that a cell travelling with a speed of 10 μm a minute in biology would step 0.2 squares per time step.

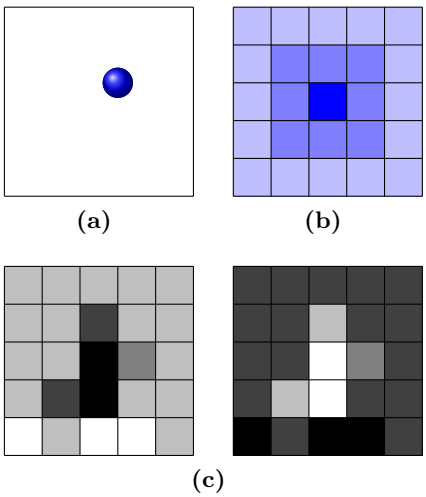

Figure 2.27: Types of grid that are used in the model. (a) Continuous grids are used for all cells in the model and allow agents to have any location $(x, y), \quad x, y \in \mathbb{R}$. (b) Discrete grids are used for cytokines and available locations $(x, y), \quad x, y \in \mathbb{N}$ and each square is $50\mu m$. The darker the colour in the square, the higher the concentration of cytokine. To secrete cytokines a cells location is discretised by rounding to the nearest whole number so the cell shown in (a) would secrete cytokines to the darkest location in (b). (c) Is another version of the discrete grid but here there are a pair of grids, one for cells and one for nutrients. This representation is used for bacteria in the lumen.

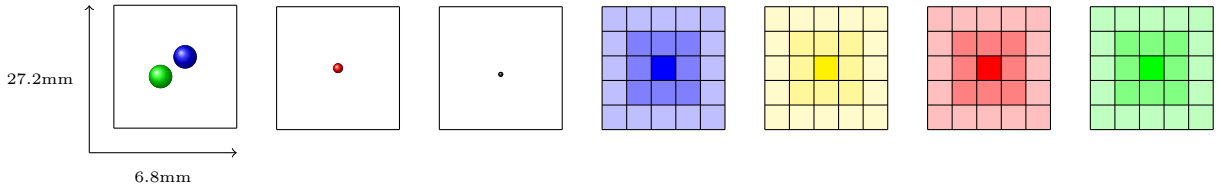

(a) Cecum

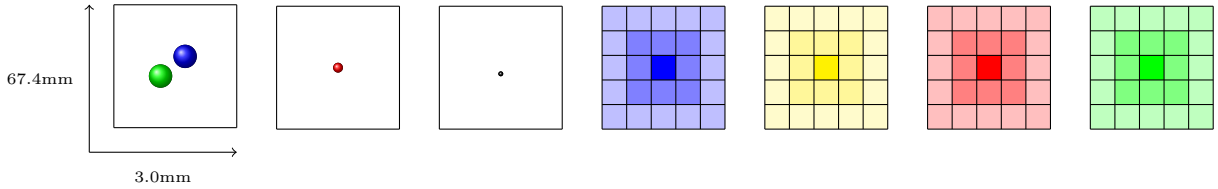

(b) Colon

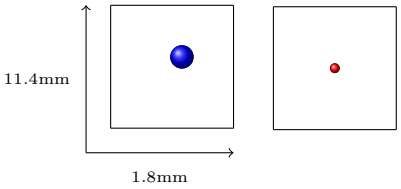

(c) MLN

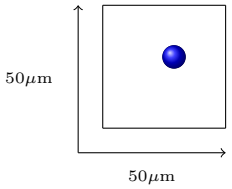

(d) Lymph

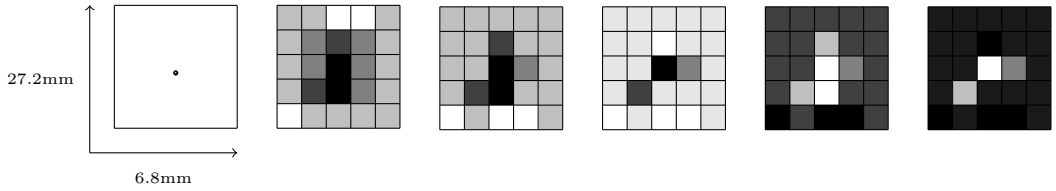

(e) Cecal Lumen

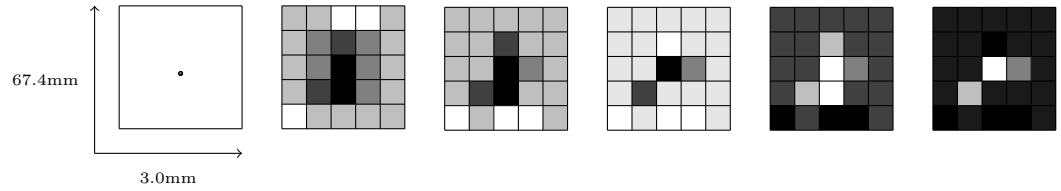

(f) Colonic Lumen

Figure 2.28: Depiction of cell and cytokine grids that make up each compartment. The types of grid that make up the environment of each compartment in the model, as well as the cells that are located on each grid, and the equivalent biological dimensions are shown. Continuous grids contain cells and unique grids exist for APCs (DCs (blue), macrophage (green)), T cells (red), and bacteria (black). Cytokine grids are discrete and represent IFN-γ (blue), IL12 (yellow), IL6 + TGF-β (red) and IL21 (green), with darker colours representing higher concentrations of cytokines. Bacteria and nutrient grids for the cecal and colonic lumen compartments are shown as discrete grids coloured in gray with darker squares representing higher bacteria and nutrient concentrations (note that squares with higher numbers of bacteria correspond to squares with lower number of nutrients).

2.4 Simulation Platform

The simulation platform deals with the development and calibration of an executable model (Section 2.4.1). It is in this module of the modelling process that the ABM described by the platform model in the previous section will be built and executed. This model, IBDSim, has been implemented using the Java programming language and MASON simulation environment, a cross-platform toolkit for the creation of multi-agent simulations (Luke et al., 2005). A full description of the architecture of the simulation can be found in Section 2.10.1.

2.4.1 Model Calibration

Calibrating computational models of biological systems, assigning parameter values to ensure the model reflects behaviours observed biologically, can greatly impact the strength of hypotheses the model generates. The calibration process of IBDSim involves the simulation being executed with a set of "best guess" parameters that are set either from data in the literature or by estimating sensible values from responses observed when parameter scans were performed for individual pathways within the model. After these parameters were set, average results from a series of simulations were collected to mitigate aleatory uncertainty, and the modeller and domain expert examine by eye how the simulated data compares to that from biology. Once a suitable set of parameters had been determined, the model was validated by simulating the effect of biological problems for which the outcome was already known. This approach increases confidence that the model can be used to perform experimentation into situations where the outcome is yet to be determined.

This section discusses how each cellular behaviour described in the platform model has been coded into a hybrid ABM simulation platform, and compares data from *in silico* simulations of each behaviour to its biological equivalent. The calibration of unknown or non-biological parameters specified in the platform model is also explained. It is important to note that individual calibration of the behaviours of each type of agent in the simulation will be crude, as when behaviours of additional agents are calibrated slight variations may occur. Only when each agent has been approximately calibrated can the whole system be studied and the parameter values fine tuned.

2.4.1.1 Bacteria

The platform model states that *Hh* in the model proliferates with a mean time of 660 mins, where sufficient nutrients are available. The grid-based model described in Section 2.2.3.1 has been calibrated by generating Latin-hypercube samples of unknown parameters and comparing them to biological data between days 2 and 4 post-infection. The effects of varying each parameter is shown in Figure 28 (Cont.). The most influential of these parameters were *removeNut* (Figure 28 (Cont.)c), and *addNut* (Figure 28 (Cont.)c), with PRCC of 0.544, and 0.404 respectively, and p-values less than 0.05. Altering other values did not result in statistically significant correlations. As these parameters are not biologically verifiable, the values are selected to produce the correct number of *Hh*. at 4-5 days post infection, which is approximately 20,000.

In the platform model, it was decided that the rate of immune response-induced *Hh* death would depend linearly on the amount of secreting epithelial cells, as suggested by Wendelsdorf et al. (2010). The relationship was determined to be

$$d(E_p) = -d_c + d_{b_1} E_p, \tag{2.24}$$

where, d_c and d_{b_1} are parameters to be identified. Similarly, it was determined that the probability that a *Hh* bacterium will switch compartments from the cecal or colonic lumen to the corresponding lamina propria compartment would be modelled using a linear relationship,

$$s(E_p) = s_c + s_{b_1} E_p, \tag{2.25}$$

where, s_c and s_{b_1} are parameters to be determined. Parameters d_c, d_{b_1}, s_c, and s_{b_1} were varied over ranges defined in Table 2.6 where the maximum and minimum values were estimated based on the reduction of *Hh* in the lumen between days 7 and 14 post infection. Using these ranges, 200 parameter sets were generated using Spartan (Alden et al., 2013). Executing the model a number of times for each parameter set revealed parameter constraints for producing biologically relevant output, and a suitable parameter

set that resulted in a model that adequately captured the decline of the number of *Hh* cells in the cecal lumen, was determined within these constraints. Performing a sensitivity analysis (Figure 28 (Cont.)) on the results of these simulations revealed that the most important parameter in controlling the amount of *Hh* present in the lumen is d_{b1}, the rate at which a change in the number of secreting epithelial cells (E_p) affects the probability that a *Hh* bacterium in the cecal or colonic lumen compartment will die in a given time step. d_{b1} is the only parameter that had highly significant ($p<0.01$) correlations with the number of bacteria at all time points post *Hh* infection (Figure 2.29a). Figure 2.29 (b-f) show the how the spartan-generated values for parameter d_{b1} compare to the approximate *in vivo Hh* counts at days 2, 4, 7, 14, and 21 post *Hh* infection. Potential parameter sets are identified as those that sit closest to the grey area in all plots.

As there is no sampling of *Hh* in the lumen by APCs in the model, the number of bacteria in the lamina propria is an important factor in controlling behaviours of other agents in the model. The parameters relating to the switching rate, as well as the lifespan of the bacteria, were calibrated to produce adequate tissue dynamics during the fine tuning stage of model development. The lifespan of a bacteria (both *Hh* and commensal) in the lamina propria was calibrated by hand to a value of 840 mins by trying values in the range of 750-1000 mins, and exploring the effect that the lifespan of bacteria in the lamina propria had on cell counts.

Parameter	**Range (min, max)**	**Value**
d_c	$(3.29 \times 10^{-6}, 3.29 \times 10^{-3})$	3.29×10^{-6}
d_{b_1}	$(8 \times 10^{-9}, 8 \times 10^{-3})$	$(8 \times 10^{-9}$
s_c	$(2.91 \times 10^{-8}, 2.91 \times 10^{-3})$	2.91×10^{-8}
s_{b_1}	$(6.54 \times 10^{-9}, 6.54 \times 10^{-3})$	6.54×10^{-9}

Table 2.6: Calibration of *Hh* death and compartment switching rates. 200 parameter sets were generated within the ranges specified and values from the model that best matched biological data were recorded.

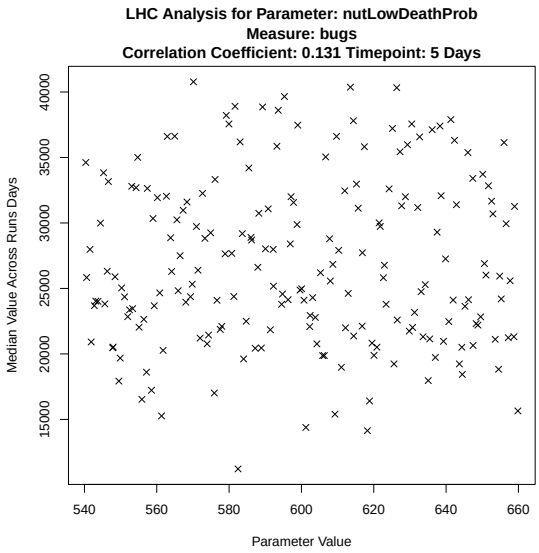
LHC Analysis for Parameter: nutLowDeathProb
Measure: bugs
Correlation Coefficient: 0.131 Timepoint: 5 Days
Median Value Across Runs Days
Parameter Value

(a)

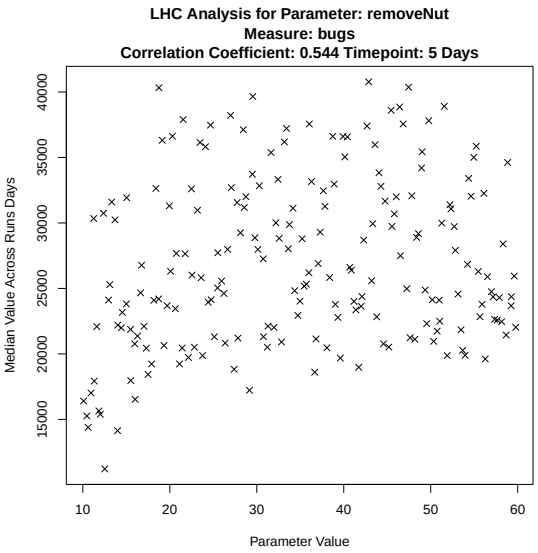
LHC Analysis for Parameter: removeNut
Measure: bugs
Correlation Coefficient: 0.544 Timepoint: 5 Days
Median Value Across Runs Days
Parameter Value

(b)

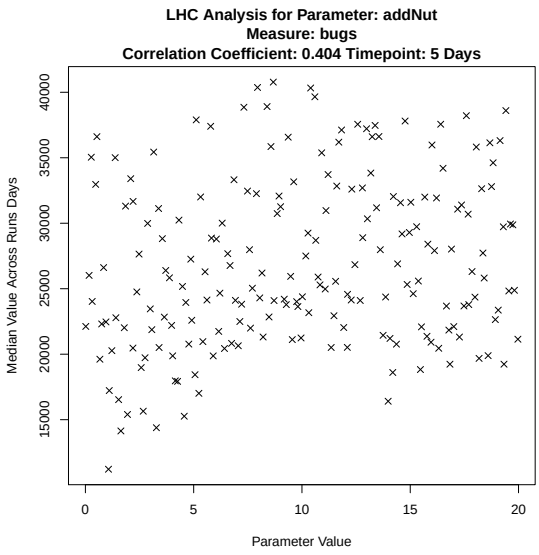
LHC Analysis for Parameter: addNut
Measure: bugs
Correlation Coefficient: 0.404 Timepoint: 5 Days
Median Value Across Runs Days
Parameter Value

(c)

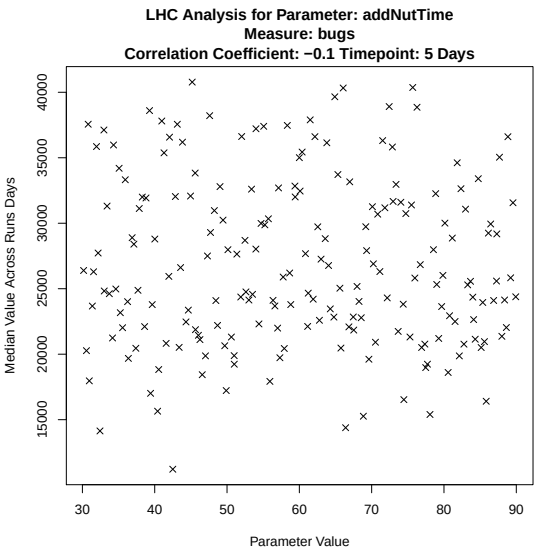
LHC Analysis for Parameter: addNutTime
Measure: bugs
Correlation Coefficient: −0.1 Timepoint: 5 Days
Median Value Across Runs Days
Parameter Value

(d)

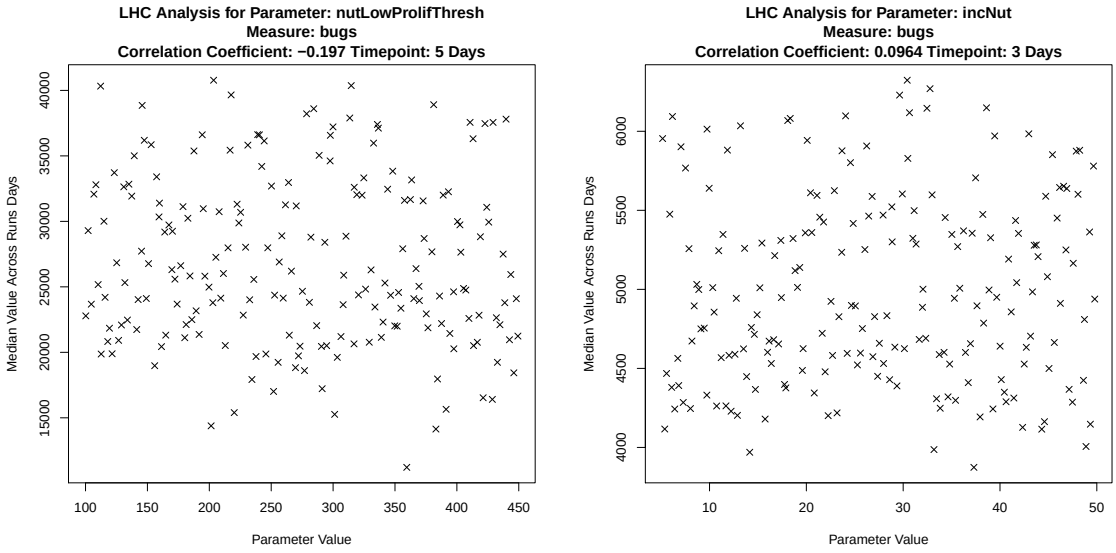

(a) **(b)**

Figure 28 (Cont.): Parameter calibration for the grid-based model of *Hh*. 200 parameter sets were generated using latin hypercube sampling and simulations were run using each parameter set. Partial rank correlation coefficients between the maximum number of *Hh* bacteria between days 4 and 5 post infection, and each non biologically verifiable parameter in the model. (a) nutLowDeathProb, (b)removeNut, (c) addNut, (d) addNutTime, (e) nutLowProlifThresh, and (f) incNut.

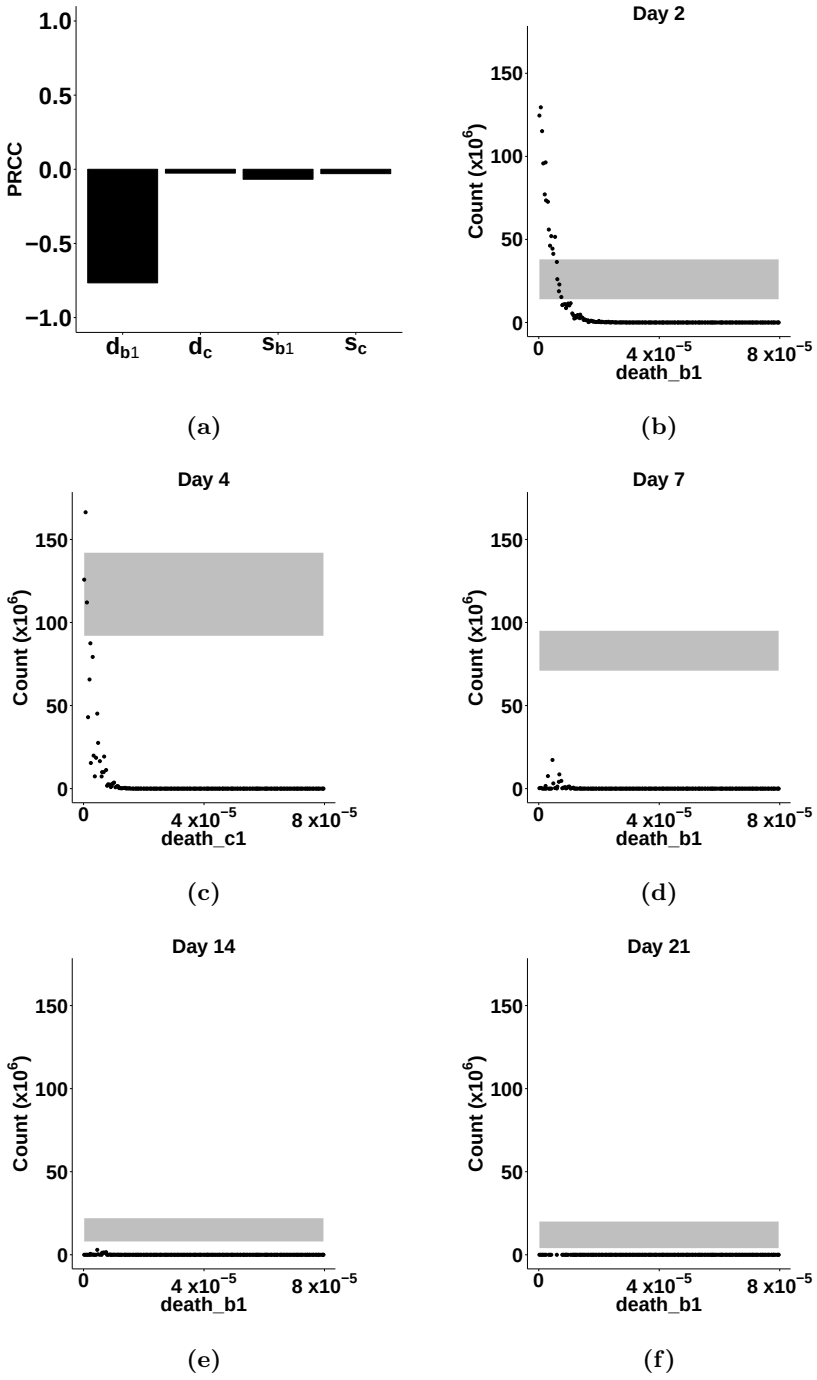

Figure 2.29: Parameter calibration for the abstraction that bacteria switch compartment at a rate dependant of the number of secreting epithelial cells. 200 parameter sets were generated using latin hypercube sampling and simulations were run using each parameter set. (a) Partial rank correlation coefficients between the maximum number of *Hh* bacteria and each parameter in the model. (b-f) Simulation results of running the bacteria model with different parameter sets (black dots) and *in vivo Hh* counts at each time point.

2.4.1.2 Macrophages

The platform model highlighted a set of macrophage-specific parameters for which calibration using the simulation platform is required. The first of these parameters is *maxBugs*, the number of bacteria that a macrophage can ingest before dying. As this parameter increases, the death rate of macrophages decreases, resulting in the number of macrophages in the tissue at a given time point post infection also increasing (Figure 2.30). Unpublished data estimates the number of inflammatory macrophages in the colon at days 0 and 14 to be approximately 0.5×10^5 and 8×10^5 respectively, and the number of regulatory macrophages at the same time points to be approximately 1×10^5 and 6.5×10^5 (Bain and Kullberg, unpublished). The parameter *maxBugs* was calibrated by comparing the number of macrophages in the cecum and colon in the simulation to this biological data, and was set to 125 .

The next thing to calibrate was the amount of cytokine to be secreted in different environmental conditions. In the platform model, non-linear regression was used to model the total amount of IFN-γ secreted by 10^6 macrophages in biology (Equation (2.4)). In the simulation platform, the total number of macrophages in the lamina propria has been transformed so that one simulated cell represents 5000 in biology, thus 10^6 *in vitro* macrophages 200 *in silico* macrophages. The amount of cytokine to be secreted was determined using the Equation (2.4) but dividing the parameters in the model by 200 so that a population of uniformly secreting *in silico* macrophages replicate the *in vitro* data shown in Figure 2.21. An additional scaler term was added to reflect the fact that the amount of cytokine in the environment depends not only on the secretion rate, but also the decay rate of that cytokine, something that is known in biology. Thus just dividing the total amount by the secretion rate results in a model that widely overestimates the concentration that should actually be secreted by a macrophage in the model. Figure 2.31 shows the concentration of IFN-γ secreted by 10^6 macrophages in biology (Figure 2.31a), and of IFN-γ, IL12, and IL6 + TGF-β secreted by 200 simulated macrophages over time (Figures 2.31b to 2.31d). The models assume that all macrophages are inflammatory and have been pre-stimulated with IFN-γ to ensure maximum cytokine production. As determined in the platform model, the secretion rates of IFN-γ and IL12 are similar (Figures 2.31b,2.31c). The secretion rate

for IL6 + TGF-β has been modelled to be the same as that for IL6, i.e. three times the level of IL12 and IFN-γ since the purpose of this cytokine in the model is to polarise T cells into a Th17 phenotype and the *in vitro* polarisation protocols advocate a significantly higher concentration of IL6 than TGF-β (Bedoya et al., 2013) (Figure 2.31d).

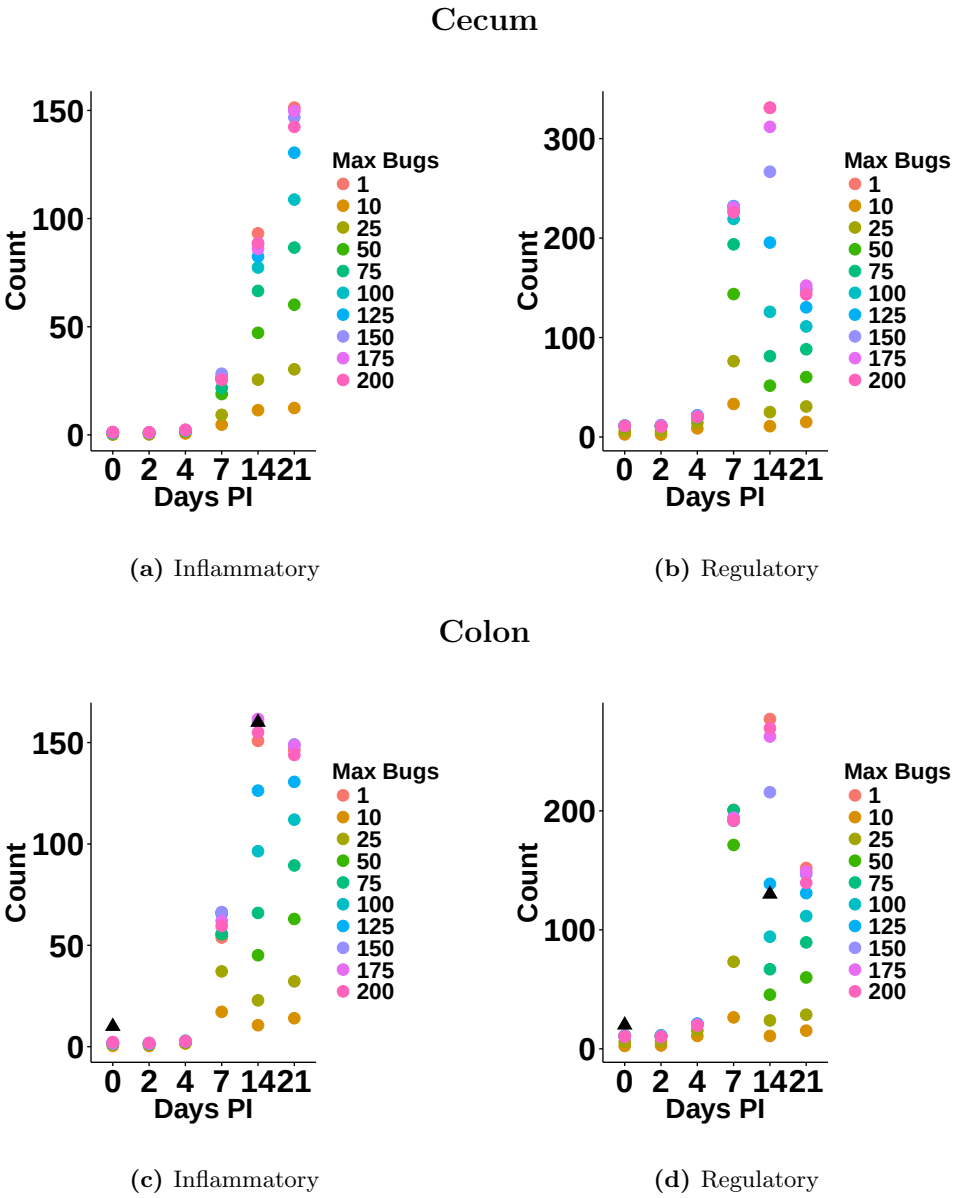

(a) Inflammatory **(b)** Regulatory

(c) Inflammatory **(d)** Regulatory

Figure 2.30: Calibrating *maxBugs* parameter for macrophages. Infections were simulated allowing the *maxBugs* parameter to take values ranging from 1-200. The total number of inflammatory and regulatory macrophages were counted in the cecum (a, b) and in the colon (c,d) at several timepoints post infection. Each point represents average counts from 25 runs for each parameter set.

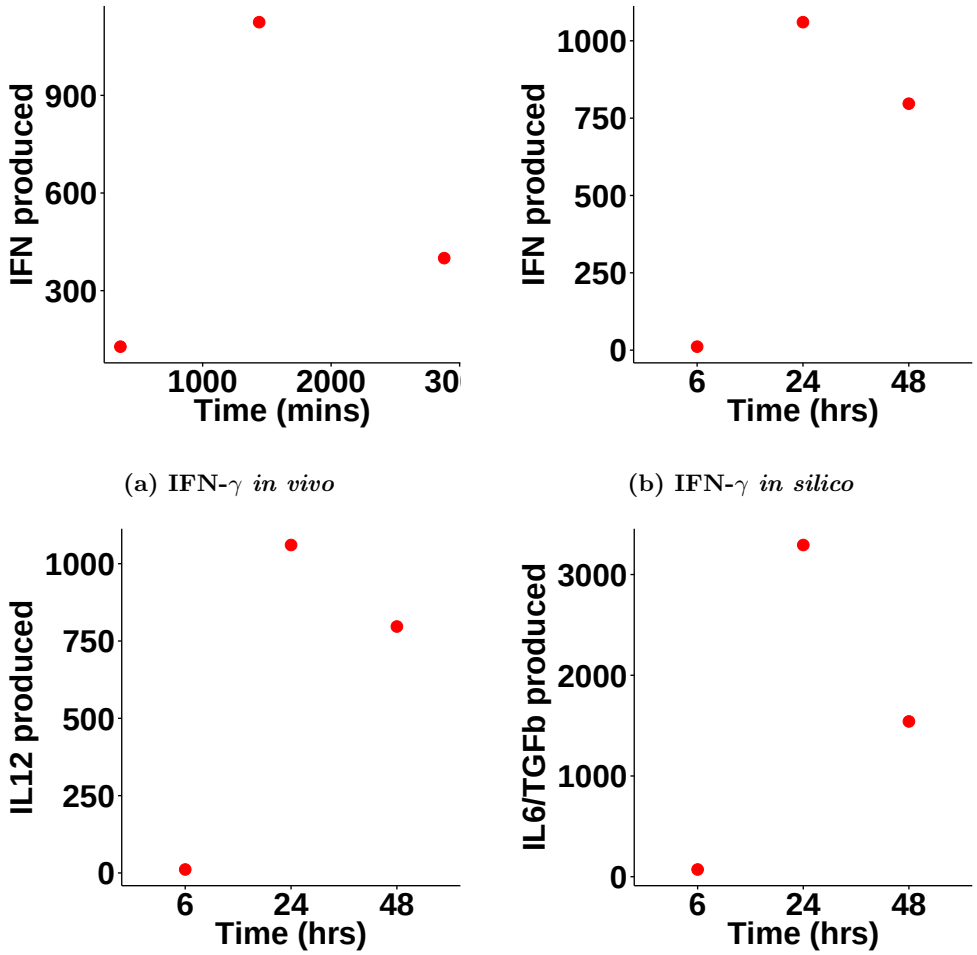

(a) IFN-γ *in vivo* **(b) IFN-γ *in silico***

(c) IL12 *in silico* **(d) IL6/TGF-β *in silico***

Figure 2.31: Modelling cytokine secretion by macrophages. (a) Amount of IFN-γ secreted by 10^6 macrophages that have been pre-stimulated with the highest concentration of IFN-γ *in vivo*. (b)-(d) 200 *in silico* macrophages stimulated with the highest concentration of IFN-γ were placed in an empty simulated compartment and allowed to secrete either IFN-γ (b), IL12 (c) or IL6/ TGF-β (d) for 48hrs and total concentration of cytokine in the compartment was recorded.

DCs

From developing the platform model it was determined that the number of bacteria to be taken up and presented by a single DC needed to be calibrated using the simulation platform. Once a DC has taken up the specified number of bacteria, it will migrate to the MLN so increasing this parameter also leads to an increase in the number of DCs in the lamina propria compartments Figure 2.32. Setting the maximum number of bacteria to be taken up and presented by a single DC to 17 resulted in an adequate distribution of DCs across the system at each time point. When a DC takes up a bacterium it will secrete IL12

or IL6/TGF-β depending on the integer type variable of the bacterium. If the bacterium is of type 1:$numberOfSpecificities/2$, the DC will secrete IL12, else it will secrete IL6/TGF-β d. In the platform model, an equation representing IL12 secretion by 5×10^6 DCs in response to high or low stimulation was generated Equation (2.3). To use this equation to model the amount of cytokine to be secreted by a single DC in the ABM, an additional multiplier term has been added to capture the dynamics of secretion for any cytokine by adding a multiplier to the equation. The multiplier is in the form $\frac{m_c}{n}$ to give an individual rather than population based model where m is the fold change between the observed concentration of cytokine c and the concentration of IL12 and n is the simulation equivalent of the number of DCs that were secreting the cytokine, where 5×10^6 DCs in biology $\approx$ 1000 cells in the model. The amount of stimulation was related to the number of bacteria the DChas phagocytosed. To keep the level of stimulation in the 0-1 range, the level of stimulation was rescaled as $\frac{\text{total number of cytokine } c\text{-inducing bacteria phagocyosed}}{\text{maximum number of bacteria that can be phagocytosed}}$. Allowing 1000 DCs to secrete IL12 at the highest level, that is when 16 bacteria have been phagocytosed since 17 would cause the DC to migrate to the MLN, and lowest levels, 4 bacteria, result in concentrations of IL12 that are statistically similar to biology (Figure 2.33,$p = 0.2286$).

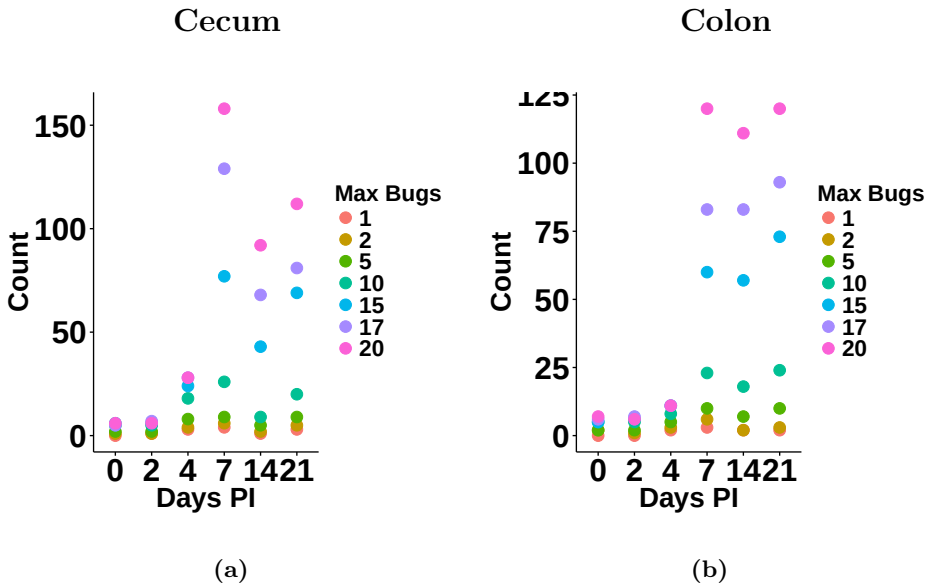

(a) (b)

Figure 2.32: Calibrating *maxBugs* parameter for DCs. Infections were simulated allowing the *maxBugs* parameter to take values ranging from 1-20. The total number of DCs were counted in the cecum (a) and in the colon (c) at several timepoints post infection. Each point represents average counts from 25 runs for each parameter set.

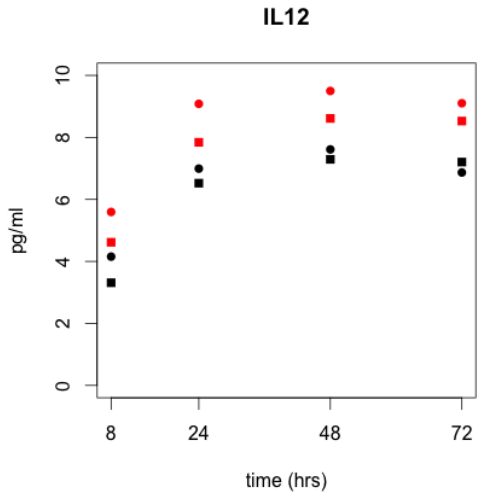

Figure 2.33: Cytokine secretion by dendritic cells in the model is representative of biology. 200 DCs (representative of 5×10^5 in biology) secreted cytokine IL12 at an amount determined by the length of time they had been secreting and based on the assumption they had injested their full complement of bacteria (red squares) or LPS (black squares)and the level of cytokine in the compartment was recorded and compared to data from Kranzer et al. (2004) (red and black circles).

T Cells

The platform model states that T cells travel under directed random motion with an average speed of $11\mu m$/min. Each time step in the simulation is representative of 1 minute in real time, and the grid is measured in $50\mu m$ squares that are each displayed as 1 pixel, so the average distance travelled by a T cell per time step is 0.2 pixels. The average distance to travel in the next time step from location B (x_b, y_b) depends on the previous location, A (x_b, y_b), as shown in Figure 2.14b. In each time step, the distance to travel is calculated by:

$$\begin{aligned} d &= \sqrt{(x_b - x_a)^2 + (y_b - y_a)^2} \\ &= \sqrt{(0.2 \cdot \sin(\theta + s_\theta) - x_a)^2 + (0.2 \cdot \sin(\phi + s_\phi) - y_a)^2}. \end{aligned}$$

Variables x_a and y_a, and angles θ and phi, are determined by the current location and the previous location but s_θ and s_ϕ, the standard deviation in the angle of travel, are unknown and must be calibrated. The platform model states that T cells spend an average of 9.6hrs

in the MLN, so the standard deviation in the angle of movement is determined such that in the simulation each T cell spends an average of 9.6hrs (576mins) in the MLN compartment.

To identify the value that results in the correct standard deviation, a calibration experiment was performed. It was assumed that $s_\theta = s_\phi$ so the standard deviation of the angle of movement was allowed to take values $s = \left(0, \frac{\pi}{32}, \frac{\pi}{16}, \frac{3\pi}{32}, \frac{\pi}{8}, \frac{5\pi}{32}, \frac{3\pi}{16}, \frac{7\pi}{32}, \frac{\pi}{4}\right)$. For each value of s, 1000 T cells were placed in the MLN and the time that each cell exited was recorded. To eliminate aleatory uncertainty the experiments were performed 100 times for each value of the parameter. The mean time taken for a cell to leave the lymph node was calculated for each of the 100 runs, for each value of s, and a t test was performed for each $s_i, i \in [1, 9]$, where the hypotheses being tested was that the mean lymph node transit time under parameter set $angSD_i$ was significantly different to 9.6hrs (Figure 2.35). Usually when performing multiple t tests a multiplicity correction should be applied to reduce type I error, that is, the chance of seeing a false positive. Here, the desired result is one where there is no significant difference between the observed and hypothesised means so a multiplicity correction is not appropriate. Performing a t test reveals that the standard deviation of $\frac{\pi}{16}$ is the only value that results in a transit time that is not significantly different from the 9.6hrs observed *in vivo* by Mandl et al. (2012). To calibrate the number of T-cell specificities, the parameter was varied by hand to values in the range [1000, 3000]. The correct phenomena emerged when the *numberOfSpecificities* parameter was set to 2000.

The ODE model developed in the platform model was added to the `TCell` class by first discretising the equations and then replacing C_1 and C_{17} with actual levels of IL12 and IFN-γ or IL6/TGF-β and IL21 respectively. The parameter values selected from the ODE model were retained and used in the ABM and the dynamics of polarisation were examined under a range of conditions (Figure 2.34). The experiments performed were representative of *in vitro* experiments. For polarisation *in vivo* to be possible with the correct dynamics, cells must travel with true random motion so that they remain close to a cytokine source for long enough for the transcription factor governing polarisation to become stably expressed at a level higher than that of the unpolarised state, i.e. in the absence of polarising cytokine, denoted by "none" in Figure 2.34. In the presence of a high concentration of IL12 and IFN-γ, T cells expressed high levels of T-bet and IFN-γ,

therefore exhibiting a Th1 phenotype. If the environment consisted of IL6 and TGF-β, the T cells became Th17 cells and expressed high levels of ROR-γt and IL17.

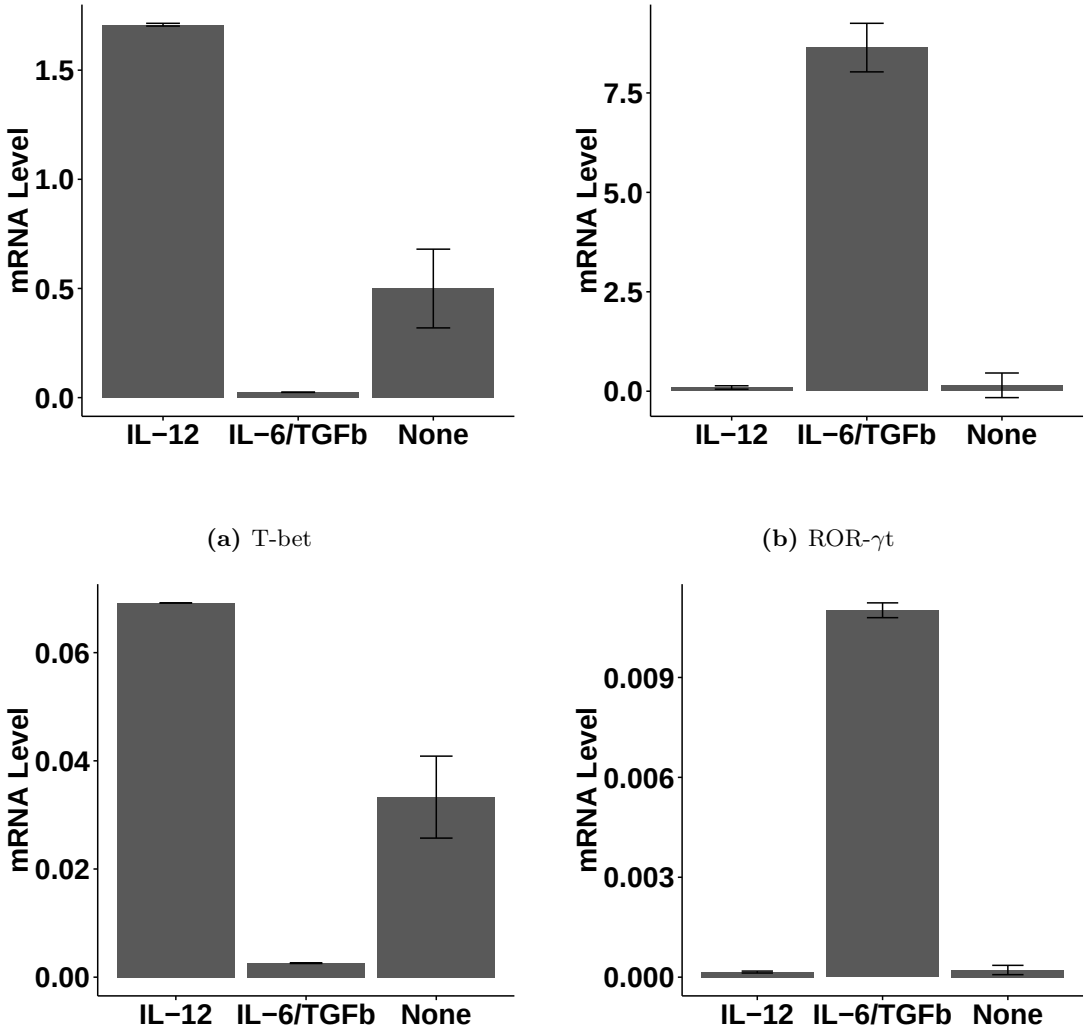

(a) T-bet

(b) ROR-γt

(c) IFN-γ

(d) IL17

Figure 2.34: Levels of Tbet, ROR-γt, IFN-γ, and IL17 in simulations of a single cell in the absence or presence of polarising cytokines. 1000 T cells were polarised in the presence of either no external cytokines, 1000 pg/ml of IL12 and IFN-γ or 1000pg/ml or IL6/TGF-β, IL23 and IL21 and amounts of (a) T-bet, (b) ROR-γt, (c) IFN-γ and (d) IL17 mRNA were measured in each cell after 48hrs.

2.4.1.3 Epithelial Cells

The platform model defined the subset of the ODE model by (Wendelsdorf et al., 2010) given by Equations (2.16) to (2.18) for estimating the total number of epithelial cells (E) and the number of secreting epithelial cells (E_p). These equations give the rate of change

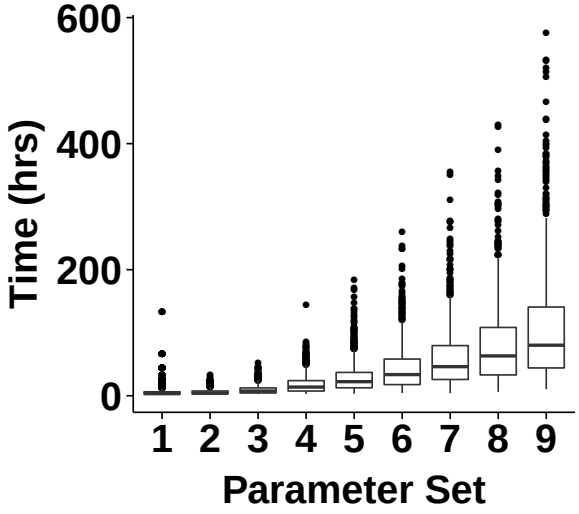

(a)

Parameter Set	Parameter Value	Significance level compared to 9.6hrs
1	0	$***$
2	$\frac{\pi}{32}$	$***$
3	$\frac{\pi}{16}$	p=0.2408
4	$\frac{3\pi}{32}$	$***$
5	$\frac{\pi}{8}$	$***$
6	$\frac{5\pi}{32}$	$***$
7	$\frac{3\pi}{16}$	$***$
8	$\frac{7\pi}{32}$	$***$
9	$\frac{\pi}{4}$	$***$

(b)

Figure 2.35: Calibration of T-cell movement. The standard deviation of the angle that a cell travels in at each time step in the lymph node was varied and the transit time of 1000 cells was recorded for 50 simulations with each parameter set. The mean transit time was calculated and a t test was performed to identify whether the mean transit time was significantly different to 9.6hrs. (a) Box plots of transit times of 1000 cells. Results shown are from one representitive experiment with each parameter set. (b) T test was performed on means of 50 simulation runs with each parameter set and results were compared to 9.6hrs $***$, $p < 0.001$.

in the numbers of epithelial cells and secreting epithelial cells per 6 hours, in terms of the number of T cells, DCs and macrophages that have been calculated using additional ODEs in the system in the full model (Wendelsdorf et al., 2010). To use the subset Equations (2.16) to (2.18), to calculate the numbers of the two types of epithelial cell in

mice, the terms for the number of T cells, macrophages and DCs will be replaced with equivalent measures from the simulation. The counts of T cells, DCs and macrophages in the simulation must be multiplied by a scale factor that makes them comparable with the actual cell counts from the mouse model, since the cell numbers in the simulation have been scaled down by a factor of 5000. The time step dt in Equations (2.16) to (2.18) is representative of 6 hours, but each time step in the simulation is only 1 minute so any parameters dependent on time must be scaled down by a factor of 360 to modify the time scale to 1 minute time steps. Finally, Wendelsdorf et al. (2010) estimates several parameters in the model to fit the data and produce adequate results. These parameters have been refined to better fit the expected output of the simulation.

2.5 Calibrating the Inflammation Score

In the platform model, a description of a scoring system to quantify inflammation in the model was developed. Using the simulation platform, two different implementations of the simulation scoring system were developed (Table 2.7). In implementation 1, the number of cells in the cecum or colon at a given time point were turned into an inflammation score by summing up the number of cells and concentrations of cytokines, and dividing by the maximum counts or concentrations expected from the *in vivo* data presented in Table 2.4. The results were scaled up to give a score within the ranges defined by Table 2.7 so that it can be used to compare how inflammation has developed. Using this method of calculating the inflammation score results in data that matches the biology reasonably well in early and late inflammation but not at day 7 (Figure 2.36c). Comparison with unpublished data by Bain and Kullberg suggests that this discrepancy most likely occurred because at day 7 there are a large number of cell macrophage precursors in the cecum and colon that are not included in the model. These precursors do not interact with other cells directly to cause inflammation but as histology scoring is done by looking at sections of tissue in which all immune cells are considered, regardless of whether they are inflammatory, regulatory or precursors. This means that both regulatory cells, which are acting to reduce inflammation, and precursors, which are not yet involved in the inflammatory process, contribute to the histology score in the same way as inflammatory cells. To make

the scoring system better reflect biology we needed to introduce a representation of these cells. By fitting a linear model of the form

$$precursors \ = \ a + b \times inf \ mac$$

to predict the relationship between inflammatory macrophages and precursor populations in biology, it was determined that precursors can be approximated to 6.798 × number of inflammatory macrophages (Figure 2.36a). When a term is added to the simulated inflammation score that represents these additional cells that are counted in biology, the score at day 7 more closely captures the behaviours observed in biology (Figure 2.36c), thus implementation 2 will be used representative biological behaviours.

Biological Measure	**Score**	**Implementation 1**	**Implementation 2**
Lamina Propria infiltration	0-3	Total number of immune cells in compartment	Total number of immune cells in compartment + 6.798 ×number of inflammatory macrophages
Epithelial damage	0-3	Number of inflammatory epithelial cells	Number of inflammatory epithelial cells
Goblet cell depletion	0-1	Amount of IFN-γ in compartment	Amount of IFN-γ in compartment
Crypt abscesses	0-1	Amount of IL17 in compartment	Amount of IL17 in compartment

Table 2.7: *In silico* inflammation scoring system.

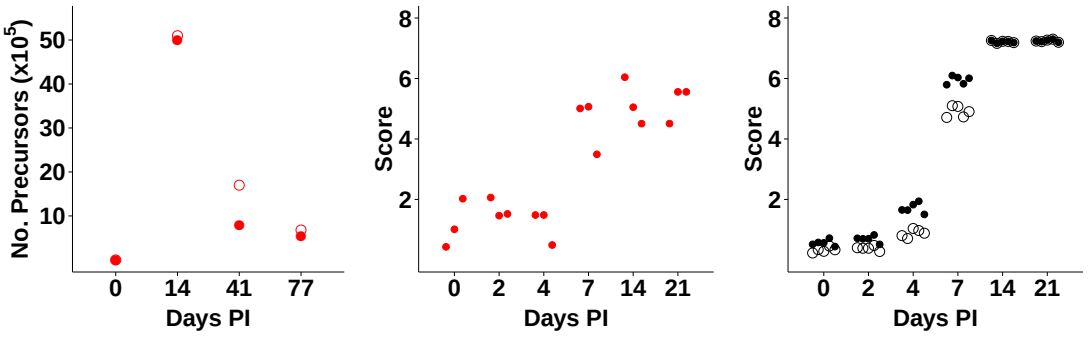

(a) (b) (c)

Figure 2.36: Comparison of biological and simulated measures of inflammation. (a) Actual (●) and predicted (○) numbers of macrophage precursors in the colon of *Hh* infected IL10 KO mice. (b) Biological histology score for the ascending colon taken from Morrison et al. (2013). (c) Simulated inflammation score using implementation 1 (○) implementation 2 (●).

2.6 Model Analysis

As discussed in Section 1.8.0.1, before a model can be used for experimentation, uncertainty and sensitivity analyses should be performed.

2.6.1 Aleatory Analysis

Aleatory analysis was performed using the confidence interval method described in Section 1.8.0.2 (Robinson, 2014) to determine the number of simulated replicates that needed to be performed Figure 2.37. Although some measures like the number of T cells in the MLN only require 5 replicates to reach a 5% deviation of the confidence interval from the mean (Figure 2.37a), the maximum number of replicates required for all simulated measures to be accurately represented in the results is 35 (Figure 2.37b,c).

2.6.2 Sensitivity Analysis

Using the results from the previous section to identify the number of replicates required to get a representative result, a sensitivity analysis can be performed to determine the model parameters that have the greatest effect on output.

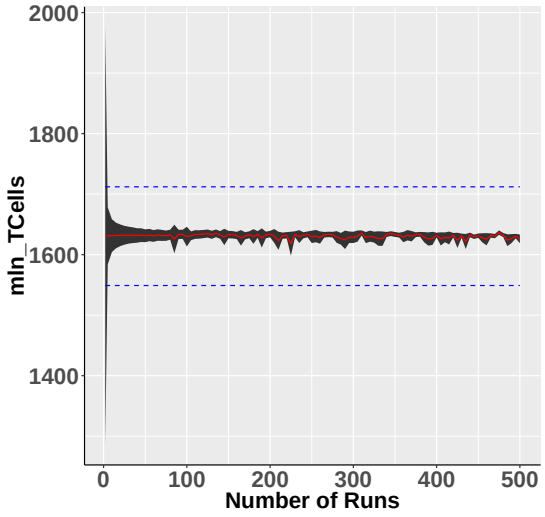

(a) Least variable

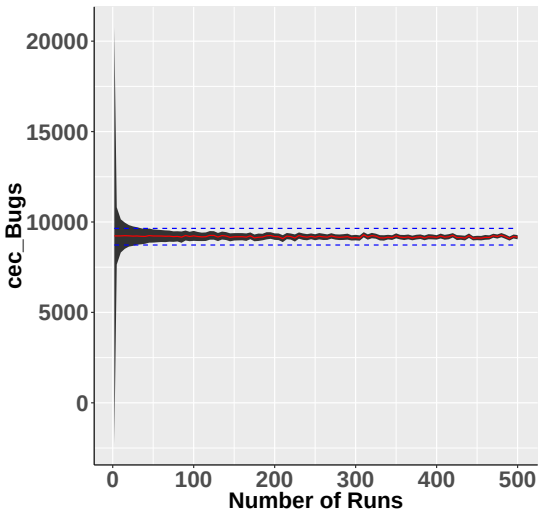

(b) Most variable

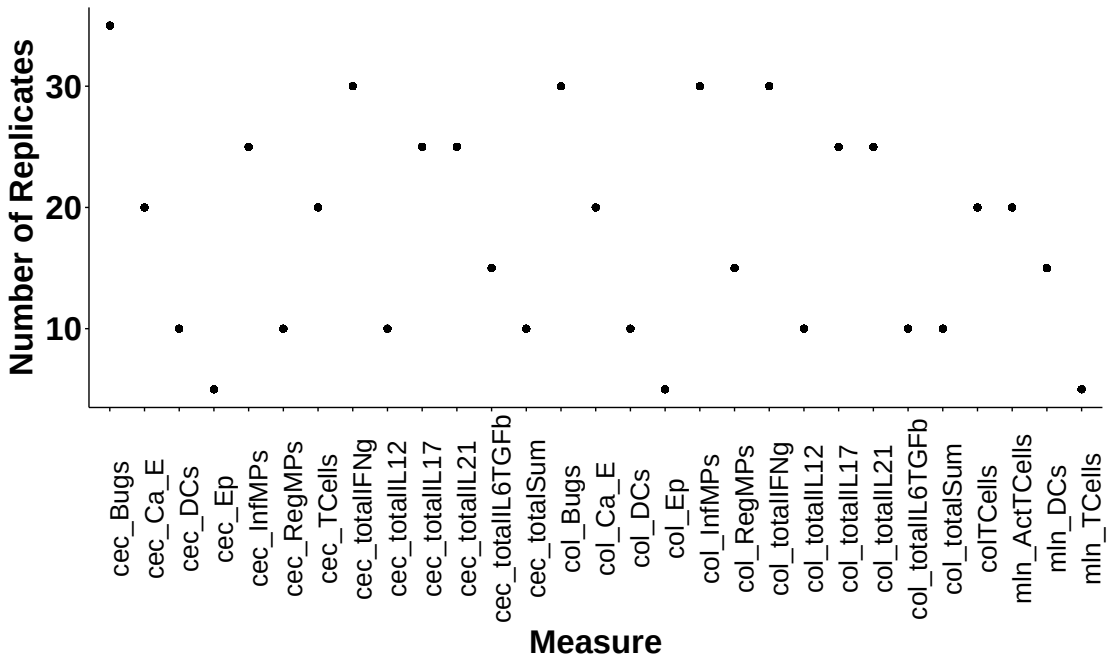

(c) All measures

Figure 2.37: Determining the number of simulation replicates that need to be performed. The confidence interval method (Robinson, 2014) was used with a confidence level of 5%. The confidence interval (black), mean value over the specified number of runs (red) and 5% deviation level from the mean (blue, dashed) are shown for the least variable measure (a), and the most variable measure (b). The number of replicates required for the deviation of the confidence interval to be less than 5% of the mean for each simulated measure is also shown (c).

Latin Hypercube Analysis

For a full model, global sensitivity analysis, 200 parameter sets were generated using ranges of 10% either side of the accepted baseline levels from Appendix A, and 35 replicates were performed with each parameter set to eliminate aleatory uncertainty. The most important parameters in determining overall model behaviour are defined as those that significantly affect the highest number of simulated measures at peak inflammation (14 days post infection). Of the 72 parameters examined the average number measures significantly affected by any parameter was 15, and only 4 parameters were significantly correlated with 20 or more of the 29 simulated measures (Figure 2.38a). These were

- $\boldsymbol{maxBugsD}$: the maximum number of bacteria that a DC can phagocytose before migrating to the lymph node.
- $\boldsymbol{S_{b1}}$: The coefficient of t in the secretion equation (Equation (2.3)).
- $\boldsymbol{phagTime}$: The time it takes for an APC to phagocytose a bacterium.
- $\boldsymbol{inRateDC}$: The baseline rate at which DCs enter the cecum and colon.

Increasing any of these these parameters increased the number of all cells in the cecum, colon, and MLN, and decreased the number of *Hh* in the cecal and colonic lumen (Figure 2.38b). These parameters are all model-derived, and therefore cannot be biologically verified so it is important to see how strongly these parameters effect the model output. A one at a time analysis to determine changes that can be attributed to each specific parameter, will be performed in the next section.

Parameter Robustness

The compound effects of altering parameters have been identified. One at a time parameter alteration has been used to determine how robust the important parameters are to variation around the value that was assigned through calibration. The parameters identified as important in the previous section have been varied over ranges, 10% either side of their calibrated value and a Cohen's D test has been used to determine the size of the effect of setting each parameter to the new value, compared to the baseline calibrated value.

- ***maxBugsD***: This parameter is an integer so taking a 10% range either side of the calibrated value of 17, and rounding to the nearest integer meant that the parameter could take values 16, 17, 18, and 19. The analysis showed that overall, the majority of simulated measures are not too sensitive to alterations in the $maxBugsD$ parameter, over a small range (Figure 2.39a). Setting the value of $maxBugsD$ 16 had a reasonably sized effect on all measures, with a mean effect size magnitude over all simulated measures of 0.16. Setting the parameter to either 17 or 18 had no significant effect with mean effect size magnitudes of 0.046, and 0.037, respectively. When the value of $maxBugsD$ was 19, there was a very small effect with mean effect size magnitude of 0.091. This means that selecting a value of 17, rather than 16, 18 or 19, through calibration does not dramatically effect the output of IBDSim.

- ***phagTime***: This parameter is also an integer and can therefore only take on integer values. Taking a 10% range either side of the calibrated value of 180, and rounding to the nearest integer meant that the parameter could take values within the range of 165 to 201. At lower values, this parameter has a small to medium effect on the output of IBDSim, but once the threshold of around 180 is reached there is no longer a significant effect (Figure 2.39b). The average effect size magnitude over all measures ranges from 0.17 to 0.03 as the parameter value increases. The results of this robustness analysis suggests that the calibrated value of 180, is the threshold value for which Macrophages die from phagocytic burst at a rate slow enough that they are replaced in the population. This would explain the fact that there are no significant effects from altering the parameter above this value. Further these results could suggest that inducing macrophage death could reduce the level of inflammation in the system because lowering bug tolerance has been shown to reduce the total number of cells and cytokines in the model.

- ***nutLow***: This parameter can take on integer values in the range 28 to 33. There is only significant effect of changing the parameter over these values is when $nutLow$=33 when there is an average effect size magnitude of 0.16. This means that over a very small ($< 10\%$) range the parameter is robust, but increasing the parameter by 10% or above can strongly affect the behaviour of the system.

- s_{b1}: This parameter can take on any real numbered values in the range 1.858 to 2.259, and its baseline value is 2.024. Lower values of s_{b1} negatively effect the number of cells and cytokines with a mean effect size magnitude over all measures of 0.13. At values greater than 2, there is no significant effect. This means that if the cytokine secretion rate has been under estimated, increasing it would not significantly alter behaviour. Figure 2.19 shows that for IL12 at least, although there is no significant difference between the concentration of IL12 secreted by DCs in IBDSim when compared to *in vitro* data for the same stimulation level, the concentration secreted by DCs *in silico* is slightly lower at certain time points. The result from this parameter scan shows that increasing the secretion rate would not effect the simulation results so the calibrated level does not need to be changed.

2.7 Results Model

Following on from simulation development, the CoSMoS process dictates that the simulation output must be compared to real-world data to form a results model. Data from simulations is collected and then compared with real-world data collected in the Kullberg lab.

2.7.1 Experimental Procedure

Each compartment in the simulation starts in an empty state. Simulations start from day -20, allowing the compartments time to reach an uninfected steady state before *Hh* is added to the cecal lumen compartment at day 0. Several data points are collected from each compartment every 1440 time steps, equal to 1 day, for 21 simulated days. The counts of all cells and total amounts of all cytokines in each compartment are collected resulting in 29 data points in total for each time point, as specified in Section 2.3.5.

2.7.2 Comparing *In silico* Results to Biology

Figure 2.40 shows how the simulation output compares to the available *in vivo* data. Data shown are means and standard error of 100 simulated runs *in silico* and of 3 mice in biology. There are five simulated measures that can be directly compared with biology data, total

numbers of T cells in the cecum and colon, numbers of *Hh* bacteria in the cecal lumen, and the number of T cells and percentage of activated T cells in the MLN. Paired t-tests reveal no significant differences between simulated and biological data distributions (Table 2.8) suggesting that the model adequately reflects what is observed in biology. Despite the results of the statistical analysis, it is clear that there is some discordance between what is observed *in silico* and *in vivo* when considering the percentage of activated T cells in the MLN. It is expected that this is a result of the simulation not containing all of the cell types that are present in the MLN in biology, thus the percentage is skewed, and also a result of inaccurate measurements *in vivo*. This is especially true when inflammation becomes more severe when the markers used to distinguish between cell types in biology can become more difficult to separate using flow cytometry. While other simulated measures have been recorded and are shown for transparency, they cannot be compared to biological data as none is available. The simulation platform satisfactorily reproduces the *in vivo* dynamics of the development of intestinal inflammation in *Hh*-infected IL10 KO mice.

Measure	**P-value**
T cells (cecum)	0.9883
T cells (colon)	0.1181
T cells (MLN)	0.2386
T cells (activated)	0.5913
Hh (cecal lumen)	0.05502

Table 2.8: Simulation adequately reflects biology distributions.

.

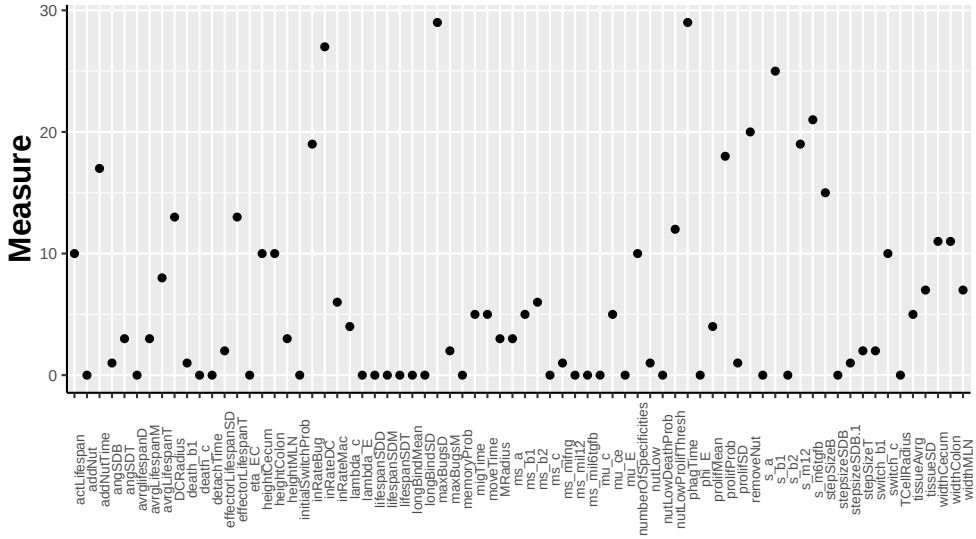

(a) Number of measures significantly affected

(b) PRCCs

Figure 2.38: Sensitivity of simulated measures to variations in all model parameters. (a) The number of simulated measures that each parameter was significantly correlated with ($p < 0.05$). (b) PRCC between each measure and parameter in the simulation.

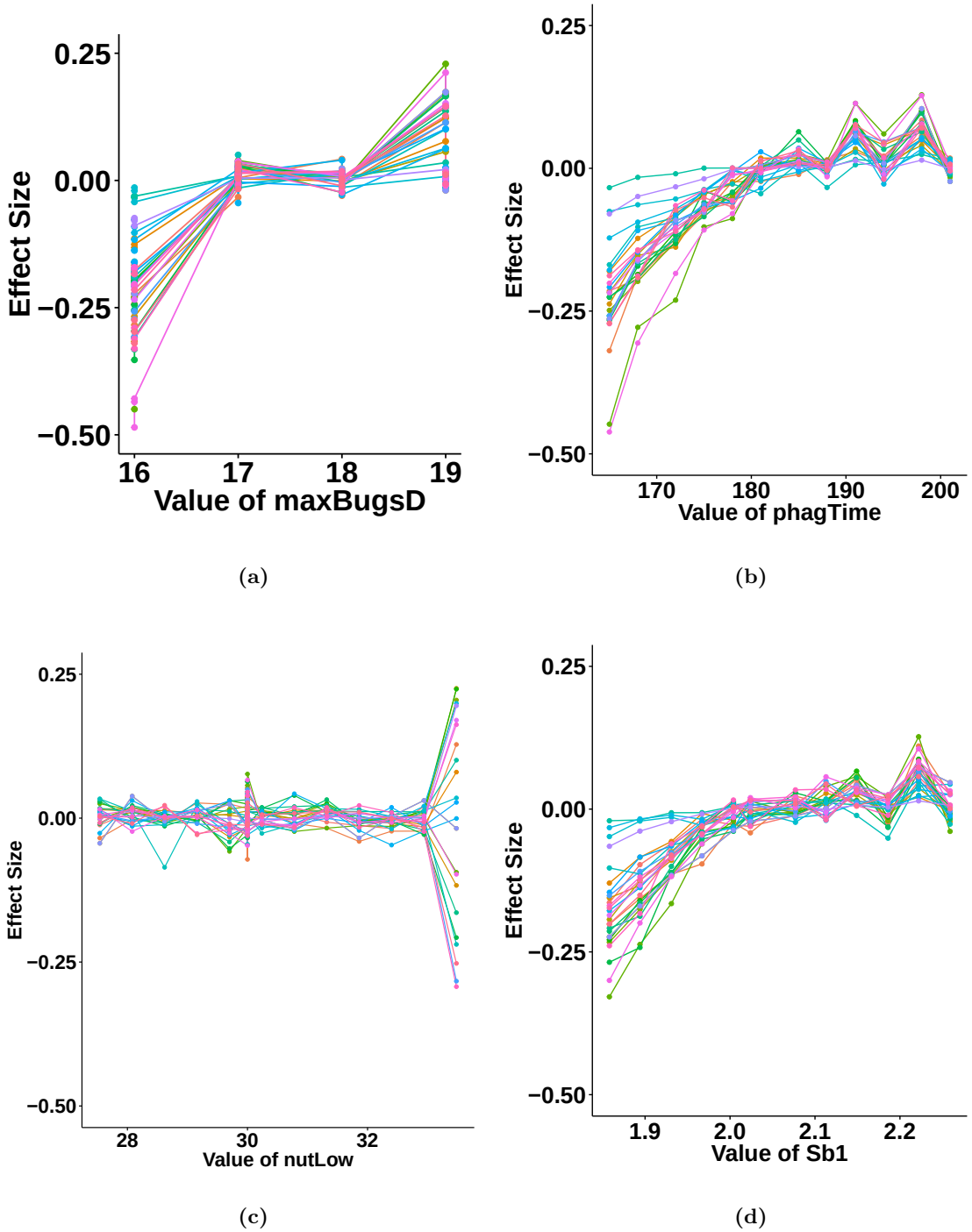

Figure 2.39: Effect of one at a time parameter alteration on simulation measures. Parameters $maxBugsD$ (a), $phagTime$ (b), $nutLow$ (c), and s_{b1} (d) were varied over ranges that were 10% either side of their calibrated value and the Cohens D effect size calculated, using the calibrated value as a baseline. Data shown is from the average of 35 runs.

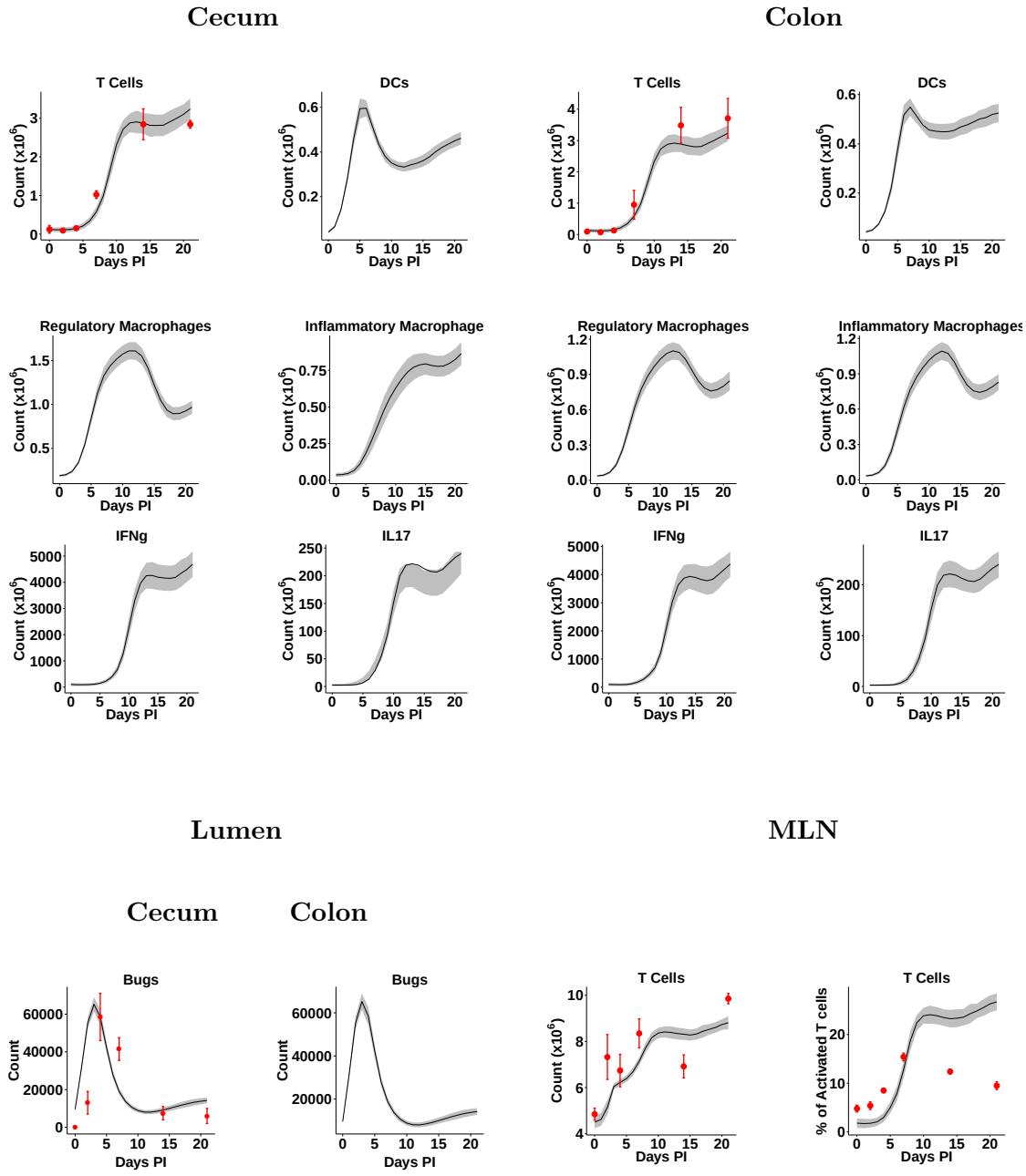

Figure 2.40: Comparison between *in vivo* and *in silico* data. Black lines and grey bars show mean and standard error of 100 runs of the simulated model. Means and standard error of biological data, collected by Morrison et al. (2013), are shown in red.

2.8 Confirmative Experimentation Using IBDSim

Before the model can be used to drive *in vivo* experimentation, it is important to perform experiments for which the biological outcome is already known. This helps to demonstrate that the model adequately represents the behaviours of the system rather than just fits to the data for a specific case. Therefore, two confirmative experiments have been performed with the aim of replicating two known results from biology;

Experiment 1 Uninfected IL10 KO mice do not develop inflammation when kept in specific pathogen free (SPF) facilities (Berg et al., 1996)

Experiment 2 IL10 KO mice kept in germ-free conditions, which lack commensal flora, display little pathology following *Hh* infection (Dieleman et al., 2000)

For Experiment 1, it was expected that running the simulation without adding *Hh* would not result in the inflammation score remaining at the steady state level throughout inflammation, and for Experiment 2, if commensal bacteria is removed from the model there should not be a significant increase in the inflammation score following infection with *Hh*

2.8.1 Confirmative Experiment 1: Uninfected IL10KO mice housed in SPF conditions do not develop inflammation *in silico*

The first experiment was performed by setting the parameter *CecLum.inTimeBug=step+1* meaning that the instance to bring in a new bacterium to the cecal lumen compartment is always bigger than the current time step. The compartments all started with no cells in them and the simulation ran for 28800 time steps (20 days) to allow a base line to emerge before the data collector was initialised. 50 simulations, representative of 50 mice, were then allowed to run for 30240, steps which is the equivalent of 21 simulated days. An inflammation score was developed from the scoring system developed in the previous section and the results showed that over the 21 day modelling period, no inflammation developed (Figures 2.41c,2.41d, blue circles). Further examination of the full simulation output showed that there was no change in the number of inflammatory cells and cytokines in the absence of *Hh*. This experiment shows that inflammation in the system is induced

by *Hh* and not hard coded to develop at a given time point, and also that the baseline reached 28800 time steps after initialisation is a stable steady state.

2.8.2 Confirmative Experiment 2: Germ-free IL10KO mice in SPF conditions do not develop inflammation following *Hh* infection *in silico*

To perform this experiment, the method that adds commensal bacteria to the cecal and colonic compartments was removed, stopping the occurrence of commensal bacteria in the system. As in the previous experiment the simulation was allowed 28800 steps (10 days) to reach a base line in the absence of *Hh*. At this time point *Hh* was added to the cecal lumen, the data collector was initialised, and data was generated for 50 simulations, representative of 50 mice per time point for 30240 time steps (21 days). The inflammation score was used to determine the level of inflammation in the simulation (Figures 2.41c,2.41d, yellow squares). Analysis of the full data showed that there is a slight change in the number of inflammatory cells and cytokines but it is significantly less than the infected case. This result verifies that inflammation *in silico* depends, as it does *in vivo*, on the presence of both commensal bacteria and *Hh*.

2.9 Materials and Methods

The infrastructure and methods used to develop and run IBDSim are listed in this section.

2.10 Infrastructure

The model presented in this thesis was written in Java using the MASON toolkit (Luke et al., 2005). Simulations were executed using a Linux Cluster running Fedora 22. The Linux Cluster has a SUN Grid Engine, SGE, that is made up 64 CPU 256GB memory nodes.

2.10.1 Simulation Architecture

A executable model was created from the specification in the platform model. This model has been implemented using the Java programming language and MASON simulation en-

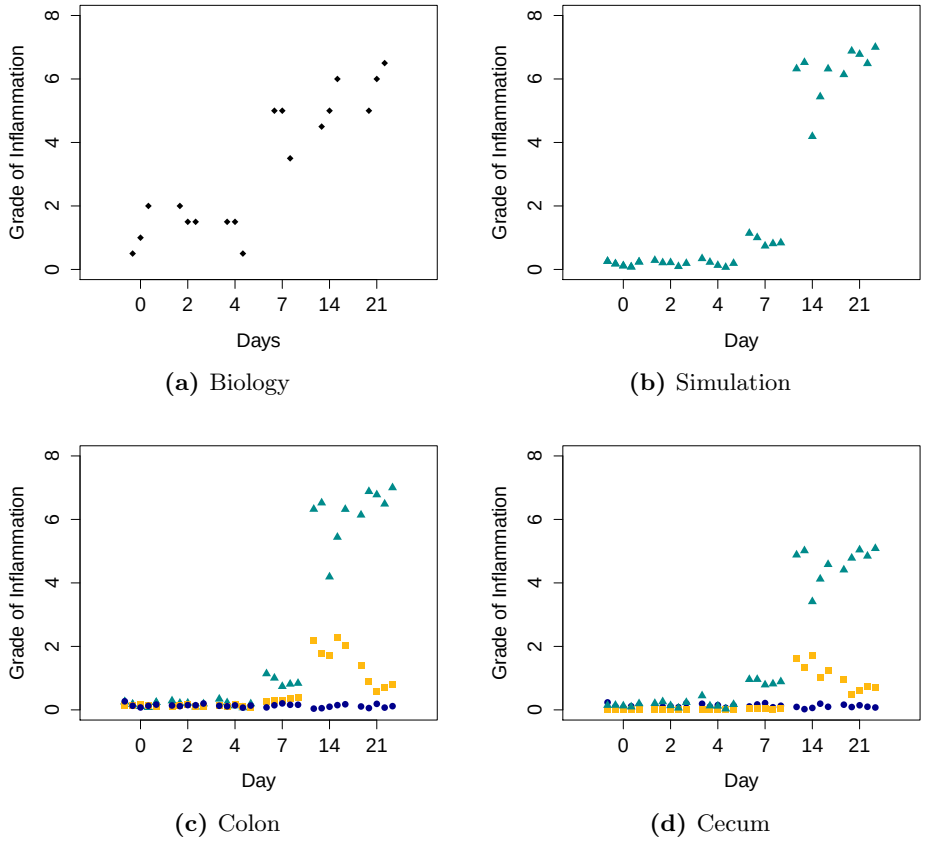

(a) Biology **(b)** Simulation

(c) Colon **(d)** Cecum

Figure 2.41: *In silico* inflammation score gives similar results to the biological histology score.(a) Biological histology scores from the ascending colon with 3 mice per timepoint (taken from (Morrison et al., 2013)). (b) *In silico* inflammation score calculated from the average of 100 simulation runs, 5 samples per timepoint. (c), (d)*In silico* inflammation score from colon (c) and cecum (d) in a *Hh*-infected IL10KO experiment (green triangles), a germ free experiment (yellow squares) and an uninfected experiment (blue circles)

vironment, a cross-platform toolkit for the creation of multi-agent simulations (Luke et al., 2005). Each of the cell types detailed in the previous sections have been implemented as individual Java classes and methods have been created to mirror the processes in the state machine diagrams described in the previous section. MASON simulations are executed in steps. At every step, each agent performs a behaviour set by its current state, as defined in the platform model, each simulated time step to represent one minute of real time. All parameter values listed in Appendix A are stored in an external parameter file.

Figure 2.42 depicts the organisation of classes in the simulation platform. The simulation ultimately consists of cells that inherit methods from the abstract `Cell` class, and spatial compartments in which they exist, that inherit from the `Compartment` class. All

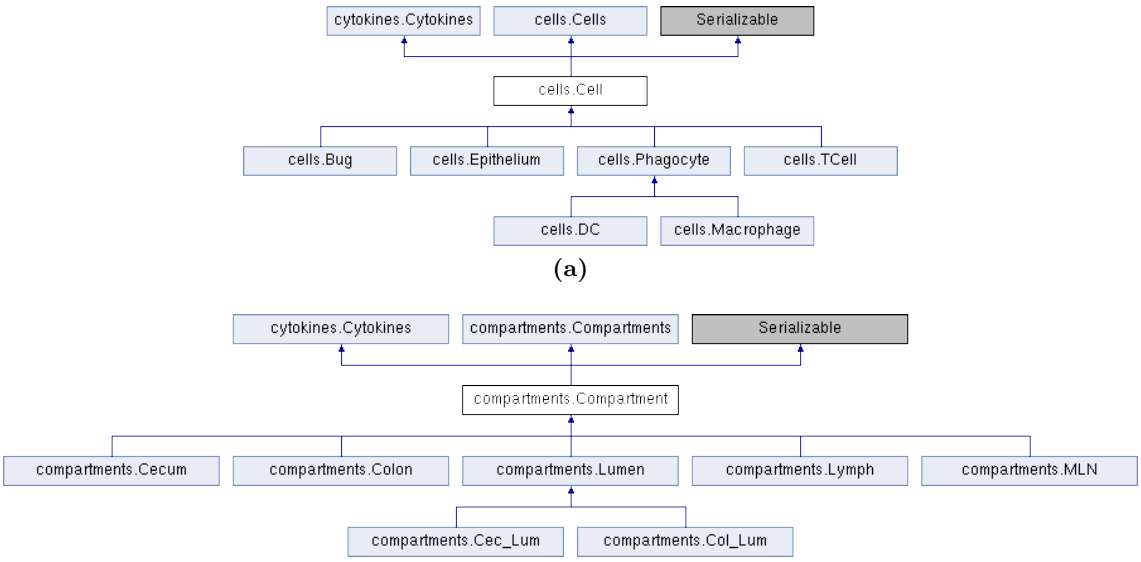

Figure 2.42: Inheritance structure of Java classes in IBDSim. Diagrams shown represent inheritance of methods by cells (a) and compartments (b). Arrows indicate the direction in which methods are shared, so a phagocyte shares its methods with both DCs and macrophages.

non-abstract classes implement `Steppable`, the MASON interface required for execution within the simulation engine. The class `IBDSim` is the driver of the simulation, and is responsible for its initialisation.

2.10.2 Dynamic Time Warping

Dynamic time warping is a technique commonly used in speech recognition. It allows a non-linear mapping of one signal to another by minimizing the distance between them and allows sequences that are similar despite having slight time dependent variations to be analysed (Ratanamahatana and Keogh, 2004). This technique is useful for simulation data where the behaviours occur at slightly different time scales. An example of data that would be deemed to be similar under the dynamics time warping method is shown in Figure 2.43a, while Figure 2.43b shows a case where the data is highly dissimilar.

2.10.3 SBML Model Development and Java Integration

SBML was developed in 2002 to provide a methodology that would allow models of biological processes to be evaluated, developed and exchanged (Hucka et al., 2003). LibSBML is an application programming interface library for reading, writing, manipulating and

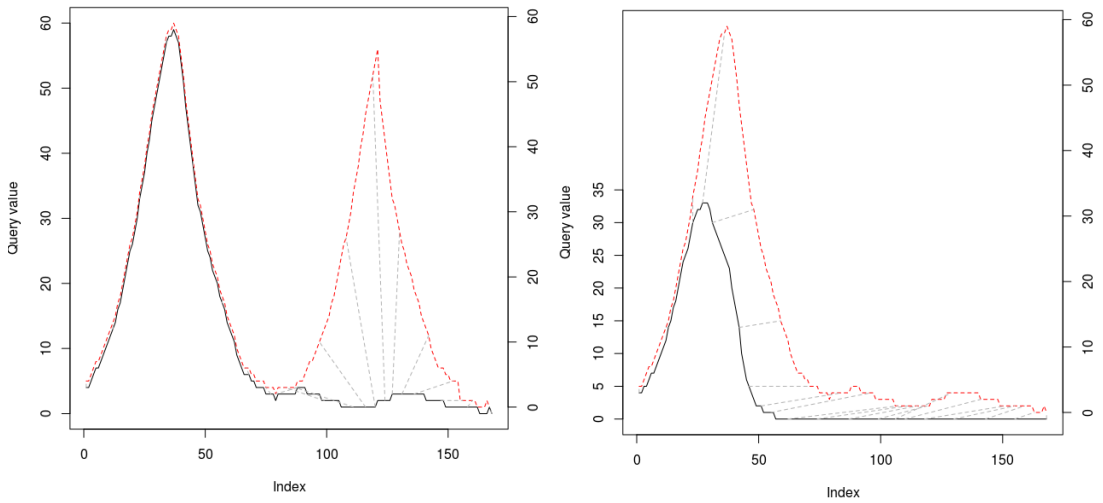

(a) (b)

Figure 2.43: Using dynamic time warping to identify similar time course results. An example of data that is similar (a) and dissimilar (b) using the dynamic time warping approach.

validating content expressed in the SBML format (Bornstein et al., 2008). It is written in ISO C and C++ but provides bindings for many other programming languages including Java. However, libSBML does not have any functionality for solving or simulating SBML models. To do this, packages such as LibSBMLSim (Takizawa et al., 2013) must be used. LibSBMLSim contains a method simulateSBML that uses a user-defined method to solve systems of ODEs numerically (Butcher, 1996). In this work, the 4th order Runge-Kutta method is used to reduce stiffness. The Java bindings in both of these libraries meant that they that could be integrated into the simulation environment to allow SBML models to be simulated directly within the ABM. This allows SBML models to be developed, calibrated and tested outside the ABM environment before incorporating them but can be computationally expensive. To reduce computational burden brought by the addition of SBML models into IBDSim, the concept of dynamic tuneable resolution was developed.

2.10.4 The Simulation Parameter Analysis R Toolkit ApplicatioN (Spartan)

Spartan is a toolkit for performing model analysis in R (Alden et al., 2013). It was developed to determine how representative a simulation is of its biological system and to understanding of how *in silico* results can be interpreted in the context of the biological

domain. Spartan is a compilation of four statistical techniques previously described by Read et al. (2012)Marino et al. (2008), and Saltelli and Bollardo (1998). These techniques are consistency analysis, robustness analysis and two different sensitivity analysis methods, providing both global and local analyses. Of these methods, aleatory analysis, robustness analysis, and Latin-hypercube sampled sensitivity analysis have been performed on the models presented here. The methods provided by spartan assume that a model has been calibrated to a steady state and uses parameter sampling techniques to determine how perturbations in parameter values or differences in the number of replicates of a simulation can affect the outcome. It has found uses in a variety of systems biology models, a variety of which are discussed by Alden et al. (2013).

2.10.5 Model Fitting with Mathematica

Models that were fitted using Mathematica (Wolfram Research, Inc, 2016) were done so using the `NonLinearModelFit` command. This fits model parameters using the quasi-newton method (Shanno, 1970).

2.11 Summary

In this chapter, an ABM that captures the processes active in the gut during *Hh*-induced intestinal inflammation in IL10 KO mice has been developed. The model was developed following the CoSMoS process (Section 1.5.0.2) and been grounded in biology using a series of diagrams, that have been developed in collaboration with a domain expert. The executable model can be used for performing *in silico* experimentation by varying the model parameters to reflect a different experimental set up, or can be expanded to add in the effects of other cells and cytokines on the system, or to look at intervention with a therapeutic treatment, as will be performed in the next chapter.

Chapter 3

Exploring the Effects of FTY720 on *Hh*-Induced Intestinal Inflammation

Lymphocyte egress from both primary and secondary lymphoid tissue requires the lipid mediator S1P (Ley and Morris, 2005). Signals initiated by S1P are transduced by five G protein-coupled receptors, named $S1P_{1\text{-}5}$ (Chun et al., 2010). Combinations of these receptors are expressed on almost all immune cell types including DCs, macrophages, epithelial cells, endothelial cells, and lymphocytes (Blaho and Hla, 2014). $CD4^+$ T cells are specifically known to express the receptor $S1P_1$ (Allende et al., 2004). $S1P_1$ agonists have been shown to be immunosupressive and there are two alternative hypotheses about how they accomplish this. One hypothesis, referred to as functional antagonism, states that agonists directly bind to $S1P_1$ receptors on lymphocytes, causing receptor internalisation and degradation, resulting in lymphocytes being unable to respond to endogenous S1P (Matloubian et al., 2004). The second hypothesis states that $S1P_1$ agonists target the endothelial cells around the sinus region of the lymph node effectively closing the stromal gate through which lymphocytes would usually exit (Wei et al., 2005). Studies investigating the effects of blocking lymphocyte egress with $S1P_1$ agonists, such as Fingolimod (FTY720) have reported a reduction in inflammation in many autoimmune diseases (Table 3.1). Conversely, other studies have observed S1P1 agonoists exacerbating disease

(Table 3.2).

This chapter describes the development of a pharmacokinetic (PK) model that predicts the concentration of FTY720 in the gut draining MLN in mice, the main lymph node involved in the induction of *Hh*-induced colitis. The model is based on an established PK model for FTY720 in rats (Meno-Tetang et al., 2006). The development of a pharmacodynamics (PD) model under the hypothesis of functional antagonism is also discussed here. A combination of these mouse PK and PD models incorporated into IBDSim have been used to examine *in silico* the effects of blocking lymphocyte egress from lymph nodes on *Hh*-induced colitis.

3.1 Pharmacokinetic (PK) Model for FTY720 in Mice

PK models quantify the absorption, distribution, and elimination of drug in the body, leading to the understanding, interpretation, and prediction of blood concentration-time profiles (Aarons, 2005). To determine the concentration of FTY720 in the MLN of IL10 KO mice, a PK model has been developed. The new PK model is based on an existing PK model that describes the distribution of FTY720 in rats over 5 days, following a single intravenous administration of FTY720, and considering 13 organs with the remaining sites being combined into one rest of the body compartment (Meno-Tetang et al., 2006). The mouse PK model has been developed following a two-step approach. First the output from the rat model has been reproduced in a reduced system representing the organs that are important in *Hh*-induced colitis, and then allometric scaling has been used to transform the reduced rat model into one that is sufficient for predicting drug concentrations in mice. In all models concentrations of drug within each of these organs are described using either one or two ODEs, depending on whether the drug is assumed to distribute instantly and homogeneously throughout the organ (a 'well stirred' model, applied to organs such as lungs, liver and spleen ((3.1)) or to distribute into the organ via a rate-limited process (as is the case of the lymph nodes (3.2)-(3.3)). In the latter case, the two equations represent the drug concentration in the blood (3.2) and in the interstitial and intracellular space (3.3).

Table 3.1: The positive effects of FTY720 in disease.

Model	Genus	Drug	Details	Ref
EAE	Mouse	FTY720	Daily $0.1-1mg/kg$ doses from start of infection and daily on established disease results in amelioration of disease and inhibition of relapse.	(Kataoka et al., 2005)
Collagen-Induced Arthritis	Mouse	TASP0277308	Daily $100mg/kg$ from start of infection blocks disease	(Fujii et al., 2012)
Alzheimer's disease	Rat	SEW2871	Daily $0.5mg/kg$ doses from first day after surgery. Improvement in cognitive function.	(Asle-Rousta et al., 2013)
Multiple sclerosis	Human	FTY720	Doses of either $1.25mg$ or $5.0mg$ given daily reduced relapse of disease compared to placebo.	(Chun and Hartung, 2010)
Psoriasis	Human	Ponesimod	$20mg$ and $40mg$ daily doses reduced severity of disease	(Ryan and Menter, 2014)
IL10 KO colitis	Mouse	FTY720	Daily doses of $o.3mg/kg$ ameliorated established disease	(Mizushima et al., 2004)
$CD4^+CD62L$ transfer colitis	Mouse	FTY720	$0.3mg/kg$ daily from one day before T-cell transfer suppressed colitis	(Fujii et al., 2006)
DSS colitis & $CD4^+CD62L$	Mouse	FTY720	Daily doses of $0.3mg/kg$ of drug from start of infection reduced inflammation	(Deguchi et al., 2006)
Oxazolone colitis	Mouse	FTY720	Daily administration of $1mg/kg$ or $3mg/kg$ of FTY720 from 2 hours before oxazolone for 3 days blocked disease from developing. Daily dosing of FTY720 from 3-5 days post infection, that is on established disease also significantly ameliorated disease.	(Daniel et al., 2007)

Table 3.2: The negative effects of FTY720 in experimental diseases.

Model	Genus	Drug	Details	Ref
Citrobacter rodentium induced colitis	Mouse	FTY720	Daily $3mg/kg$ doses from 6 days prior to start of infection increases pathogen burden and impairs bacterial clearance.	(Kataoka et al., 2005)
Influenza	Mouse	FTY720	Daily $3mg/kg$ doses doubled mortality rate.	(Ntranos et al., 2014)
Traumatic brain injury	Mouse	FTY720	Single $1mg/kg$ dose of drug immediately before induction of focal cryolesion or diffuse weight drop injury does not prevent injury.	(Mencl et al., 2014)

Well stirred:

$$\frac{dX_T}{dt} = Q_T \times \frac{X_{art}}{V_T} - Q_T \times \frac{X_T}{(R_T \times V_T)}. \tag{3.1}$$

Permeability rate-limited, blood:

$$\frac{dX_{T_1}}{dt} = Q_T \times \frac{X_{art}}{V_{T_1}} - Q_T \times \frac{X_{T_1}}{V_{T_1}} - PS_T \times f_{ub} \times \frac{X_{T_1}}{V_{T_1}} + PS_T \times \frac{f_{ub}}{R_T} \times \frac{X_{T_2}}{V_{T_1}}. \tag{3.2}$$

Permeability rate-limited, intracellular and interstitial space:

$$\frac{dX_{T_2}}{dt} = PS_T \times f_{ub} \times \frac{X_{T_1}}{V_{T_2}} - PS_M \times f_{ub} \times \frac{X_{T_2}}{V_{T_2}}. \tag{3.3}$$

In all models, X_T represents the concentration of FTY720 in organ T, measured in ng/ml, Q_T is the blood flow rate into organ T, V_T is the volume of organ T, X_{art} is the input from arterial blood, PS_T is the permeability-surface area product, R_T is the tissue-to-blood partition coefficient, and f_{ub} is the free fraction of FTY720 in the blood. The value of these parameters in rats can be found in Meno-Tetang et al. (2006).

The only compartment not modelled by any of these equations is the the concentration of FTY720 in arterial blood, X_{art}, that has been fitted to an exponential equation of the

form

$$C_{art} = Ae^{\alpha t} + Be^{\beta t} + Ce^{\gamma t}, \tag{3.4}$$

where $A,\ B,\ C,\ \alpha,\ \beta$ and γ are constants and t represents time. For a single dose, fitting data to a model of this form adequately captures drug concentrations in arterial blood. However, for the model to be able to capture the dynamics of multiple doses of FTY720, the concentration in arterial blood must be represented by an ODE that captures the dependency of the concentration of drug in arterial blood as a function of drug dose. This is because the explicit representation in (3.4) is based only on time, and not on the administered concentration of drug, and so cannot be used for repeated doses. The equation for the concentration of drug in arterial blood can be calculated from the model equations (3.2)-(3.3) and is given by the following equation

$$\frac{dX_{art}}{dt} = Q_{tot} \times \frac{X_{lung}}{R_{lung}} - \sum_{T \in \text{ organs}} Q_T \times X_{art}, \tag{3.5}$$

where Q_{tot} is the blood flow rate from the lung, X_{lung} is the concentration of FTY720 in the lung, and R_{lung} is the tissue-to-blood partition coefficient, as specified in equations (3.2)-(3.3). For *Hh*-induced colitis, the concentration of FTY720 in some of the organs modelled by Meno-Tetang et al. (2006) is not important. Thus for modelling purposes the PK model was reduced to nine equations; one for each of the well mixed compartments, (lungs, spleen, liver and gut), one for each of the veneous and arterial blood compartments, two for the the lymph nodes that represent the concentrations in the blood (LN1) and interstitial space (LN2), and one for the rest of the body (Figure 3.3). Reducing the number of compartments was done by increasing the size of the rest of the body compartment, and then reparameterising the equations governing the flow of drug into and out of this compartment. Implementing these changes to the model should not alter the concentration of drug in any remaining compartments when compared to the original model. To develop the reduced model, parameters that relate to the rest of the body were varied over ranges shown in Table 3.3, and models were simulated for 120 hours, on a minute time scale, using the Runge-Kutta algorithm with step size 0.012 for stability. These parameters were the

tissue to blood partition coefficient ($Rrob$) and the blood flow rate for the rest of the body compartment ($Qrob$). The clearance rate of drug in the liver (CL) was also altered to account for any clearance coming from compartments that have been absorbed into the rest of body compartment. In all models, the initial concentration of drug in the veneous blood compartment was set to be $6637ng/ml$, representing a single intravenous dose of $0.3mg/kg$ of FTY720, assuming that adult rats weigh $250g$ and have $11.3ml$ of venous blood as these were the parameters used by (Meno-Tetang et al., 2006). Comparing the results of the parameter scan to biological data that has estimated from Meno-Tetang et al. (2006) allowed the model that best represented the dynamics in rats to be identified. The three parameters scanned significantly affected the maximum concentration in the lymph node following inoculation with FTY720, and the strongest correlation was between the maximum concentration in the lymph node and Q_{rob} (Figure 3.1), making this the key parameter to consider when selecting the parameter set that best matches the data. To determine if the selected model was an adequate representation of the dynamics of FTY720 in rats in general, rather than for just the specific $0.3mg/kg$ dose, a higher dose of $2.0mg/kg$ was simulated, and the concentration of FTY720 in the lymph node compared to the data reported in the original publication (Meno-Tetang et al., 2006). The model that was previously selected to represent the lower $0.3mg/kg$ dose successfully represented the concentration of FTY720 in the rat lymph node following a higher dose of $0.2mg/kg$ (Figure 3.2). Taken together this means that the refitted model can adequately simulate the concentration of FTY720 in a rat lymph node following intravenous administration of the drug.

Table 3.3: Ranges used for ASPASIA parameter estimation. Parameter ranges were chosen to be 10 times either side of values used by Meno-Tetang et al. (2006) to ensure that a global parameter space was sampled.

Parameter	**Range**		**Value**
CL	Min:	0.00001	0.0769
	Max:	0.1	
R_{rob}	Min:	0.00001	1894.43
	Max:	2000	
Q_{rob}	Min:	0.00001	1958.83
	Max:	2000	

To transform the calibrated rat PK model into a model that could be used to predict the

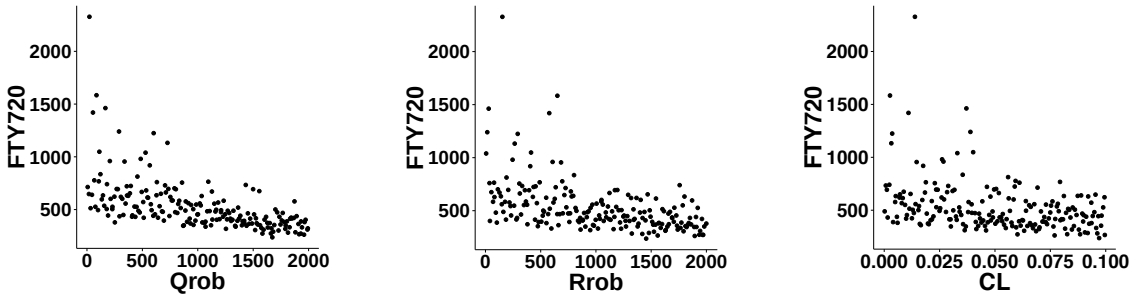

(a) **(b)** **(c)**

Figure 3.1: Maximum concentration of FTY720 in the lymph node of rats depends on Q_{rob}, R_{rob}, and CL. Parameters were varied over ranges defined in Table 3.3 and maximum concentrations of FTY720 in the lymph node compartment were recorded and plotted against Q_{rob}, the rate of blood flow into the rest of the body compartment (a), R_{rob}, the tissue-to-blood partition coefficient for the rest of the body compartment (b), and CL, the clearance rate of the drug from the liver (c).

FTY720 dynamics in mice, allometric scaling was used. Allometric equations are equations of the form $Y = aM^b$ where Y is a biological variable, M is a measure of body size, and a and b are scaling constants. Here, Y was taken to be PS_T, the permeability-surface area product, and a and b were assumed to be the same in mice as in rats. Meno-Tetang et al. (2006) do not explicitly define values for a and b in rats so these parameters had to be determined by model fitting.

Before a and b could be determined in the allometric equation, the unknown constants in equation (3.4) must be determined. The concentration of FTY720 in arterial blood at 10 timepoints following inoculation with FTY720 were estimated from Meno-Tetang et al. (2006) and a non-linear model was fitted to this data to determine values for A, B, C, α, β and γ in equation (3.4) using Mathematica (Wolfram Research, Inc, 2016). Next the ODEs for FTY720 in the lymph node were used to fit a and b in the allometric equation using the equation for C_{art} (3.4) in place of that for X_{art} (3.5). The parameters identified using this method are shown in Table 3.4.

In addition to using the allometric equation, for every parameter in the model equivalent parameters in mice have been identified (Appendix B).

The PK model that was developed in the previous section can be used to simulate the concentration of FTY720 in mice following either single or multiple interventions (Figure 3.4b) by replacing the rat specific parameters with those described in Appendix B.

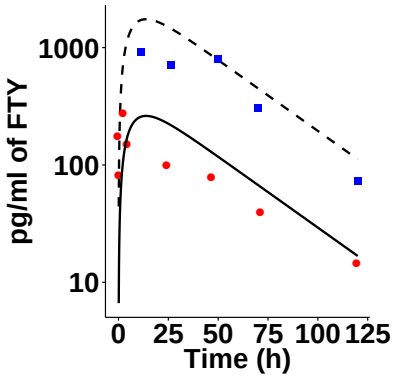

Figure 3.2: Reduced pharmacokinetic model adequately represents biological concentrations of FTY720 in the rat lymph node. The model selected using APSASIA was run with initial concentrations of FTY720 in veneous blood set to $6637ng/ml$ (solid line) and $44246ng/ml$ (dashed line), representative of a single dose of $0.3mg/kg$ and $2.0mg/kg$ of drug, respectively. Biological concentrations of FTY720 in rat lymph nodes are shown for low dose (red) and high dose (blue), estimated from Meno-Tetang et al. (2006).

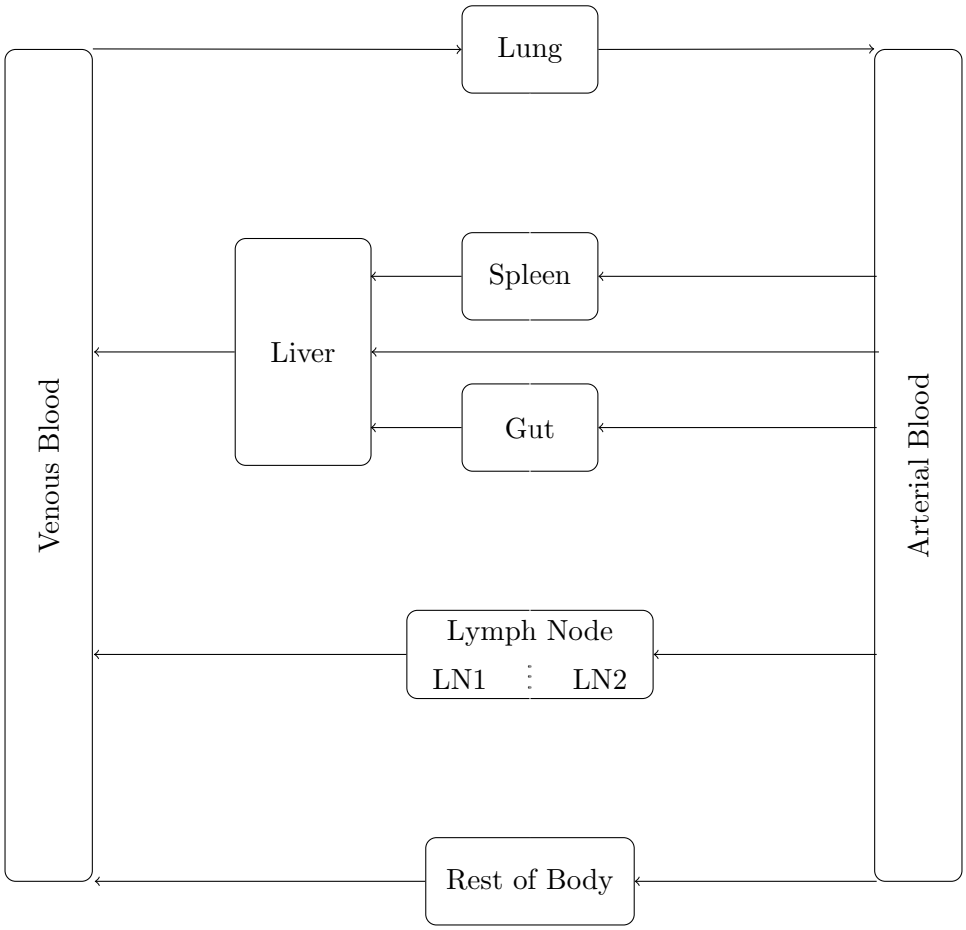

Figure 3.3: Schematic representation of the reducedPK model. 7 of the compartments used by Meno-Tetang et al. (2006) have been removed and incorporated into the rest of body compartment.

Parameter	Equation	Value
A	(3.4)	81.53
B	(3.4)	29.50
C	(3.4)	23.96
α	(3.4)	-6.68
β	(3.4)	-0.15
γ	(3.4)	-0.15
a	Allometric	188.84
b	Allometric	0.67

Table 3.4: Fitted model parameters. Model parameters were fitted to data estimated from Meno-Tetang et al. (2006) and used to determine the allometric scaling constants.

In the single dose scenario, a dose of $0.3mg/kg$ of drug was added to the veneous blood compartment and the model was simulated for 10 days (Figure 3.4a). For multiple doses, a dose of $0.3mg/kg$ was added to the concentration of FTY720 in the veneous blood at the start of day 0 and then the model was simulated for 24hours before another dose of the drug was added using ASPASIA (Evans, Stephanie et al.). This was repeated for 10 days and Figure 3.4b shows that by 6 days the concentrations of FTY720 in the lymph node have reached maximum levels.

During colitis, the number of cells in the MLN, and therefore the volume of the interstitial and intracellular space significantly increases (Dieleman et al., 2000). Although there is no data available for the volume of the lymph node during inflammation, unpublished data from the Kullberg lab shows that there is a 3.4-fold change in cell numbers in the MLN between uninfected and 21 day *Hh*-infected IL10KO mice. Morrison et al. (2013) showed that during inflammation there is up to a 9-fold increase in total lamina propria (LP) cells in the cecum. The PK model described by equations (3.1)-(3.5) uses organ volumes as parameter inputs so before integrating it into IBDSim it was important to determine how much of an affect altering the organ volume has on the distribution of drug around the body. Figure 3.5a shows that altering the organ volume of the MLN had very little effect on the concentration of drug in the blood in any of the compartments in the model with all PRCC between -0.1 and 0.1, and all pvalues greater than 0.1. This is verified for the MLN in Figure 3.5b, that shows how X_{ln1}, the maximum concentration of FTY720 in the blood compartment of the MLN, varies very little when the volume of the compartment is increased, and by Figure 3.5c, that shows the time course of X_{ln1} over time with daily doses of FTY720 over the range of organ volumes simulated. Conversely,

increasing the volume of the MLN causes the amount of drug in the cellular and interstitial compartment to significantly increase, with a PRCC between MLN volume and the peak concentration of drug in the MLN of 0.575 (Figure 3.5d) with a p-value of less than 0.001. This relationship is further demonstrated in Figure 3.5e that shows a strong positive correlation between X_{ln2}, the concentration of FTY720 in the intracellular and interstitial space of the MLN, and the volume of the compartment, and by Figure 3.5f), that shows a time course of multiple doses of the drug over a range of values for the volume of the MLN. Importantly, both Figure 3.5a and Figure 3.5d show that increasing the volume of other compartments does not have a significant effect on the concentration of FTY720 in the MLN, with all PRCCs being smaller than 0.1, and all p-values being greater than 0.05, so for modelling purposes only the increased volume of the MLN needs to be considered. Using data collected from IBDSim in Chapter 2, the change in the volume of the MLN during inflammation can be modelled. Data from IBDSim shows that there is a 2.3-fold change in the total number of immune cells modelled in the MLN during inflammation. A linear relationship between the volume of the MLN and the number of immune cells in the MLN can be developed and the resulting model is shown in Equation (3.6).

$$V_{ln2} = -0.643842 + 0.001568 \times \text{total MLN cells.} \tag{3.6}$$

3.2 Single Cell Pharmacodynamic (PD) Model for FTY720 in Mice

Once the concentration of drug in the lymph node has been calculated, a PD model was developed to determine the amount of drug taken up by each T cell. PD models are commonly composed of a system of mass balance ODEs of the form;

$$\frac{dR}{dt} = k_{off} \times D:R - k_{on} \times D \times R, \tag{3.7}$$

$$\frac{dD:R}{dt} = k_{on} \times D \times R - k_{off} \times D:R, \tag{3.8}$$

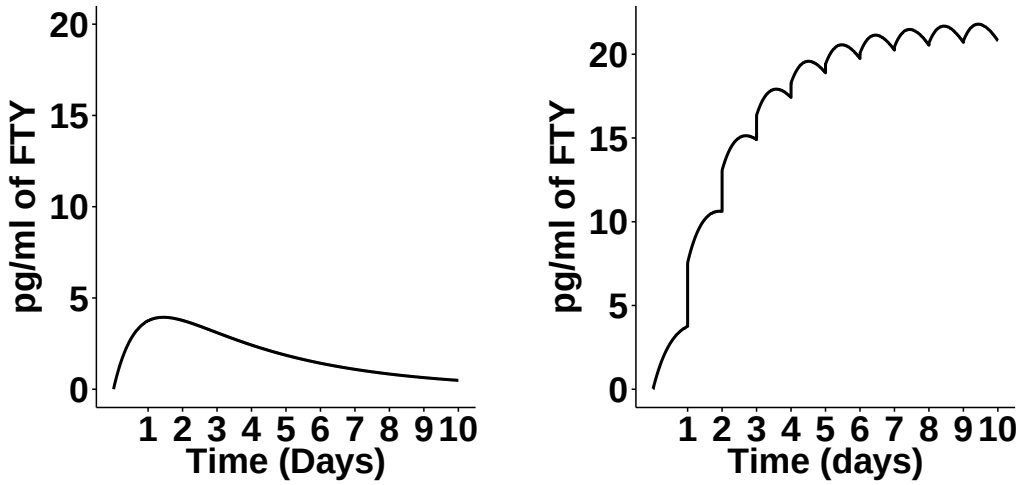

(a) **(b)**

Figure 3.4: Concentration of FTY720 in the lymph node of mice. Either single (a) or daily (b) doses of $0.3mg/kg$ of FTY720 were added to the PK model that was reparameterised with mouse data from Appendix B and the concentration of FTY720 in the MLN *in silico* was recorded over 10 days.

where R is free receptor, D is free drug, $D : R$ is the drug receptor complex, k_{on} is the rate at which the drug receptor complex is formed, and k_{off} is the rate at which this complex breaks down. The units of the species and parameter values must all be coherent. To use this model within IBDSim, the total number of $S1P_1$ receptors on a T cell had to be calculated, and k_{on} and k_{off} determined. The concentration of drug in the PK model presented in the previous section is measured in units of ng/ml but it is sensible to calculate receptor numbers in terms of absolute number of moluecules and as such, all parameter values for the PD model will be calculated using dimensions number of molecules, grid squares, and minutes.

3.2.1 Total number of S1P1 receptors on a T cell

To calculate the number of receptors per cell there were several assumptions that had to be made. Sykes et al. (2014) give the value of $Bmax$, the total concentration of receptors in Chinese hamster ovary (CHO) cells, an epithelial cell line, in units of $pmol/mg$. As there is no data relating to the number of $S1P_1$ receptors in a T cell, it has been assumed that there is the same number of receptors in $1mg$ of T cells as in $1mg$ of CHO cells. Under this assumption there are $2.64pmol$ of receptors per mg of T cells, which can be

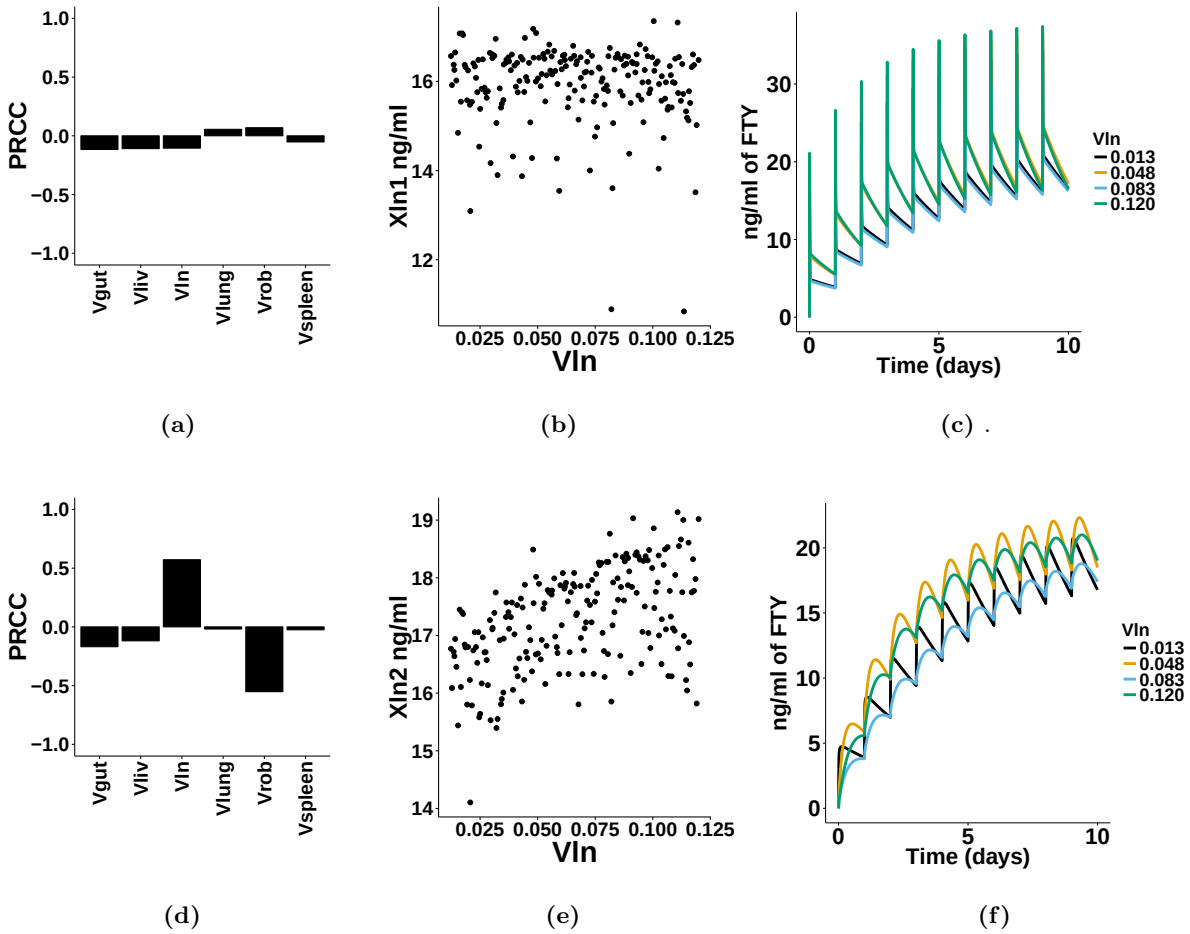

Figure 3.5: Sensitivity of the concentration of FTY720 in the lymph node to changes in organ volumes. Organ volumes were varied up to 10 times their normal size and daily doses of $0.3mg/kg$ of FTY720 were simulated for 10 days. (a) PRCC between X_{ln1}, the volume of FTY720 in the blood compartment of the MLN and all other organ volumes. (b) Correlation between X_{ln1} and the volume of the MLN, V_{ln} for all 200 values of V_{ln} that were simulated. (c) Time course of concentrations of X_{ln1} for a range of values of V_{ln}. (d) PRCC between X_{ln2}, the concentration of FTY720 in the interstitial and intracellular spaces of the MLN and all other organ volumes. (e) Correlation between X_{ln2} and V_{ln} for all 200 values of V_{ln} that were simulated. (f) Time course of concentrations of X_{ln2} for a range of values of V_{ln}.

converted to molecules per T cell as follows;

Although in reality they are slightly larger, assuming that T cells are the same weight as red blood cells, that is $27pg = 2.7 \times 10^{-8}mg$, (Phillips et al., 2012), gives the amount of receptor in *pmol* as;

$$2.64 \times 2.7 \times 10^{-8} = 7.128 \times 10^{-8}. \tag{3.9}$$

This can be turned into the number of molecules per cell using a number called the Avogadro constant. This is defined as the number of molecules per mole of substance, denoted N_A, and $N_A = 6.022 \times 10^{23}\ mol^{-1}$. Since $1\ pmol = 10^{-12}\ mol$,

$$7.128 \times 10^{-8} pmol = 7.128 \times 10^{-20}\ mol \tag{3.10}$$

$$\implies \quad 7.128 \times 10^{-20} \times N_A \approx 42910\ molecules, \tag{3.11}$$

so there are approximately 43000 receptors per cell.

3.2.2 Rates of FTY:Receptor complex formation

Sykes et al. (2014) give the dissociation constant, K_d, to be $0.238nM$, and k_{off} to be 17.2 min^{-1}. Using the relationship $k_d = \frac{k_o ff}{k_o n}$ implies that $k_{on} = 72.3\ min^{-1} nM^{-1}$. To make these units compatible with uptake by T cells, the units of k_{on} had to be converted to $molecules^{-1}\ gridsquare^{-1}\ min^{-1}$.

$$1\ nM = 10^{-9}\ M \quad \implies \quad k_{on} = 72.3\ nM^{-1} min^{-1} \tag{3.12}$$

$$= 72.3 \times 10^{9}\ M^{-1} min^{-1}, \tag{3.13}$$

and using the Avogadro constant the number of molecules per litre can be calculated,

$$6.022 \times 10^{23}\ molecules\ mol^{-1} \text{ and } 1\ M = 1\ mol\ litre^{-1}. \tag{3.14}$$

Hence,

$$k_{on} = 72.3 * 10^{9}/(6.022 \times 10^{23}) \tag{3.15}$$

$$= 1.20048 \times 10^{-13} molecules^{-1}\ litre^{-1}\ min^{-1}. \tag{3.16}$$

As a T cell in the ABM will determine the concentration of drug from its local pool rather than the overall concentration, k_{on} had to be reported in units per grid square, not per

litre. It can be estimated that the volume of a grid square is in litres, V_{gl}, is

$$\begin{aligned} V_{gl} &= \textit{(total volume of MLN)/(number of grid squares)} \\ &= \frac{V}{36 \times 228} \qquad (3.17) \\ \implies \quad k_{on} &= 1.20048 \times 10^{-13} / \left(\frac{V}{36 \times 228} \right) \; molecules^{-1} \; gridsquare^{-1} \; min^{-1}, \qquad (3.18) \end{aligned}$$

where V is the volume of the lymph node, that changes during inflammation and 36×228 are the dimensions of the lymph node compartment in IBDSim.

3.3 FTY720 significantly reduces cell numbers but not intestinal inflammation in *Hh*-induced colitis

To examine the effect of blocking lymphocyte egress with FTY720 on *Hh*-induced colitis, the PK and PD models described in this chapter have been integrated into the ABM of intestinal inflammation, IBDSim. Using this hybrid ABM, FTY_IBDSim, the effects of FTY720 administration at three different time points has been examined (Figure 3.6). At each time point, the number of T cells in the cecum and colon has been compared with *in silico* cell counts in simulations of conventional *Hh*-infected IL10 KO mice, and with simulations of uninfected mice. The conventional and uninfected simulations were performed using IBDSim as described in the previous chapter.

3.3.1 Experimental Procedure

The integration of the PK model describing the dynamics of FTY720 into IBDSim, was done by adding an SBML-model simulator to the MLN compartment, details are given in Section 2.10.3

As described in the previous chapter, each compartment in IBDSim starts in an empty state and simulations start from day -20, allowing the compartments time to reach an uninfected steady state by day 0. The effects of beginning FTY720 administration at three different time points has been examined. The first experiment looked at the effect of beginning FTY720 administration concurrently with *Hh*-infection to determine if FTY720 can effectively block inflammation from occurring. The next experiment was an extension

of the previous case where FTY720 is added 6 days before *Hh*. This allowed FTY720 to reach saturating levels in the MLN prior to infection. The final experiment looked at the ability of FTY720 to resolve or reduce established inflammation by beginning administration of FTY720 at 14 days post-infection. In all experiments, *Hh* was added to the cecal lumen compartment at the start of day 0. Depending on the experiment, at the start of either 0, -6, or 14 days post infection, the PK model describing the dynamics of FTY720 in the lymph node was simulated for one day, on a minute time scale, with step size 0.012. For the next 1440 time steps, equal to one day, the concentration of drug in each grid square in the MLN was set to the value of $\frac{X_{ln2}}{\text{Number of grid squares}}$ At the end of this time period the model describing the blood profile of FTY720 was updated to reflect the levels at the end of the previous days simulation and a new dose of drug was added to the value for X_{ven}, the concentration of FTY720 in the veneous blood. At the beginning of each subsequent day, i.e. after 1440 time steps, the PK model was run again and the process repeated.

3.3.2 Results

Following the experimental procedure defined in the previous section, 20 simulations were run and the average number of all immune cells in the simulation, that is DCs, inflammatory and regulatory macrophages, and $CD4^+$ T cells, were recorded at each time point post infection with *Hh* with or without daily administation of FTY720 (Figure 3.7) at time points defined in Figure 3.6.

3.3.2.1 Experiment 1: FTY720 given at day 0 significantly reduces cell numbers in *Hh*-induced colitis

An *in silico* experiment has been performed to examine the effects of daily administration at doses of doses of $0.3mg/kg$ of FTY720 starting from day 0, the time of *Hh* infection. Performing a one-way ANOVA comparing *in silico* cell numbers following *Hh* infection between FTY720+ and FTY720- experiments showed that total cell numbers were significantly reduced in the cecum ($p < 0.01$, Figure 3.7a). A post-hoc Tukey test was performed to identify differences in numbers of each cell type over time due to the addition of FTY720. After using a bonferoni correction to account for the multiple tests that were performed,

significant differences in cell numbers were observed for all populations at days 14, 21 and 45, at day 7 for T cells and both inflammatory and regulatory macrophages, and at day 4 for T cells ($p < 0.001$). As expected, FTY720 has the greatest effect on the T cell population with a 2.5-fold reduction in numbers at day 7 and a 4-fold decrease by day 45. The second largest change was in the number of regulatory macrophages with as many as 1.6 times more regulatory macrophages entering the gut in FTY720+ mice. Blocking lymphocyte egress from the MLN also affects the cytokine concentrations (Figure 3.7b), with up to 1.5 fold decrease in total tissue cytokine, a 5-fold decrease in the amount of IFN-γ and up to a 3-fold decrease in IL17 observed in the cecum between *Hh* alone and *Hh* with FTY720. Similar trends were seen in the colon (Figure 3.8). Although a reduction is observed in the cell numbers and cytokine concentrations in both the cecum and colon compartments following FTY720 administration compared to *Hh* alone, they are still significantly higher than those in an uninfected case, at day 0 ($p < 0.001$). When taken together, the changes in cell counts and cytokine levels are not sufficient to reduce overall inflammation in the tissue as measured by the inflammation score developed in Section 2.5(Figure 3.9).

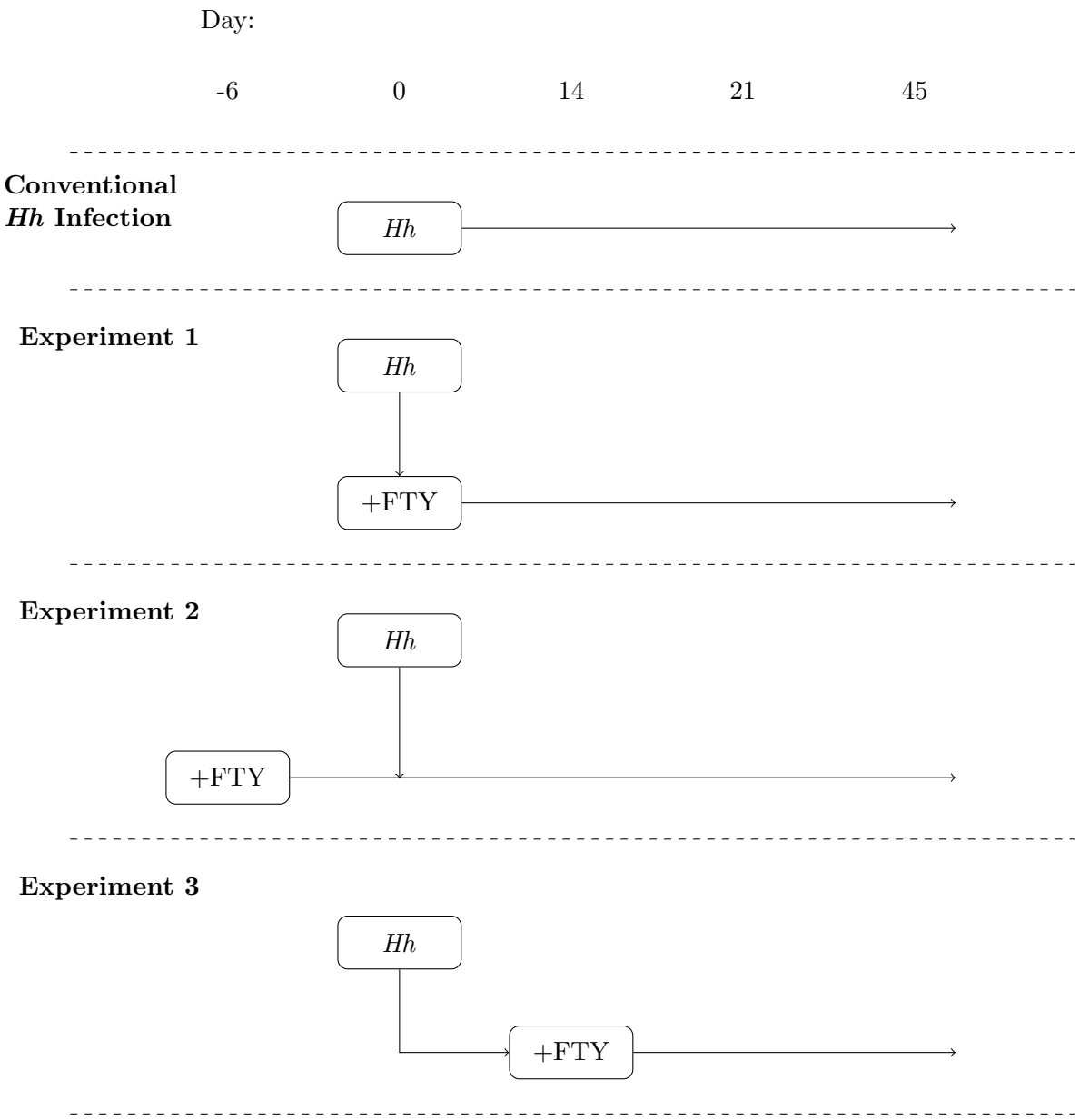

Figure 3.6: Procedure for *in silico* FTY720 experiments.

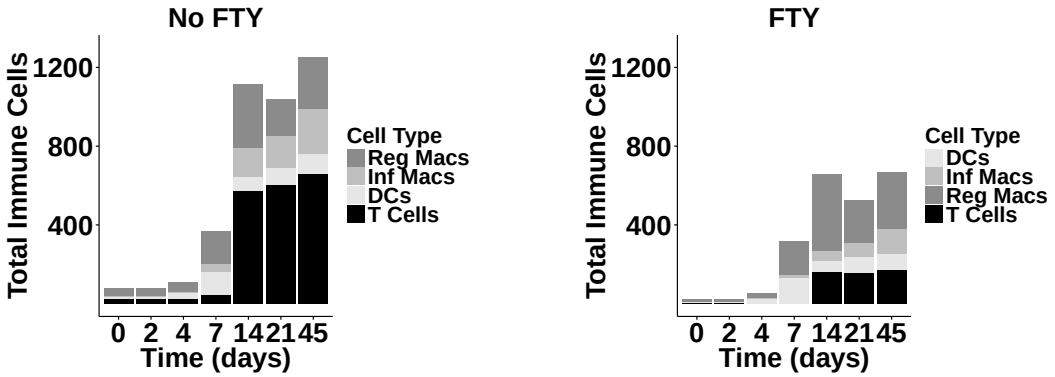

(a)

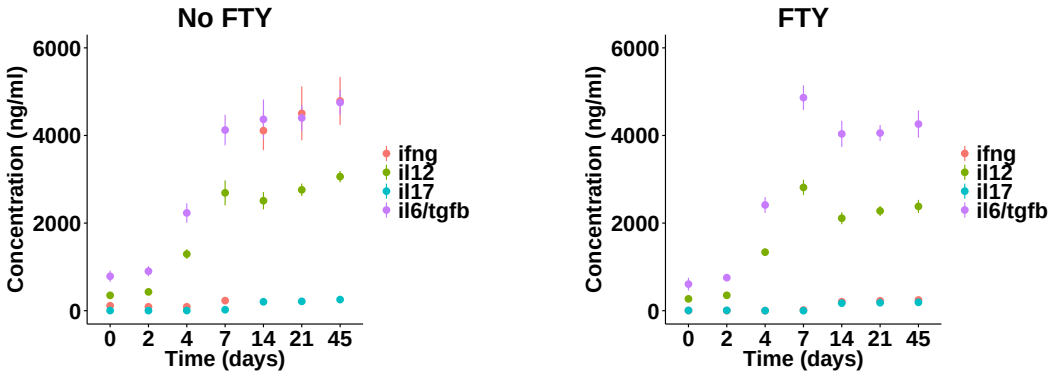

(b)

Figure 3.7: Daily administration of FTY720 significantly reduces cell numbers in the cecum (Experiment 1). Counts of immune cells (a) and concentration of cytokines (b) in the cecum, following infection with *Hh* alone (left) and with daily administration of FTY720 from the start of *Hh* infection (right).

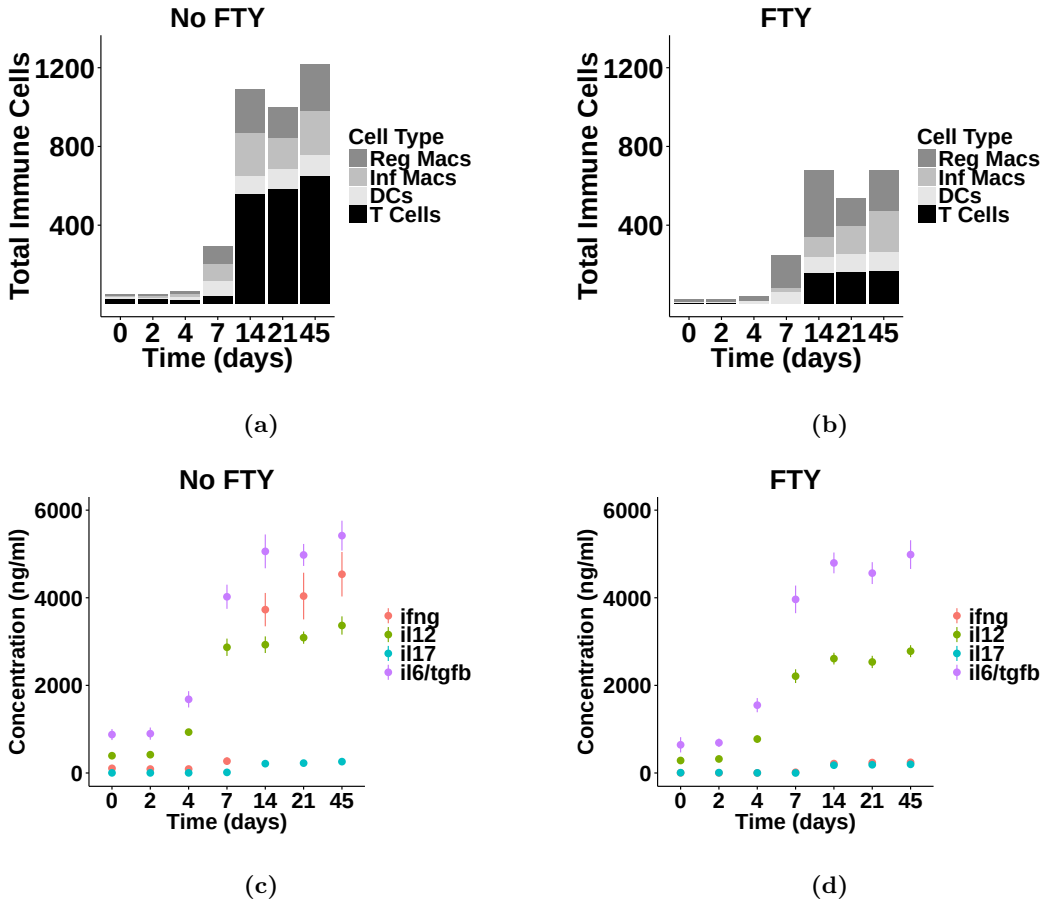

Figure 3.8: Daily administration of FTY720 significantly reduces cell numbers in the colon (Experiment 1). Counts of immune cells (a) and concentration of cytokines (b) in the colon, following infection with *Hh* alone (left) and with daily administration of FTY720 from the start of *Hh* infection (right).

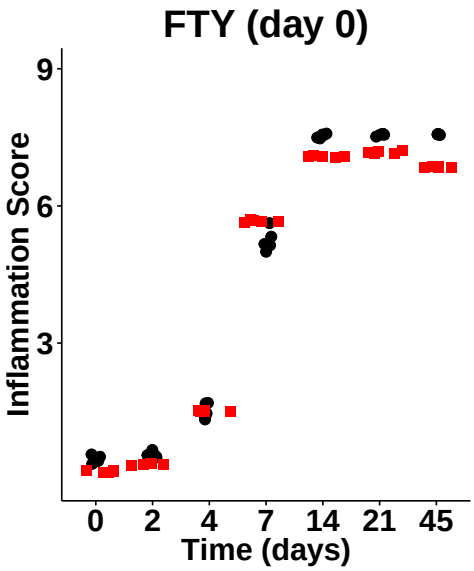

Figure 3.9: There is no significant difference in the inflammation score in the colon following daily administration of FTY720 (Experiment 1). The inflammation score developed in Section 2.5 was calculated for the colon compartment following infection with *Hh* alone (black circles) and with daily administration of FTY720 from the start of *Hh* infection (red squares).

3.3.2.2 Experiment 2: FTY720 given 6 days prior to *Hh* infection does not have a significant advantage over FTY720 given at day 0 in *Hh*-induced colitis

The second *in silico* experiment to be performed examined the effects of daily administration at doses of doses of $0.3mg/kg$ of FTY720 starting six days before *Hh* infection to allow the drug to saturate the MLN. This experiment further examines the effectiveness of FTY720 for preventing intestinal inflammation from developing in IL10 KO mice following *Hh* infection. Performing a one-way ANOVA to compare *in silico* cell numbers following *Hh* infection between FTY720+ day -6, and FTY720+ day 0 experiments showed that neither cell numbers nor cytokine levels are significantly reduced in the cecum or colon when FTY720 is added 6 days prior to *Hh* infection, FTY720 treatment beginning on the same day as *Hh* infection ($p = 0.078$, Figure 3.10a). Thus the changes in cell counts and cytokine levels following FTY720 administration either from 6 days, or 0 days, before *Hh* infection are not sufficient to reduce overall inflammation in the tissue as measured by the inflammation score developed in Section 2.5(Figure 3.12).

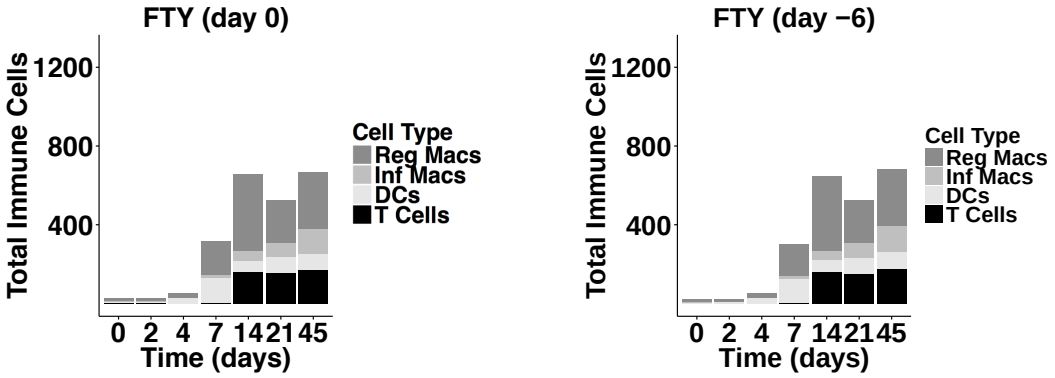

(a)

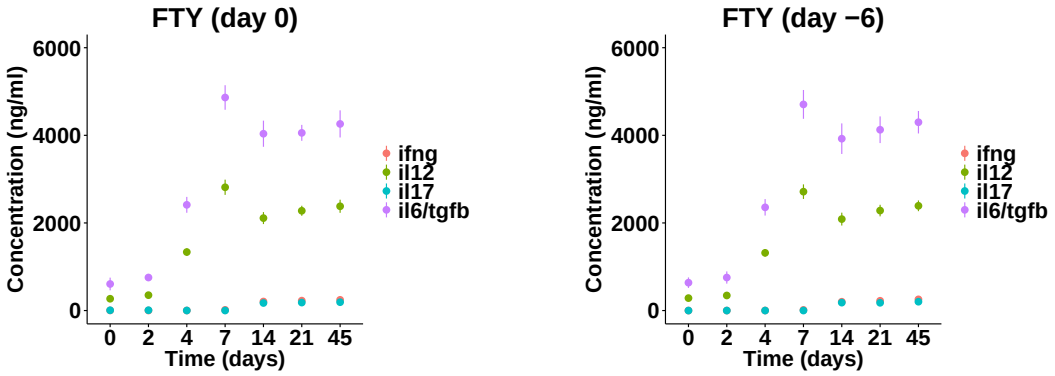

(b)

Figure 3.10: There is no significant difference in cell numbers in the cecum following daily administration of FTY720 from 6 days prior to *Hh* infection when compared to concurrent *Hh* infection and FTY720 innoculation (Experiment 2). Counts of immune cells (a) and concentration of cytokines (b) in the cecum from the point of *Hh* infection following daily administration of FTY720 from the start of *Hh* infection (left) and from 6 days before *Hh* (right).

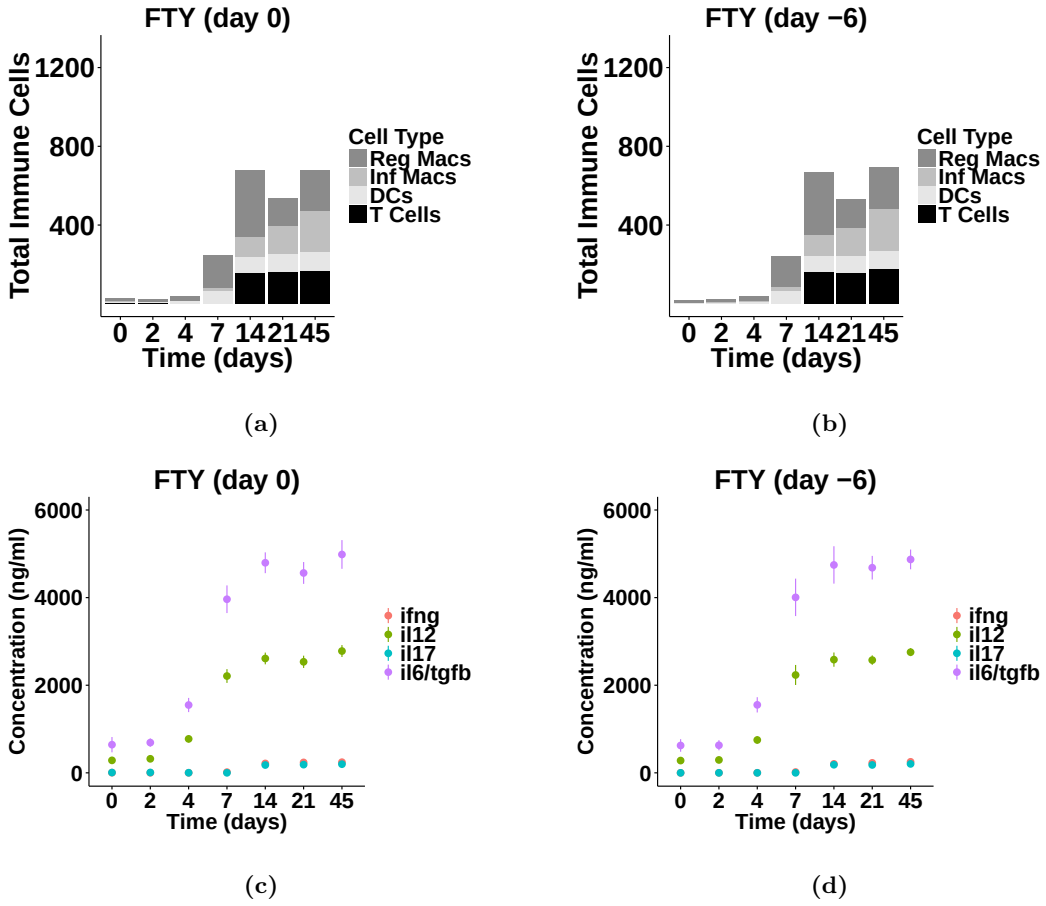

Figure 3.11: There is no significant difference in cell numbers in the colon following daily administration of FTY720 from 6 days prior to *Hh* infection when compared to concurrent *Hh* infection and FTY720 innoculation (Experiment 2). Counts of immune cells (a) and concentration of cytokines (b) in the colon from the point of *Hh* infection following daily administration of FTY720 from the start of *Hh* infection (left) and from 6 days before *Hh* (right).

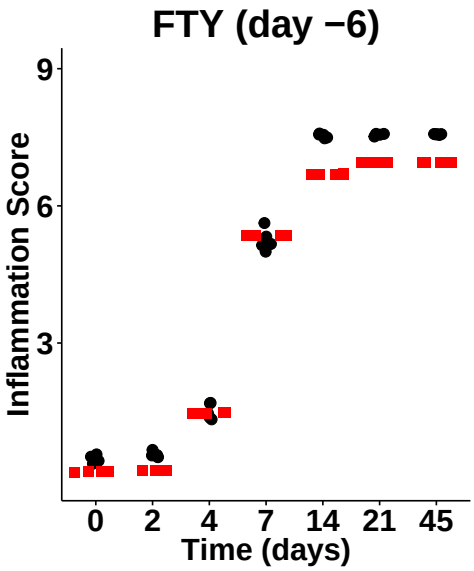

Figure 3.12: There is no significant difference in the inflammation score in the colon following daily administration of FTY720 from 6 days prior to *Hh* infection (Experiment 2). The inflammation score developed in Section 2.5 was calculated for the colon compartment following infection with *Hh* alone (black circles) and with daily administration of FTY720 starting from 6 days prior to *Hh* infection (red squares).

3.3.2.3 Experiment 3: FTY720 given 14 days after *Hh* infection can significantly reduce inflammation in *Hh*-induced colitis

The final *in silico* experiment to be performed examined the ability of FTY720 to resolve established inflammation by administering daily doses of $0.3mg/kg$ of FTY720 from 14 days post-*Hh* infection to allow inflammation to develop before the drug was added. Performing a one-way ANOVA to compare *in silico* cell numbers following *Hh* infection without FTY720 and with FTY720+ from day 14 shows that both cell numbers and cytokine levels are significantly reduced in the cecum and colon by 21 days post-infection ($p < 0.001$, Figure 3.13). Performing A post-hoc Tukey test identified where the differences in cell numbers appear. As with the first experiment, the biggest reduction was seen in the number of T cells with significant differences at both 21 and 45 days post-infection, that is 7 and 31 days after commencing treatment with FTY720 ($p < 0.001$). Unlike the first experiment where the DC population did not see any effect until 21 days post-addition of FTY720, adding the drug at day 14 caused the number of DCs in the cecum to be significantly reduced by 21 days post-infection, that is 7 days after beginning drug administration ($p < 0.001$). By 45 days post infection, both inflammatory and regulatory macrophages showed significant reductions in numbers ($p < 0.001$). This differs from the results when FTY720 was added from day 0, where the number of regulatory macrophages had significantly increased 21 days after commencing treatment with FTY720. The same trends were also observed in the colon (Figure 3.14). The inflammation score developed in Section 2.5 shows that 7 days after starting FTY720 administration in this experiment (21 days post infection), the level of inflammation in the colon is reduced Figure 3.15, however, by 45 days post infection there is no difference between the inflammation score with or without FTY720.

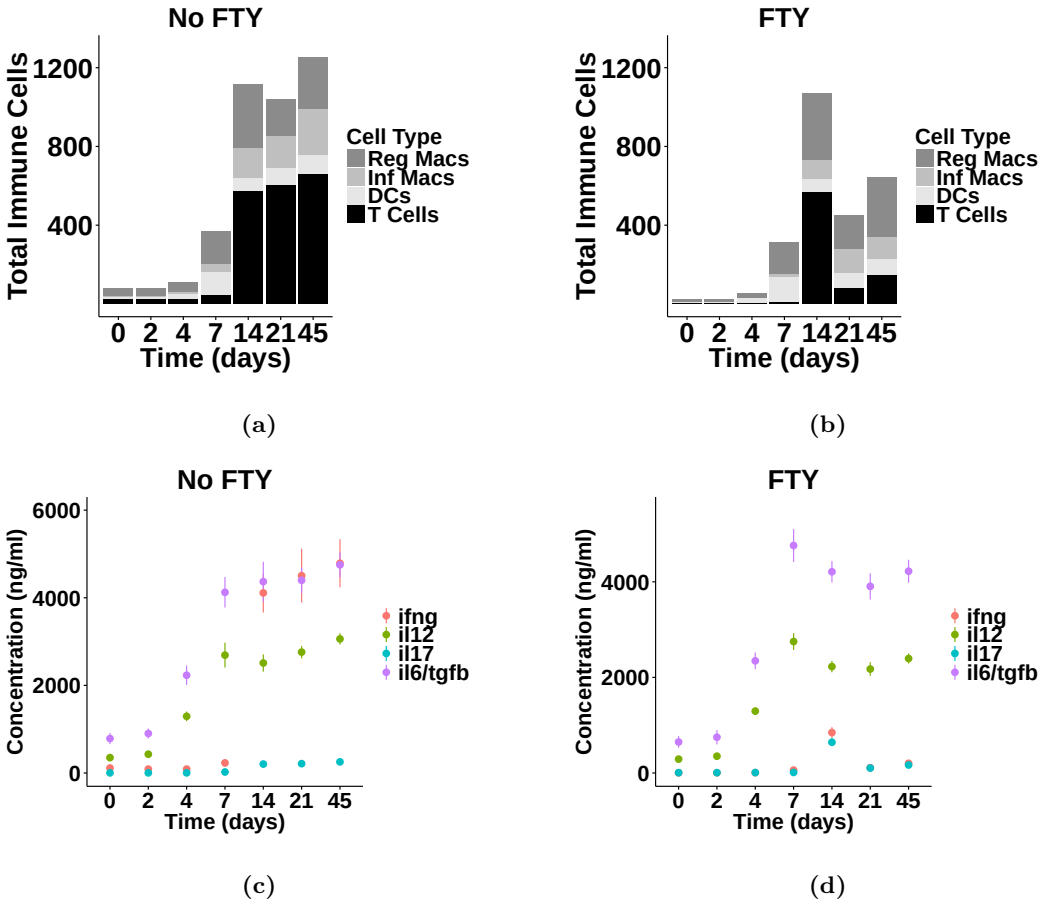

Figure 3.13: Daily administration of FTY720 significantly reduces cell numbers in the inflammed cecum (Experiment 3). Counts of immune cells (a) and concentration of cytokines (b) in the cecum, following infection with *Hh* alone (left) and with daily administration of FTY720 from the 14 days post *Hh* infection (right).

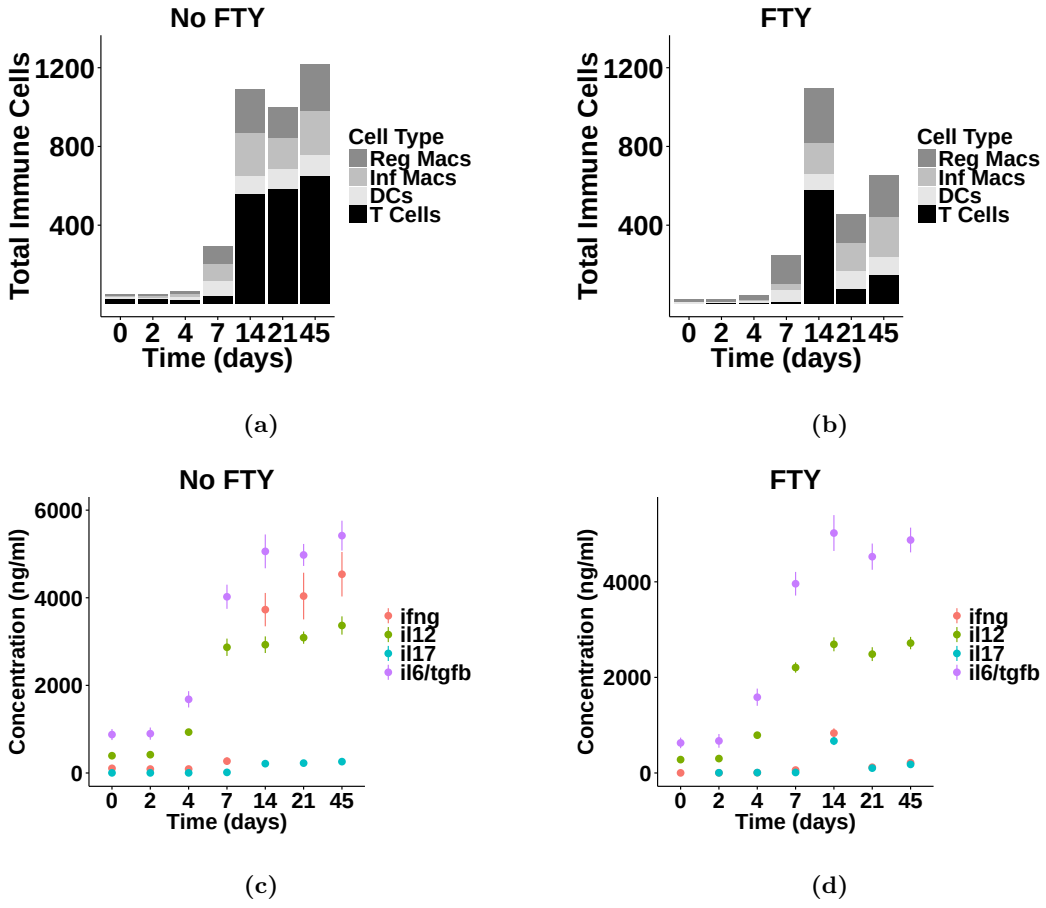

Figure 3.14: Daily administration of FTY720 significantly reduces cell numbers in the inflammed colon (Experiment 3). Counts of immune cells (a) and concentration of cytokines (b) in the colon, following infection with *Hh* alone (left) and with daily administration of FTY720 from the 14 days post *Hh* infection (right).

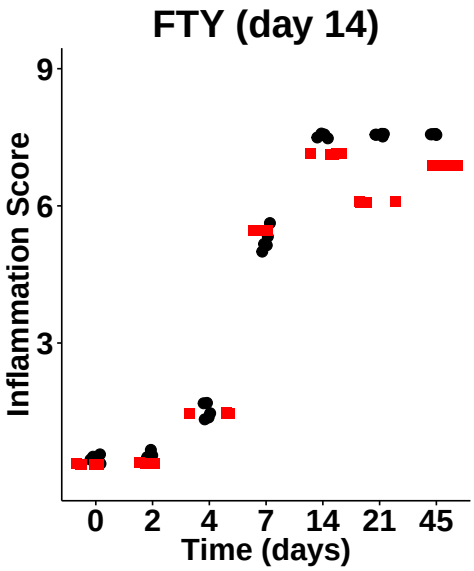

Figure 3.15: There is no significant difference in the inflammation score in the colon following daily administration of FTY720 from 14 days prior to *Hh* infection (Experiment 3). The inflammation score developed in Section 2.5 was calculated for the colon compartment following infection with *Hh* alone (black circles) and with daily administration of FTY720 starting from 14 days post infection with *Hh* (red squares).

3.3.3 Summary

This chapter details the development of a PK-PD model to describe the dynamics of FTY720 in the lymph node of mice, and the effect that the drug has on T-cells. The PK model is based on a previous model by Meno-Tetang et al. (2006) that predicted the concentration of FTY720 in several organs in rats, at different time points. The PD part of the model follows a standard framework for modelling receptor-binding dynamics in systems pharmacology, however, it is not certain that this modelling approach accurately captures the dynamics in this system. As this case study focusses on the affect of lymphocytes being sequestered in the lymph node has on intestinal inflammation, it is sufficient in this case that the dynamics of T-cell recirculation from the lymph node were calibrated to biological data, given the chosen model. However, if this study had instead focussed on the change in the level of receptor in the lymph node, or in determining the required efficacy of FTY720 to reduce inflammation, the choice of PD model would be more important, and biological experiments would have to be performed to allow a more accurate model to be developed and parameterised. The results presented in this section demonstrate that FTY720 has the potential to reduce the cell numbers in the cecum and colon but not to resolve intestinal inflammation in *Hh*-infected IL10 KO mice. Further, FTY720 cannot completely block inflammation from occurring in the *Hh* colitis model as it has done in other models of inflammation (Table 3.1). The outcome of FTY720 on *Hh*-induced inflammation is more similar to that observed by Murphy et al. (2012) following infection of wild type mice with bacteria *Citrobacter rodentium*. Murphy et al. (2012) saw that FTY720 has an adverse effect in this experimental scenario because it inhibited the clearance of the bacteria by lowering the immune response, something that also happens in the model presented in this thesis. To increase confidence in this result, the inflammation scoring system needs to be properly calibrated using a *Hh*-infected IL10KO as a control, before the experiments can be ran again, and the output re-evaluated.

Chapter 4

Exploring the Effects of microbial composition on disease outcome in *Hh*-induced intestinal inflammation

An alteration of microbial community structure has been associated with intestinal disease in both human and animal models of IBD (Seksik et al., 2003; D'Argenio et al., 2013; Buffie et al., 2012; Nagalingam et al., 2013). In the *Hh*-induced colitis model, the composition of gut microbiota has been implicated in determining susceptibility to intestinal inflammation (Yang et al., 2013). Moreover, Morrison et al. (2013) observed that inflammation in the *Hh*-induced colitis model begun to resolve by 45 days post infection and was fully resolved by 91 days, however earlier work by Kullberg et al. (1998) using the same experimental system showed that inflammation persisted up to at least 77 days post infection. In both cases, the experiments were performed using the same strain of mice and *Hh*, thus the key differences between the experiments were the food the mice were fed and the facilities they were kept in. It has been shown that both of these factors can be responsible for shaping the microbiota (Jakobsson et al., 2015), and also that the composition of microbiota has significant effects on mucus thickness and on barrier function (Littman and Pamer, 2011; Silva et al., 2015; Lopetuso et al., 2013).

Chapter 2 details the development of IBDSim, a computational model that captures the development of intestinal inflammation in *Hh*-induced colitis. IBDSim assumes that the gut microbiota can be modelled as evenly distributed bacteria that cause either type-1 or type-17-inducing responses from DCs and macrophages. Under this assumption, the model adequately captures the development of inflammation following *Hh* infection. However the resolution and switch in response from predominantly Th1 to predominantly Th17 at later time points post infection, as observed by Morrison et al. (2013) is not captured (Figure 4.1). Analysis of the literature reveals that the assumption of evenly distributed, homogeneous commensal flora used in IBDSim is incorrect.

Nagalingam et al. (2013); Yang et al. (2013) looked at the composition of microbiota in IL10 KO mice with and without *Hh* infection and showed that different bacterial phenotypes are not evenly distributed *in vivo*. Nagalingam et al. (2013) showed that infection with *Hh* changed the composition of the microbial communities in the gut, and that treatment with either broad-spectrum or gram positive-specific antibiotics did not cause inflammation to resolve. Moreover, the authors conclude that the presence of *Hh* altered the composition of commensal flora in the gut. Moreover, the specific composition of commensal flora has been shown to be important in susceptibility to *Hh*-induced colitis. Yang et al. (2013) observed that IL10 KO mice kept different facilities had different microbial communities and suggested that these differences could be responsible for the different susceptibility to *Hh*-induced inflammation.

To examine whether altering the composition of commensal flora alone is sufficient to produce different disease phenotypes, both in an uninfected scenario and following *Hh* infection, IBDSim has been extended to capture behaviours in all of these cases. IBDSim_Microbiota considers different populations of microbiota as initial conditions, and the development of this model is discussed here. Unlike in the previous iteration of IBDSim where cytokines were considered to be only Th1- or Th17-inducing, to gain insight into the contributions of different types of bacteria, the cytokines need to be decoupled into IFN-γ, IL12, TGF-β and IL6. This means that an implicit representation of cytokine-inducing bacterial species in the cecal and colonic lumen must be developed.

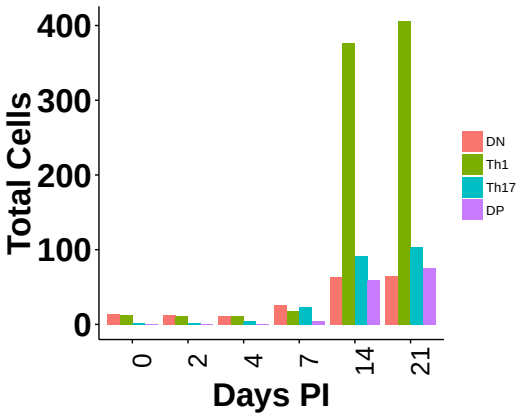

Figure 4.1: Numbers of T cells of each phenotype in IBDSim. Counts of double negative (double negative (DN)) cells (coral), Th1 cells (green), Th17 cells (turquoise) and double positive (DP) cells (purple) are shown at 0, 2, 7, 14, and 21 days post infection (PI), as estimated by the level of transcription factors T-bet and ROR-γt.

4.0.1 Mathematical Model

Suitable combinations of cytokine-inducing bacterial species were generated using a mathematical model that represents competition between the bacterial species. This bacterial composition model was developed using SBML, assuming that the commensal flora can be categorised by the type of cytokine they induce. The bacterial competition was based on the basic Lotka-Volterra competition model (Cushing, 1986) with a single carrying capacity representing the nutrients available to bacteria, causing indirect competition for resources between the species. The model also incorporates direct competition between species. The source of this direct competition could be factors secreted by certain species that are either beneficial or harmful to other specific species. Analysing direct correlations between bacterial species in the colon of *Hh*-infected IL10 KO mice suggests that this phenomenon of direct competition exists in biology (Figure 4.2) Incorporating the two types of competition (indirect and direct) into a standard logistic population growth model results in a set of equations, one for each bacterial species in the model, that take the form;

$$\frac{dX_i}{dt} = a_i X_i \left(1 - \frac{X_i}{K - \sum_{j=1, j\neq i}^{n} X_j}\right) + \sum_{j=1, j\neq i}^{n} b_{ij} X_i X_j - \mu_i X_i, \tag{4.1}$$

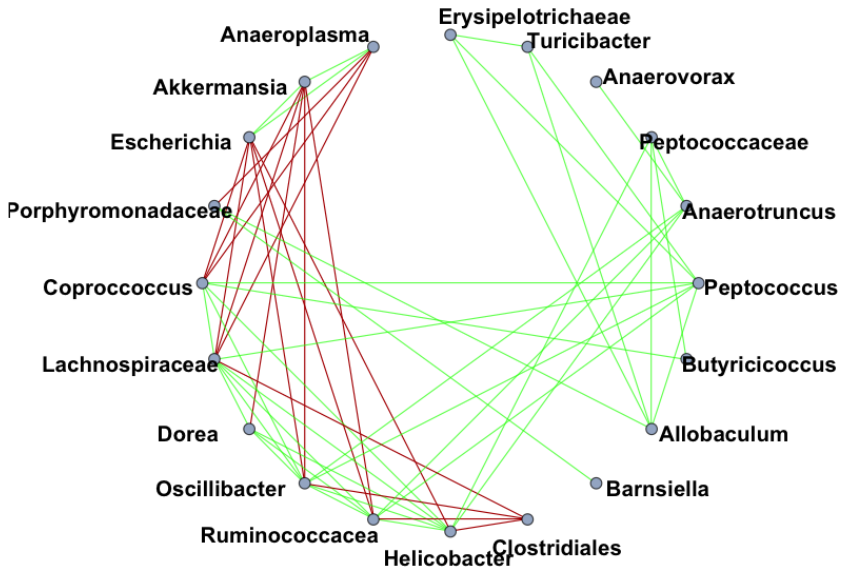

Figure 4.2: Competition between bacterial species in the colon of IL10 KO mice following infection with *Hh*. Correlations were calculated using SPARCC (Friedman and Alm, 2012) on data taken from Nagalingam et al. (2013). Red represents negative correlation coefficients, while green represents positive correlation coefficients.

where X_i is the number of bacteria of species i, K is the carrying capacity for all of the bacteria, n is the total number of species being modelled, b_{ij} is the rate of promotion or inhibition of bacteria i by bacteria j, a_i is the proliferation rate of species i and μ_i is the death rate of species i.

Using ASPASIA (Evans et al., submitted) to vary the parameters as defined in Table 4.1, and solving the equations on a minute scale using the Runge-Kutta algorithm with a step size of 0.012, 1000 models were generated that each represent a potential microbial composition. Of these 1000 models, 158 were numerically unstable, due to the stiffness of the equations, in the absence of *Hh*, and were therefore excluded. Moreover, it was determined that suitable candidates for potential compositions of microbiota must contain all species in steady state. Removing models that did not meet this criterion left 34 models to be used as initial conditions (Figure 4.3a). To add *Hh* to the model, the rules governing interactions between *Hh* and all other populations had to be defined. The values of $b_{Hh,j}$ and $b_{j,Hh}$ were the same for all j and for all models, and 3 possible

Table 4.1: Parameter values used for ASPASIA generated SBML models.

Parameter	Min	Max
a_ifng	1.38E-4	1.38×10^{-2}
a_il12	1.38E-4	1.38×10^{-2}
a_il6	1.38E-4	1.38×10^{-2}
a_tgfb	1.38E-4	1.38×10^{-2}
b_ifng_il12	-2×10^{-12}	2×10^{-12}
b_ifng_il6	-2×10^{-12}	2×10^{-12}
b_ifng_tgfb	-2×10^{-12}	2×10^{-12}
b_il12_ifng	-2×10^{-12}	2×10^{-12}
b_il12_il16	-2×10^{-12}	2×10^{-12}
b_il12_tgfb	-2×10^{-12}	2×10^{-12}
b_il6_ifng	-2×10^{-12}	2×10^{-12}
b_il6_il12	-2×10^{-12}	2×10^{-12}
b_il6_tgfb	-2×10^{-12}	2×10^{-12}
b_tgfb_ifng	-2×10^{-12}	2×10^{-12}
b_tgfb_il12	-2×10^{-12}	2×10^{-12}
b_tgfb_il6	-2×10^{-12}	2×10^{-12}
mu_ifng	1.4×10^{-5}	1.4×10^{-2}
mu_il12	1.4×10^{-5}	1.4×10^{-2}
mu_il6	1.4×10^{-5}	1.4×10^{-2}
mu_tgfb	1.4×10^{-5}	1.4×10^{-2}
X_ifng_prop	0.5	1
X_il12_prob	0.5	1
X_il6_prob	0.5	1
X_tgfb_prob	0.5	1

values were chosen by using Mathematica to vary parameter values. Nagalingam et al. (2013) suggested that there was no significant difference in total bacterial burdens before and after infection with *Hh*, and similar results have been demonstrated by the Kullberg lab (Figure 4.4). Simulations of the models generated showed that when *Hh* inhibits the growth of other phenotypes there is a significant change in the total number of bacteria; thus, *Hh* cannot inhibit other species in the model (Figure 4.5b). However, when *Hh* has no direct effect on other commensal species (Figure 4.5c), there is a non-significant change in the total number of bacteria. Allowing *Hh* to promote the growth of commensal species (Figure 4.5d) also results in a non-significant change in the total number of bacteria but in this case, further numerical instability is induced. Therefore, it was decided that *Hh* will not directly compete with other species in the model. The proportions of each bacterial species in the 34 resulting models, following the addition of *Hh* is shown in Figure 4.3a

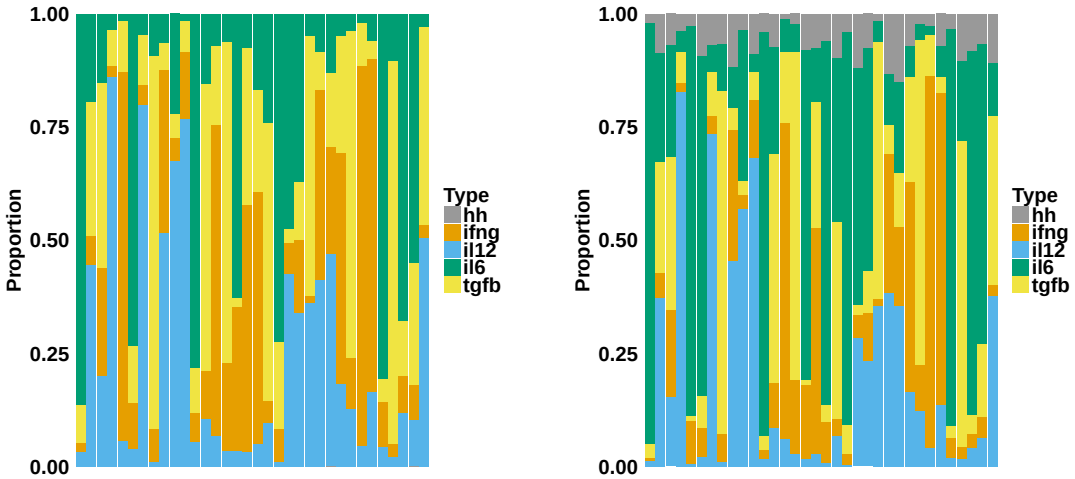

(a) Uninfected **(b)** Infected

Figure 4.3: Amount of *Hh*-, IFN-γ-, IL12-, IL6- and TGF-β- inducing bacteria as a proportion of the total population of bacteria in each of the 34 models that were selected as suitable candidates for microbial compositions *in silico*. Proportions were calculated using steady state levels of each group of bacteria using the model described in Equation (4.1) in the absence (a), or presence (b) of *Hh*.

4.1 Extending IBDSim

The bacterial composition models described in the previous section were subsequently integrated with the ABM to determine the differential effects of microbiota on simulation

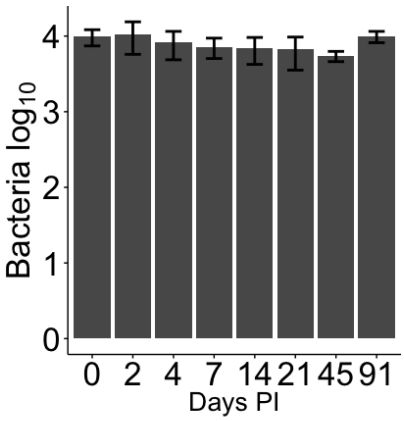

Figure 4.4: Numbers of bacteria in the cecum following infection with *Hh*. Counts of bacteria estimated from total DNA yields from cecal contents *in vivo* (Kullberg lab, unpublished). Calulations assume that all bacteria follow the relationship that 14 bacteria contain 20 fg of DNA, as with *Hh* (Ge et al., 2001).

behaviour. This integration was done by replacing the cecal and colonic lumen with an SBML model simulator that runs the SBML model for 1 minute using the Runge-Kutta method, with a step size of 0.012, in line with each time step in the ABM (Figure 4.6). Integrating this new implementation of the commensal flora into IBDSim, and simulating over a longer time period, required several changes to be made to the model.

4.1.1 Recruitment of bacteria into the Cecum and Colon

In the previous version of IBDSim, bacteria entered the cecum and colon at a rate determined by the level of damage to the epithelial wall, a concept that was represented by the number of epithelial cells that were secreting cytokines (Section 2.3.4). In IBDSim_Microbiota, the cecal and colonic lumen compartments were replaced by the system of ODEs, with the number of agents that enter the cecum and colon being determined as a fraction of the number of bacteria removed from the lumen at each time point, represented by the $\mu_i X_i$ term in the ODE model.

To maintain the behaviours from the previous iteration of IBDSim, the removal rate μ_i, and thus the number of bacteria entering the cecum and colon increases with the level of epithelial damage but the fraction of $\mu_i X_i$ that enter the tissue compartments remains constant. This parameter was calibrated using the dynamics of the number of epithelial cells from the previous iteration of the cecum compartment. Under the previous

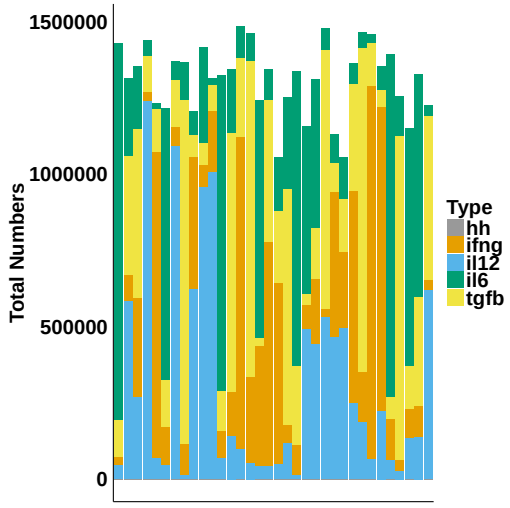

(a) No *Hh*

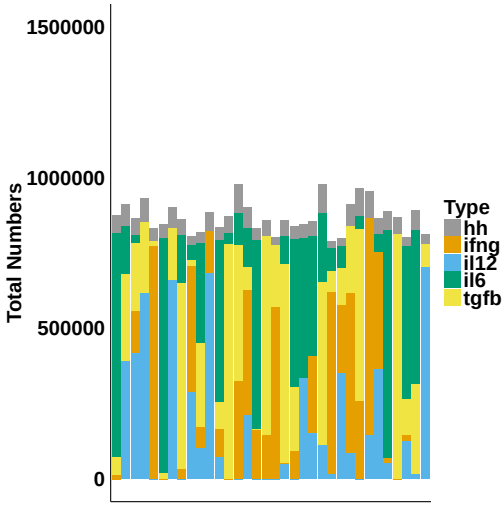

(b) *Hh* inhibitits other bacterial species

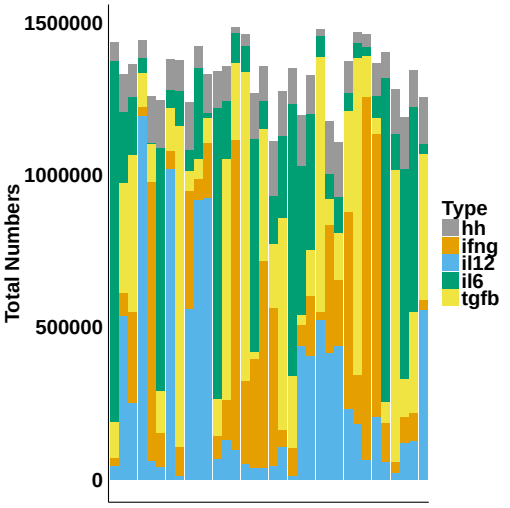

(c) No competition between *Hh* and other species

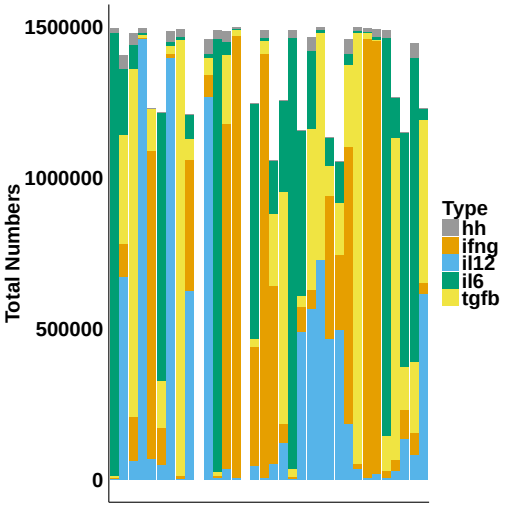

(d) *Hh* promotes other bacterial species

Figure 4.5: Total numbers of *Hh*-, IFN-γ-, IL12-, IL6- and TGF-β inducing bacteria iin each of the 34 models that were selected as suitable candidates for microbial compositions *in silico*. Counts are shown at steady state levels using the model described in Equation (4.1) in the absence of *Hh* (a), or under different hypotheses of how *Hh* interacts with the rest of the bacterial species (b-d). (b) represents inhibition of all species, (c) represents no interaction with any other species, and (d) represents promotion of all other species

representation, in an uninfected state, bacteria entered the tissue at a rate of 1 bacterium every 1.7 minutes. This equates to approximately 0.588 bacteria per minute. Taking the mean value of $\sum_i \mu_i \times \sum_i X_i$ reveals that on average, 21656 bacteria are removed per minute in the ODE model, thus the proportion of removed bacteria that enters the cecum or colon from the cecal and colonic lumen can be estimated to be 2.7×10^{-5}. At each

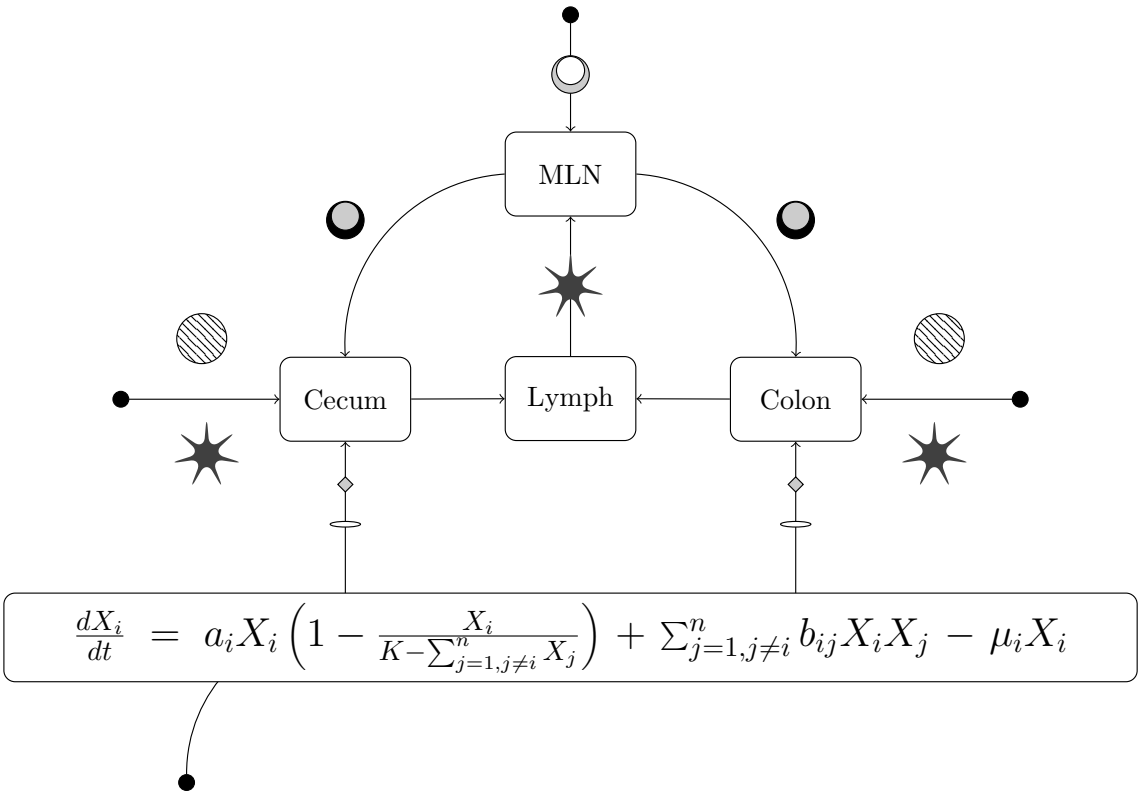

Figure 4.6: Integration of commensal bacteria model with IBDSim. Legend: ◯: Naive T cells , ●: Activated T cells, ✸: DCs, ▨: Macrophages, ◇: Commensal Bacteria, ⬭: *Hh*.

simulated time step the rate of bacteria switching compartments in the ABM are updated according to the numbers of bacteria estimated from the results of simulating the SBML model and the death rate of *Hh* in the SBML model is modified in accordance with the ABM. The death rate of *Hh* is calculated using the following equation, calibrated to match the switching probability defined in IBDSim (Equation (4.2), Figure 4.7).

$$\mu_{hh} = 0.0017 + 0.0000039 \times E_p \tag{4.2}$$

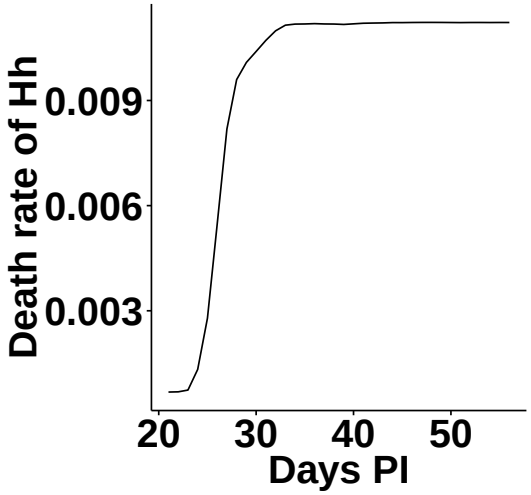

Figure 4.7: Predicted death rate of *Hh* at different time points post *Hh* infection. Values of parameter μ_{Hh} were calculated using equation (4.2) for the average value of E_p (the number of secreting epithelial cells) in the original version of IBDSim to predict what the death rate might look like in the new iteration of IBDSim.

4.1.2 Decoupling of T-cell Polarisation Pathways

The implementation of new cytokines meant that the T-cell polarisation model had to be updated to take into consideration all 4 types of cytokine included in the new iteration of IBDSim. Thus the addition of a Treg like T-cell phenotype, defined by the expression of the transcription factor forkhead-box protein 3 (Foxp3) was necessary to adequately represent the response of a single cell to any well mixed cytokine millieu. A Treg phenotype arises in response to TGF-β in the absence of IL6, and secretes only TGF-β. This is because IBDSim is calibrated to data from IL10 KO mice, so no IL10 can be produced. Adding an additional pathway to the model described in Section 2.3.4, required the model to be recalibrated, using additional biological data relating to the ROR-γt-Foxp3 and T-bet-Foxp3 interactions. The original equations (Section 2.3.4.3) also needed to be modified so that the response to C_1 and C_{17} can be decoupled into a response to IFN-γ and IL12, or TGF-β and IL6, respectively (Figure 4.8). As in the previous version of the polarisation model, cytokine secretion is separated into internal mRNA production and external protein secretion using the following equations. The new model becomes a system of 14 ODEs (Appendix C). The dynamics between transcription factors in the model can be understood as follows;

The rate of change in T-bet, ROR-γt or Foxp3

$$\frac{dTbet}{dt} \qquad \frac{dRORgt}{dt} \qquad \frac{dFOXp3}{dt}$$

The rate of increase in T-bet, ROR-γt or Foxp3 expression through external stimulation

$$\left(\frac{s_{t_{il12}} \cdot eIL12}{(e_{t_{il12}} + eIL12)} + \frac{s_{t_{ifng}} \cdot eIFNg}{\left(e_{t_{ifng}} + eIFNg\right)}\right) \cdot \frac{1}{\left(1 + \frac{ROR_{\gamma t}}{g_{tr}}\right) \cdot \left(1 + \frac{Foxp3}{g_{tf}}\right)}$$

$$\left(\frac{s_{r_{il6,tgfb}} \cdot eIL6 \cdot eTGFb}{(e_{r_{il6}} + eTGFb) \cdot \left(e_{r_{tgfb}} + eTGFb\right)} + \frac{s_{r_{il21}} \cdot eIL21}{(e_{r_{il21}} + eIL21)}\right) \cdot \frac{1}{\left(1 + \frac{Tbet}{g_{rt}}\right) \cdot \left(1 + \frac{Foxp3}{g_{rf}}\right)}$$

$$\left(\frac{s_{f_{tgfb}} \cdot eTGFb}{\left(e_{r_{tgfb}} + eTGFb\right)} \cdot \frac{1}{\left(1 + \frac{Tbet}{g_{ft}}\right) \cdot \left(1 + \frac{ROR-\gamma t}{g_{fr}}\right)}\right)$$

The rate of increase of T-bet,ROR-γt, Foxp3 through self stimulation

$$\left(\frac{a_t \cdot Tbet^n}{(k_t^n + Tbet^n)} \cdot \frac{1}{\left(1 + \frac{ROR_{\gamma t}}{g_{tr}}\right) \cdot \left(1 + \frac{Foxp3}{g_{tf}}\right)}\right)$$

$$\left(\frac{a_r \cdot ROR_{\gamma t}^n}{\left(k_r^n + ROR_{\gamma_t}^n\right)} \cdot \frac{1}{\left(1 + \frac{Tbet}{g_{rt}}\right) \cdot \left(1 + \frac{Foxp3}{g_{rf}}\right)}\right)$$

$$\left(\frac{a_f \cdot Foxp3^n}{\left(k_f^n + Foxp3^n\right)} \cdot \frac{1}{\left(1 + \frac{Tbet}{g_{ft}}\right) \cdot \left(1 + \frac{ROR_{\gamma t}}{g_{fr}}\right)}\right)$$

The rate of baseline transcription or T-bet, ROR-γt and Foxp3

$$\beta_t \qquad \beta_r \qquad \beta_f$$

The rate of removal of T-bet or ROR-γt through natural decay or degradation

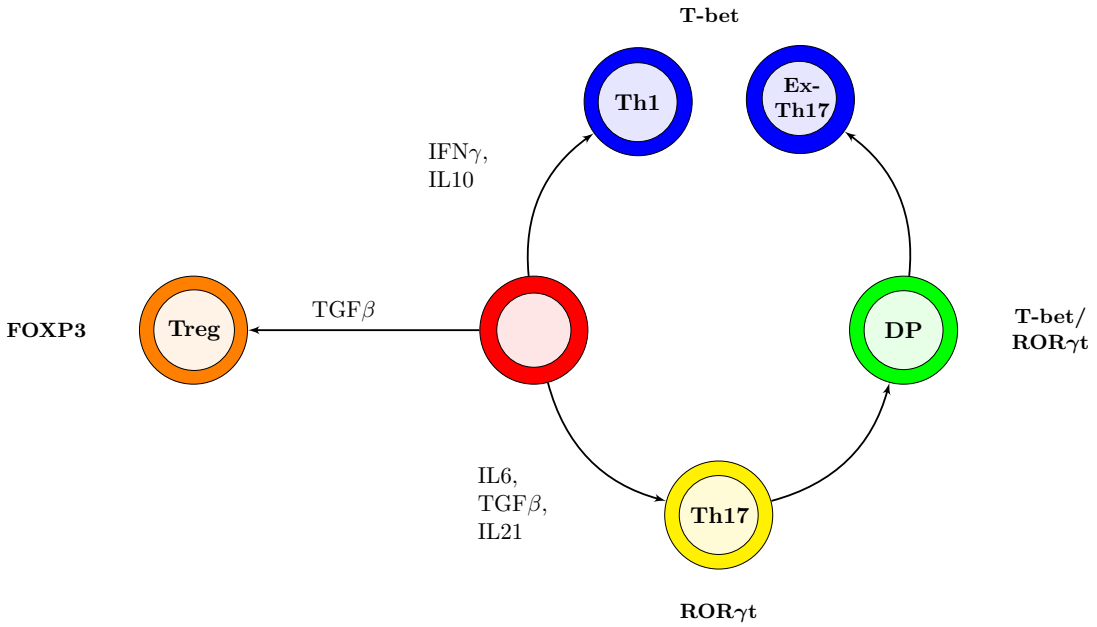

Figure 4.8: T cell polarisations in the updated model. The cytokines and transcription factors are modelled by the equations in Appendix C.

$$\mu_t Tbet \qquad \mu_r ROR_{\gamma t} \qquad \mu_f Foxp3$$

where a_i is the autostimulation rate for transcription factor i, β_i is the basal transcription rate for transcription factor i, $e_i j$ is the inhibition constant for stimulation of transcription factor i by cytokine j, s_{ij} is the cytokine j-induced stimulation of transcription factor i, $g_i j$ is the level of inhibition of transcription factor i by opposing transcription factor j, μ_i is the decay rate for transcription factor i, n is the hill-coefficinet, k_i is the inhibition constant for transcription factor i.

4.1.3 Alterations to DCs

The DCs in the model have to be modified to separate out secretions of TGF-β and IL6 in line with the new bacteria model. To do this, the non-linear model described in Section 2.3.4 was recalibrated to match biological data from (Kranzer et al., 2004). The equation modelling secretion of IL12 is the same as in IBDSim but there are now additional modifiers for IFN-γ, TGF-β, and IL6.

There is evidence that DCs secrete 1.5 times as much TGF-β as they do IL12 and the concentration of IL6 should be similar to the concentration of IL12 at 24hrs (Abdi

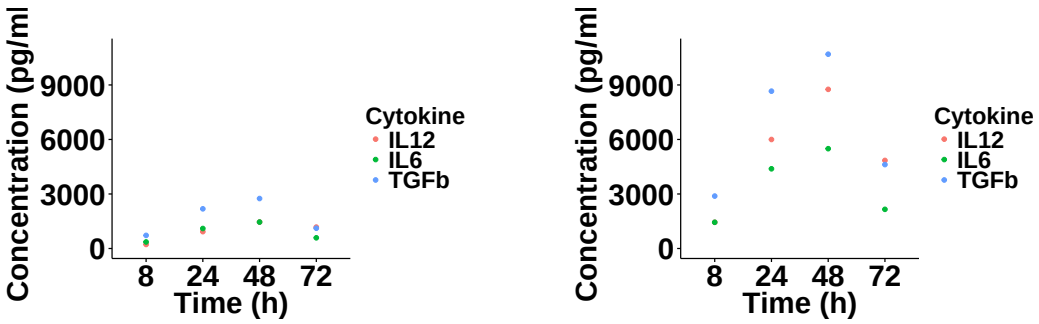

(a) 4 Bacteria **(b)** 16 bacteria

Figure 4.9: Concentration of cytokines secreted by 100 simulated DCs *in silico*. Concentrations are shown using the model modified version of the model described in Section 2.3.4. Data is shown for low (a) and high (b) levels of stimulation and cell counts are the equivalent of 5×10^5 *in vivo*.

et al., 2012; Kranzer et al., 2004) thus the modeifier for TGF-β in the model defined in Chapter 2 was calibrated to produce such a result (Figure 4.9).

4.2 Exploring the Effects of Different Microbiota on *Hh*-Induced Colitis

This section discusses the experiments that were performed to explore the effect of altering the microbiota on system behaviour.

4.2.1 Experimental Procedure

As described in Section 2.7, each compartment in the simulation starts in an empty state and simulations start from day -20, allowing the compartments time to reach an uninfected steady state by day 0. To integrate the SBML models describing the microbiota that were developed in this chapter into IBDSim, an SBML-model simulator was added to the cecal and colonic lumen compartments. Details are given in Section 2.10.3. The SBML model was allowed to run for 1 minute, the result was stored and then the numbers of each type of bacteria (IL12-, IFN-γ-, IL6-, TGF-β-, inducing and *Hh*) in the ABM were updated. Following the introduction of *Hh* to the cecal and colonic lumen, the death rate of *Hh* was modified in the file using the number of secreting epithelial cells as defined in Equation (4.2), and both the SBML model and the ABM were stepped for 1 more minute.

This process was repeated at every timestep throughout the simulation, with tuneable resolution applied to modify the computational burden where necessary (Section 1.9) The ABM was simulated 10 times with each of the 34 models selected in section 4.0.1, and an average result under each unique SBML model were generated, both in the absence and presence of *Hh* from the simulated day 0, i.e. the day of *Hh*-infection. Analyses were performed on the results of these simulations to try and identify groups of parameters that were influential in determining the susceptibility to, or severity of intestinal inflammation, in the absence or presence of *Hh*.

4.2.2 Alteration of the Microbiota Can Cause Intestinal Inflammation in the Absence of *Hh*

Running the updated version of IBDSim with different initial microbial compositions results in differences in the numbers of cells in MLN as well as in the cecum and colon (Figure 4.10). The level of inflammation in each group can be estimated from the cell counts and cytokine levels that emerge from simulations with each composition of microbiota. Inflammation is classified as "low", meaning that the cell counts are slightly higher than expected in an uninfected case, "moderate" meaning that the cell counts are higher than in those models classified as "low", and "medium" that is the highest level of inflammation observed in an uninfected mouse, but the cell counts are not as high as in an infected mouse. From Figure 4.10 it can be determined that the group highlighted in blue corresponds to a single parameter set that resulted in a medium level of inflammation, the group highlighted in green corresponds of two parameter sets that resulted in a moderate level of inflammation, the group highlighted in red corresponds to six sets with a low level of inflammation and the 25 remaining sets that have similar cell counts to those observed under the previous iteration of IBDSim in the absence of *Hh*, displayed in black, are not considered to result in inflammation (Figure 4.10). To try and identify distinct inflammatory phenotypes from the results, a hierarchical cluster analysis was performed, using average linkage, on the mean results of the 10 simulations with each parameter set. The analysis was performed on the mean value over time for the measures collected. The mean is an appropriate measure to take for clustering uninfected data because each set of runs has reached a stable level by day 0. Figure 4.13a shows that there are four distinct groups

of unequal sizes but there is no obvious link between the initial microbial compositions in each group. Comparison with the groups that emerged when the compositions themselves were clustered indicates that groups of similar microbial compositions cannot be used to predict the level of inflammation that will arise in the simulations (Figure 4.13b).

The microbial compositions that resulted in inflammation (blue, red, green) saw a dramatic increase in the the numbers of T cells, inflammatory macrophages and DCs compared to the microbial compositions that did not induce inflammation (black) in both the cecum (Figure 4.11a),a and the colon (Figure 4.12a). Further, the cecum and colon of the non-inflamed parameter sets were mainly populated by regulatory macrophages suggesting a lack of IFN-γ to drive macrophage polarisation into an inflammatory state. This suggestion was confirmed by Figures 4.11b,4.12b that show lower levels of IFN-γ in the non-inflamed sets than in those that develop inflammation. Many of the compositions that did not result in inflammation in an uninfected state, those shown in black in Figure 4.13, have a high proportion of IFN-γ-inducing bacteria, and conversely some of the inflamed subset have relatively low proportions of IFN-γ-inducing bacteria. Thus it is expected that in simulations that correspond to inflamed sets there must be a high number of IFN-γ-secreting cells. T cells in IBDSim can be classified as DN if they do not have high levels of mRNA of any cytokine, Th1 if they have high levels of IFN-γ mRNA, Th17 if they have high levels of IL17 mRNA, or DP if they express high levels of both IFN-γ and IL17. The relative numbers of T cells of each type were calculated using the level of iIFN-γ and iIL17 inside the cell, according to the equations that represent T-cell polarisation (Appendix C). In the absence of *Hh*, all of the microbial compositions that resulted in inflammation had a large number of Th1 cells present in the cecum, and the highest level of inflammation was correlated with a large number of DP (Figure 4.22a).

As it appeared that no clear link could be established between the initial microbial composition and the level of inflammation in the absence of *Hh* (Figure 4.13), a sensitivity analysis was performed to identify any significant correlations between all parameters in the ODE model describing the competition between the species and the output measures that arise from simulations using each parameter set. The PRCCs obtained through sensitivity analysis are shown in Figure 4.15. The significant PRCCs are defined as those with a p-value of less than 0.05 and the key parameters are listed in Appendix F. Using

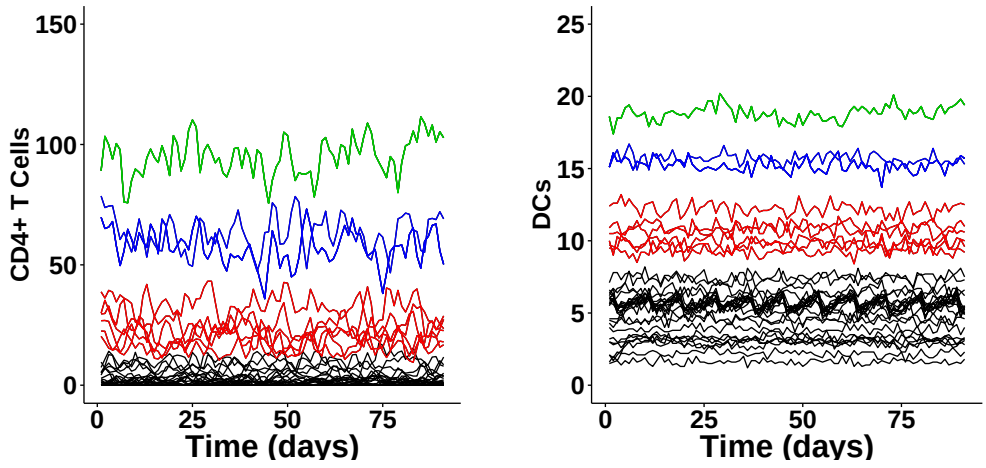

(a) T cells

(b) DCs

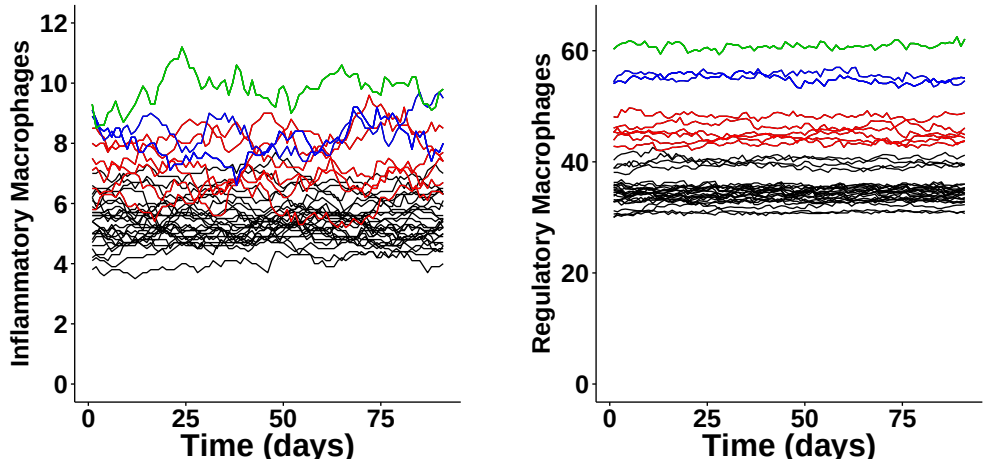

(c) Inflammatory Macrophages

(d) Regulatory Macrophages

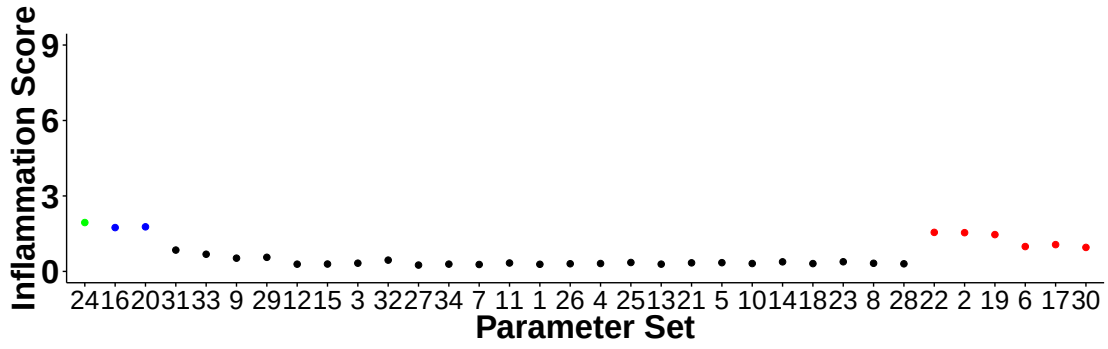

(e) Inflammation Score

Figure 4.10: Numbers of cells and the level of inflammation in the cecum differ depending on the initial composition of microbiota in the absence of *Hh*. The average number of (a) T cells, (b) DCs, (c) inflammatory, and (d) regulatory macrophages, as well as the inflammation score (e) in the cecum with different compositions of microbiota.

these correlations, the role of certain cells and cytokines in contributing to intestinal inflammation can be understood.

IFN-γ is implicated in playing a role in inducing intestinal inflammation in the absence of *Hh*

Several of the PRCCs generated from the sensitivity analysis that was performed, indirectly suggest that IFN-γ could be an important cytokine in causing intestinal inflammation in the absence of *Hh*. The positive correlation of $b_{ifng,il12}$ and negative correlation of $b_{il12,ifng}$ with the number of T cells in the cecum, colon and MLN means that the more IL12-inducing bacteria promote IFN-γ-inducing bacteria, and the more IFN-γ-inducing bacteria inhibit IL12-inducing bacteria, the higher the number of T cells in the system is likely to be (Figure 4.15,Appendix F). This suggests that overall, IFN-γ is more important in causing inflammation than IL12. A possible reason for this that IL12 in the simulation is only directly responsible for the initial polarisation of T cells, whereas IFN-γ is responsible for polarising inflammatory macrophages and increasing cytokine secretion by macrophages. This means that although increasing $b_{ifng,il12}$, or decreasing $b_{il12,ifng}$ did not lead to a significant increase in the number of inflammatory macrophages, it is likely that the inflammatory macrophages that were present secreted higher levels of cytokines. This assertion is supported at least in part by the significant increase in IL12, TGF-β and IL6 in the tissue in the colon, and the increase IL17 and IL21 that are only produced in the system by polarised T cells (Figure 4.15,Appendix F). The results presented here suggest that the increased number of Th1 and DP cells observed in Figure 4.14 are driving inflammation in the absence of *Hh*.

Inflammation in an uninfected state correlated with factors that drive the development of Th17 cells

The PRCCs generated from the sensitivity analysis also indirectly suggest that Th17 cells could be important in causing intestinal inflammation in the absence of *Hh*. The positive correlation between $b_{tgfb,ifng}$ and the number of T cells in the cecum, colon and MLN means that the more TGF-β is promoted by IFN-γ, the more T cells there are in the tissue. It is interesting that increasing the number of bacteria that induce TGF-

β, typically thought to be an anti-inflammatory cytokine, increases the concentration of inflammatory cytokines. However, as the models that were considered to be potential microbial compositions contain all four species of cytokine-inducing bacteria, IL6 will be present in all of them, and TGF-β is required to induce Th17 cells in the presence of IL6. Therefore, it would be expected that in the cases where the concentration of TGF-β are high, the number of Th17 cells will also increase.

There is also a positive correlation between $il6$, that is the number of IL6-inducing bacteria that are present in the lumen at the start of infection (X_{il6}), and the number of T cells and regulatory macrophages in the tissue. IL6 has a similar role in the system to IL12, but acts to induce Th17 cells instead of Th1. This means that unlike the previous important correlations that can be possibly be explained by the duel functionality of IFN-γ in the model, IL6 only directly affects the population of Th17 cells. However, Th17 cells can switch phenotypes during inflammation to begin secreting IFN-γ, meaning that although there is no significant correlation between $il6$ and the concentration of IFN-γ in the tissue it is likely that in the subsets where $il6$ is higher, IFN-γ will be increased just not statistically significantly. This supports the idea that phenotype switching of Th17 cells is important in inducing more severe inflammation and correlates with the trend observed in Figure 4.14.

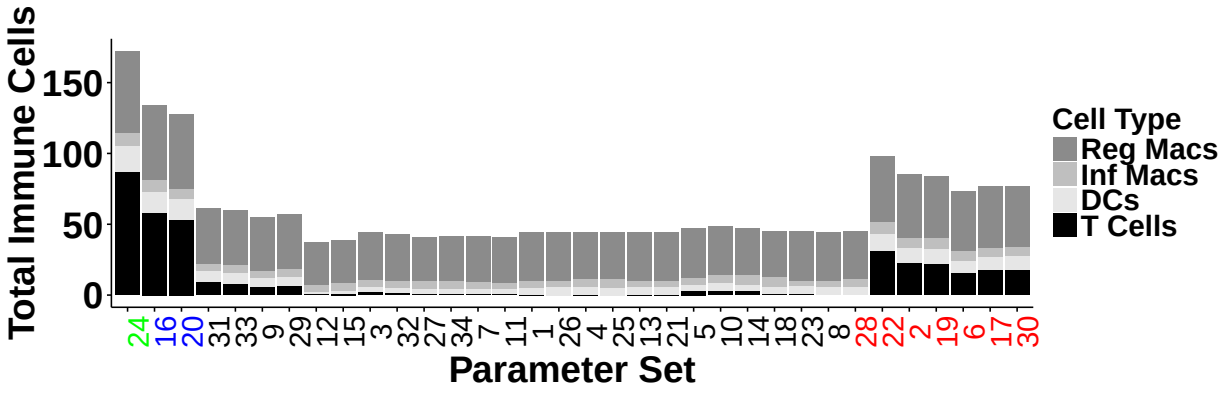

(a)

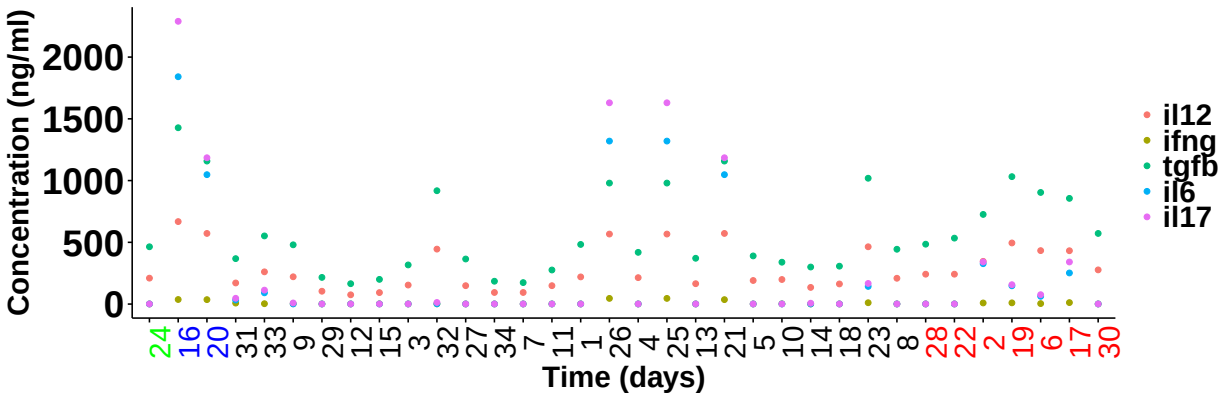

(b)

Figure 4.11: Specific compositions of microbiota differentially effect the cell numbers and cytokine levels in the cecum. Counts of immune cells (a) and concentration of cytokines (b) for each initial microbial composition in the cecum in the absence of *Hh*. Data represented is the mean of 10 simulations for each of the 34 initial microbial compositions in the absence of *Hh*. Parameter sets are coloured to correspond to the groups identified in the cluster analysis presented in Section 4.2.2.

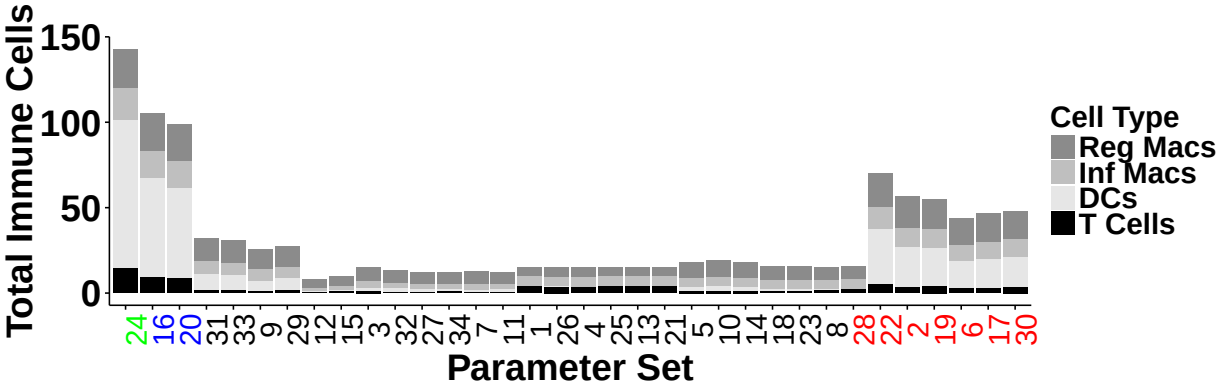

(a)

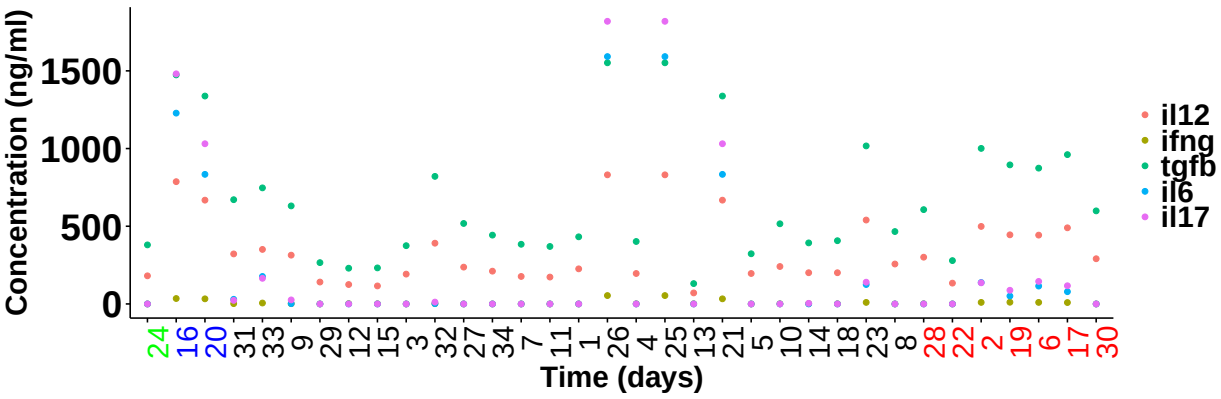

(b)

Figure 4.12: Specific compositions of microbiota differentially effect the cell numbers and cytokine levels in the colon. Counts of immune cells (a) and concentration of cytokines (b) for each initial microbial composition in the cecum in the absence of *Hh*. Data represented is the mean of 10 simulations for each of the 34 initial microbial compositions in the absence of *Hh*. Parameter sets are coloured to correspond to the groups identified in the cluster analysis presented in Section 4.2.2.

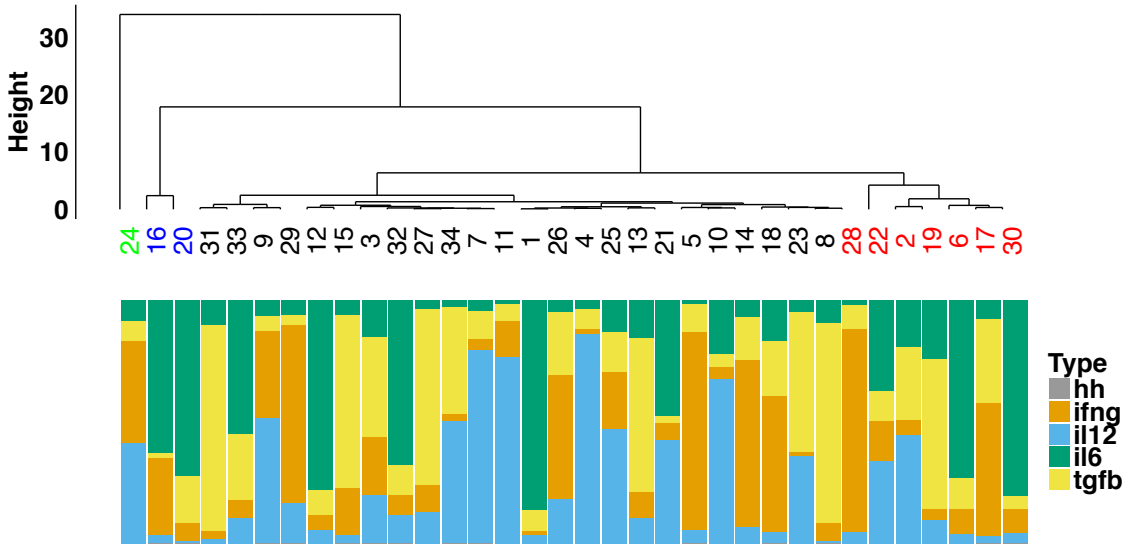

(a)

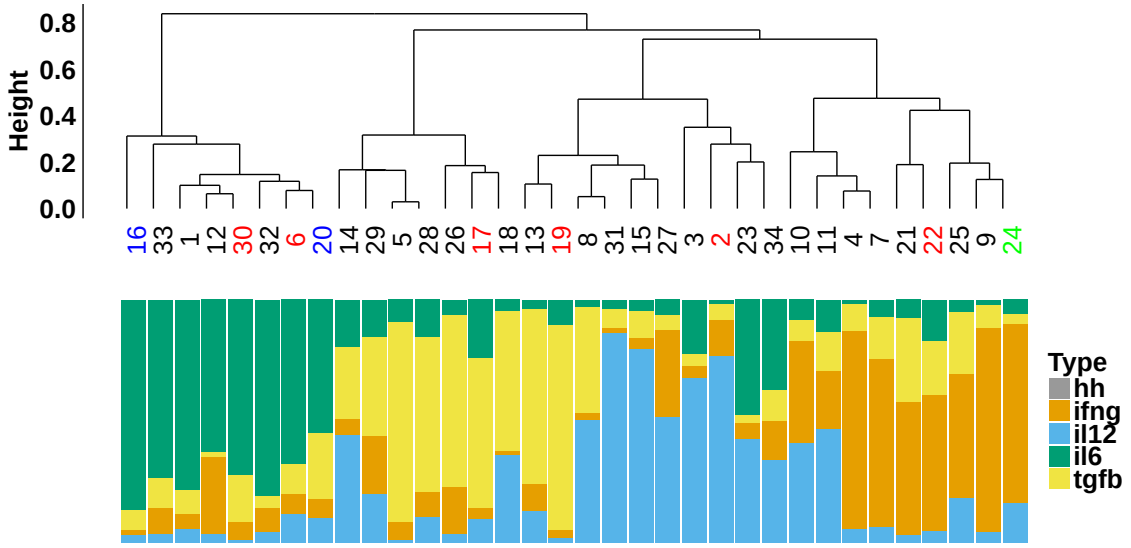

(b)

Figure 4.13: Cluster analysis that demonstrates how specific compositions of microbiota result in differences in the mean numbers of cells and levels of cytokines in the cecum and colon. (a) Dendrogram clustering the mean results under the 34 initial compositions generated in Section 4.0.1. The parameter sets in each of the four distinct clusters are highlighted in different colours. (b) Dendrogram of the same results as in (a) clustered by the initial microbial compositions. Parameter set colours are representative of the cluster in (a) that the results belonged to. Data represented is the mean of 10 simulations for each of the 34 initial microbial compositions.

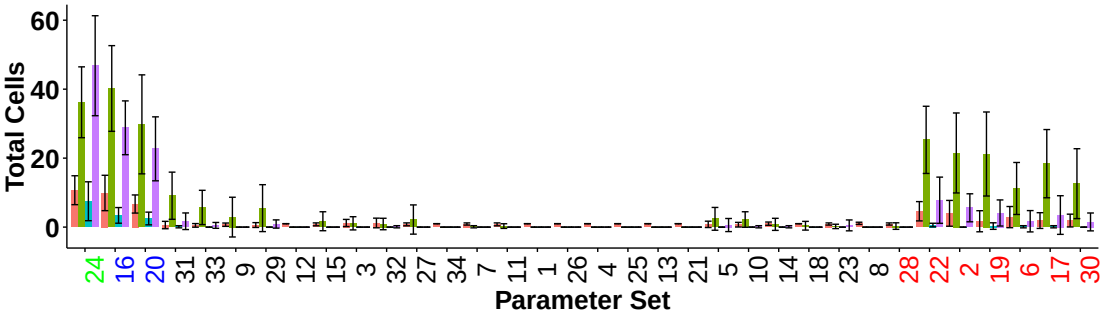

Figure 4.14: Inflammation in the absence of *Hh* is predominantly driven by Th1 cells. *In silico* T cells in the cecum at day 0 were categorised as either double negative (DN, coral), Th1 (green), Th17 (blue), or double positive (DP))(purple) based on levels of IFN-γ or IL17 mRNA inside the cell for simulations of each initial microbial composition in the cecum in the absence of *Hh*. Parameter set colours are representative of the cluster in (Figure 4.13a) that the results belonged to. Data represents the mean $\pm$ standard deviation of 10 simulations for each of the 34 initial microbial compositions in the absense of *Hh*.

.

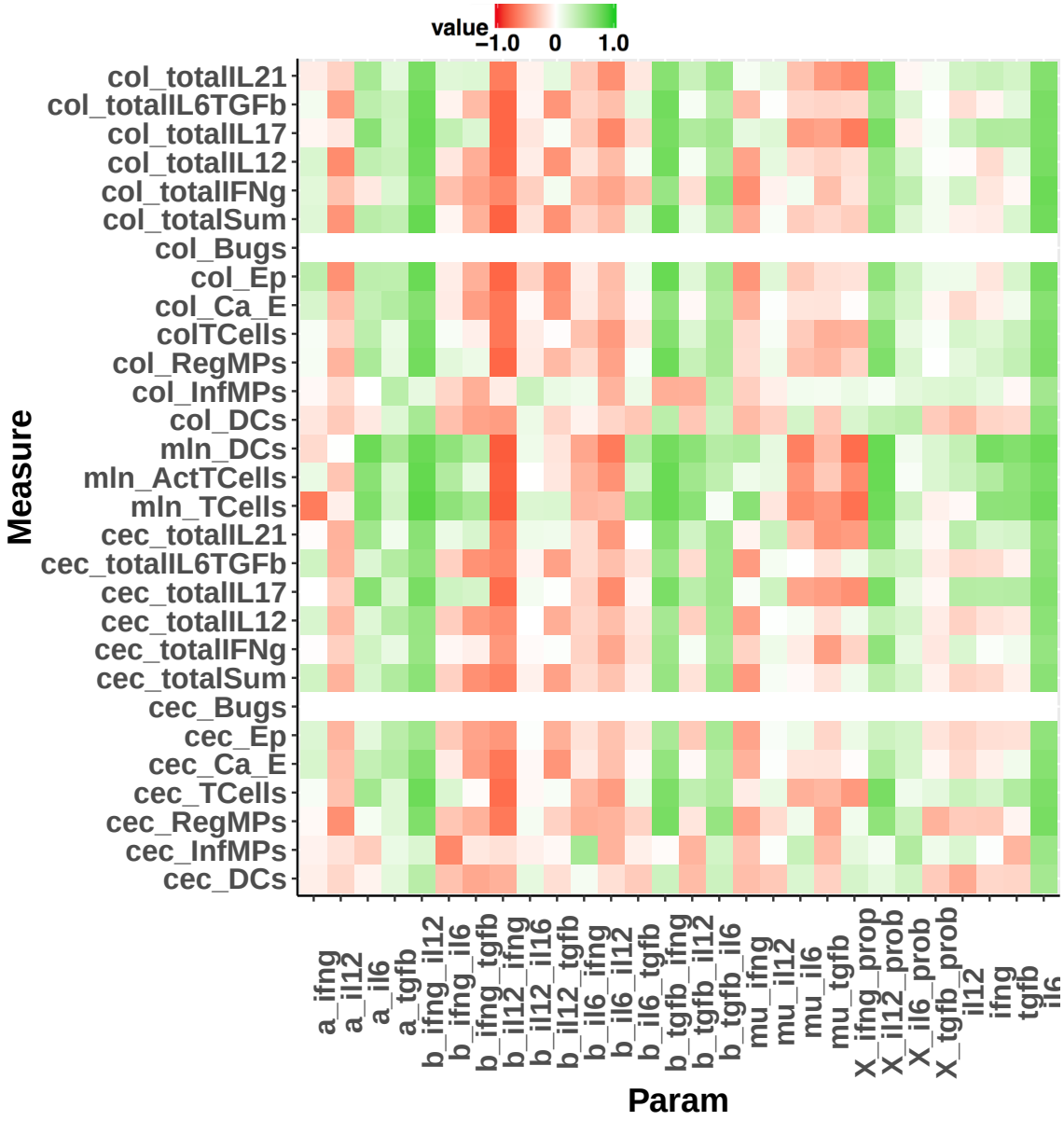

Figure 4.15: PRCCs between the ODE parameters and the corresponding simulated measures. Correlations shown are between the average results of 10 simulated runs with each parameter set with strong negative correlation indicated in red and strong positive correlation in green with white representing no correlation. Definitions of parameters on the X and measures on the Y axis are given in Appendix E.

4.2.3 Alteration of the Microbiota Affects Disease Outcome in *Hh*-Induced Intestinal Inflammation

Once the level of inflammation in the absence of *Hh* had been explored, the model was used to explore whether the differences in microbial composition would result in differences in disease phenotype following infection with *Hh*. Looking at the numbers of cells over all potential microbial compositions gave an idea of the disease phenotypes that can emerge following infection with *Hh* (Figure 4.16). Three distinct patterns could be identified by looking at how the number of cells change over time. One group had no change in cell numbers throughout infection and is highlighted in red (Figure 4.16, left panels). There are two subsets of this group in terms of *Hh*, the first is a case where *Hh* failed to colonise, and the second is a case where *Hh* did colonise but never reached sufficiently high levels in the population of microbiota to cause inflammation to occur. The second group that could be identified from looking at the how the numbers of cells change over time corresponded to non-resolving disease phenotype and is highlighted in green (Figure 4.16, middle panels). In this group, cell numbers showed an initial increase in response to *Hh* that peaked early on in infection and remained at a higher stable level throughout the remainder of the simulation. The *Hh* load in this group either peaked early in infection and fell to lower levels where it remains throughout the rest of the simulation, or reached its peak and then remained there for the rest of the simulation. The final group, highlighted in blue, appeared to be a *Hh*-driven relapsing remitting phenotype, highlighted in blue (Figure 4.16, right panels). In this group, both cell numbers and *Hh* burdens oscillate over time and there was a huge amount of variation in the change in the number of cells over time.

Performing a cluster analysis on all of the simulated data would determine if there was a relationship between the initial microbial compositions and the level of inflammation that developed following infection with *Hh*. In the absence of *Hh*, a cluster analysis could be performed on the mean value of the cell numbers and cytokine levels in the tissue as they had reached a steady state prior to infection. However, following infection with *Hh*, the cell numbers changed significantly over time (Figure 4.16), thus the mean is not an appropriate representation of model behaviour in this case. Instead, cluster analysis

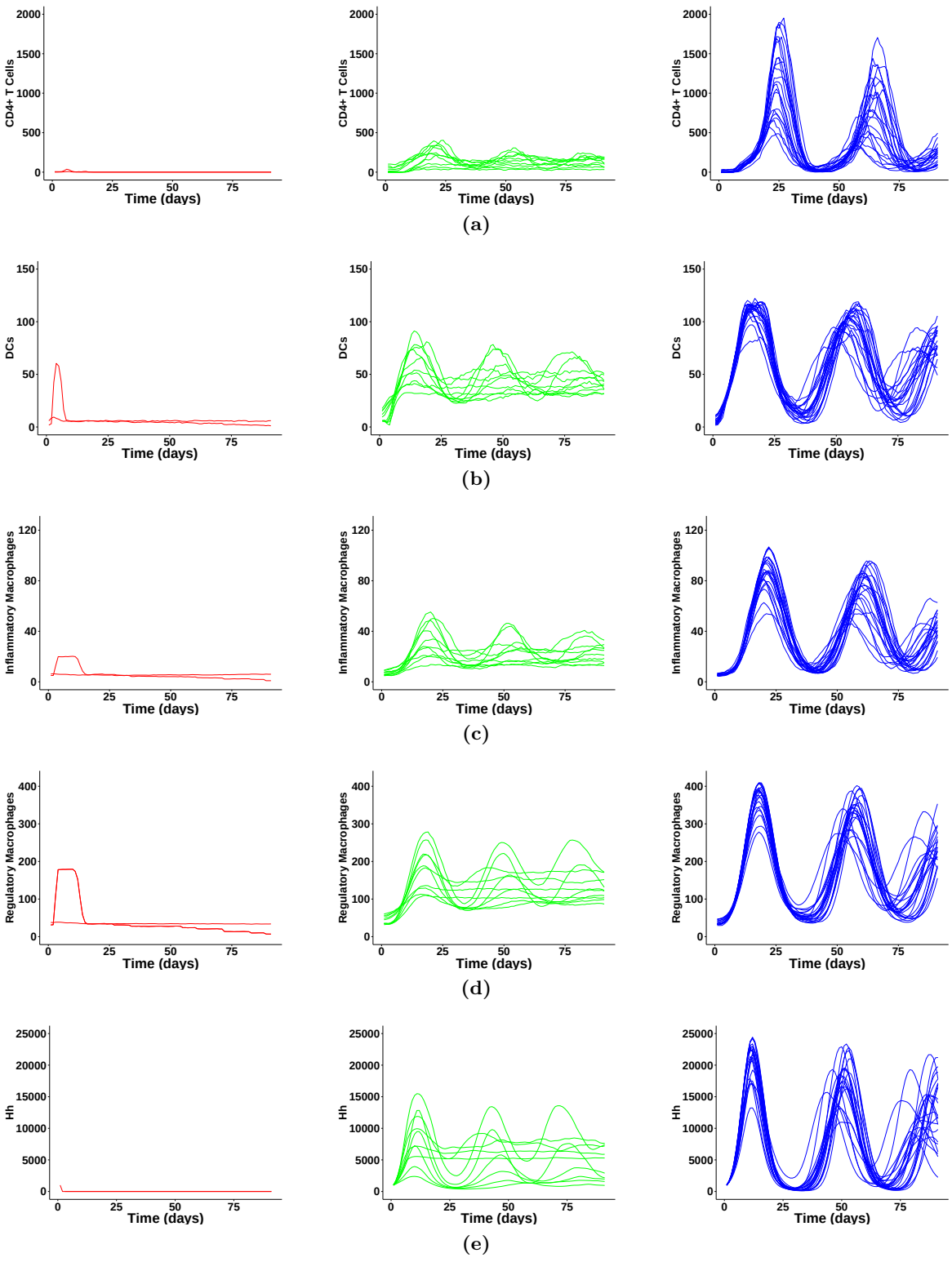

Figure 4.16: Phenotypes of inflammation observed following infection with *Hh*. Groups were selected by looking at numbers of (a) T cells, (b) DCs, (c) inflammatory macrophages, and (d) regulatory macrophages in the cecum. The dynamics of *Hh* bacteria in the cecal lumen are also shown for each group (e). Colours represent non-inflamed results (red), non-resolving inflammation (green), and relapsing remitting inflammation (blue).

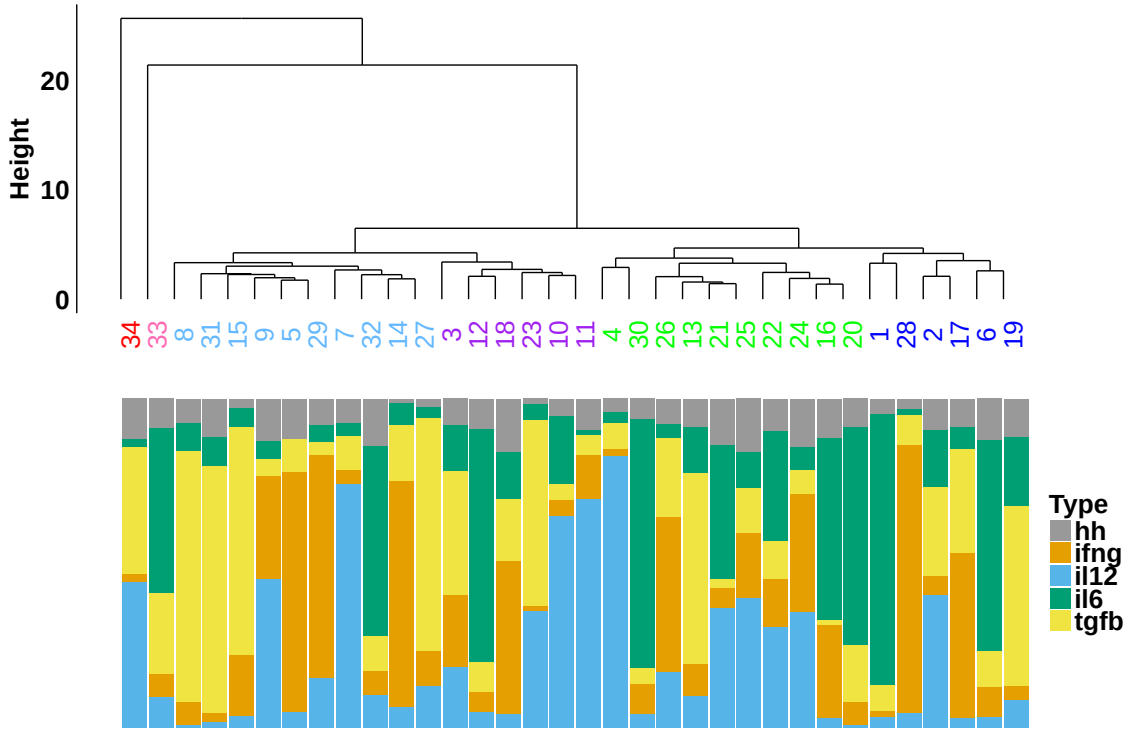

Figure 4.17: Cluster analysis that demonstrates how specific compositions of microbiota result in differences in the time course of the numbers of cells and levels of cytokines in the cecum and colon. (a) Dendrogram using dynamic time warping to cluster the time courses of results under the 34 initial compositions generated in Section 4.0.1. The parameter sets in each of the four distinct clusters are highlighted in different colours.

was performed, using the technique of dynamic time warping to generate a distance metric (Section 2.10.2), to compare the shape of simulations. Using cluster analysis on the distances obtained from using dynamic time warping on the data resulted in six clusters being identified (Figure 4.17). Each cluster corresponded to a group of microbial compositions that when simulated within IBDSim, resulted in each of the measures described in Section 2.5 following similar patterns over time. As discussed with the uninfected case in the previous section, the number of cells and cytokines could be used to determine what each of the groups identified by the dendrogram in Figure 4.17 represented.

The first two clusters (Figure 4.17) contain only one parameter set each and are shown in red and pink. Further exploration of the parameter sets in these two clusters revealed that they represented the two subsets identified in Figure 4.16 that do not develop inflammation following infection with *Hh*.

The cluster highlighted in green (Figure 4.17) represents models that exhibited dif-

ferent levels of non-relapsing inflammation, and corresponds to the subsets identified in Figure 4.16 that do not develop inflammation. The simulations in this cluster had a higher concentration of cytokines early in inflammation than the other clusters in both the cecum and colon but by 21 days post infection, the concentration of cytokines in the green cluster was much lower than the concentration in the the light blue or purple clusters. The green cluster also has the highest population of polarised T cells at days 0 and 7, mostly displaying a Th1 and DP phenotype (Figures 4.22a,4.22b).

The remaining three clusters (Figure 4.17) represent relapsing-remitting inflammation, and all correspond to the group highlighted in blue in Figure 4.16. This means that cluster analysis has led to the identification of three subsets within the relapsing remitting group in Figure 4.16 that are phenotypically distinct from each other. The cluster that is highlighted in dark blue (Figure 4.17, far right hand side) represents less severe relapsing-remitting inflammation than the two groups highlighted in light blue and purple. Looking at the changes in the cells and cytokines in the cecum (Sections 4.2.3,4.2.3) and colon (Sections 4.2.3,4.2.3) during inflammation can help to determine the differences between the cases of relapsing remitting inflammation. The inflammation in the cluster highlighted in dark blue differs from the other clusters of relapsing-remitting inflammation in a number of ways. Firstly, the number of cells and concentrations of cytokines at day 0 are higher under the microbial compositions in the dark blue cluster than in the other two clusters that represent relapsing-remitting inflammation in both the cecum (Figures 4.18a,4.19a) and colon (Figures 4.20a,4.21a). This is also true at day 45, during the resolution phase (Figures 4.18e,4.19e, Figures 4.20e,4.21e). Secondly, the number of cells and levels of cytokines at peak inflammation, at day 21, are lower in the simulations that are in the dark blue cluster than in the light blue or purple clusters in both the cecum (Figure 4.18d), and the colon (Figure 4.19d). Specifically, simulations that fall into the dark blue cluster have less inflammatory macrophages when compared to those in the light blue and purple clusters, suggesting a lack of IFN-γ. This is not surprising since most of the parameter sets in the dark blue cluster are the same as those that induced moderate inflammation in the absence of *Hh* in the previous section, where the same trend was identified.

The light blue and purple clusters are more similar to each other than to the dark blue cluster in terms of total cell numbers, especially up to day 21 post infection (Fig-

ures 4.20d,4.21d). However, by day 45 during the remission phase (Figures 4.18e,4.19e, Figures 4.20e,4.21e) and at day 91 during the relapse (Figures 4.18f,4.19f, Figures 4.20f,4.21f), the total cell numbers are higher in the cluster highlighted in light blue than those highlighted in purple. Further, at later time points in infection, the number of regulatory macrophages is significantly higher in the cluster highlighted in light blue than those highlighted in purple, suggesting a much lower level of IFN-γ in the light blue cluster. However there is no evidence that the microbial compositions that were used in simulations that were clustered into the light blue cluster have a lower number of IFN-γ-inducing bacteria . Exploring the T-cell populations did not lead to any further insight into the cause of the increased population of regulatory macrophages in the light blue group (Section 4.2.3). Conversely, the number of regulatory macrophages is higher in the light blue group than in the purple one throughout inflammation (Section 4.2.3). This could be due to a slight increase in the number of cells that are double positive for both IFN-γ and IL17 in the dark blue group at days 21 and 45 (Section 4.2.3).

As with the uninfected case, the initial microbial compositions cannot be used to predict the kind of inflammation that will occur following *Hh* infection. Neither can the microbial compositions be used to identify the cause of the differences in the severity of inflammation (in terms of cell numbers and cytokine concentrations) between the clusters. Exploring the significant correlations at different time points post *Hh* infection can help to elucidate the important processes governing each phase of inflammation. Correlations were analysed at 7, 14, 21, 45, and 91 days post-*Hh* infection, however significant correlations were only found at days 7, 14, and 91 (Figure 4.23, Appendix F). At day 7, *Hh*-induced inflammation is in the development phase (Figure 4.18b,Figure 4.20b). Significant correlations at this time point give information into parameters that are responsible for how quickly or slowly inflammation develops. At day 14, cell numbers in *Hh*-induced non-relapsing inflammation have peaked and the number of cells in the two most severe group of relapsing-remitting phenotypes have reached a higher level (Figure 4.18c,Figure 4.20c). Significant correlations at this time point give information into parameters responsible for the severity of inflammation in the system. At day 91, *Hh*-induced relapsing remitting inflammation is in a remission phase, and is starting to relapse (Figure 4.18f,Figure 4.20f). Significant correlations at this time point give information into parameters responsible for

the resolving inflammation in the system.

IFN-γ is implicated in determining the onset of inflammation, as well as the severity

As in the uninfected case, the positive correlation of $b_{ifng,il12}$ and negative correlation of $b_{il12,ifng}$ with the number of T cells in the cecum, colon and MLN at day 7 means that the more IL12-inducing bacteria promotes IFN-γ-inducing bacteria, and the more IFN-γ-inducing bacteria inhibits IL12-inducing bacteria, the higher the number of T cells in the system is likely to be. Conversely, the number of *Hh* bacteria in the system is expected to be lower since it has a negative correlation with $b_{ifng,il12}$ and a positive correlation with $b_{il12,ifng}$. This suggests that overall, IFN-γ is more important than IL12 in causing an immune response earlier in inflammation that will quickly reduce the bacterial burden. The positive correlation with IL17 and IL21 is most likely to be a result of the increasing T cell numbers in the tissue caused by IFN-γ. In addition, parameter $b_{tgfb,ifng}$ is strongly positively correlated with an increase in the number of DCs and the concentration of IFN-γ, IL17, and IL21 in the cecum, an increase in the number of T cells and regulatory macrophages in the colon, and the number of activated cells in the MLN. This further demonstrates that IFN-γ plays an important role in T cell induced inflammation because IL17 and IL21 are only produced by T cells in the model.

At day 14, $b_{ifng,il12}$ and $b_{il12,ifng}$ are positively and negatively correlated with the number of T cells in the same way as at day 7. These parameters are also significantly correlated with the total concentration of activating cytokine C_{a_E}. This suggests that a non-significant increase in IFN-γ can lead to an increase in other cytokines that lead to a significant difference in the total amount. This is most likely due to the non-significant increases in IFN-γ stimulating macrophages to secrete a higher concentration cytokines and due to increasing the level of Th1-cell polarisation.

IL6 is implicated in determining both the onset of inflammation, and in increasing the severity of inflammation, but is not expected to play a key role in disease induction

At day 7, the proliferation rate of X_{il6} in the competition model, a_{il6}, is positively correlated with with the number of T cells and inflammatory and regulatory macrophages as well as the concentration of cytokines IL17 and IL21 in the cecum. In the colon, a_{il6} positively correlates with the number of secreting epithelial cells, and in the MLN, there is a positive correlation between a_{il6} and the numbers of both DCs and T cells (Figure 4.23, Appendix F). This means that the faster IL6-inducing bacteria proliferate, the more of these cells and cytokines emerge in the system by day 7. No significant correlations were identifies for the proliferation rates of other bacterial species indicating that the proliferation rate of IL6-inducing bacteria, but not the proliferation rate of any other bacterial populations, is partly responsible for controlling the onset of inflammation.

As IL6 is responsible for the development of Th17 cells, these result suggests that the presence of Th17 cells early in inflammation leads to an immune response that develops quicker than inflammation with a smaller number of these cells. This is evidenced by the fact that the models where inflammation reaches a stable level early in inflammation have a large number of cells that are double positive for IFN-γ and IL17 at 7 days post-infection (Figure 4.22c) that can only occur following the development of Th17 cells. In addition, at day 7 there is a negative correlation $b_{il6,il12}$ and the number of T cells in the cecum meaning that the more IL6 is inhibited by IL12, the less T cells and cytokines there are in the tissue. The reason for these trends occurring are similar to those observed in an uninfected state, and further confirms that IL6 is an important component in controlling the speed at which the immune response to *Hh* is mounted.

At day 14, a_{il6} was positively correlated with the number of T cells and inflammatory macrophages in the cecum as it was at day 7 Figure 4.23, Appendix F). At day 14, a_{il6} was also correlated with the number of secreting epithelial cells (E_p), as well as the concentrations of cytokines IFN-γ, IL12, IL17, TGF-β, and IL21, and the overall concentration of activating cytokine C_{a_E} (Figure 4.23, Appendix F). In the colon a_{il6} was positively correlated with the total number of T cells, inflammatory and regulatory macrophages

and epithelial cells, as well as the concentration of cytokines IL17 and IL21, and the total concentration of activating cytokine C_{a_E} Figure 4.23, Appendix F). This suggests that the proliferation rate of IL6-inducing bacteria is important in determining the severity of inflammation, and that it causes a large number of Th17 cells to occur. This is further evidenced by the number of Th17 and double positive cells in simulations that have resulted in a high level of inflammation infection with *Hh* (Figure 4.22c).

At day 91, a_{il6} is only significantly positively correlated with the number of DCs in the cecum and colon as well as with the number of activated T cells in the MLN. This suggests that a_{il6} is not as much of an important factor in causing a relapse in inflammation following resolution.

The positive correlation between $il6$, the number of IL6-inducing bacteria that are present in the lumen at the start of infection (X_{il6}), and the number of T cells in the tissue, and the negative correlation of this parameter with the number of DCs agrees with what was observed for a_{il6}. Interestingly at day 91, this parameter is negatively correlated with cell numbers and cytokine concentrations indicating that during relapsing phase, suggesting that a large level of IL6 later on in inflammation may be responsible for inducing resolution.

TGF-β plays a role in controlling the onset of inflammation, but not in determining the severity or inducing a relapse.

The positive correlation $b_{tgfb,ifng}$ and the number of T cells in the colon and MLN at day 7 means that the more TGF-β is promoted by IFN-γ, the more T cells and cytokines there are in these compartments Figure 4.23, Appendix F). As TGF-β is an anti-inflammatory cytokine, and does not contribute to epithelial cell wall damage, it is expected that this trend links strongly with an increase in the number of Th17 cells in the tissue. Thus, in the context of severe inflammation where there is a well mixed cytokine milieu, TGF-β actually serves as an inflammatory cytokine. This idea has also been suggested by Sanjabi et al. (2009). The parameter $b_{tgfb,ifng}$ does not significantly effect cell numbers in the cecum or colon at days 14, or 21 post infection.

4.2.4 Conclusion

Th17 cells are important in determining both the onset of inflammation, and in increasing the severity of inflammation, but do not play a key role in disease induction. This is demonstrated by the PRCCs listed above that show that both IL6 and TGF-β increase at days 7 and 14 post *Hh* infection when inflammation is being induced, but not at days 0 or 91 post *Hh* infection when inflammation is developing or relapsing. In fact, there is evidence that Th17 cells play a role in reducing inflammation at day 91 post infection, meaning that these cells could be responsible for inducing the remission of disease seen by Morrison et al. (2013). This idea correlates with data presented by Morrison et al. (2013) that shows that Th17 cells are increased (compared to Th1 cells) in resolving and resolved disease.

In addition, Th1 cells are also important in inducing inflammation and it has been shown that IFN-γ is important in the induction but not necessarily the maintenance of *Hh*-induced intestinal inflammation, and in particular the role of IFN-γ is more important than IL12.

4.2.5 Summary

Taken as a whole the results in this chapter demonstrate that an alteration of the microbiota alone is sufficient to produce different phenotypes of inflammation. This chapter also demonstrates the importance of both Th1 and Th17 cells in driving, maintaining, and resolving *Hh* intestinal inflammation.

The model of the commensal bacteria presented in this chapter is highly theoretical and although it captures total numbers of different groups of bacteria in the cecal and colonic lumen, in reality a spatial model similar to that used in the original representation of *Hh* in Chapter 2 would better represent the dynamics of an invading species of bacteria. Such a model would include several species of bacteria each with their own growth, death and competition parameters and currently there is insufficient data to support a model of this kind. Further, for a more complex model to be integrated into the system a better understanding of how each type of bacteria interacts with the immune system would be required.

The concept of grouping of bacteria by the cytokine responses it induces in innate immune cells as has been done in this work removes the requirement of knowing exactly how each species reacts with the environment but it is not known if in biology a single species of bacterium can induce more than one type of cytokine response from the innate cells. However, because the total number of bacteria in the cecal and colonic lumen are only estimates, it is possible that each bacterium contributes to a number of different groups. In an ABM of the bacteria in the lumen it would be possible to assign multiple cytokine-inducing types to each agent in the model resulting in a model that was much closer to biology but collecting the data behind the model would be extremely time consuming and involve several *in vitro* experiments to examine the response of polarised APCs to species of bacteria that had been isolated from the gut of IL10KO mice.

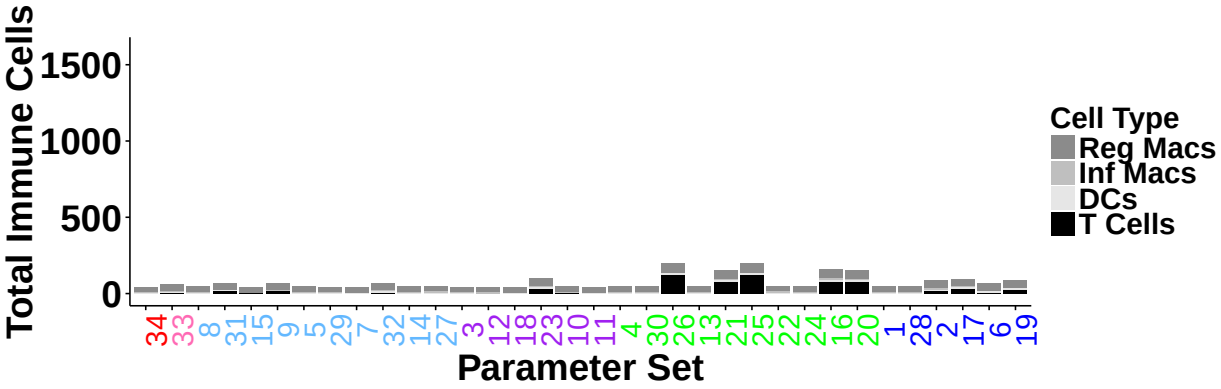

(a) 0 days PI

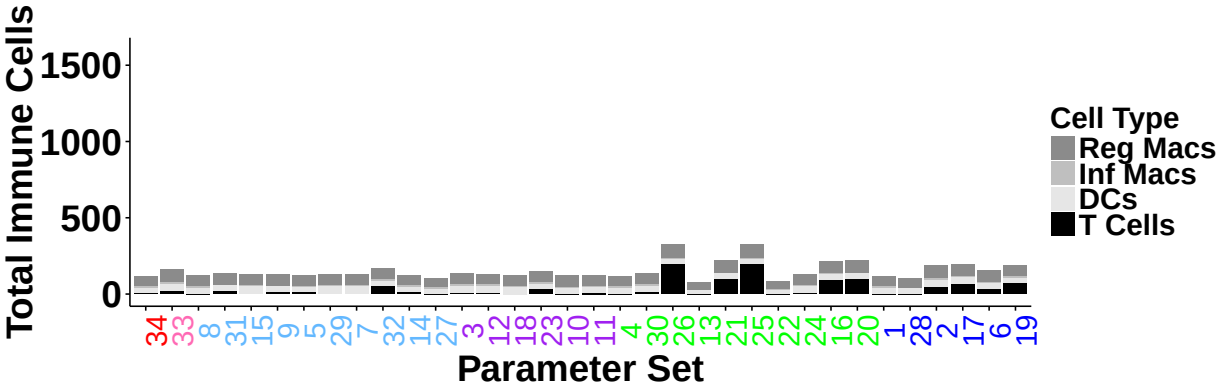

(b) 7 days PI

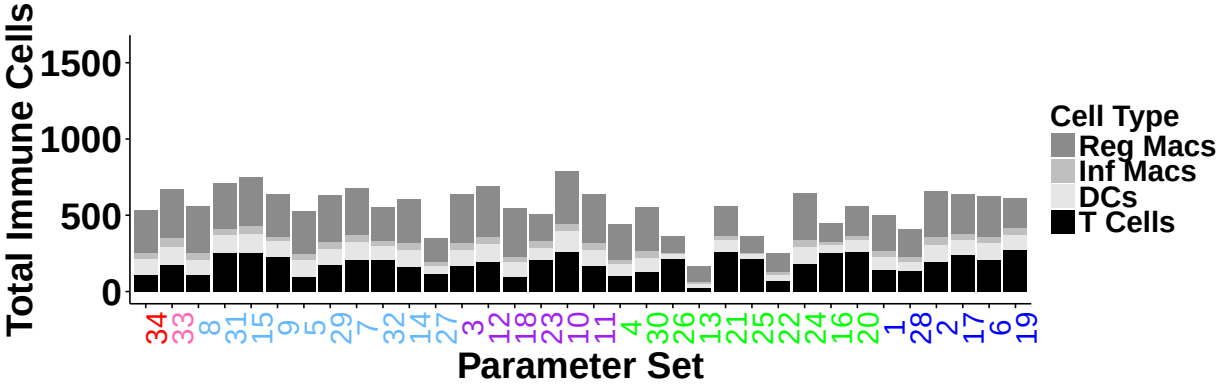

(c) 14 days PI

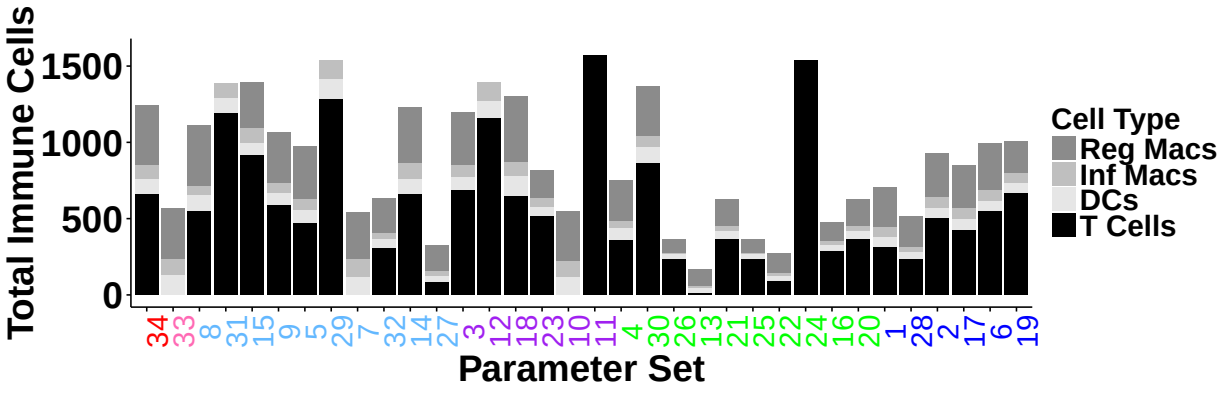

(d) 21 days PI

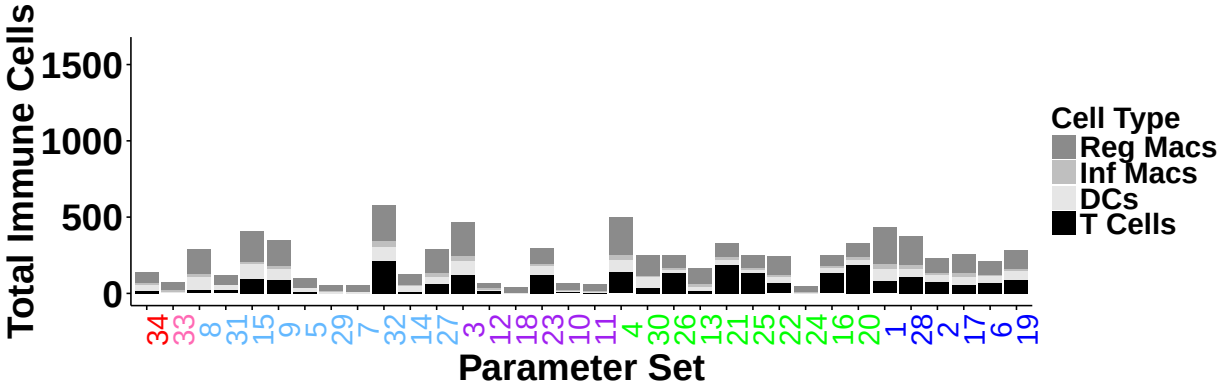

(e) 45 days PI

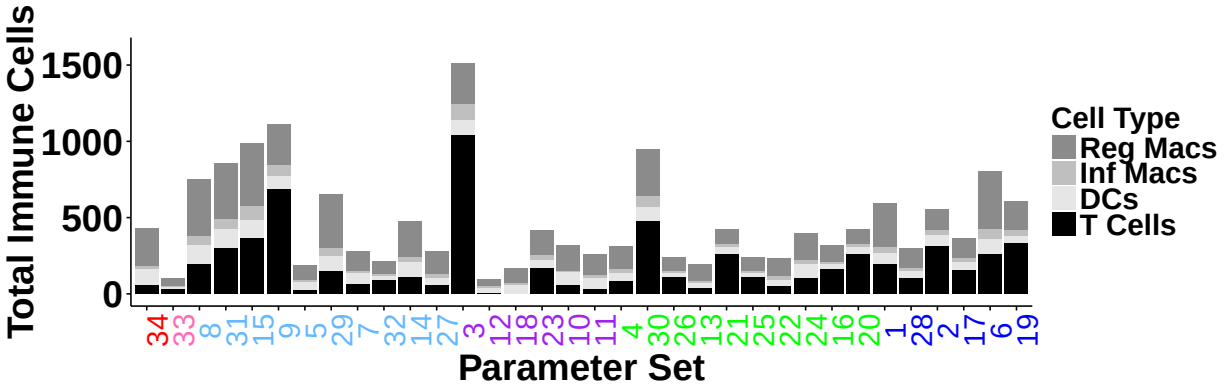

(f) 91 days PI

Figure 4.18: Specific compositions of microbiota differentially effect the cell numbers in the cecum over the course of *Hh* infection. Counts of immune cells for each initial microbial composition in the cecum are shown at days (a) 0, (b) 7, (c) 14, (d) 21, (e) 45 and (f) 91 days post infection with *Hh* (PI). Data represented is the mean of 10 simulations for each of the 34 initial microbial compositions developed in Section 4.0.1.

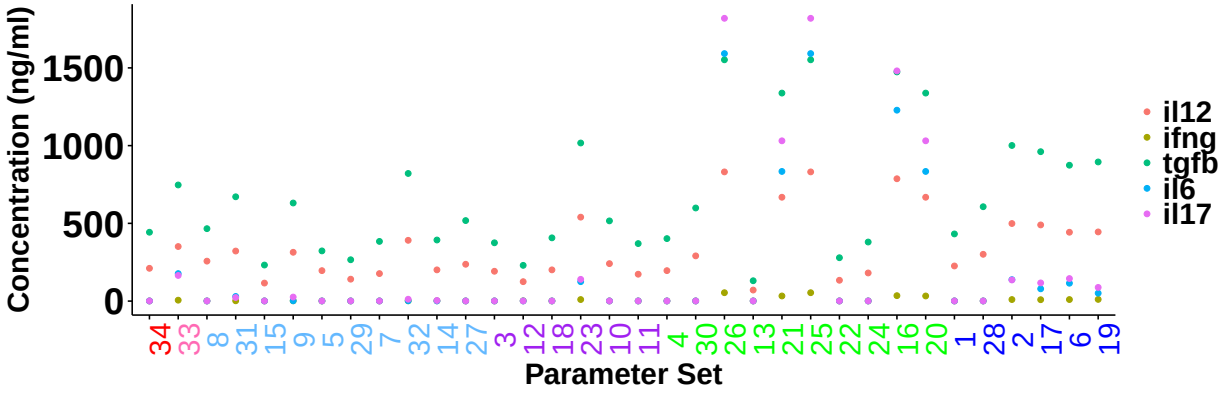

(a) 0 days PI

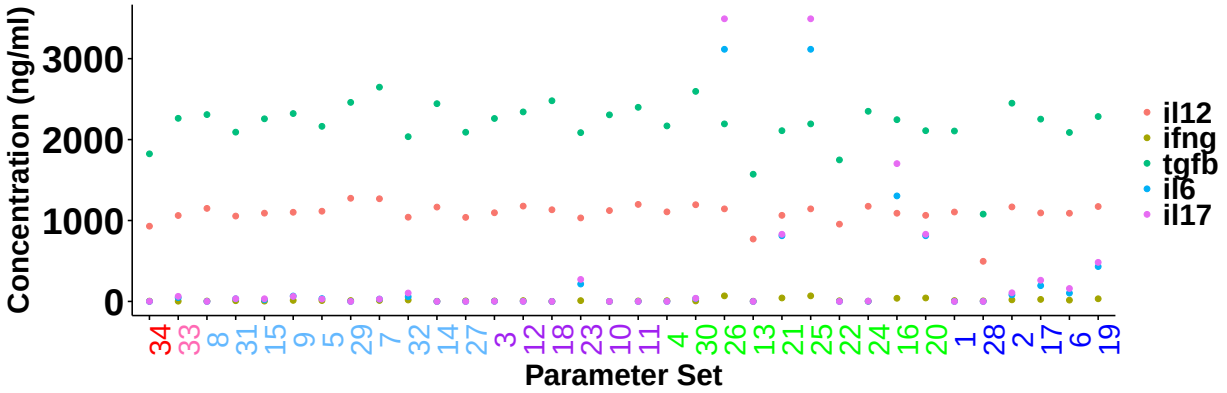

(b) 7 days PI

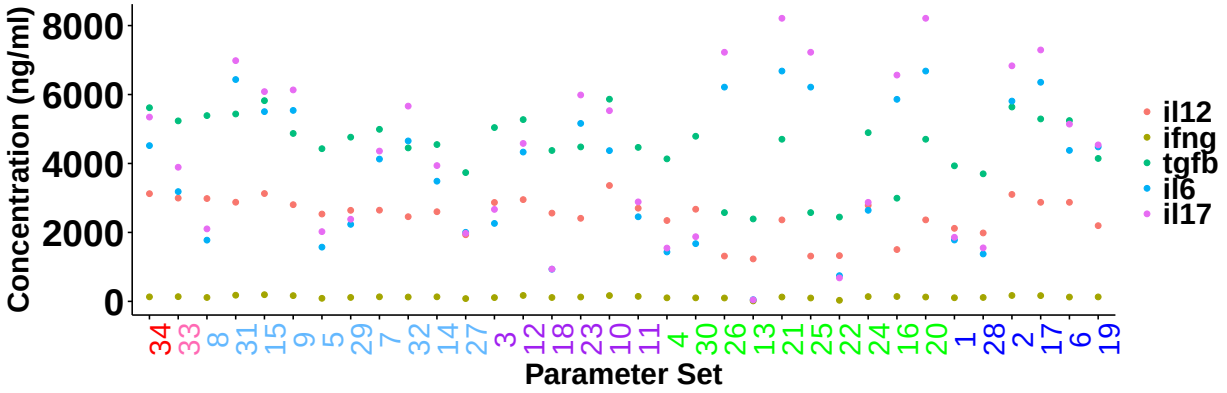

(c) 14 days PI

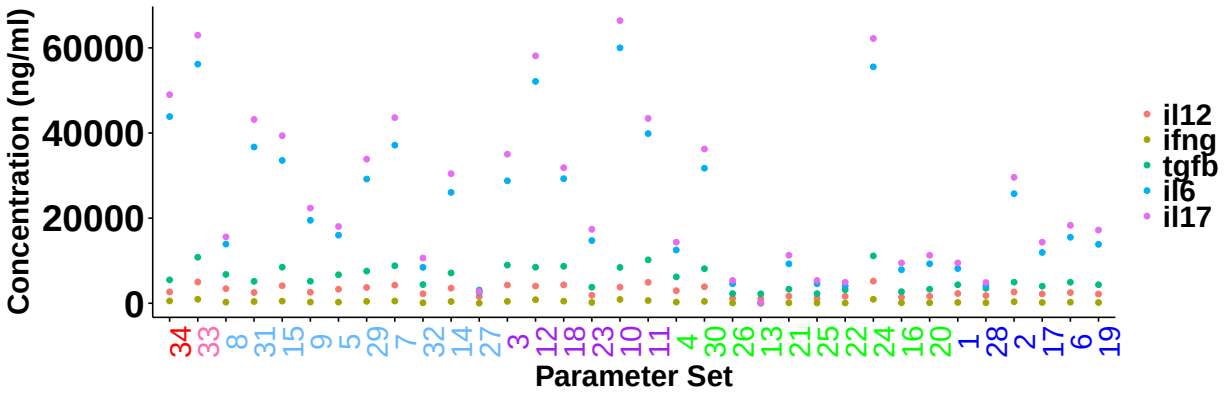

(d) 21 days PI

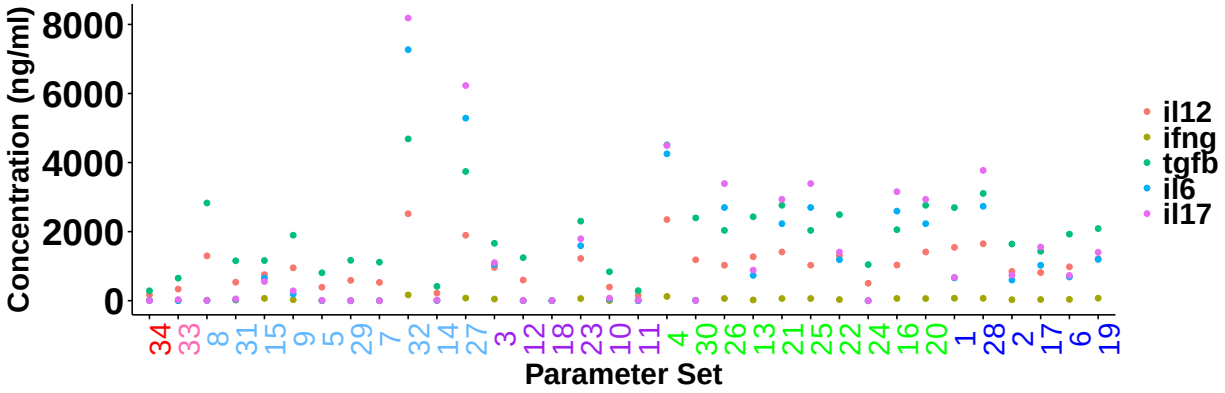

(e) 45 days PI

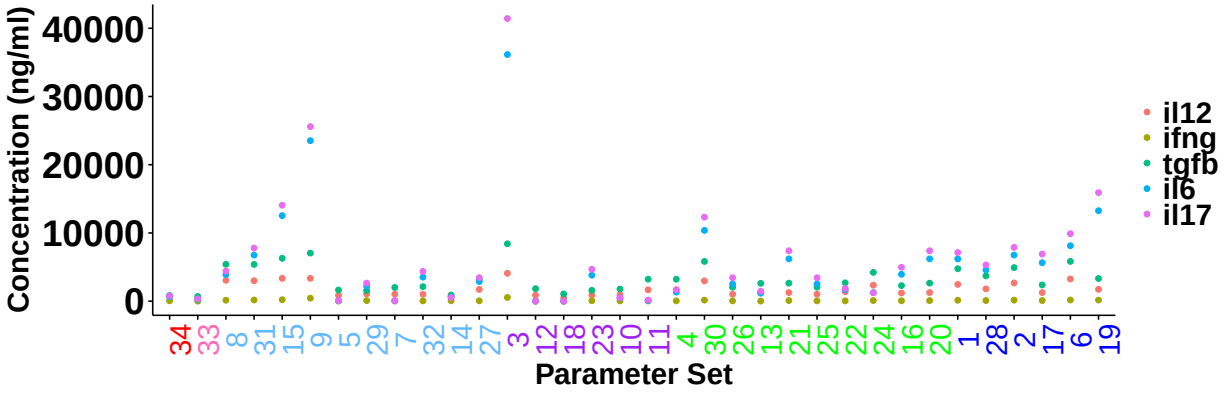

(f) 91 days PI

Figure 4.19: Specific compositions of microbiota differentially effect cytokine concentrations in the cecum over the course of *Hh* infection. Concentrations of cytokines for each initial microbial composition in the cecum are shown at days (a) 0, (b) 7, (c) 14, (d) 21, (e) 45 and (f) 91 days post infection with *Hh* (PI). Data represented is the mean of 10 simulations for each of the 34 initial microbial compositions developed in Section 4.0.1.

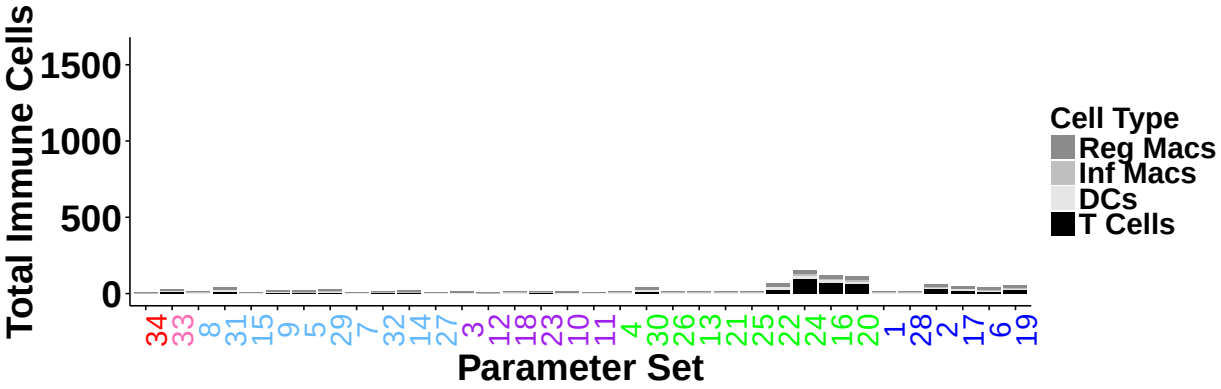

(a) 0 days PI

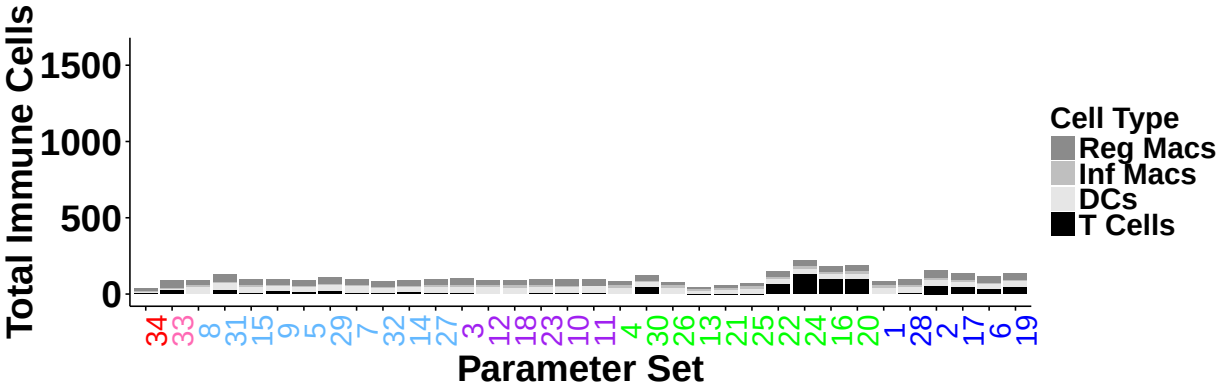

(b) 7 day PI

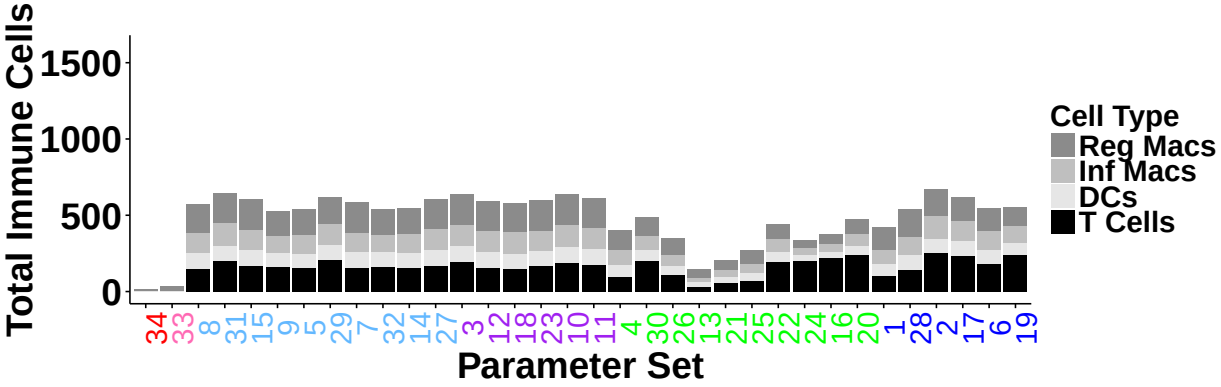

(c) 14 days PI

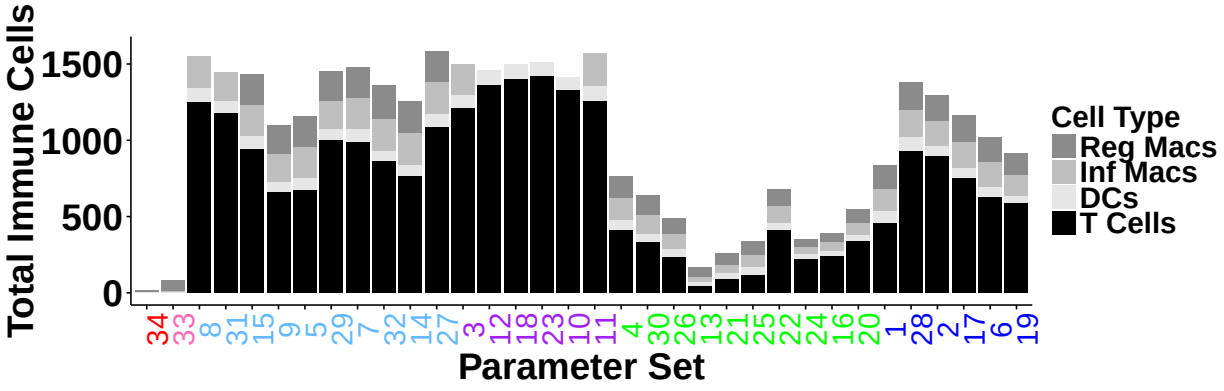

(d) 21 days PI

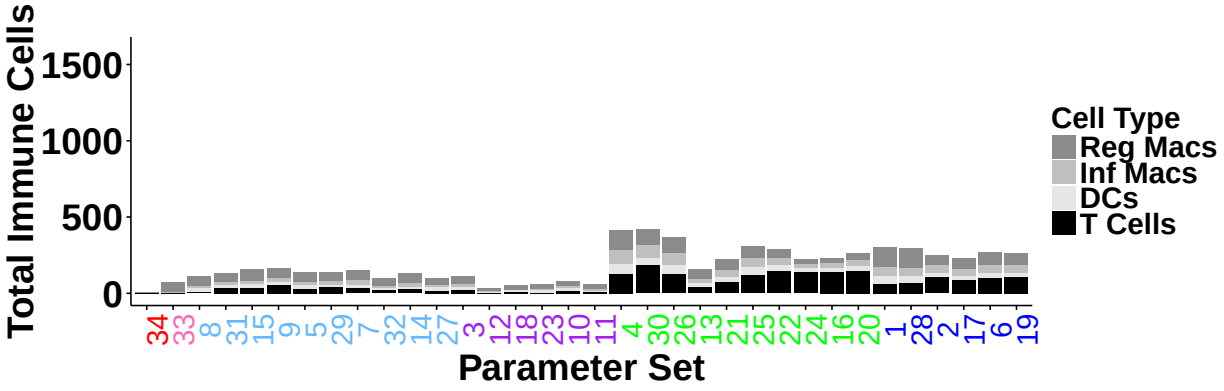

(e) 45 days PI

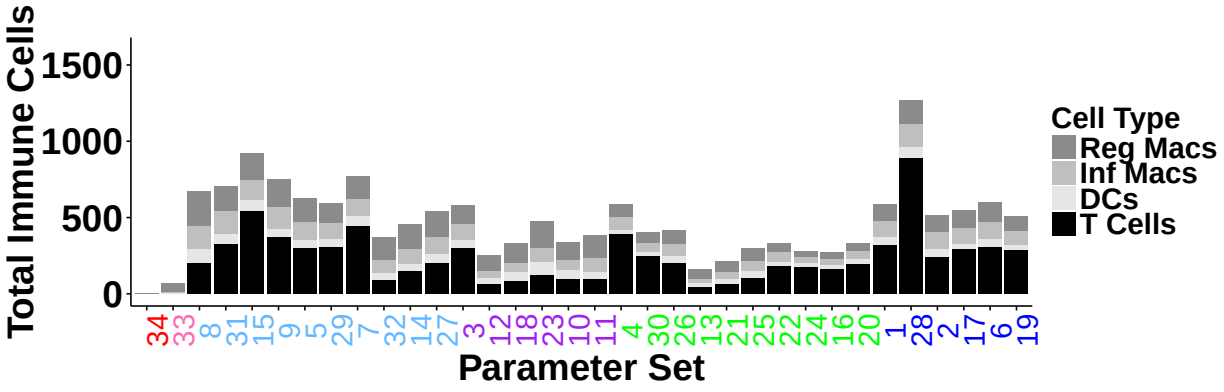

(f) 91 days PI

Figure 4.20: Specific compositions of microbiota differentially effect the cell numbers and cytokine levels in the colon over the course of *Hh* infection. Counts of immune cells for each initial microbial composition in the cecum are shown at days (a) 0, (b) 7, (c) 14, (d) 21, (e) 45 and (f) 91 days post infection with *Hh* (PI). Data represented is the mean of 10 simulations for each of the 34 initial microbial compositions developed in Section 4.0.1.

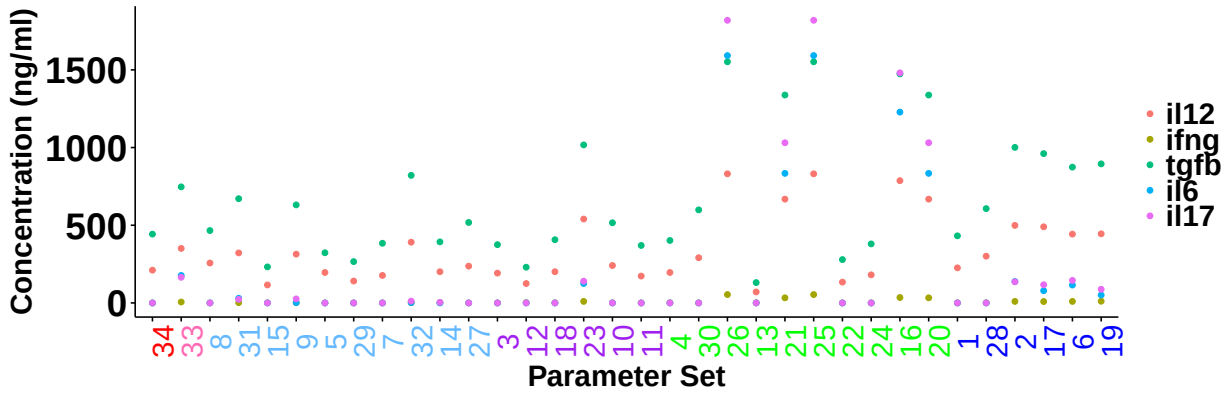

(a) 0 days PI

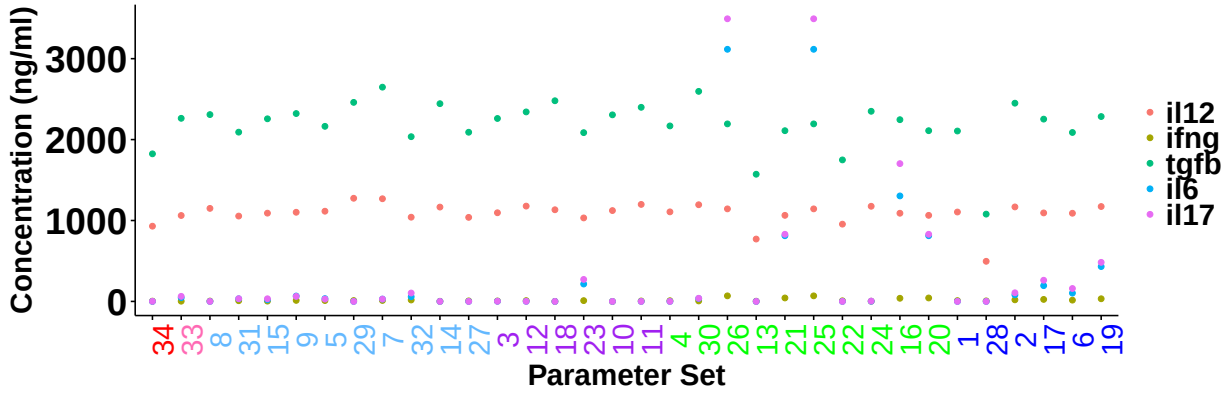

(b) 7 days PI

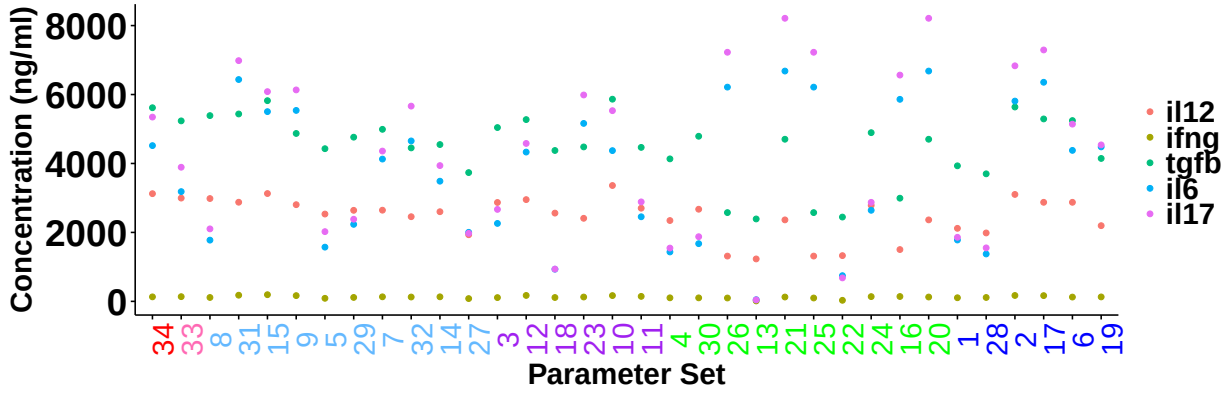

(c) 14 days PI

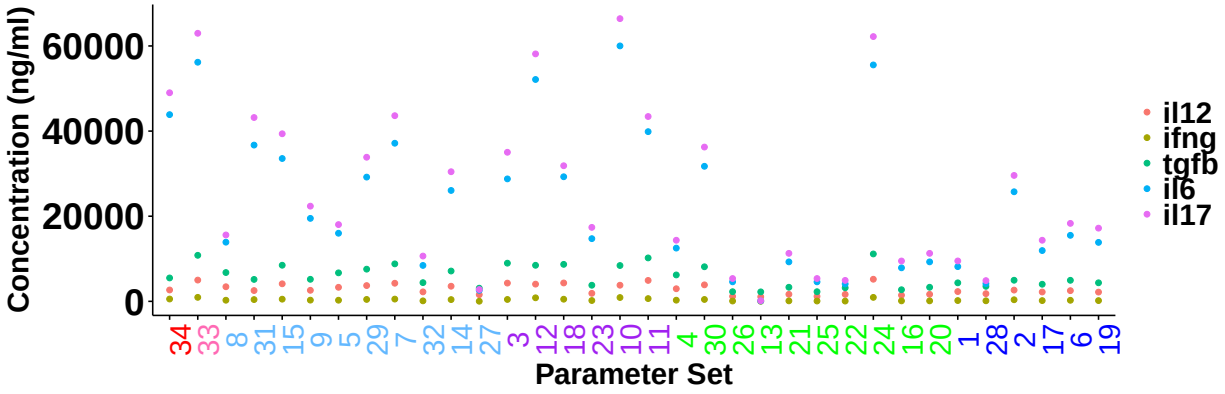

(d) 21 days PI

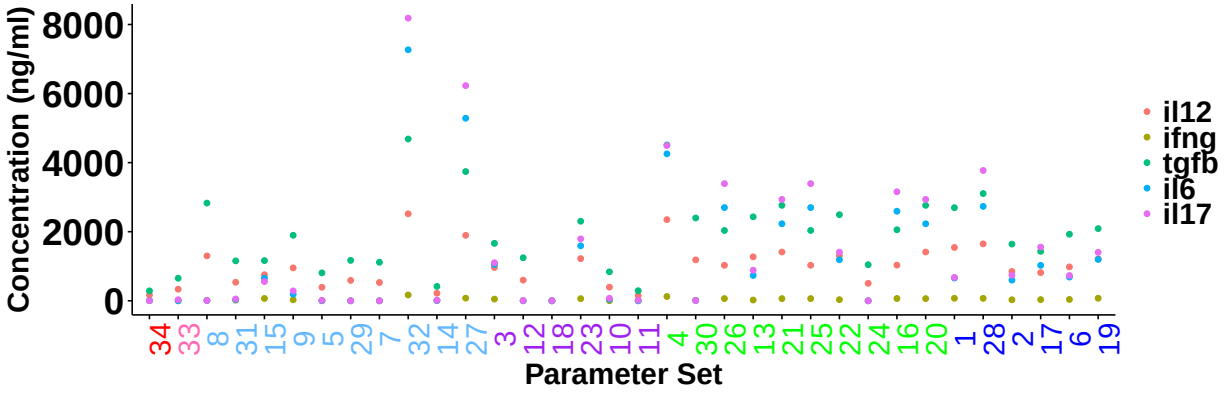

(e) 45 days PI

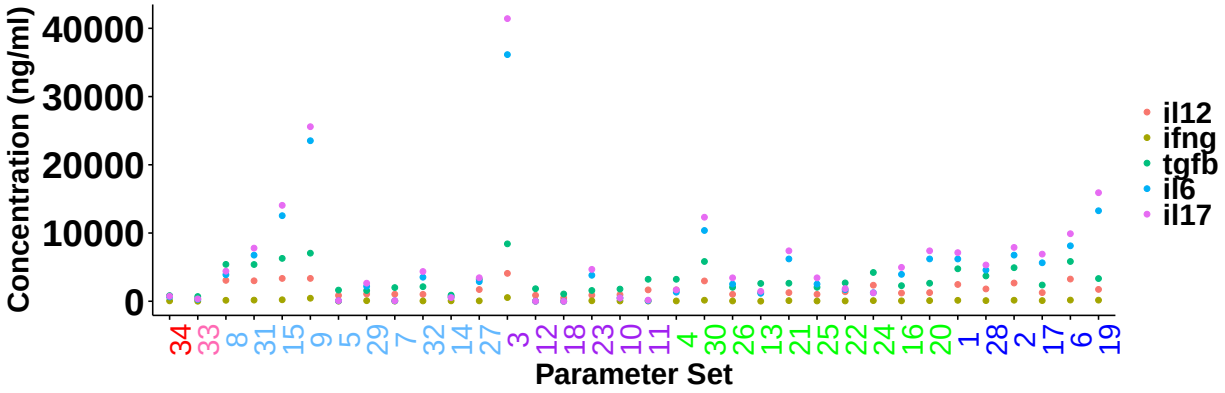

(f) 91 days PI

Figure 4.21: Specific compositions of microbiota differentially effect cytokine concentrations in the colon over the course of *Hh* infection. Concentrations of cytokines for each initial microbial composition in the cecum are shown at days (a) 0, (b) 7, (c) 14, (d) 21, (e) 45 and (f) 91 days post infection with *Hh* (PI). Data represented is the mean of 10 simulations for each of the 34 initial microbial developed in Section 4.0.1.

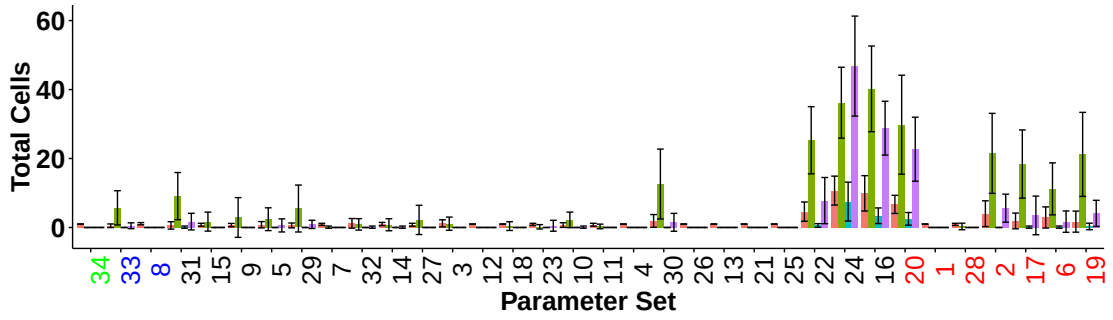

(a) 0 Days PI

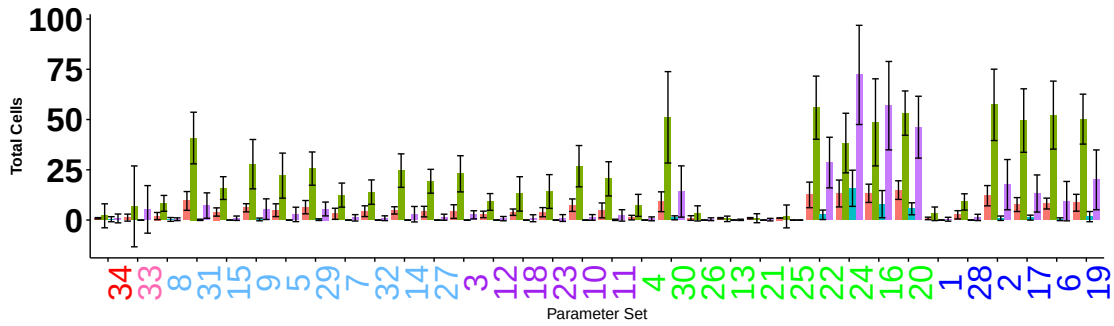

(b) 7 Days PI

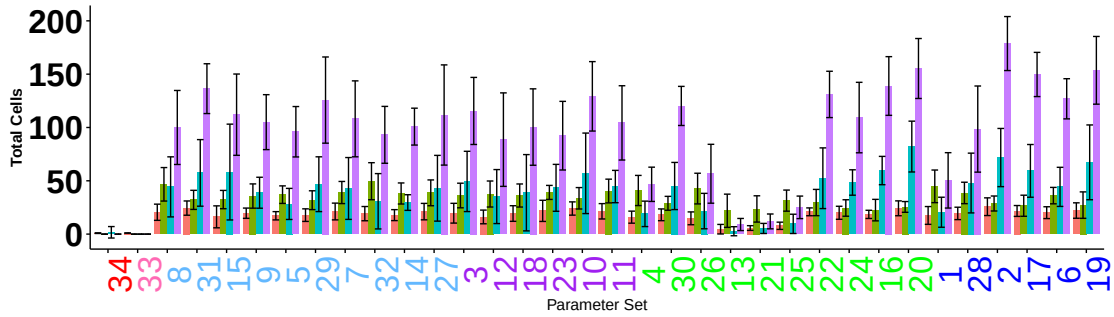

(c) 14 Days PI

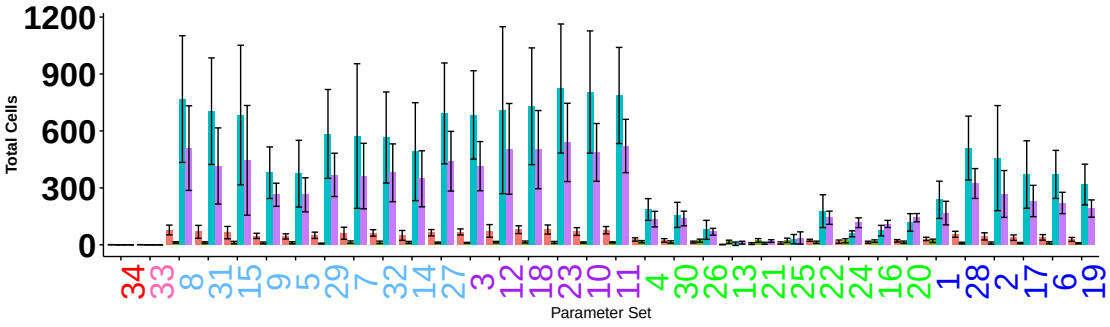

(d) 21 Days PI

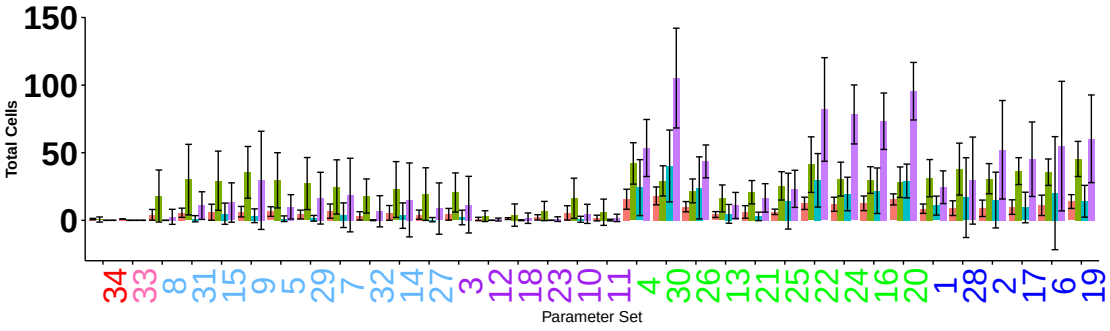

(e) 45 Days PI

Figure 4.22: T cell populations change over the course of *Hh*-infection but similar trends are observed for all phenotypes. The number of double-negative (DN, pink), Th1 (green), Th17 (blue) and double-positive (DP, purple) cells in the cecum are shown at days 0 (a), 7 (b), 14 (c), 21 (d) and 45 (e) days post *Hh*infection for each microbial composition developed in Section 4.0.1. The data shown is the mean ± standard deviation of 10 runs

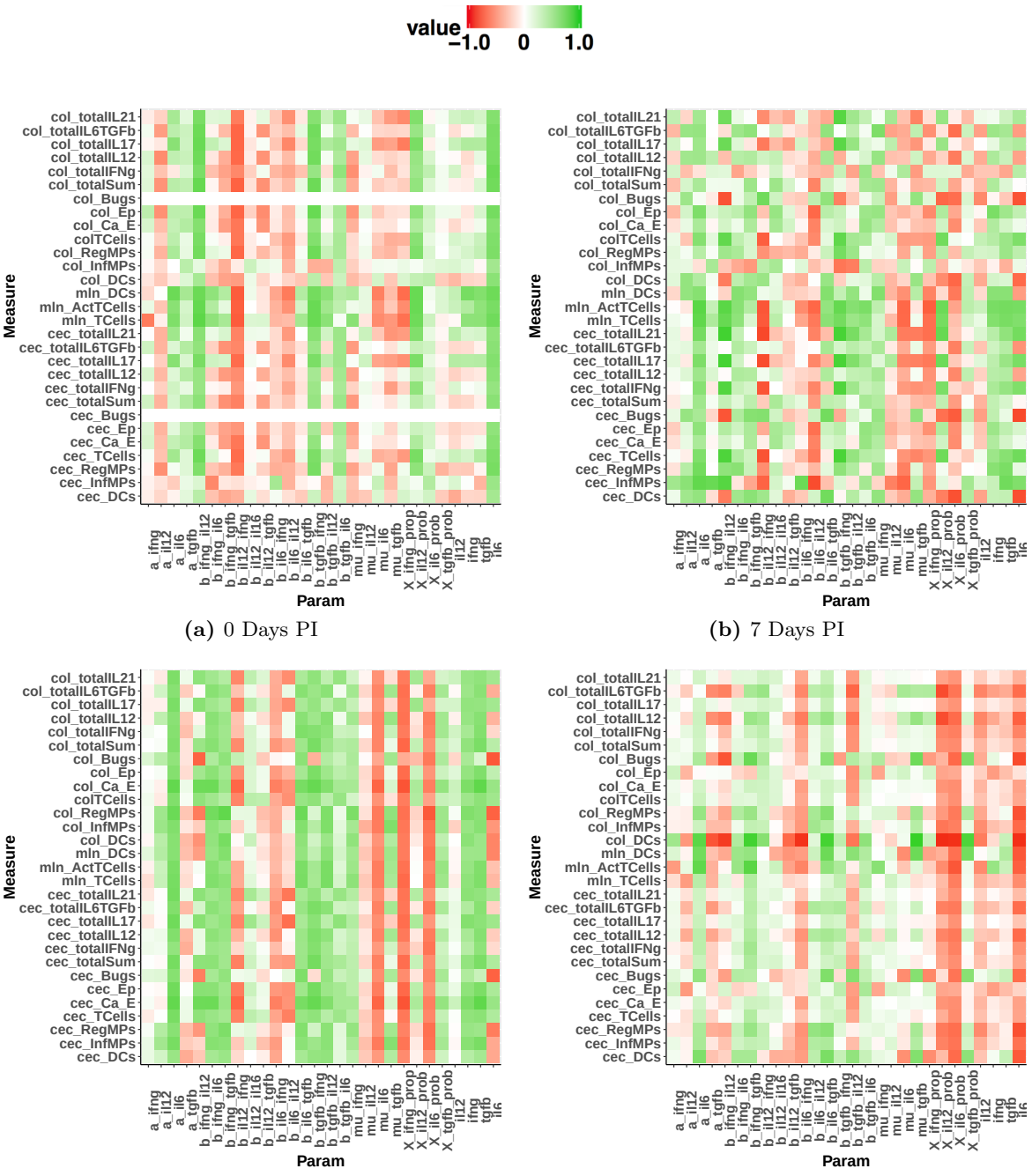

(a) 0 Days PI

(b) 7 Days PI

(c) 14 Days PI

(d) 45 Days PI

Figure 4.23: PRCCs between the ODE parameters and the corresponding simulated measures. Correlations shown are between the average results of 10 simulated runs with each microbial composition generated in Section 4.0.1, with strong negative correlation indicated in red and strong positive correlation in green with white representing no correlation. Correlations are shown at 0 (a), 7 (b), 14 (c) and 45 (d) days post infection with *Hh*.

Chapter 5

Discussion

This thesis aimed to develop a computational model of the processes active in the gut during *Hh*-induced intestinal inflammation that could be used for performing *in silico* experimentation. The purpose of the model was to explore the effects of a lymphocyte blocking drug, and determine whether differences in microbiota alone are sufficient to cause alterations in the phenotypes of disease in *Hh*-induced colitis. This chapter reviews the ways in which these aims have been met and how this study has contributed to the wider field of systems biology by the development of the ASPASIA toolkit.

5.1 Development of a Computational Model of *Hh*-Induced Colitis

Chapter 2 of this thesis details the development of IBDSim, a computational model of the inflammatory processes active in the intestinal tract during *Hh*-induced colitis The CoSMoS process (Andrews et al., 2010), reviewed in Section 1.5.0.2, has provided a framework for developing and validating the model, and a series of diagrams have been developed to document the way in which the biological domain has been modelled. These diagrams make up the domain and platform models for IBDSim (Section 2.2 and Section 2.3, respectively), and have been developed as a result of a collaboration between experimental immunologists and computational modellers. The diagrams shown in this thesis are the final result of several iterations of models that were developed to ensure that the model adequately captured the important aspects of biology, and to highlight gaps in biological

knowledge. The domain model that describes the biology behind IBDSim (Section 2.2) was approved by the domain expert, and it was decided that what was known about the biological processes driving the development of intestinal inflammation in *Hh*-induced colitis had been captured in the diagrams. Subsequently, the platform model (Section 2.3) was developed, and IBDSim was implemented using the platform model diagrams as a blue print. During the model development phase as part of the simulation platform, unknown parameters were calibrated so that each individual cell type behaved as expected using methods previously utilised by (Read et al., 2012). The parameter values found through calibration led to model output that was statistically similar to data collected from *in vivo* studies by Morrison et al. (2013). Moreover, IBDSim captured the emergent behaviours defined in Section 2.2.1:

Emergent Behaviour 1 The bacterial load in the cecal lumen is undetectable before *Hh* inoculation, peaks at around 4 days post infection, is low by day 14, and remains low at all further time points.

Emergent Behaviour 2 The level of inflammation in the large intestine is moderate by 7 days post *Hh* infection, and severe by day 14.

Emergence of the first behaviour was important to ensure that the mechanisms causing inflammation were adequately captured. The *Hh* bacterial load in infected RAG KO mice is higher than in infected IL-10 KO mice, thus there is evidence that adaptive cells in the lamina propria contribute to the immune response against *Hh*. If *Hh* dynamics were hard-coded into the model, rather than emerging as a result of interactions between other cells in the system, IBDSim would not adequately capture this concept. In this instance, there would be no confidence that the behaviours of cells that contribute to the immune response against *Hh* had been adequately captured, and it would be unclear whether results obtained through explorative experimentation were truly representative of the conditions under which the experiment was performed, or whether they were an artefact of misrepresenting the bacterial burden.

The second emergent behaviour was intentionally vaguely defined to reduce bias that could be introduced by predefining what is contributing to inflammation at these time points. Morrison et al. (2013) demonstrated that there is a 10-fold increase in immune

cells, and a 4-fold increase in $CD4^+$ T cells in the cecum and colon by 14 days post infection with *Hh*. It has also been shown by ELISA that the concentration of IFN-γ and IL17 in the colonic lamina propria is increased at day 14, and the distribution of Th1 and Th17 cells at these time points have been recorded (Morrison et al., 2013). Any of these features could have been defined as an observable phenomena, but this assumes that relationships identified between these observations and the level of inflammation recorded by histology scoring are causative. Had the observable phenomena that the model was expected to reproduce been defined in terms of specific cell types or cytokines, instead of more broadly, in terms of inflammation, it would have led to a biased assumption of the important factors that drive inflammation. The development of an *in silico* inflammation scoring system that can be directly linked to features of inflammation in biology has provided a less biased way to determine how predicted alterations in cell counts and cytokine levels from *in silico* experimentation would relate to the overall level of inflammation in the *in vivo* system.

After the emergent behaviours had been adequately captured, validation experiments were performed to assess the predictive capabilities of IBDSim (Section 2.8). The aim was to perform a set of experiments where the *in vivo* results had already been published so that conclusions drawn from *in silico* experimentation could be verified. The *in vivo* results chosen to be replicated using IBDSim were:

Experiment 1 Uninfected IL-10 KO mice do not develop inflammation when kept in SPF facilities (Berg et al., 1996)

Experiment 2 IL-10 KO mice kept in germ-free conditions, which lack commensal flora, display little pathology following *Hh* infection (Dieleman et al., 2000)

These experiments validated that the inflammation in the model was emergent. Inflammation did not develop in the absence of either *Hh* or commensal bacteria. Thus, the mechanisms defined to govern the interactions between cells and cytokines were deemed to appropriately represent what occurs *in vivo*. Further, direct comparison of *in silico* cell numbers and cytokine levels with *in vivo* data, as well as the simulated inflammation score with the *in vivo* histology score, verified that the *in silico* inflammation score that had been developed adequately captured the level of inflammation.

As a result of model calibration and confirmative experimentation, IBDSim was con-

sidered to be an appropriate tool for performing *in silico* experimentation that informed the *in vivo Hh*-induced colitis model.

Chapter 1 detailed previous models for studying intestinal inflammation. None of these models were appropriate for this case study as they did not have the flexibility to incorporate changes to the model required to investigate the impact of therapeutic drugs. Neither did they capture the phenomena of Th17-cell phenotype switching that was important in capturing the dynamics in our model. Instead, concepts from these models, were integrated into a bespoke simulation, IBDSim. A toolkit for experimentation, as well as the source code for the simulation will be made available from the York Computational Immuology Lab website (*https://www.york.ac.uk/computational-immunology/*). By making the toolkit and the source code available, there is potential for this model to be used to drive further insight into biology without any additional modelling required, or to be redeveloped and integrated into other models by someone with the right expertise.

5.2 Biological Hypotheses Explored by IBDSim

The experiments outlined in Chapter 3 and Chapter 4 are examples of how the model can be used for testing therapeutic targets, and for increasing understanding of the processes driving inflammation. In Chapter 3, the effects of blocking lymphocyte egress from the MLN on inflammation using an S1P agonist, FTY720, were explored. FTY720 has been used in several animal disease models with varying effects, but its efficacy in *Hh*-induced colitis had not yet been analysed. To perform this experiment a PK model of the distribution of FTY720 in mice was developed, and a PD model was also developed to examine the effect that the drug had on an individual T cell. These two models were integrated with IBDSim and the effects of the drug on the level of inflammation *in silico* was examined in three different scenarios.

1. **FTY720 as a treatment for blocking the development of intestinal inflammation** The first scenario explored the suitability of FTY720 to block the development of intestinal inflammation when FTY720 was administered daily from the same time point as *Hh*. In this case, FTY720 significantly reduced cell numbers compared to *Hh* alone but did not significantly reduce inflammation.

2. **FTY720 as a treatment for blocking the development of intestinal inflammation (early administration)**

   The second scenario explored the suitability of FTY720 as a therapeutic treatment to blocking the development of intestinal inflammation when administered daily from 6 days prior to *Hh* inoculation. This allowed FTY720 to saturate the lymph node before infection. The results demonstrated that allowing FTY720 to saturate before *Hh* administration does not result in a more effective blocking of *Hh*-induced intestinal inflammation than if FTY720 was given from day 0.

3. **FTY720 as a treatment for resolving established disease (late administration)**

   The final scenario explored the suitability of FTY720 as a therapeutic treatment for blocking established disease. In this study FTY720 was administered daily from 14 days post *Hh* infection, when peak inflammation had developed. In this case FTY720 administration significantly reduced cell numbers and cytokine levels in the lamina propria, but did not effectively resolve inflammation back to the levels seen at day 0.

Unlike other colitis models where FTY720 has proved to be effective in both blocking inflammation and resolving established disease (Daniel et al., 2007; Deguchi et al., 2006; Fujii et al., 2006; Mizushima et al., 2004), in *Hh*-induced colitis the drug failed to have any significant overall effect. Thus, the results suggest that FTY720 is not a good therapeutic treatment for *Hh*-induced intestinal inflammation. The results observed for FTY720 treatment using IBDSim are not the first to find FTY720 to have no effect on disease. For example an *in vivo* study by Kataoka et al. (2005), showed that treating with FTY720 enhanced disease symptoms in mice infected with *Citrobacter rodentium*. In that case study, the *Citrobacter* load was increased following administration of FTY720, leading to a worsening of disease symptoms (Kataoka et al., 2005). Taken together, the results from the *in silico* experimentation, combined with the *Citrobacter rodentium* study by Kataoka et al. (2005), present the case that FTY720 treatment is not appropriate for bacterially-driven disease, because it impairs clearance of the bacterium. However, in humans, IBD is not thought to be driven by a specific type of bacteria thus this does not rule out the

efficacy of FTY720 in human disease.

Intestinal inflammation in *Hh*-induced colitis in IL-10 KO mice *in vivo* has been shown to be dependent on the presence of commensal bacteria (Dieleman et al., 2000). Further, Yang et al. (2013) hypothesised that the composition of the microbiota in IL-10 deficient mice could contribute to the susceptibility to *Hh*-induced colitis. IBDSim was used to explore the way in which different microbial compositions could contribute to the susceptibility to, and severity of *Hh*-induced intestinal inflammation (Chapter 4). The model developed in Chapter 4 to describe the compositions of intestinal microbiota was highly theoretical. As the bacterial species in the model are representative of several species combined in biology, the model cannot be calibrated to biological data, and has instead had to be phenomenologically linked to *in vivo* data. A similar approach was used to look at the interactions between the mucosal immune system and the gut microbiome during *Clostridium difficile* infection (Leber et al., 2015). However, in that model, the commensal flora was divided into a population of infection-exacerbating commensal species, a population of protective species, and the *Clostridium difficile* population (Leber et al., 2015). In the model of *Clostridium difficile* infection, the protective species can grow and die at rates defined by the parameter value, but the infection exacerbating species only has a death rate, not a birth rate, so its population is constantly declining, an abstraction that could bias the model and force resolution. In the model presented in Chapter 4, the bacterial species are grouped by the cytokine that they induce in DCs and macrophages. The groups were defined as IFN-γ-inducing, IL-12-inducing, IL-6-inducing and TGF-β-inducing, with the intention that they would be used to induce Th1 (IFN-γ, and IL-12), Th17 (IL-6 + TGF-β), and Treg (TGF-β alone) cells. Unlike the *Clostridium difficile* infection model where the microbiome was biased to become purely protective, the dual functionality of TGF-β to induce either a Th17, or a Treg phenotype in the models used in Chapter 4 meant that it is not possible to predict how a simulation will react by purely increasing the proportion of supposedly protective bacteria in the population. Using this model, it was shown that alteration of the microbiota alone is sufficient to cause changes in pathology following *Hh* infection, as proposed by Yang et al. (2013). Performing sensitivity analyses on the parameters used in the competition models suggested that, in the absence of *Hh*, an increased concentration of IFN-γ, and the the development of Th17

cells were essential for inducing intestinal inflammation. Further, it was suggested that following *Hh* infection,

- IFN-γ is important in determining the speed at which inflammation develops, as well as the severity of disease.
- IL-6 is important in determining both the speed at which inflammation develops, and in increasing its severity, but does not play a key role in the induction of disease.
- TGF-β plays a role in controlling the speed at which inflammation develops but not in determining its severity, or inducing a relapse of resolved inflammation.

The role of IFN-γ early in infection identified by the model supports results by Kullberg et al. (2001), who found that blocking IFN-γ could not resolve established inflammation, but that mice treated with an anti-IFN-γ antibody did not develop inflammation following infection with *Hh*. The inability of IL6 and TGF-β to induce inflammation fit with results by (Morrison et al., 2013) who observed an increase in the proportion of Th17 cells in the cecum and colon when during severe inflammation, and when inflammation was resolving but not during the initial development phase.

5.3 Contribution to the wider Systems Biology Field

Through creating IBDSim, developments have been made that will benefit the wider systems biology field. ASPASIA was developed by Evans et al. (submitted) to allow sensitivity analysis of SBML models where an intervention was required to adequately model behaviours. The ASPASIA toolkit was initially developed to aid calibration of the T-cell polarisation model demonstrated in Section 2.3.4.3. It was later used to calibrate the PK model to capture the dynamics of FTY720 in Chapter 3, and again to generate a set of models for the experiments performed in Chapter 4. This toolkit will be of use to the wider systems biology field and complements other tools available to allow detailed analysis of SBML models.

Following the development of SBML models to represent certain aspects of IBDSim, a system was developed for simulating SBML models inside agents in the ABM, a novel development in the field. Thus, this work details a system for modular module development

in which parts of a hybrid ABM can be developed and the behaviours explored individually before being integrated to form a more complex hybrid model. Two examples of the advantages to this approach are demonstrated by the use of the T-cell polarisation model in Chapter 2, and the PK model of the distribution of FTY720 in Chapter 3. The T-cell polarisation model was developed and tested by Evans et al. (submitted), where it was used to generate insight into the properties that a receptor hypothetically responsible for driving phenotype switching of Th17 cells must possess. Through the development of the SBML-Java integration framework, this model was able to be directly incorporated into T-cell agents in IBDSim, and the same tests performed on the integrated model. Furthermore, using this approach allowed data on the phenotype of T cells to be collected using similar methods *in silico* to *in vivo* flow cytometry.

The PK model of the distribution of FTY720 in Chapter 3 was developed and tested as a self-contained SBML model, allowing for experimentation into how the increasing volume of a compartment during inflammation might effect the pharmacokinetics of the drug. Integrating this model with the ABM using the SBML-Java integration framework allowed the compartment volume to be dynamically updated. This was important as the concentration of FTY720 in each compartment was shown to be highly sensitive to the compartment volume (Section 3.1), and the effects of FTY720 on compartment volumes were unknown *a priori*.

5.4 Future Directions

5.4.1 Verifying model predictions *in vivo*

The prediction that FTY720 reduces cell numbers and inflammation to a moderate level has been generated by simulating cell behaviour and recording cell counts and cytokine concentrations at different time points post *Hh* infection. To build confidence in future predictions generated by the model, the best practice is to verify predictions *in vivo*. The results of comparing *in vivo* and *in silico* data could then be used to better inform the next iteration of the model, as advocated by the CoSMoS process (Andrews et al., 2010). Comparison of *in vivo* and *in silico* data would also be a way to validate the inflammation scoring system generated in Chapter 2. Work is currently in progress to complete this

experimentation *in vivo*.

5.4.2 Improving IBDSim

The theoretical model used to represent the microbiota in Chapter 4 resulted in three different phenotypes of inflammation. While the non-inflammed case matches what has been observed by Yang et al. (2013), and the non-resolving phenotype matches what was observed by (Kullberg et al., 1998), the relapsing remitting phenotype has not been observed *in vivo*. However, there is no evidence to suggest that this phenotype cannot develop *in vivo*, and in some circumstances this might occur, as this phenotype of disease is most similar to human IBD. It would however be an interesting problem to try and calibrate this model to replicate what was observed by Morrison et al. (2013) in the University of York facility, that inflammation develops and spontaneously resolves. In this model, inflammation cannot be re-induced after resolution by infecting with another dose of *Hh* (unpublished data). To fit the model to a specific case, there are two options, either the model can be recalibrated so that the dynamics of *Hh* are correct and then the parameter set that gives results that are most similar to those observed by Morrison et al. (2013) can be identified and experimentation can be performed, or if data was available for the composition of intestinal flora of IL-10 KO mice at the University of York, a more complex microbiota model could be developed that can be used to determine which types of bacteria are correlated with more or less severe disease progression, and with the appearance of resolving inflammation. Such a model would incorporate metabolites such as butyrate, acetate and propionate, and environmental factors such as the pH of the gut environment to accurately capture the processes that shape the composition of the intestinal microbiota. A similar model has recently been developed for human data by Kettle et al. (2015).

Integration of a more complicated model would drive experimentation into the factors influencing disease resolution and subsequent resistance in *Hh*-induced colitis. This information could lead to the development of new therapeutic targets for inducing resolution and resistance of humans to IBDs.

5.4.3 Extending IBDSim

The BioModels data base (Li et al., 2010) hosts a wide variety of SBML models that can easily be extended or modified. Through the use of the SBML-Java integration model, any existing SBML model can be imported into the ABM to extend the model; however, the interactions between the simulation and the SBML model would need to be coded in every time. Nevertheless, this method provides the opportunity for IBDSim to be extended in numerous ways. Firstly, any PK-PD model can be integrated into the simulations to quickly and ethically explore the effects of a drug on intestinal inflammation. Based on the correlations observed in Chapter 4, treatments that target IFN-γ early in disease, or work to flip the balance of Th1 to Th17 cells in established inflammation, could help reduce the level of inflammation, or lower the chance of a relapse.

Another potential extension would be to better model the epithelial barrier. The current representation is crude and deterministic. A mechanistic model of barrier development and function could be linked to the microbiota models discussed in Chapter 4 to help gain a better understanding of how barrier function is altered during disease progression. CompuGut (Moorthy et al., 2015) is a newly developed tool for modelling the gut environment. Integrating a system like this into IBDSim, in place of the current representation of the cecal and colonic lumen compartments, would greatly increase the complexity of the gut environment and introduce into the model more causative factors, such as the type of diet that the mice are being fed. This would allow the IBDSim to predict the effects of diet on disease development.

5.5 Further Challenges in the Systems Biology Field

5.5.1 Confidence in Simulation

Building confidence in a newly developed simulation is one of the greatest challenges modellers face. Uncertainty in a model is present throughout the modelling process including variability the underlying data, the stochastic nature of a model and in the suitability of abstractions made throughout the modelling process. Documenting the model following protocols such as ODD or the CoSMoS framework go some way towards providing transparency and traceability throughout the modelling process but there is still a degree of

scepticism surrounding the results of computational models of biological systems. By using the spartan toolkit to provide techniques to quantify aleatory uncertainty and model sensitivity, confidence can increase further. However, quantifying uncertainty does not remove it from the system and it is important that modelling results are always given in the context of a suitable margin of error in which confidence in the way in which the results effect the biological system is high.

5.5.2 Standardising Modelling Frameworks

A key challenge in the development of computational models is that there is no standardised framework that can be adopted by modellers to ensure that models can be shared, and understood, between different groups and fields. While the development of SBML (Hucka et al., 2003) has partly bridged this gap for systems modelling using ODEs, the existence of other frameworks such as CellML (Lloyd et al., 2004), SED-ML (Bergmann et al., 2015), and PharmML (Swat et al., 2015) means that there is still not one consistent language used by modellers. Although packages for developing ABMs do exist, they do not have any functionality to directly interact with other modelling languages. Addressing the challenge of standardisation and integration of modelling techniques, although not a trivial task, would allow computational approaches to be more widely used in biology, and increase confidence in results. Moreover, increasing model portability has the potential to dramatically speed up the modelling process.

Appendix A

Model Parameters

Table A.1: Parameters in IBDSim

Parameter	Definition	Value	Evidence
IBDSim			
heightMLN	Length of shortest edge of MLN compartment	36sq (1.8mm)	Figure 2.11a
widthMLN	Length of longest edge of MLN compartment	228sq (11.4mm)	Figure 2.11a
heightCecum	Length of shortest edge of Cecum compartment	136sq (6.8mm)	Figure 2.11b
widthCecum	Length of longest edge of Cecum compartment	544sq (27.2mm)	Figure 2.11b
heightColon	Length of shortest edge of Colon compartment	60sq (3.0mm)	Figure 2.11b
widthColon	Length of longest edge of Colon compartment	1348sq (67.4mm)	Figure 2.11b
LaminaPropria			
inRateDC	Minimum rate of entry of the DCs into the cecum or colon compartments	3.8×10^{-5} (cell/min)	(Jaensson et al., 2008)
inRateM	Minimum rate of entry of the macrophages into the cecum or colon compartments	5×10^{-5} (cell/min)	(Bain et al., 2013)

inRateB	Minimum rate of entry of the bacteria into the cecum or colon compartments	0.092 (cell/min)	Arbitrary
TCell			
stepSizeT	The velocity of a T cell	0.25 sq/min ($11\mu m$)	(Miller et al., 2004) Section 2.4.1.2
angSDT	The standard deviation of the angle of travel away from the straight line	0.13 rad	Figure 2.35 Figure 2.14
avrgLifespanT	The average lifespan of a T cell that is in an activated state	5760 mins	(Gong et al., 2013)
lifespanSDT	The standard deviation of the lifespan of a T cell that is in an activated state	240 mins	(Gong et al., 2013)
effectorLifespanT	The average lifespan of a T cell that is in an effector state	5760 mins	Estimated from (Westera et al., 2013)
effectorLifespanSDT	The standard deviation of the lifespan of a T cell that is in an effector state	5760 mins	Estimated from (Westera et al., 2013)
effectorLifespanSDT	The average lifespan of a T cell that is in an effector state	5760 mins	Estimated from (Westera et al., 2013)
numberOfSpecificities	number of different types of antigens that the total pool of T cells can detect.	2000	Section 2.4.1.2
tcellRadius	Radius of a T cell	0.1sq ($5\mu m$)	(Lokeshwar, 2003)
detachTime	Minimum amount of time for a T cell to be separated from a DC before it can bind again	60	Estimated
longBindMean	Mean time that a T cell can bind to a cognate DC	240	(Gong et al., 2013)

longBindSD	Standard deviation of the time that a T cell can bind to a cognate DC	30 mins	(Gong et al., 2013)
prolifMean	Mean time for a proliferating T cell to produce an identical daughter cell	720 mins	(De Boer et al., 2003)
prolifSD	Standard deviation of the time that a T cell can bind to a cognate DC	60 mins	(Gong et al., 2013)
memoryProb	Probability that proliferation results in a T cell entering a memory state	0.05	(Gong et al., 2013)
DC			
avrgLifespanD	Lifespan of a DC	6000 mins	(Chen et al., 2007)
avrgLifespanSDD	Standard deviation of the lifespan of a DC	1080 mins	Estimated from Chen et al. (2007)
DCradius	Radius of a DC	0.5sq ($25\mu m$)	(Miller et al., 2004)
migrateTime	The time it takes for a DC to enter the MLN from the gut	480 mins	(Martn-Fontecha et al., 2003)
s_a	Parameter in secretion equation	89.9	**??**
s_{b1}	Parameter in secretion equation	2.024	**??**
s_{b2}	Parameter in secretion equation	3.7×10^{-4}	**??**
s_{m12}	Scaling parameter for IL-12 in secretion equation	6.5×10^{-5}	Section 2.3.4.2
s_{m6}	Scaling parameter for IL-6 alone in secretion equation	3.6×10^{-4}	Section 2.3.4.2
s_{m6tgfb}	Scaling parameter for IL-6 + TGF-β in secretion equation	3.6×10^{-4}	Section 2.3.4.2
Macrophage			
avrgLifespanD	Lifespan of a Macrophage	14400 mins (10 days)	(Italiani and Boraschi, 2014)

avrgLifespanSDM	Standard deviation of the lifespan of a Macrophage	1440 mins	Estimated from (Italiani and Boraschi, 2014)
Mradius	Radius of a DC	0.1sq ($10\mu m$)	(Krombach et al., 1997)
ms_a	Parameter in secretion equation	89.9	Equation (2.4)
ms_{b1}	Parameter in secretion equation	2.024	Equation (2.4)
ms_{b2}	Parameter in secretion equation	3.7×10^{-4}	Equation (2.4)
ms_{m12}	Scaling parameter for IL-12 in secretion equation	5	Section 2.3.4.2
ms_{m12}	Scaling parameter for IFN-γ in secretion equation	64	Section 2.3.4.2
ms_{m12}	Scaling parameter for IL-6 alone in secretion equation	8.0	Section 2.3.4.2
ms_{m6tgfb}	Scaling parameter for IL-6+TGF-βin secretion equation	8.0	Section 2.3.4.2
Bug			
stepSizeB	The velocity of *Hh* in the lumen	4 sq/min	Section 2.3.4.1
angSDB	The standard deviation of the angle of travel away from the straight line	0.3 rad	Section 2.3.4.1 Figure 2.14
avrgLifespanTissue	The average lifespan of a bacterium in the tissue compartment	6600 mins	Section 2.3.4.1
avrgLifespanTissueSDB	The standard deviation of the lifespan of a bacterium in a tissue compartment	30 mins	Section 2.3.4.1
phagTime	The time taken for a bacterium to be phagocytosed by a DC	180 mins	Figure 2.39c
Lumen			
prolifProb	Probability of a single *Hh* bacterium in the lumen proliferating	0.0011 /min	Section 2.4.1.1

nutLowDeathProb	Probability that a single *Hh* bacterium will die when the level of nutrients in the environment is low	8.35×10^{-4} /min	Section 2.4.1.1
nutLow	Level of nutrients below which *Hh* bacteria will die at with probability *nutLowDeathProb*	8.35×10^{-4}	Section 2.4.1.1
removeNut	Amount of nutrients removed by a single *Hh* bacteria	15 /cell/min	Section 2.4.1.1
addNut	Amount of nutrient added every *addNutTime*	3	Section 2.4.1.1
addNutTime	Time at which every grid square is increased by *addNut*	30 mins	Section 2.4.1.1
nutLowProlifThresh	The threshold above which *Hh* will proliferate with probability *prolifProb*	250	Section 2.4.1.1
incNut	Amount of nutrients added to the nutrient grid square corresponding to that of the *Hh* bacterium when it dies	15	Section 2.4.1.1
switch_c	Constant term in switching equation	2.9×10^{-5}	Section 2.4.1.1
switch_b1	Rate term in switching equation	6.5×10^{-8}	Section 2.4.1.1
switch_c	Constant term in death equation	3.9×10^{-6}	Section 2.4.1.1
switch_b1	Rate term in switching equation	8×10^{-9}	Section 2.4.1.1
Epithelium			
lambda_E	Rate of duplication of an epithelial cell	1.85	Section 2.4.1.3
mu_E	Death rate of an epithelial cell	0.5/min	Section 2.4.1.3
phi_E	Rate of removal of non-secreting epithelial cells due to the lack of space caused by the presence of secreting and non-secreting cells (aka. crowding coefficient of epithelial cells)	1.8×10^{-4} /min/cell	Section 2.4.1.3

eta_EC	Rate of duplication of an epithelial cell	1.85/min/cell	Section 2.4.1.3
mu_CE	death rate of secreting epithelial cells due to the presence of cytokines in the environment	/ml/min/cell	Section 2.4.1.3

Appendix B

FTY720 Mouse PK Model Parameter Table

Parameters used in PK model of FTY720 in mice.

Parameter	Meaning	Value	Reference
CO	Cardiac output	20ml/min	(Janssen et al., 2002)
Q_{tot}	Blood flow into lung (ng/ml)	35 (ml/min/100g) 36% of CO	(Brown et al., 1997) (Freitas et al., 1983)
Q_{ln}	Blood flow into MLN	0.32% of CO 0.064ml/min	(Freitas et al., 1983)
Q_{rob}	Blood flow into rest of body (ml/min)	158.34	Assume 1/10 of rat
Q_{gut}	Blood flow into splanchic (ml/min)	131 (ml/min/100g) 8.82% of CO 0.5-0.792ml/min	(Brown et al., 1997) (Freitas et al., 1983)
Q_{spleen}	Blood flow into spleen (ml/min)	0.92% of CO	(Freitas et al., 1983)

R_{lung}	Tissue to blood partition coefficient in lung	41.4	(Meno-Tetang et al., 2006) Partition coefficients are dimensionless and therefore do not need scaling (Hayes and Kruger, 2014)
R_{ln}	Tissue to blood partition coefficient in MLN	22.9	
R_{gut}	Tissue to blood partition coefficient in gut	11.1	
R_{liv}	Tissue to blood partition coefficient in liver	34.9	
R_{spleen}	Tissue to blood partition coefficient in spleen	34.7	
R_{rob}	Tissue to blood partition coefficient in rest-of-body	1965.4	
V_{lung}	Volume of lung (taken to be equal to mass)	5.49% of BW 1.3725g	(Brown et al., 1997)
V_{ln}	Volume of MLN	12mg	(Kim et al., 2008)
V_{gut}	Volume of gut	2.53% of BW 0.5875g	(Brown et al., 1997)
V_{liv}	Volume of liver	1.67% of BW 0.4175g	(Brown et al., 1997)
V_{spleen}	Volume of spleen	0.35% of BW 0.0875g	(Brown et al., 1997)
V_{art}	Volume of arterial blood	0.485	58.5ml/kg total (NC3Rs). Assume proportions of arterial and venous blood are same as in rat (5.6:11.3)
V_{ven}	Volume of venous blood	0.978	

f_{ub}	Free fraction of FTY720 in blood	0.000333	Assumed to be same as rats (Meno-Tetang et al., 2006)
PS_{ln}	Interspecies scale down for MLN, $PS_{ln} = A(M)^b$.	$B = 0.67$ $A = 188.84$ $M = 12mg$	

Appendix C

Equations for T-cell polarisation and cytokine secretion

$$\frac{dTbet}{dt} = \left(\frac{a_t \cdot Tbet^n}{(k_t^n + Tbet^n)} + \frac{s_{t_{il12}} \cdot eIL12}{(e_{t_{il12}} + eIL12)} + \frac{s_{t_{ifng}} \cdot eIFNg}{\left(e_{t_{ifng}} + eIFNg\right)} \right) \cdot \frac{1}{\left(1 + \frac{ROR_{\gamma t}}{g_{tr}}\right) \cdot \left(1 + \frac{Foxp3}{g_{tf}}\right)} + \beta_t - \mu_t \cdot Tbet \tag{C.1}$$

$$\frac{dROR-\gamma t}{dt} = \left(\frac{a_r \cdot ROR-\gamma t^n}{(k_r^n + ROR-\gamma t^n)} + \frac{s_{r_{il6,tgfb}} \cdot eIL6 \cdot eTGFb}{(e_{r_{il6}} + eIL6) \cdot \left(e_{r_{tgfb}} + eTGFb\right)} \right) \cdot \frac{1}{\left(1 + \frac{Tbet}{g_{rt}}\right) \cdot \left(1 + \frac{Foxp3}{g_{rf}}\right)} + \beta_r - \mu_r \cdot ROR-\gamma t \tag{C.2}$$

$$\frac{dFoxp3}{dt} = \left(\frac{a_f \cdot Foxp3^n}{\left(k_f^n + Foxp3^n\right)} + \frac{s_{f_{tgfb}} \cdot eTGFb}{\left(e_{f_{tgfb}} + eTGFb\right)} \right) \cdot \frac{1}{\left(1 + \frac{Tbet}{g_{ft}}\right) \cdot \left(1 + \frac{ROR-\gamma t}{g_{fr}}\right)} + \beta_f - \mu_f \cdot Foxp3 \tag{C.3}$$

$$\frac{diIFNg}{dt} = \left(\frac{a_{iifng} \cdot Tbet}{k_{iifng} + Tbet}\right) - \mu_{iifng} \cdot iIFNg - d_{iifng} \cdot iIFNg \tag{C.4}$$

$$\frac{diIL17}{dt} = \left(\frac{a_{iil17} \cdot ROR - \gamma t}{k_{iil17} + ROR - \gamma t}\right) - \mu_{iil17} \cdot iIL17 - d_{iil17} \cdot iIL17 \tag{C.5}$$

$$\frac{diIL21}{dt} = \left(\frac{a_{iil21} \cdot ROR - \gamma t}{k_{iil21} + ROR - \gamma t}\right) - \mu_{iil21} \cdot iIL21 - d_{iil21} \cdot iIL21 \tag{C.6}$$

$$\frac{diTGFb}{dt} = \left(\frac{a_{itgfb} \cdot Foxp3}{k_{itgfb} + Foxp3}\right) - \mu_{itgfb} \cdot TGFb - d_{itgfb} \cdot iTGFb \tag{C.7}$$

$$\frac{deIFNg}{dt} = d_{iifng} \cdot iIFNg - mu_{eifng} eIFNg \tag{C.8}$$

$$\frac{deIL17}{dt} = d_{iil17} \cdot iIL17 - mu_{eiil17} eIl17 \tag{C.9}$$

$$\frac{deIL21}{dt} = d_{iil21} \cdot iIL21 - mu_{eil21} eIL21 \tag{C.10}$$

$$\frac{deTGFb}{dt} = d_{itgfb} \cdot iTGFb - mu_{eitgfb} eTGFb \tag{C.11}$$

Appendix D

Ranges for LHC Sampling for the T Cell Transcription Factor Model

Table D.1: Ranges used in T cell transcription factor model calibration

ID	Description	Value	Range	Data
a_1	Maximum auto-activation rate of T-bet	0.203833		Yates et al. (2004)
a_2	Maximum auto-activation rate of ROR-γt	0.815603	Min: 0.00203833 Max: 2.03833	10 $\times$ either side of value for T-betYates et al. (2004)
a_3	Maximum production rate of IFN-γ	0.007497877	Min: 0.00203833 Max: 2.03833	10 $\times$ either side of value for IFN-γ Schulz et al. (2009)
a_4	Maximum production rate of IL21	0.019987613	Min: 0.000203833 Max: 0.0203833	10 $\times$ either side of value for IFN-γ Schulz et al. (2009)

a_5	Maximum stimulation rate of receptor X	0.019987613	Min: 5 Max: 30	Schulz et al. (2009)
a_6	Rate of T-bet promotion or ROR-γt inhibition	0.304618	Min: 0.002 Max: 2	10 × either side of value for IL12 Schulz et al. (2009)
b_1	Basal transcription rate of T-bet (per min)	0.00203833		Yates et al. (2004)
b_2	Basal transcription rate of ROR-γt	0.0172893	Min: 0.00203833 Max: 0.203833	10 × either side of value for T-betYates et al. (2004)
g_1	Level of ROR-γt when transcription of T-bet is at half maximum	0.456596	Min: 0.0001 Max: 1.0	10 × either side of value for T-bet/GATA-3 Yates et al. (2004)
g_2	Level of T-bet when transcription of ROR-γt is at half maximum	0.83170631	Min: 0.0001 Max: 1.0	10 × either side of value for T-bet/GATA-3 Yates et al. (2004)
g_3	Level of ROR-γt when transcription of IFN-γ is at half maximum	0.625864154	Min: 0.0001 Max: 1.0	10 × either side of value for T-bet/GATA-3 Yates et al. (2004)

g_4	Level of T-bet when transcription of IL21 is at half maximum	0.760239275	Min: 0.0001 Max: 1.0	10 × either side of value for T-bet/GATA-3 Yates et al. (2004)
μ_1	Decay rate of T-bet mRNA	0.096016199	Min: 0.00020833 Max: 0.020833	10 × either side of value for T-betYates et al. (2004)
μ_2	Decay rate of ROR-γt mRNA	0.18586844	Min: 0.00020833 Max: 0.020833	10 × either side of value for T-betYates et al. (2004)
μ_3	Decay rate of C_1	0.1734	Decay rate of IL12	Bajetta et al. (1998)
μ_4	Decay rate of C_{17}	2.038828189	Min: 0.4026 Max: 2.082	Range of decay rates of TGF-β, IL-6 and IL-23 Kaminska et al. (2005); Waage et al. (1989)
μ_5	Decay rate of IFN-γ mRNA	0.18586844	Min: 0.00020833 Max: 0.020833	10 × either side of value for T-betSchulz et al. (2009)
μ_6	Decay rate of IL21 mRNA	0.18586844	Min: 0.00020833 Max: 0.020833	10 × either side of value for T-betSchulz et al. (2009)

μ_7	Decay rate of IL21 mRNA	0.633595	Min: 0.004026 Max: 2.082	10 × either side of value for IL12R Schulz et al. (2009)
μ_8	Decay rate of receptor X-C_X complex	0.527035	Min: 0.004026 Max: 2.082	10 × either side of value for IL12R Schulz et al. (2009)
μ_9	Decay rate of C_X	0.125304	Min: 0.004026 Max: 2.082	10 × either side of range for IL12, IL6 and TGF-β Schulz et al. (2009)
k_1	Level of C_1 at which T-bet transcription is at half maximum	1		Yates et al. (2004); Schulz et al. (2009)
k_2	Level of C_{17} at which ROR-γt transcription is at half maximum	1		Same as T-bet Yates et al. (2004); Schulz et al. (2009)
k_3	Level of T-bet at which T-bet transcription is at half maximum	1		Same as T-bet Yates et al. (2004); Schulz et al. (2009)
k_4	Level of ROR-γt at which ROR-γt transcription is at half maximum	1		Same as T-betYates et al. (2004); Schulz et al. (2009)

k_5	Level of Tbet at which transcription of IFN-γ mRNA is at half maximum	1		Schulz et al. (2009)
k_6	Level of RORgt at which transcription of IL21 mRNA is at half maximum	1		Same as T-bet Schulz et al. (2009)
k_7	Rate of conversion of IL21 mRNA into protein	0.481067361		Yates et al. (2004); Schulz et al. (2009)
k_8	Rate of conversion of IFN-γ mRNA into protein	0.307552055		Yates et al. (2004); Schulz et al. (2009)
k_9	Level of RORgt at which transcription of receptor X is at half maximum	66.7474	Min:1 Max: 100	$\times$ either side of value for T-bet and IL12 Schulz et al. (2009)
k_{10}	Level of C_X-receptor X at which promotion of T-bet or inhibition of RORγt is at half maximum	2.60342	Min: 0.5 Max: 5	10$\times$ either side of value used by Schulz et al. (2009)

k_{11}	Rate of formation of C_X-receptor X complex	0.545609	Min: 0.01 Max: 1	10 × value used by Schulz et al. (2009) for IL12R
s_1	Rate of stimulation of T-bet by external cytokines	0.208033		Yates et al. (2004); Schulz et al. (2009)
s_2	Rate of stimulation of RORgt by external cytokines	1.35863	Min: 0.020833 Max: 2.08033	Yates et al. (2004); Schulz et al. (2009)

Appendix E

Definitions of Parameters and Measures in Microbial Composition Models and Experiments

Parameter	**Definition**
X_i	Total number of bacteria of species i, where $i = ifng,\ il12,\ il6,\ tgfb$.
a_i	Proliferation rate of species i, where $i = ifng,\ il12,\ il6,\ tgfb$.
μ_i	Death rate of species i, where $i = ifng,\ il12,\ il6,\ tgfb$.
$b_{i,j}$	Rate of promotion (if > 0) or inhibition (if < 0) of species i by species j where $i, j = ifng,\ il12,\ il6,\ tgfb$, and $j \neq i$.
Cec_TCells	Total number of T cells in the cecum.
Cec_DCs	Total number of DCs in the cecum.
Cec_RegMPs	Total number of regulatory macrophages in the cecum.
Cec_InfMPs	Total number of inflammatory macrophages in the cecum.
Cec_Eps	Total number of inflammatory epithelial cells in the cecum.
Cec_Ca _E	Total number concentration of inflammatory cytokine.
Cec_totalIL12	Total concentration of IL12 in the cecum
Cec_totalIFNg	Total concentration of IFN-γ in the cecum

Cec_totalIL21	Total concentration of IL21 in the cecum
Cec_totalIL17	Total concentration of IL17 in the cecum
Cec_totalIL6TGFb	Total concentration of IL6 + TGF-β the cecum
Cec_totalSum	Total concentration of cytokines in the cecum.
Col_TCells	Total number of T cells in the colon.
Col_DCs	Total number of DCs in the colon.
Col_RegMPs	Total number of regulatory macrophages in the colon.
Col_InfMPs	Total number of inflammatory macrophages in the colon.
Col_Eps	Total number of inflammatory epithelial cells in the colon.
Col_Ca _E	Total number concentration of inflammatory cytokine.
Col_totalIL12	Total concentration of IL12 in the colon.
Col_totalIFNg	Total concentration of IFN-γ in the colon.
Col_totalIL21	Total concentration of IL21 in the colon.
Col_totalIL17	Total concentration of IL17 in the colon.
Col_totalIL6TGFb	Total concentration of IL6 + TGF-β the colon.
Col_totalSum	Total concentration of cytokines in the colon.
mln_TCells	Total number of T cells in MLN.
mln_ActTCells	Total number of activated and effector T cells in MLN.
mln_DCs	Total number of DCs in MLN.

Appendix F

Correlation Tables of SBML Model Parameters with Measures from IBDSim

a_{il6}: the proliferation rate of IL6-inducing bacteria. Significantly correlated with

Cecum

Day	DCs	T cells	Inf Macs	Reg Macs	C_{a_E}	E_p	Hh	IFN-γ	IL12	IL17	TGF-β	IL21
0							NA					
7		0.68	0.80	0.74						0.69		0.72
14		0.71	0.71		0.81	0.74		0.67	0.75	0.67	0.72	
91	0.68											

Colon

Day	DCs	T cells	Inf Macs	Reg Macs	C_{a_E}	E_p	Hh	IFN-γ	IL12	IL17	TGF-β	IL21
0							NA					
7						0.68						
14		0.67	0.67	0.76	0.8	0.66				0.70		0.69
91	0.82											

MLN

Day	DCs	T cells	Activated T cells
0	0.78	0.68	
7		0.81	0.83
14		0.72	0.70
91			0.81

$\boldsymbol{b_{ifng,il12}}$**:** the rate at which species X_{ifng} is inhibited or promoted by X_{il12}. Significantly correlated with

Cecum

Day	DCs	T cells	Inf Macs	Reg Macs	C_{a_E}	E_p	Hh	IFN-γ	IL12	IL17	TGF-β	IL21
0		0.76		0.68	0.66		NA			0.71		
7		0.87	0.84				-0.81	0.85		0.89		0.91
14		0.76			0.75		-0.75					
91												

Colon

Day	DCs	T cells	Inf Macs	Reg Macs	C_{a_E}	E_p	Hh	IFN-γ	IL12	IL17	TGF-β	IL21
0	0.80					-0.82			0.76		0.74	
7	0.80					-0.82			0.76		0.74	
14	0.80					-0.82			0.76		0.74	
91	-0.89					-0.85						

MLN

Day	DCs	T cells	Activated T cells
0	0.76	0.82	0.80
7		0.78	0.83
14			
91			

$\boldsymbol{b_{il12,ifng}}$**:**the rate at which species X_{il12} is inhibited or promoted by X_{ifng}. Significantly correlated with

Cecum

Day	DCs	T cells	Inf Macs	Reg Macs	C_{a_E}	E_p	Hh	IFN-γ	IL12	IL17	TGF-β	IL21
0		-0.71		-0.66	-0.67		NA			-0.72		
7		-0.75	-0.82				0.66			-0.84		-0.86
14					-0.74							
91												

Colon

Day	DCs	T cells	Inf Macs	Reg Macs	C_{a_E}	E_p	Hh	IFN-γ	IL12	IL17	TGF-β	IL21
0		-0.67		-0.74		-0.82	NA		-0.73	-0.74		0.74
7		-0.77					- 0.74					
14					-0.73							
91												

MLN

Day	DCs	T cells	Activated T cells
0	0.76	0.82	0.80
7		-0.79	-0.80
14			
91			

$b_{il6,il12}$**:**the rate at which species X_{il6} is inhibited or promoted by X_{il12} Significantly correlated with

Cecum

Day	DCs	T cells	Inf Macs	Reg Macs	C_{a_E}	E_p	Hh	IFN-γ	IL12	IL17	TGF-β	IL21
0							NA					
7		-0.75	-0.82				0.66			0.76		0.74
14										-0.70		-0.66
91												

Colon

Day	DCs	T cells	Inf Macs	Reg Macs	C_{a_E}	E_p	Hh	IFN-γ	IL12	IL17	TGF-β	IL21
0							NA					
7								-0.74				
14					-0.73							
91												

MLN

Day	DCs	T cells	Activated T cells
0			
7			-0.73
14			
91			

$b_{il6,tgfb}$: the rate at which species X_{il6} is inhibited or promoted by X_{tgfb} Significantly correlated with

Cecum

Day	DCs	T cells	Inf Macs	Reg Macs	C_{a_E}	E_p	Hh	IFN-γ	IL12	IL17	TGF-β	IL21
0							NA					
7	0.74						0.74					
14				0.66	0.71		0.68					
91	0.70				0.68							

Colon

Day	DCs	T cells	Inf Macs	Reg Macs	C_{a_E}	E_p	Hh	IFN-γ	IL12	IL17	TGF-β	IL21
0							NA					
7												
14			0.67	0.76	0.68		0.68					
91	0.89		0.66									

MLN

Day	DCs	T cells	Activated T cells
0			
7	0.66		
14		0.71	0.7
91	0.76		

$b_{tgfb,ifng}$: the rate at which species X_{tgfb} is inhibited or promoted by X_{ifng} Significantly correlated with

Cecum

Day	DCs	T cells	Inf Macs	Reg Macs	C_{a_E}	E_p	Hh	IFN-γ	IL12	IL17	TGF-β	IL21
0		0.69		0.71			NA			0.7		
7	0.88						0.74	0.87		0.89		0.89
14						0.72	0.78	0.66	0.68		0.70	
91												

Colon

Day	DCs	T cells	Inf Macs	Reg Macs	C_{a_E}	E_p	Hh	IFN-γ	IL12	IL17	TGF-β	IL21
0							NA					
7		0.81	-0.67	0.72							0.82	0.84
14					0.78	0.70						
91												

MLN

Day	DCs	T cells	Activated T cells
0			
7		0.78	0.73
14		0.79	0.73
91			

$\boldsymbol{b_{tgfb,il12}}$**:** the rate at which species X_{tgfb} is inhibited or promoted by X_{il12} Significantly correlated with

Cecum

Day	DCs	T cells	Inf Macs	Reg Macs	C_{a_E}	E_p	Hh	IFN-γ	IL12	IL17	TGF-β	IL21
0							NA					
7											0.67	0.71
14					0.67							
91												

Colon

Day	DCs	T cells	Inf Macs	Reg Macs	C_{a_E}	E_p	Hh	IFN-γ	IL12	IL17	TGF-β	IL21
0							NA					
7												
14			0.69	0.68								
91	-0.67								-0.67		-0.73	

MLN

Day	DCs	T cells	Activated T cells
0			
7	0.66		
14		0.71	0.71
91			

***ifng*:** the initial proportion of species X_{ifng} in the population. Significantly correlated with

Cecum

Day	DCs	T cells	Inf Macs	Reg Macs	C_{a_E}	E_p	Hh	IFN-γ	IL12	IL17	TGF-β	IL21
0		0.69		0.71			NA				0.67	
7	-0.85	0.75	0.68		-0.86	0.68		0.71		0.71		
14							-0.76					
91	-0.80		-0.69	-0.83			-0.71		-0.72		-0.71	

Colon

Day	DCs	T cells	Inf Macs	Reg Macs	C_{a_E}	E_p	Hh	IFN-γ	IL12	IL17	TGF-β	IL21
0		0.68		0.71		0.73	NA				0.67	
7	-0.72	0.69					-0.82					
14					0.69							
91	-0.93		-0.73	-0.82			-0.85		-0.76		-0.71	

MLN

Day	DCs	T cells	Activated T cells
0		74	71
7		0.71	0.64
14			
91	-0.80		-0.77

Abbreviations

μm microns.

Hh *Helicobacter hepaticus*.

ABM agent-based model.

AICD activarion-induced cell death.

AMP antimicrobial peptide.

APC antigen-presenting cell.

ASPASIA Automated Simulation Paramater Alteration and SensItivity Analysis toolkit.

BCR B-cell receptor.

CHO Chinese hamster ovary.

COPASI COmplex PAthway SImulator.

CoSMoS Complex Systems Modelling and Simulation.

DC dendritic cell.

DN double negative.

DP double positive.

DSS dextran sulfate sodium.

EAE experimental autoimmune encephalomyelitis.

ELISA enzyme-linked immunosorbent assay.

ENISI ENteric Immunity SImulator.

FBA flux balance analysis.

FLAME Flexible Large-scale Agent-based Modelling Environment.

Foxp3 forkhead-box protein 3.

FTY720 fingolimod.

GATA-3 GATA binding protein 3.

HIV human immunodeficiency virus.

IBD inflammatory bowel disease.

IFN-γ Inteferon-γ.

IL Interleukin.

ILC innate lympoid cell.

JAK-STAT Janus kinase-signal tranducer and activator of transcription.

KO knock out.

LP lamina propria.

LPS lipopolysaccharide.

MASON Multi-Agent Simulation Of Neighbourhoods.

MHC major histocompatibility complex.

MLN mesenteric lymph node.

NF-$_{\mathbf{K}}$B nuclear factor-kappa B.

ODD overview, design concepts, and details.

ODE ordinary differential equation.

PAMP pathogen-associated molecular patterns.

PD pharmacodynamics.

PDE partial differential equation.

PK pharmacokinetic.

PRCC partial-rank correlation coefficient.

PRR pattern-recognition receptor.

RAG recombination activating gene.

ROR-γt Retinoic-acid Related Orphan Receptor-γt.

S1P sphingosine 1-phosphate.

SBML Systems Biology Mark-up Language.

SCID severe combined immunodeficiency.

Spartan Simulation Parameter Analysis R Toolkit ApplicatioN.

SPF specific pathogen free.

STAT signal tranducer and activator of transcription.

T-bet T-box transcription factor T.

TBNS 2,4,6-trinitrobenz- enesulfonic acid.

TCR T-cell receptor.

TGF-β Transforming Growth Factor-β.

Th T-helper.

TNF-α Tumour Necrosis Factor-α.

UML Unified Modelling Language.

XML eXtensible Markup Language.

References

Aarons, L. Physiologically based pharmacokinetic modelling: a sound mechanistic basis is needed. *British Journal of Clinical Pharmacology*, 60(6):581–583, December 2005. ISSN 0306-5251. doi: 10.1111/j.1365-2125.2005.02560.x.

Abdi, K., Singh, N. J., and Matzinger, P. Lipopolysaccharide-activated dendritic cells: "exhausted" or alert and waiting? *Journal of Immunology (Baltimore, Md.: 1950)*, 188 (12):5981–5989, June 2012. ISSN 1550-6606. doi: 10.4049/jimmunol.1102868.

Achard, F., Vaysseix, G., and Barillot, E. XML, bioinformatics and data integration. *Bioinformatics (Oxford, England)*, 17(2):115–125, February 2001. ISSN 1367-4803.

Ahern, P. P., Schiering, C., Buonocore, S., McGeachy, M. J., Cua, D. J., Maloy, K. J., and Powrie, F. Interleukin-23 Drives Intestinal Inflammation through Direct Activity on T Cells. *Immunity*, 33(2):279–288, August 2010. ISSN 1074-7613. doi: 10.1016/j.immuni.2010.08.010.

Akira, S., Uematsu, S., and Takeuchi, O. Pathogen Recognition and Innate Immunity. *Cell*, 124(4):783–801, February 2006. ISSN 0092-8674. doi: 10.1016/j.cell.2006.02.015.

Alberts, B., Johnson, A., and Lewis, J. *Molecular Biology of the Cell*. Garland Science, New York, 4th edition edition, 2002.

Alden, K. *Simulation and Statistical Techniques to Explore Lymphoid Tissue Organogenesis*. Thesis, University of York, August 2012.

Alden, K., Read, M., Timmis, J., Andrews, P. S., Veiga-Fernandes, H., and Coles, M. Spartan: A Comprehensive Tool for Understanding Uncertainty in Simulations of Bio-

logical Systems. *PLoS Comput Biol*, 9(2):e1002916, February 2013. doi: 10.1371/journal.pcbi.1002916.

Allen, L. J. *An Introduction to Stochastic Processes with Applications to Biology*. Pearson, New Jersey, 1st edition, 2003.

Allende, M. L., Dreier, J. L., Mandala, S., and Proia, R. L. Expression of the sphingosine 1-phosphate receptor, S1p1, on T-cells controls thymic emigration. *The Journal of Biological Chemistry*, 279(15):15396–15401, April 2004. ISSN 0021-9258. doi: 10.1074/jbc.M314291200.

An, G., Mi, Q., Dutta-Moscato, J., and Vodovotz, Y. Agent-based models in translational systems biology. *Wiley interdisciplinary reviews. Systems biology and medicine*, 1(2): 159–171, 2009. ISSN 1939-5094. doi: 10.1002/wsbm.45.

Andrews, P. S., Polack, F. A. C., Sampson, A., Stepney, S., and Timmis, J. The CoSMoS Process, Version 0.1: A Process for the Modelling and Simulation of Complex Systems. Technical report, University of York, 2010.

Antia, R., Bergstrom, Carl, T., Pilyugin, S., S., Kaech, S. M., and Ahmed, R. Models of CD8+ Responses: 1. What is the Antigen-independent Proliferation Program. *Journal of Theoretical Biology*, 221(4):585–598, April 2003. ISSN 0022-5193. doi: 10.1006/jtbi.2003.3208.

Arciero, J. C., Ermentrout, G. B., Upperman, J. S., Vodovotz, Y., and Rubin, J. E. Using a Mathematical Model to Analyze the Role of Probiotics and Inflammation in Necrotizing Enterocolitis. *PLoS ONE*, 5(4):e10066, April 2010. doi: 10.1371/journal.pone.0010066.

Asle-Rousta, M., Oryan, S., Ahmadiani, A., and Rahnema, M. Activation of sphingosine 1-phosphate receptor-1 by SEW2871 improves cognitive function in Alzheimer's disease model rats. *EXCLI Journal*, 12:449–461, June 2013. ISSN 1611-2156.

Bain, C. C., Scott, C. L., Uronen-Hansson, H., Gudjonsson, S., Jansson, O., Grip, O., Guilliams, M., Malissen, B., Agace, W. W., and Mowat, A. M. Resident and pro-inflammatory macrophages in the colon represent alternative context-dependent fates

of the same Ly6chi monocyte precursors. *Mucosal Immunology*, 6(3):498–510, May 2013. ISSN 1935-3456. doi: 10.1038/mi.2012.89.

Bajetta, E., Del Vecchio, M., Mortarini, R., Nadeau, R., Rakhit, A., Rimassa, L., Fowst, C., Borri, A., Anichini, A., and Parmiani, G. Pilot study of subcutaneous recombinant human interleukin 12 in metastatic melanoma. *Clinical Cancer Research: An Official Journal of the American Association for Cancer Research*, 4(1):75–85, January 1998. ISSN 1078-0432.

Barnes, B. and Fulford, G. R. *Mathematical Modelling with Case Studies: A Differential Equations Approach using Maple and MATLAB, Second Edition*. CRC Press, March 2011. ISBN 978-1-4200-8350-7.

Bauer, A. L., Beauchemin, C. A., and Perelson, A. S. Agent-based modeling of host-pathogen systems: The successes and challenges. *Information sciences*, 179(10):1379–1389, April 2009. ISSN 0020-0255.

Beauchemin, C., Dixit, N. M., and Perelson, A. S. Characterizing T Cell Movement within Lymph Nodes in the Absence of Antigen. *The Journal of Immunology*, 178(9): 5505–5512, May 2007. ISSN 0022-1767, 1550-6606. doi: 10.4049/jimmunol.178.9.5505.

Bedoya, S. K., Wilson, T. D., Collins, E. L., Lau, K., and Larkin, J. Isolation and Th17 Differentiation of Nave CD4 T Lymphocytes. *Journal of Visualized Experiments : JoVE*, (79), September 2013. ISSN 1940-087X. doi: 10.3791/50765.

Belkaid, Y. and Hand, T. W. Role of the Microbiota in Immunity and Inflammation. *Cell*, 157(1):121–141, March 2014. ISSN 0092-8674. doi: 10.1016/j.cell.2014.03.011.

Belkaid, Y., Bouladoux, N., and Hand, T. W. Effector and Memory T cell Responses to Commensal Bacteria. *Trends in immunology*, 34(6):299–306, June 2013. ISSN 1471-4906. doi: 10.1016/j.it.2013.03.003.

Beltman, J. B., Mare, A. F. M., Lynch, J. N., Miller, M. J., and Boer, R. J. d. Lymph node topology dictates T cell migration behavior. *The Journal of Experimental Medicine*, 204 (4):771–780, April 2007. ISSN 0022-1007, 1540-9538. doi: 10.1084/jem.20061278.

Belzer, C., Stoof, J., Beckwith, C. S., Kuipers, E. J., Kusters, J. G., and van Vliet, A. H. M. Differential regulation of urease activity in Helicobacter hepaticus and Helicobacter pylori. *Microbiology (Reading, England)*, 151(Pt 12):3989–3995, December 2005. ISSN 1350-0872. doi: 10.1099/mic.0.28188-0.

Bennink, R. J., Jonge, W. J. d., Symonds, E. L., Wijngaard, R. M. v. d., Spijkerboer, A. L., Benninga, M. A., and Boeckxstaens, G. E. Validation of Gastric-Emptying Scintigraphy of Solids and Liquids in Mice Using Dedicated Animal Pinhole Scintigraphy. *Journal of Nuclear Medicine*, 44(7):1099–1104, July 2003. ISSN 0161-5505, 2159-662X.

Berg, D. J., Davidson, N., Khn, R., Mller, W., Menon, S., Holland, G., Thompson-Snipes, L., Leach, M. W., and Rennick, D. Enterocolitis and colon cancer in interleukin-10-deficient mice are associated with aberrant cytokine production and CD4(+) TH1-like responses. *Journal of Clinical Investigation*, 98(4):1010–1020, August 1996. ISSN 0021-9738.

Bergmann, F. T., Cooper, J., Le Novre, N., Nickerson, D., and Waltemath, D. Simulation Experiment Description Markup Language (SED-ML) Level 1 Version 2. *Journal of Integrative Bioinformatics*, 12(2):262, 2015. ISSN 1613-4516. doi: 10.2390/biecoll-jib-2015-262.

Bersini, H. Immune System Modeling: The OO Way. In Bersini, H. and Carneiro, J., editors, *Artificial Immune Systems*, number 4163 in Lecture Notes in Computer Science, pages 150–163. Springer Berlin Heidelberg, September 2006. ISBN 978-3-540-37749-8 978-3-540-37751-1. DOI: 10.1007/11823940_12.

Bertolino, P., Trescol-Bimont, M.-C., Thomas, J., Groth, B. F. d. S., Pihlgren, M., Marvel, J., and Rabourdin-Combe, C. Death by neglect as a deletional mechanism of peripheral tolerance. *International Immunology*, 11(8):1225–1238, August 1999. ISSN 0953-8178, 1460-2377. doi: 10.1093/intimm/11.8.1225.

Blaho, V. A. and Hla, T. An update on the biology of sphingosine 1-phosphate receptors. *Journal of Lipid Research*, 55(8):1596–1608, August 2014. ISSN 1539-7262. doi: 10.1194/jlr.R046300.

Bois, F. Y. Physiologically Based Modelling and Prediction of Drug Interactions. *Basic & Clinical Pharmacology & Toxicology*, 106(3):154–161, March 2010. ISSN 1742-7843. doi: 10.1111/j.1742-7843.2009.00488.x.

Bona, C. A. and Revillard, J.-P. *Cytokines and Cytokine Receptors: Physiology and Pathological Disorders*. CRC Press, March 2001. ISBN 978-90-5702-634-8.

Bonilla, F. A. and Oettgen, H. C. Adaptive immunity. *The Journal of Allergy and Clinical Immunology*, 125(2 Suppl 2):S33–40, February 2010. ISSN 1097-6825. doi: 10.1016/j.jaci.2009.09.017.

Bornstein, B. J., Keating, S. M., Jouraku, A., and Hucka, M. LibSBML: an API library for SBML. *Bioinformatics (Oxford, England)*, 24(6):880–881, March 2008. ISSN 1367-4811. doi: 10.1093/bioinformatics/btn051.

Bosselut, R. CD4/CD8-lineage differentiation in the thymus: from nuclear effectors to membrane signals. *Nature Reviews Immunology*, 4(7):529–540, July 2004. ISSN 1474-1733. doi: 10.1038/nri1392.

Bousso, P. T-cell activation by dendritic cells in the lymph node: lessons from the movies. *Nature Reviews Immunology*, 8(9):675–684, September 2008. ISSN 1474-1733. doi: 10.1038/nri2379.

Bray, T. *Extensible Markup Language (XML) 1.0*. 1998.

Brown, G. R., Lindberg, G., Meddings, J., Silva, M., Beutler, B., and Thiele, D. Tumor necrosis factor inhibitor ameliorates murine intestinal graft-versus-host disease. *Gastroenterology*, 116(3):593–601, March 1999. ISSN 0016-5085.

Brown, R. P., Delp, M. D., Lindstedt, S. L., Rhomberg, L. R., and Beliles, R. P. Physiological parameter values for physiologically based pharmacokinetic models. *Toxicology and Industrial Health*, 13(4):407–484, August 1997. ISSN 0748-2337.

Brucklacher-Waldert, V., Ferreira, C., Innocentin, S., Kamdar, S., Withers, D. R., Kullberg, M. C., and Veldhoen, M. Tbet or Continued RORt Expression Is Not Required for Th17-Associated Immunopathology. *The Journal of Immunology Author Choice*, 196 (12):4893–4904, June 2016. ISSN 0022-1767. doi: 10.4049/jimmunol.1600137.

Buffie, C. G., Jarchum, I., Equinda, M., Lipuma, L., Gobourne, A., Viale, A., Ubeda, C., Xavier, J., and Pamer, E. G. Profound Alterations of Intestinal Microbiota following a Single Dose of Clindamycin Results in Sustained Susceptibility to Clostridium difficile-Induced Colitis. *Infection and Immunity*, 80(1):62–73, January 2012. ISSN 0019-9567. doi: 10.1128/IAI.05496-11.

Butcher, J. A history of Runge-Kutta methods. *Applied Numerical Mathematics*, 20(3): 247–260, March 1996. ISSN 01689274. doi: 10.1016/0168-9274(95)00108-5.

Carbo, A., Bassaganya-Riera, J., Pedragosa, M., Viladomiu, M., Marathe, M., Eubank, S., Wendelsdorf, K., Bisset, K., Hoops, S., Deng, X., Alam, M., Kronsteiner, B., Mei, Y., and Hontecillas, R. Predictive computational modeling of the mucosal immune responses during Helicobacter pylori infection. *PloS One*, 8(9):e73365, 2013. ISSN 1932-6203. doi: 10.1371/journal.pone.0073365.

Celada, F. and Seiden, P. E. Affinity maturation and hypermutation in a simulation of the humoral immune response. *European Journal of Immunology*, 26(6):1350–1358, June 1996. ISSN 0014-2980. doi: 10.1002/eji.1830260626.

Celada, F. and Seiden, P. E. A computer model of cellular interactions in the immune system. *Immunology Today*, 13(2):56–62, February 1992. ISSN 0167-5699. doi: 10.1016/0167-5699(92)90135-T.

Chakraborty, A. K., Dustin, M. L., and Shaw, A. S. In silico models for cellular and molecular immunology: successes, promises and challenges. *Nature Immunology*, 4(10): 933–936, October 2003. ISSN 1529-2908. doi: 10.1038/ni1003-933.

Chan, J. M., Bhinder, G., Sham, H. P., Ryz, N., Huang, T., Bergstrom, K. S., and Vallance, B. A. CD4+ T Cells Drive Goblet Cell Depletion during Citrobacter rodentium Infection. *Infection and Immunity*, 81(12):4649–4658, December 2013. ISSN 0019-9567. doi: 10.1128/IAI.00655-13.

Chen, M., Huang, L., Shabier, Z., and Wang, J. Regulation of the Lifespan in Dendritic Cell Subsets. *Molecular immunology*, 44(10):2558–2565, April 2007. ISSN 0161-5890. doi: 10.1016/j.molimm.2006.12.020.

Chun, J. and Hartung, H.-P. Mechanism of action of oral fingolimod (FTY720) in multiple sclerosis. *Clinical Neuropharmacology*, 33(2):91–101, April 2010. ISSN 1537-162X. doi: 10.1097/WNF.0b013e3181cbf825.

Chun, J., Hla, T., Lynch, K. R., Spiegel, S., and Moolenaar, W. H. International Union of Basic and Clinical Pharmacology. LXXVIII. Lysophospholipid Receptor Nomenclature. *Pharmacological Reviews*, 62(4):579–587, December 2010. ISSN 0031-6997. doi: 10.1124/pr.110.003111.

Cockrell, R. C., Christley, S., Chang, E., and An, G. Towards Anatomic Scale Agent-Based Modeling with a Massively Parallel Spatially Explicit General-Purpose Model of Enteric Tissue (SEGMEnT_hpc). *PLOS ONE*, 10(3):e0122192, March 2015. ISSN 1932-6203. doi: 10.1371/journal.pone.0122192.

Cong, Y., Brandwein, S. L., McCabe, R. P., Lazenby, A., Birkenmeier, E. H., Sundberg, J. P., and Elson, C. O. CD4+ T cells reactive to enteric bacterial antigens in spontaneously colitic C3h/HeJBir mice: increased T helper cell type 1 response and ability to transfer disease. *The Journal of Experimental Medicine*, 187(6):855–864, March 1998. ISSN 0022-1007.

Cope, A. P., Schulze-Koops, H., and Aringer, M. The central role of T cells in rheumatoid arthritis. *Clinical and Experimental Rheumatology*, 25(5 Suppl 46):S4–11, October 2007. ISSN 0392-856X.

Cosgrove, J., Butler, J., Alden, K., Read, M., Kumar, V., Cucurull-Sanchez, L., Timmis, J., and Coles, M. Agent-Based Modeling in Systems Pharmacology. *CPT: Pharmacometrics & Systems Pharmacology*, 4(11):615–629, November 2015. ISSN 2163-8306. doi: 10.1002/psp4.12018.

Cravens, P. D. and Lipsky, P. E. Dendritic cells, chemokine receptors and autoimmune inflammatory diseases. *Immunology and Cell Biology*, 80(5):497–505, October 2002. ISSN 0818-9641. doi: 10.1046/j.1440-1711.2002.01118.x.

Cushing, J. M. Periodic Lotka-Volterra competition equations. *Journal of Mathematical Biology*, 24(4):381–403, 1986. ISSN 0303-6812.

Dampier, W. and Tozeren, A. Signaling perturbations induced by invading H. pylori proteins in the host epithelial cells: A mathematical modeling approach. *Journal of Theoretical Biology*, 248(1):130–144, September 2007. ISSN 0022-5193. doi: 10.1016/j.jtbi.2007.03.014.

Daniel, C., Sartory, N. A., Zahn, N., Schmidt, R., Geisslinger, G., Radeke, H. H., and Stein, J. M. FTY720 ameliorates oxazolone colitis in mice by directly affecting T helper type 2 functions. *Molecular Immunology*, 44(13):3305–3316, July 2007. ISSN 0161-5890. doi: 10.1016/j.molimm.2007.02.026.

D'Argenio, V., Precone, V., Casaburi, G., Miele, E., Martinelli, M., Staiano, A., Salvatore, F., and Sacchetti, L. An Altered Gut Microbiome Profile in a Child Affected by Crohn's Disease Normalized After Nutritional Therapy. *The American Journal of Gastroenterology*, 108(5):851–852, May 2013. ISSN 0002-9270. doi: 10.1038/ajg.2013.46.

Davenport, E. R., Cusanovich, D. A., Michelini, K., Barreiro, L. B., Ober, C., and Gilad, Y. Genome-Wide Association Studies of the Human Gut Microbiota. *PLoS ONE*, 10 (11):e0140301, November 2015. doi: 10.1371/journal.pone.0140301.

De Boer, R. J., Homann, D., and Perelson, A. S. Different dynamics of CD4+ and CD8+ T cell responses during and after acute lymphocytic choriomeningitis virus infection. *Journal of Immunology (Baltimore, Md.: 1950)*, 171(8):3928–3935, October 2003. ISSN 0022-1767.

Deguchi, Y., Andoh, A., Yagi, Y., Bamba, S., Inatomi, O., Tsujikawa, T., and Fujiyama, Y. The S1p receptor modulator FTY720 prevents the development of experimental colitis in mice. *Oncology Reports*, 16(4):699–703, October 2006. ISSN 1021-335X.

Deo, S. S., Mistry, K. J., Kakade, A. M., and Niphadkar, P. V. Role played by Th2 type cytokines in IgE mediated allergy and asthma. *Lung India : Official Organ of Indian Chest Society*, 27(2):66–71, 2010. ISSN 0970-2113. doi: 10.4103/0970-2113.63609.

DeVoss, J. and Diehl, L. Murine models of inflammatory bowel disease (IBD): challenges of modeling human disease. *Toxicologic Pathology*, 42(1):99–110, January 2014. ISSN 1533-1601. doi: 10.1177/0192623313509729.

Dias, O., Rocha, M., Ferreira, E. C., and Rocha, I. Reconstructing genome-scale metabolic models with merlin. *Nucleic Acids Research*, 43(8):3899–3910, April 2015. ISSN 1362-4962. doi: 10.1093/nar/gkv294.

Dieleman, L. A., Arends, A., Tonkonogy, S. L., Goerres, M. S., Craft, D. W., Grenther, W., Sellon, R. K., Balish, E., and Sartor, R. B. Helicobacter hepaticus does not induce or potentiate colitis in interleukin-10-deficient mice. *Infection and Immunity*, 68(9): 5107–5113, September 2000. ISSN 0019-9567.

D'Souza, M. L. a. R. M. A Framework for Megascale Agent Based Model Simulations on Graphics Processing Units, October 2008.

Efroni, S., Harel, D., and Cohen, I. R. Reactive animation: realistic modeling of complex dynamic systems. *Computer*, 38(1):38–47, January 2005. ISSN 0018-9162. doi: 10.1109/MC.2005.31.

Efroni, S., Harel, D., and Cohen, I. R. Toward rigorous comprehension of biological complexity: modeling, execution, and visualization of thymic T-cell maturation. *Genome Research*, 13(11):2485–2497, November 2003. ISSN 1088-9051. doi: 10.1101/gr.1215303.

Elson, C. O., Cong, Y., and Sundberg, J. The C3h/HeJBir mouse model: a high susceptibility phenotype for colitis. *International Reviews of Immunology*, 19(1):63–75, 2000. ISSN 0883-0185.

Elson, C. O. and Cong, Y. Host-microbiota interactions in inflammatory bowel disease. *Gut Microbes*, 3(4):332–344, August 2012. ISSN 1949-0984. doi: 10.4161/gmic.20228.

Eriksson, O., Andersson, T., Zhou, Y., and Tegnr, J. Decoding complex biological networks - tracing essential and modulatory parameters in complex and simplified models of the cell cycle. *BMC Systems Biology*, 5:123, August 2011. ISSN 1752-0509. doi: 10.1186/1752-0509-5-123.

Evans, Stephanie, Cucurull-Sanchez, Lourdes, Larminie, Christopher, Timmis, Jon, Kullberg, Marika, and Alden, Kieran. ASPASIA: A toolkit for evaluating the effects of biological interventions on SBML model behaviour. *PLoS Comput Biol*.

Farache, J., Koren, I., Milo, I., Gurevich, I., Kim, K.-W., Zigmond, E., Furtado, G. C., Lira, S. A., and Shakhar, G. Luminal Bacteria Recruit CD103+ Dendritic Cells into the Intestinal Epithelium to Sample Bacterial Antigens for Presentation. *Immunity*, 38 (3):581–595, March 2013. ISSN 1074-7613. doi: 10.1016/j.immuni.2013.01.009.

Farmer, J. D., Packard, N. H., and Perelson, A. S. The immune system, adaptation, and machine learning. *Physica D: Nonlinear Phenomena*, 22(13):187–204, October 1986. ISSN 0167-2789. doi: 10.1016/0167-2789(86)90240-X.

Feist, A. M., Henry, C. S., Reed, J. L., Krummenacker, M., Joyce, A. R., Karp, P. D., Broadbelt, L. J., Hatzimanikatis, V., and Palsson, B. . A genome-scale metabolic reconstruction for Escherichia coli K-12 MG1655 that accounts for 1260 ORFs and thermodynamic information. *Molecular Systems Biology*, 3, June 2007. ISSN 1744-4292. doi: 10.1038/msb4100155.

Figueredo, G. P., Siebers, P.-O., and Aickelin, U. Investigating mathematical models of immuno-interactions with early-stage cancer under an agent-based modelling perspective. *BMC bioinformatics*, 14 Suppl 6:S6, 2013. ISSN 1471-2105. doi: 10.1186/1471-2105-14-S6-S6.

Fletcher, J. M., Lalor, S. J., Sweeney, C. M., Tubridy, N., and Mills, K. H. G. T cells in multiple sclerosis and experimental autoimmune encephalomyelitis. *Clinical and Experimental Immunology*, 162(1):1–11, October 2010. ISSN 1365-2249. doi: 10.1111/j.1365-2249.2010.04143.x.

Fournier, B. M. and Parkos, C. A. The role of neutrophils during intestinal inflammation. *Mucosal Immunology*, 5(4):354–366, July 2012. ISSN 1933-0219. doi: 10.1038/mi.2012.24.

Fowler, M. *UML Distilled: A Brief Guide to the Standard Object Modeling Language*. Addison-Wesley Longman Publishing Co., Inc., Boston, MA, USA, 3 edition, 2003. ISBN 0-321-19368-7.

Fox, J. G., Dewhirst, F. E., Tully, J. G., Paster, B. J., Yan, L., Taylor, N. S., Collins, M. J., Gorelick, P. L., and Ward, J. M. Helicobacter hepaticus sp. nov., a microaerophilic

bacterium isolated from livers and intestinal mucosal scrapings from mice. *Journal of Clinical Microbiology*, 32(5):1238–1245, May 1994. ISSN 0095-1137.

Francke, C., Siezen, R. J., and Teusink, B. Reconstructing the metabolic network of a bacterium from its genome. *Trends in Microbiology*, 13(11):550–558, November 2005. ISSN 0966-842X. doi: 10.1016/j.tim.2005.09.001.

Frank, D. N., Robertson, C. E., Hamm, C. M., Kpadeh, Z., Zhang, T., Chen, H., Zhu, W., Sartor, R. B., Boedeker, E. C., Harpaz, N., Pace, N. R., and Li, E. Disease phenotype and genotype are associated with shifts in intestinal-associated microbiota in inflammatory bowel diseases. *Inflammatory Bowel Diseases*, 17(1):179–184, January 2011. ISSN 1536-4844. doi: 10.1002/ibd.21339.

Franz, M. and Nunn, C. L. Network-based diffusion analysis: a new method for detecting social learning. *Proceedings of the Royal Society of London B: Biological Sciences*, 276 (1663):1829–1836, May 2009. ISSN 0962-8452, 1471-2954. doi: 10.1098/rspb.2008.1824.

Freitas, A. A., Rocha, B., and Bognacki, J. Effects of Intravenous Administration of Antigen on Lymphocyte Localization and Blood Flow into the Mouse Spleen. *Acta Mdica Portuguesa*, 4(3):147–150, March 1983. ISSN 0870-399X. doi: 10.20344/amp.3784.

Friedman, J. and Alm, E. J. Inferring correlation networks from genomic survey data. *PLoS computational biology*, 8(9):e1002687, 2012. ISSN 1553-7358. doi: 10.1371/journal.pcbi.1002687.

Fujii, R., Kanai, T., Nemoto, Y., Makita, S., Oshima, S., Okamoto, R., Tsuchiya, K., Totsuka, T., and Watanabe, M. FTY720 suppresses CD4+CD44highcd62l- effector memory T cell-mediated colitis. *American Journal of Physiology. Gastrointestinal and Liver Physiology*, 291(2):G267–274, August 2006. ISSN 0193-1857. doi: 10.1152/ajpgi.00496.2005.

Fujii, Y., Hirayama, T., Ohtake, H., Ono, N., Inoue, T., Sakurai, T., Takayama, T., Matsumoto, K., Tsukahara, N., Hidano, S., Harima, N., Nakazawa, K., Igarashi, Y., and Goitsuka, R. Amelioration of collagen-induced arthritis by a novel S1p1 antagonist with immunomodulatory activities. *Journal of Immunology (Baltimore, Md.: 1950)*, 188(1):206–215, January 2012. ISSN 1550-6606. doi: 10.4049/jimmunol.1101537.

Funahashi, A., Matsuoka, Y., Jouraku, A., Morohashi, M., Kikuchi, N., and Kitano, H. CellDesigner 3.5: A Versatile Modeling Tool for Biochemical Networks. *Proceedings of the IEEE*, 96(8):1254–1265, August 2008. ISSN 0018-9219. doi: 10.1109/JPROC.2008.925458.

Gallo, R. L. and Hooper, L. V. Epithelial antimicrobial defence of the skin and intestine. *Nature Reviews Immunology*, 12(7):503–516, July 2012. ISSN 1474-1733. doi: 10.1038/nri3228.

Garnett, P., Stepney, S., Day, F., and Layser, O. Towards an Executable Model of Auxin Transport Canalisation. In *Proceedings of the 2008 workshop on complex systems modelling and simulation*, pages 63–91. 2008.

Ge, Z., White, D. A., Whary, M. T., and Fox, J. G. Fluorogenic PCR-based quantitative detection of a murine pathogen, Helicobacter hepaticus. *Journal of Clinical Microbiology*, 39(7):2598–2602, July 2001. ISSN 0095-1137. doi: 10.1128/JCM.39.7.2598-2602.2001.

Germain, R. N., Meier-schellersheim, M., Nita-lazar, A., and Fraser, I. D. C. Systems Biology in Immunology : A Computational Modeling Perspective. *Annual Review of Immunology*, 29:527–585, 2011.

Gong, C., Mattila, J. T., Miller, M., Flynn, J. L., Linderman, J. J., and Kirschner, D. Predicting lymph node output efficiency using systems biology. *Journal of Theoretical Biology*, 335:169–184, October 2013. ISSN 0022-5193. doi: 10.1016/j.jtbi.2013.06.016.

Graeler, M., Shankar, G., and Goetzl, E. J. Cutting edge: suppression of T cell chemotaxis by sphingosine 1-phosphate. *Journal of Immunology (Baltimore, Md.: 1950)*, 169(8): 4084–4087, October 2002. ISSN 0022-1767.

Grein, S., Stepniewski, M., Reiter, S., Knodel, M. M., and Queisser, G. 1d-3d hybrid modelingfrom multi-compartment models to full resolution models in space and time. *Frontiers in Neuroinformatics*, 8, July 2014. ISSN 1662-5196. doi: 10.3389/fninf.2014.00068.

Griffin, G. K., Newton, G., Tarrio, M. L., Bu, D.-x., Maganto-Garcia, E., Azcutia, V., Alcaide, P., Grabie, N., Luscinskas, F. W., Croce, K. J., and Lichtman, A. H. IL-17 and

TNF- sustain neutrophil recruitment during inflammation through synergistic effects on endothelial activation. *Journal of Immunology (Baltimore, Md.: 1950)*, 188(12): 6287–6299, June 2012. ISSN 1550-6606. doi: 10.4049/jimmunol.1200385.

Grimm, V., Berger, U., Bastiansen, F., Eliassen, S., Ginot, V., Giske, J., Goss-Custard, J., Grand, T., Heinz, S. K., Huse, G., Huth, A., Jepsen, J. U., Jrgensen, C., Mooij, W. M., Mller, B., Peer, G., Piou, C., Railsback, S. F., Robbins, A. M., Robbins, M. M., Rossmanith, E., Rger, N., Strand, E., Souissi, S., Stillman, R. A., Vab, R., Visser, U., and DeAngelis, D. L. A standard protocol for describing individual-based and agent-based models. *Ecological Modelling*, 198(12):115–126, September 2006. ISSN 0304-3800. doi: 10.1016/j.ecolmodel.2006.04.023.

Guinane, C. M. and Cotter, P. D. Role of the gut microbiota in health and chronic gastrointestinal disease: understanding a hidden metabolic organ. *Therapeutic Advances in Gastroenterology*, 6(4):295–308, July 2013. ISSN 1756-283X. doi: 10.1177/1756283X13482996.

Gunn, M. D., Tangemann, K., Tam, C., Cyster, J. G., Rosen, S. D., and Williams, L. T. A chemokine expressed in lymphoid high endothelial venules promotes the adhesion and chemotaxis of naive T lymphocytes. *Proceedings of the National Academy of Sciences*, 95(1):258–263, January 1998. ISSN 0027-8424, 1091-6490.

Haller, D., Bode, C., Hammes, W., Pfeifer, A., Schiffrin, E., and Blum, S. Non-pathogenic bacteria elicit a differential cytokine response by intestinal epithelial cell/leucocyte co-cultures. *Gut*, 47(1):79–87, July 2000. ISSN 0017-5749. doi: 10.1136/gut.47.1.79.

Hayes, A. W. and Kruger, C. L. *Hayes' Principles and Methods of Toxicology, Sixth Edition*. CRC Press, October 2014. ISBN 978-1-84214-537-1.

Helton, J. C. Uncertainty and Sensitivity Analysis for Models of Complex Systems. In Graziani, F., editor, *Computational Methods in Transport: Verification and Validation*, number 62 in Lecture Notes in Computational Science and Engineering, pages 207–228. Springer Berlin Heidelberg, January 2008. ISBN 978-3-540-77361-0 978-3-540-77362-7.

Hoops, S., Mendes, P., Sahle, S., Gauges, R., Lee, C., Pahle, J., Simus, N., Singhal,

M., Xu, L., Mendes, P., and Kummer, U. COPASI: a COmplex PAthway SImulator. *Bioinformatics*, (22):3067–74, 2006.

Hucka, M., Finney, a., Sauro, H. M., Bolouri, H., Doyle, J. C., Kitano, H., Arkin, a. P., Bornstein, B. J., Bray, D., Cornish-Bowden, a., Cuellar, a. a., Dronov, S., Gilles, E. D., Ginkel, M., Gor, V., Goryanin, I. I., Hedley, W. J., Hodgman, T. C., Hofmeyr, J.-H., Hunter, P. J., Juty, N. S., Kasberger, J. L., Kremling, a., Kummer, U., Le Novere, N., Loew, L. M., Lucio, D., Mendes, P., Minch, E., Mjolsness, E. D., Nakayama, Y., Nelson, M. R., Nielsen, P. F., Sakurada, T., Schaff, J. C., Shapiro, B. E., Shimizu, T. S., Spence, H. D., Stelling, J., Takahashi, K., Tomita, M., Wagner, J., and Wang, J. The systems biology markup language (SBML): a medium for representation and exchange of biochemical network models. *Bioinformatics*, 19(4):524–531, March 2003. ISSN 1367-4803. doi: 10.1093/bioinformatics/btg015.

Italiani, P. and Boraschi, D. From Monocytes to M1/M2 Macrophages: Phenotypical vs. Functional Differentiation. *Frontiers in Immunology*, 5, October 2014. ISSN 1664-3224. doi: 10.3389/fimmu.2014.00514.

Jaensson, E., Uronen-Hansson, H., Pabst, O., Eksteen, B., Tian, J., Coombes, J. L., Berg, P.-L., Davidsson, T., Powrie, F., Johansson-Lindbom, B., and Agace, W. W. Small intestinal CD103+ dendritic cells display unique functional properties that are conserved between mice and humans. *The Journal of Experimental Medicine*, 205(9): 2139–2149, September 2008. ISSN 1540-9538. doi: 10.1084/jem.20080414.

Jakobsson, H. E., Rodrguez-Pieiro, A. M., Schtte, A., Ermund, A., Boysen, P., Bemark, M., Sommer, F., Bckhed, F., Hansson, G. C., and Johansson, M. E. V. The composition of the gut microbiota shapes the colon mucus barrier. *EMBO reports*, 16(2):164–177, February 2015. ISSN 1469-3178. doi: 10.15252/embr.201439263.

Janeway, C. A., Travers, P., Walport, M., Shlomchik, M. J., Jr, C. A. J., Travers, P., Walport, M., and Shlomchik, M. J. *Immunobiology*. Garland Science, 5th edition, 2001. ISBN 0-8153-3642-X.

Janssen, B., Debets, J., Leenders, P., and Smits, J. Chronic measurement of cardiac output in conscious mice. *American Journal of Physiology. Regulatory, Integrative*

and Comparative Physiology, 282(3):R928–935, March 2002. ISSN 0363-6119. doi: 10.1152/ajpregu.00406.2001.

Jelley-Gibbs, D. M., Lepak, N. M., Yen, M., and Swain, S. L. Two Distinct Stages in the Transition from Naive CD4 T Cells to Effectors, Early Antigen-Dependent and Late Cytokine-Driven Expansion and Differentiation. *The Journal of Immunology*, 165(9):5017–5026, November 2000. ISSN 0022-1767, 1550-6606. doi: 10.4049/jimmunol.165.9.5017.

Jurjus, A. R., Khoury, N. N., and Reimund, J.-M. Animal models of inflammatory bowel disease. *Journal of Pharmacological and Toxicological Methods*, 50(2):81–92, October 2004. ISSN 1056-8719. doi: 10.1016/j.vascn.2003.12.002.

Kaiser, G. C. and Polk, D. B. Tumor necrosis factor alpha regulates proliferation in a mouse intestinal cell line. *Gastroenterology*, 112(4):1231–1240, April 1997. ISSN 0016-5085.

Kamath, A. T., Henri, S., Battye, F., Tough, D. F., and Shortman, K. Developmental kinetics and lifespan of dendritic cells in mouse lymphoid organs. *Blood*, 100(5):1734–1741, September 2002. ISSN 0006-4971.

Kamdar, S. R. *Profiling of microRNAs and IL-10 expression in intestinal CD4+ T cells following infection with Helicobacter hepaticus*. Ph.D., University of York, 2015.

Kaminska, B., Wesolowska, A., and Danilkiewicz, M. TGF beta signalling and its role in tumour pathogenesis. *Acta Biochimica Polonica*, 52(2):329–337, 2005. ISSN 1734-154X.

Kang, S., Kahan, S., McDermott, J., Flann, N., and Shmulevich, I. Biocellion: Accelerating Computer Simulation of Multicellular Biological System Models. *Bioinformatics*, page btu498, July 2014. ISSN 1367-4803, 1460-2059. doi: 10.1093/bioinformatics/btu498.

Kaplan, G. G. The global burden of IBD: from 2015 to 2025. *Nature Reviews. Gastroenterology & Hepatology*, 12(12):720–727, December 2015. ISSN 1759-5053. doi: 10.1038/nrgastro.2015.150.

Kataoka, H., Sugahara, K., Shimano, K., Teshima, K., Koyama, M., Fukunari, A., and Chiba, K. FTY720, sphingosine 1-phosphate receptor modulator, ameliorates experimental autoimmune encephalomyelitis by inhibition of T cell infiltration. *Cellular & Molecular Immunology*, 2(6):439–448, December 2005. ISSN 1672-7681.

Kettle, H., Louis, P., Holtrop, G., Duncan, S. H., and Flint, H. J. Modelling the emergent dynamics and major metabolites of the human colonic microbiota. *Environmental Microbiology*, 17(5):1615–1630, May 2015. ISSN 1462-2920. doi: 10.1111/1462-2920.12599.

Kim, C. S., Lee, S. C., Kim, Y. M., Kim, B. S., Choi, H. S., Kawada, T., Kwon, B. S., and Yu, R. Visceral fat accumulation induced by a high-fat diet causes the atrophy of mesenteric lymph nodes in obese mice. *Obesity (Silver Spring, Md.)*, 16(6):1261–1269, June 2008. ISSN 1930-7381. doi: 10.1038/oby.2008.55.

Kirschner, D. E., Hunt, C. A., Marino, S., Fallahi-Sichani, M., and Linderman, J. J. Tuneable resolution as a systems biology approach for multi-scale, multi-compartment computational models. *Wiley Interdisciplinary Reviews: Systems Biology and Medicine*, 6(4):289–309, July 2014. ISSN 1939-005X. doi: 10.1002/wsbm.1270.

Kislitsyn, A., Savinkov, R., Novkovic, M., Onder, L., and Bocharov, G. Computational Approach to 3d Modeling of the Lymph Node Geometry. *Computation*, 3(2):222–234, May 2015. doi: 10.3390/computation3020222.

Koboziev, I., Karlsson, F., and Grisham, M. B. Gut-associated lymphoid tissue, T cell trafficking, and chronic intestinal inflammation. *Annals of the New York Academy of Sciences*, 1207(Suppl 1):E86–E93, October 2010. ISSN 0077-8923. doi: 10.1111/j.1749-6632.2010.05711.x.

Kolaczkowska, E. and Kubes, P. Neutrophil recruitment and function in health and inflammation. *Nature Reviews Immunology*, 13(3):159–175, March 2013. ISSN 1474-1733. doi: 10.1038/nri3399.

Korn, T., Bettelli, E., Oukka, M., and Kuchroo, V. K. IL-17 and Th17 Cells. *Annual Review of Immunology*, 27(1):485–517, 2009. doi: 10.1146/annurev.immunol.021908.132710.

Kranzer, K., Eckhardt, A., Aigner, M., Knoll, G., Deml, L., Speth, C., Lehn, N., Rehli, M., and Schneider-Brachert, W. Induction of Maturation and Cytokine Release of Human Dendritic Cells by Helicobacter pylori. *Infection and Immunity*, 72(8):4416–4423, August 2004. ISSN 0019-9567. doi: 10.1128/IAI.72.8.4416-4423.2004.

Krombach, F., Mnzing, S., Allmeling, A. M., Gerlach, J. T., Behr, J., and Drger, M. Cell size of alveolar macrophages: an interspecies comparison. *Environmental Health Perspectives*, 105(Suppl 5):1261–1263, September 1997. ISSN 0091-6765.

Kullberg, M. C., Ward, J. M., Gorelick, P. L., Caspar, P., Hieny, S., Cheever, A., Jankovic, D., and Sher, A. Helicobacter hepaticus triggers colitis in specific-pathogen-free interleukin-10 (IL-10)-deficient mice through an IL-12- and gamma interferon-dependent mechanism. *Infection and Immunity*, 66(11):5157–5166, November 1998. ISSN 0019-9567.

Kullberg, M. C., Rothfuchs, A. G., Jankovic, D., Caspar, P., Wynn, T. A., Gorelick, P. L., Cheever, A. W., and Sher, A. Helicobacter hepaticus-induced colitis in interleukin-10-deficient mice: cytokine requirements for the induction and maintenance of intestinal inflammation. *Infection and Immunity*, 69(7):4232–4241, July 2001. ISSN 0019-9567. doi: 10.1128/IAI.69.7.4232-4241.2001.

Kullberg, M. C., Jankovic, D., Gorelick, P. L., Caspar, P., Letterio, J. J., Cheever, A. W., and Sher, A. Bacteria-triggered CD4+ T Regulatory Cells Suppress Helicobacter hepaticusinduced Colitis. *The Journal of Experimental Medicine*, 196(4):505–515, August 2002. ISSN 0022-1007. doi: 10.1084/jem.20020556.

Kullberg, M. C., Jankovic, D., Feng, C. G., Hue, S., Gorelick, P. L., McKenzie, B. S., Cua, D. J., Powrie, F., Cheever, A. W., Maloy, K. J., and Sher, A. IL-23 plays a key role in Helicobacter hepaticus-induced T cell-dependent colitis. *The Journal of Experimental Medicine*, 203(11):2485–2494, October 2006. ISSN 0022-1007. doi: 10.1084/jem.20061082.

Kuznetsov, Y. A. *Elements of Applied Bifurcation Theory*, volume 112 of *Applied Mathematical Sciences*. Springer New York, New York, NY, 2004. ISBN 978-1-4419-1951-9 978-1-4757-3978-7.

Khn, R., Lhler, J., Rennick, D., Rajewsky, K., and Mller, W. Interleukin-10-deficient mice develop chronic enterocolitis. *Cell*, 75(2):263–274, October 1993. ISSN 0092-8674.

Larsen, L. G., Harvey, J. W., Nes, A. E. E. H. v., and DeAngelis, E. D. L. How Vegetation and Sediment Transport Feedbacks Drive Landscape Change in the Everglades and Wetlands Worldwide. *The American Naturalist*, 176(3):E66–E79, 2010. ISSN 0003-0147. doi: 10.1086/655215.

Law, A. M. and McComas, M. G. Secrets of successful simulation studies. In *Simulation Conference, 1991. Proceedings., Winter*, pages 21–27, December 1991. doi: 10.1109/WSC.1991.185587.

Leber, A., Viladomiu, M., Hontecillas, R., Abedi, V., Philipson, C., Hoops, S., Howard, B., and Bassaganya-Riera, J. Systems Modeling of Interactions between Mucosal Immunity and the Gut Microbiome during Clostridium difficile Infection. *PLoS ONE*, 10 (7):e0134849, July 2015. doi: 10.1371/journal.pone.0134849.

Lee, H. Y., Topham, D. J., Park, S. Y., Hollenbaugh, J., Treanor, J., Mosmann, T. R., Jin, X., Ward, B. M., Miao, H., Holden-Wiltse, J., Perelson, A. S., Zand, M., and Wu, H. Simulation and prediction of the adaptive immune response to influenza A virus infection. *Journal of Virology*, 83(14):7151–7165, July 2009. ISSN 1098-5514. doi: 10.1128/JVI.00098-09.

Leonov, G. *An integrated molecular cell biology and agent-based simulation approach to dissecting microRNA regulatory networks.* phd, University of York, September 2015.

Ley, K. and Morris, M. Signals for lymphocyte egress. *Nature Immunology*, 6(12):1215–1216, December 2005. ISSN 1529-2908. doi: 10.1038/ni1205-1215.

Li, C., Donizelli, M., Rodriguez, N., Dharuri, H., Endler, L., Chelliah, V., Li, L., He, E., Henry, A., Stefan, M. I., Snoep, J. L., Hucka, M., Le Novre, N., and Laibe, C. BioModels Database: An enhanced, curated and annotated resource for published quantitative kinetic models. *BMC Systems Biology*, 4:92, June 2010.

Linderman, J. J. and Kirschner, D. E. In silico models of M. tuberculosis infection provide

a route to new therapies. *Drug Discovery Today: Disease Models*, 15:37–41, 2015. ISSN 1740-6757. doi: 10.1016/j.ddmod.2014.02.006.

Linderman, J. J., Riggs, T., Pande, M., Miller, M., Marino, S., and Kirschner, D. E. Characterizing the dynamics of CD4+ T cell priming within a lymph node. *Journal of Immunology (Baltimore, Md.: 1950)*, 184(6):2873–2885, March 2010. ISSN 1550-6606. doi: 10.4049/jimmunol.0903117.

Littman, D. R. and Pamer, E. G. Role of the commensal microbiota in normal and pathogenic host immune responses. *Cell Host & Microbe*, 10(4):311–323, October 2011. ISSN 1934-6069. doi: 10.1016/j.chom.2011.10.004.

Lloyd, C. M., Halstead, M. D. B., and Nielsen, P. F. CellML: its future, present and past. *Progress in Biophysics and Molecular Biology*, 85(2-3):433–450, July 2004. ISSN 0079-6107. doi: 10.1016/j.pbiomolbio.2004.01.004.

Lo, W.-C., Arsenescu, R. I., and Friedman, A. Mathematical model of the roles of T cells in inflammatory bowel disease. *Bulletin of Mathematical Biology*, 75(9):1417–1433, September 2013. ISSN 1522-9602. doi: 10.1007/s11538-013-9853-2.

Lokeshwar. *Textbook of Neonatal Haematology-Oncology*. Jaypee Brothers Publishers, January 2003. ISBN 978-81-8061-117-9.

Lopetuso, L. R., Scaldaferri, F., Petito, V., and Gasbarrini, A. Commensal Clostridia: leading players in the maintenance of gut homeostasis. *Gut Pathogens*, 5:23, August 2013. ISSN 1757-4749. doi: 10.1186/1757-4749-5-23.

Luke, S., Cioffi-Revilla, C., Panait, L., Sullivan, K., and Balan, G. MASON: A Multiagent Simulation Environment. *SIMULATION*, 81(7):517–527, July 2005. ISSN 0037-5497, 1741-3133. doi: 10.1177/0037549705058073.

Lythe, G., Callard, R. E., Hoare, R. L., and Molina-Pars, C. How many TCR clonotypes does a body maintain? *Journal of Theoretical Biology*, 389:214–224, January 2016. ISSN 0022-5193. doi: 10.1016/j.jtbi.2015.10.016.

Lytton, W. W., Neymotin, S. A., and Hines, M. L. The virtual slice setup. *Journal of Neuroscience Methods*, 171(2):309–315, June 2008. ISSN 0165-0270. doi: 10.1016/j.jneumeth.2008.03.005.

Mandl, J. N., Liou, R., Klauschen, F., Vrisekoop, N., Monteiro, J. P., Yates, A. J., Huang, A. Y., and Germain, R. N. Quantification of lymph node transit times reveals differences in antigen surveillance strategies of naive CD4+ and CD8+ T cells. *Proceedings of the National Academy of Sciences of the United States of America*, 109(44):18036–18041, October 2012. ISSN 1091-6490. doi: 10.1073/pnas.1211717109.

Manes, N. P., Angermann, B. R., Koppenol-Raab, M., An, E., Sjoelund, V. H., Sun, J., Ishii, M., Germain, R. N., Meier-Schellersheim, M., and Nita-Lazar, A. Targeted Proteomics-Driven Computational Modeling of Macrophage S1p Chemosensing. *Molecular & Cellular Proteomics*, page mcp.M115.048918, July 2015. ISSN 1535-9476, 1535-9484. doi: 10.1074/mcp.M115.048918.

Mankertz, J., Tavalali, S., Schmitz, H., Mankertz, A., Riecken, E. O., Fromm, M., and Schulzke, J. D. Expression from the human occludin promoter is affected by tumor necrosis factor alpha and interferon gamma. *Journal of Cell Science*, 113 (Pt 11): 2085–2090, June 2000. ISSN 0021-9533.

Mann, E. R. and Li, X. Intestinal antigen-presenting cells in mucosal immune homeostasis: Crosstalk between dendritic cells, macrophages and B-cells. *World Journal of Gastroenterology : WJG*, 20(29):9653–9664, August 2014. ISSN 1007-9327. doi: 10.3748/wjg.v20.i29.9653.

Marchuk, G. I. *Mathematical Modelling of Immune Response in Infectious Diseases*. Springer Science & Business Media, April 2013. ISBN 978-94-015-8798-3.

Marino, S., Hogue, I. B., Ray, C. J., and Kirschner, D. E. A methodology for performing global uncertainty and sensitivity analysis in systems biology. *Journal of Theoretical Biology*, 254(1):178–196, September 2008. ISSN 0022-5193. doi: 10.1016/j.jtbi.2008.04.011.

Marino, S., Myers, A., Flynn, J. L., and Kirschner, D. E. TNF and IL-10 are major factors in modulation of the phagocytic cell environment in lung and lymph node in tuberculosis:

A next-generation two-compartmental model. *Journal of Theoretical Biology*, 265(4): 586–598, August 2010. ISSN 0022-5193. doi: 10.1016/j.jtbi.2010.05.012.

Martin, F.-P. J., Dumas, M.-E., Wang, Y., Legido-Quigley, C., Yap, I. K. S., Tang, H., Zirah, S., Murphy, G. M., Cloarec, O., Lindon, J. C., Sprenger, N., Fay, L. B., Kochhar, S., van Bladeren, P., Holmes, E., and Nicholson, J. K. A top-down systems biology view of microbiome-mammalian metabolic interactions in a mouse model. *Molecular Systems Biology*, 3:112, 2007. ISSN 1744-4292. doi: 10.1038/msb4100153.

Martn-Fontecha, A., Sebastiani, S., Hpken, U. E., Uguccioni, M., Lipp, M., Lanzavecchia, A., and Sallusto, F. Regulation of Dendritic Cell Migration to the Draining Lymph Node. *The Journal of Experimental Medicine*, 198(4):615–621, August 2003. ISSN 0022-1007. doi: 10.1084/jem.20030448.

Marzio, P. D., Puddu, P., Conti, L., Belardelli, F., and Gessani, S. Interferon gamma upregulates its own gene expression in mouse peritoneal macrophages. *The Journal of Experimental Medicine*, 179(5):1731–1736, May 1994. ISSN 0022-1007, 1540-9538. doi: 10.1084/jem.179.5.1731.

Matloubian, M., Lo, C. G., Cinamon, G., Lesneski, M. J., Xu, Y., Brinkmann, V., Allende, M. L., Proia, R. L., and Cyster, J. G. Lymphocyte egress from thymus and peripheral lymphoid organs is dependent on S1p receptor 1. *Nature*, 427(6972):355–360, January 2004. ISSN 1476-4687. doi: 10.1038/nature02284.

Matsumoto, S., Okabe, Y., Setoyama, H., Takayama, K., Ohtsuka, J., Funahashi, H., Imaoka, A., Okada, Y., and Umesaki, Y. Inflammatory bowel disease-like enteritis and caecitis in a senescence accelerated mouse P1/Yit strain. *Gut*, 43(1):71–78, July 1998. ISSN , 1468-3288. doi: 10.1136/gut.43.1.71.

Mc Auley, M. T., Choi, H., Mooney, K., Paul, E., Miller, V. M., Mc Auley, M. T., Choi, H., Mooney, K., Paul, E., and Miller, V. M. Systems Biology and Synthetic Biology: A New Epoch for Toxicology Research, Systems Biology and Synthetic Biology: A New Epoch for Toxicology Research. *Advances in Toxicology, Advances in Toxicology*, 2015, 2015:e575403, January 2015. ISSN 2356-6906, 2356-6906. doi: 10.1155/2015/575403, 10.1155/2015/575403.

McKay, M. D., Beckman, R. J., and Conover, W. J. A comparison of three methods for selecting values of input variables in the analysis of output from a computer code. *Techometrics*, 21:239–245, 1979.

Meier-Schellersheim, M., Xu, X., Angermann, B., Kunkel, E. J., Jin, T., and Germain, R. N. Key role of local regulation in chemosensing revealed by a new molecular interaction-based modeling method. *PLoS computational biology*, 2(7):e82, July 2006. ISSN 1553-7358. doi: 10.1371/journal.pcbi.0020082.

Mencl, S., Hennig, N., Hopp, S., Schuhmann, M. K., Albert-Weissenberger, C., Sirn, A.-L., and Kleinschnitz, C. FTY720 does not protect from traumatic brain injury in mice despite reducing posttraumatic inflammation. *Journal of Neuroimmunology*, 274(12): 125–131, September 2014. ISSN 0165-5728. doi: 10.1016/j.jneuroim.2014.07.010.

Meno-Tetang, G. M. L., Li, H., Mis, S., Pyszczynski, N., Heining, P., Lowe, P., and Jusko, W. J. Physiologically based pharmacokinetic modeling of FTY720 (2-amino-2[2-(-4-octylphenyl)ethyl]propane-1,3-diol hydrochloride) in rats after oral and intravenous doses. *Drug Metabolism and Disposition: The Biological Fate of Chemicals*, 34(9):1480–1487, September 2006. ISSN 0090-9556. doi: 10.1124/dmd.105.009001.

Meurant, G. *The Bacteria: Molecular Basis of Bacterial Pathogenesis*. Academic Press, December 2012. ISBN 978-0-323-13760-7.

Miller, M. J., Safrina, O., Parker, I., and Cahalan, M. D. Imaging the Single Cell Dynamics of CD4+ T Cell Activation by Dendritic Cells in Lymph Nodes. *The Journal of Experimental Medicine*, 200(7):847–856, October 2004. ISSN 0022-1007. doi: 10.1084/jem.20041236.

Minkoff, S. E. and Kridler, N. M. A comparison of adaptive time stepping methods for coupled flow and deformation modeling. *Applied Mathematical Modelling*, 30(9):993–1009, September 2006. ISSN 0307-904X. doi: 10.1016/j.apm.2005.08.002.

Mirsky, H. P., Miller, M. J., Linderman, J. J., and Kirschner, D. E. Systems biology approaches for understanding cellular mechanisms of immunity in lymph nodes during infection. *Journal of theoretical biology*, 287:160–170, October 2011. ISSN 0022-5193. doi: 10.1016/j.jtbi.2011.06.037.

Mizushima, T., Ito, T., Kishi, D., Kai, Y., Tamagawa, H., Nezu, R., Kiyono, H., and Matsuda, H. Therapeutic effects of a new lymphocyte homing reagent FTY720 in interleukin-10 gene-deficient mice with colitis. *Inflammatory Bowel Diseases*, 10(3): 182–192, May 2004. ISSN 1078-0998.

Molina-Pars, C. and Lythe, G. *Mathematical Models and Immune Cell Biology*. Springer Science & Business Media, May 2011. ISBN 978-1-4419-7725-0.

Moore, K. W., Malefyt, R. d. W., Coffman, R. L., and O'Garra, A. Interleukin-10 and the Interleukin-10 Receptor. *Annual Review of Immunology*, 19(1):683–765, 2001. doi: 10.1146/annurev.immunol.19.1.683.

Moorthy, A. S., Brooks, S. P. J., Kalmokoff, M., and Eberl, H. J. A Spatially Continuous Model of Carbohydrate Digestion and Transport Processes in the Colon. *PLOS ONE*, 10(12):e0145309, December 2015. ISSN 1932-6203. doi: 10.1371/journal.pone.0145309.

Morris, G. P., Beck, P. L., Herridge, M. S., Depew, W. T., Szewczuk, M. R., and Wallace, J. L. Hapten-induced model of chronic inflammation and ulceration in the rat colon. *Gastroenterology*, 96(3):795–803, March 1989. ISSN 0016-5085.

Morrison, P. J., Bending, D., Fouser, L. A., Wright, J. F., Stockinger, B., Cooke, A., and Kullberg, M. C. Th17-cell plasticity in Helicobacter hepaticusinduced intestinal inflammation. *Mucosal Immunology*, 6(6):1143–1156, November 2013. ISSN 1933-0219. doi: 10.1038/mi.2013.11.

Morrison, P. J., Ballantyne, S. J., and Kullberg, M. C. Interleukin-23 and T helper 17-type responses in intestinal inflammation: from cytokines to T-cell plasticity. *Immunology*, 133(4):397–408, August 2011. ISSN 0019-2805. doi: 10.1111/j.1365-2567.2011.03454.x.

Morrissey, P. J., Charrier, K., Braddy, S., Liggitt, D., and Watson, J. D. CD4+ T cells that express high levels of CD45rb induce wasting disease when transferred into congenic severe combined immunodeficient mice. Disease development is prevented by cotransfer of purified CD4+ T cells. *The Journal of Experimental Medicine*, 178(1):237–244, July 1993. ISSN 0022-1007.

Mosmann, T. R., Cherwinski, H., Bond, M. W., Giedlin, M. A., and Coffman, R. L. Two types of murine helper T cell clone. I. Definition according to profiles of lymphokine activities and secreted proteins. *Journal of Immunology (Baltimore, Md.: 1950)*, 136 (7):2348–2357, April 1986. ISSN 0022-1767.

Moyo, D. *Investigating the dynamics of hepatic inflammation through simulation.* Ph.D., University of York, 2014.

Mukherjee, S., Zheng, H., Derebe, M. G., Callenberg, K. M., Partch, C. L., Rollins, D., Propheter, D. C., Rizo, J., Grabe, M., Jiang, Q.-X., and Hooper, L. V. Antibacterial membrane attack by a pore-forming intestinal C-type lectin. *Nature*, 505(7481):103–107, January 2014. ISSN 0028-0836. doi: 10.1038/nature12729.

Muniz, L. R., Knosp, C., and Yeretssian, G. Intestinal antimicrobial peptides during homeostasis, infection, and disease. *Frontiers in Immunology*, 3, October 2012. ISSN 1664-3224. doi: 10.3389/fimmu.2012.00310.

Murphy, C. T., Hall, L. J., Hurley, G., Quinlan, A., MacSharry, J., Shanahan, F., Nally, K., and Melgar, S. The Sphingosine-1-Phosphate Analogue FTY720 Impairs Mucosal Immunity and Clearance of the Enteric Pathogen Citrobacter rodentium. *Infection and Immunity*, 80(8):2712–2723, August 2012. ISSN 0019-9567. doi: 10.1128/IAI.06319-11.

Nagalingam, N. A., Robinson, C. J., Bergin, I. L., Eaton, K. A., Huffnagle, G. B., and Young, V. B. The effects of intestinal microbial community structure on disease manifestation in IL-10-/- mice infected with Helicobacter hepaticus. *Microbiome*, 1:15, May 2013. ISSN 2049-2618. doi: 10.1186/2049-2618-1-15.

Nicoletti, C., Arques, J. L., and Bertelli, E. CX3cr1 is critical for Salmonella-induced migration of dendritic cells into the intestinal lumen. *Gut Microbes*, 1(3):131–134, 2010. ISSN 1949-0976. doi: 10.4161/gmic.1.3.11711.

Niess, J. H., Brand, S., Gu, X., Landsman, L., Jung, S., McCormick, B. A., Vyas, J. M., Boes, M., Ploegh, H. L., Fox, J. G., Littman, D. R., and Reinecker, H.-C. CX3cr1-mediated dendritic cell access to the intestinal lumen and bacterial clearance. *Science (New York, N.Y.)*, 307(5707):254–258, January 2005. ISSN 1095-9203. doi: 10.1126/science.1102901.

North, M. J., Collier, N. T., Ozik, J., Tatara, E. R., Macal, C. M., Bragen, M., and Sydelko, P. Complex adaptive systems modeling with Repast Simphony. *Complex Adaptive Systems Modeling*, 1(1):3, March 2013. ISSN 2194-3206. doi: 10.1186/2194-3206-1-3.

Ntranos, A., Hall, O., Robinson, D. P., Grishkan, I. V., Schott, J. T., Tosi, D. M., Klein, S. L., Calabresi, P. A., and Gocke, A. R. FTY720 impairs CD8 T-cell function independently of the sphingosine-1-phosphate pathway. *Journal of Neuroimmunology*, 270 (1-2):13–21, May 2014. ISSN 1872-8421. doi: 10.1016/j.jneuroim.2014.03.007.

Okayasu, I., Hatakeyama, S., Yamada, M., Ohkusa, T., Inagaki, Y., and Nakaya, R. A novel method in the induction of reliable experimental acute and chronic ulcerative colitis in mice. *Gastroenterology*, 98(3):694–702, March 1990. ISSN 0016-5085.

Onsum, M. and Rao, C. V. A Mathematical Model for Neutrophil Gradient Sensing and Polarization. *PLoS Comput Biol*, 3(3):e36, March 2007. doi: 10.1371/journal.pcbi.0030036.

O'Shea, J. J. and Paul, W. E. Mechanisms underlying lineage commitment and plasticity of helper CD4+ T cells. *Science (New York, N.Y.)*, 327(5969):1098–1102, February 2010. ISSN 0036-8075. doi: 10.1126/science.1178334.

Ostaff, M. J., Stange, E. F., and Wehkamp, J. Antimicrobial peptides and gut microbiota in homeostasis and pathology. *EMBO Molecular Medicine*, 5(10):1465–1483, October 2013. ISSN 1757-4676. doi: 10.1002/emmm.201201773.

Pappalardo, F., Halling-Brown, M. D., Rapin, N., Zhang, P., Alemani, D., Emerson, A., Paci, P., Duroux, P., Pennisi, M., Palladini, A., Miotto, O., Churchill, D., Rossi, E., Shepherd, A. J., Moss, D. S., Castiglione, F., Bernaschi, M., Lefranc, M.-P., Brunak, S., Motta, S., Lollini, P.-L., Basford, K. E., and Brusic, V. ImmunoGrid, an integrative environment for large-scale simulation of the immune system for vaccine discovery, design and optimization. *Briefings in Bioinformatics*, 10(3):330–340, May 2009. ISSN 1477-4054. doi: 10.1093/bib/bbp014.

Perelson, A. S. and Ribeiro, R. M. Modeling the within-host dynamics of HIV infection. *BMC biology*, 11:96, 2013. ISSN 1741-7007. doi: 10.1186/1741-7007-11-96.

Peterson, L. W. and Artis, D. Intestinal epithelial cells: regulators of barrier function and immune homeostasis. *Nature Reviews Immunology*, 14(3):141–153, March 2014. ISSN 1474-1733. doi: 10.1038/nri3608.

Phillips, J. M., Parish, N. M., Raine, T., Bland, C., Sawyer, Y., De La Pea, H., and Cooke, A. Type 1 diabetes development requires both CD4+ and CD8+ T cells and can be reversed by non-depleting antibodies targeting both T cell populations. *The review of diabetic studies: RDS*, 6(2):97–103, 2009. ISSN 1614-0575. doi: 10.1900/RDS.2009.6.97.

Phillips, K. G., Jacques, S. L., and McCarty, O. J. T. Measurement of Single Cell Refractive Index, Dry Mass, Volume, and Density Using a Transillumination Microscope. *Physical Review Letters*, 109(11):118105, September 2012. doi: 10.1103/PhysRevLett.109.118105.

Platt, C. D., Ma, J. K., Chalouni, C., Ebersold, M., Bou-Reslan, H., Carano, R. A. D., Mellman, I., and Delamarre, L. Mature dendritic cells use endocytic receptors to capture and present antigens. *Proceedings of the National Academy of Sciences of the United States of America*, 107(9):4287–4292, March 2010. ISSN 0027-8424. doi: 10.1073/pnas.0910609107.

Podolsky, D. K. Inflammatory Bowel Disease. *New England Journal of Medicine*, 347(6): 417–429, August 2002. ISSN 0028-4793. doi: 10.1056/NEJMra020831.

Polack, F., Andrews, P., Ghetiu, T., Read, M., Stepney, S., Timmis, J., and Sampson, A. Reflections on the Simulation of Complex Systems for Science. In *2010 15th IEEE International Conference on Engineering of Complex Computer Systems (ICECCS)*, pages 276–285, March 2010. doi: 10.1109/ICECCS.2010.48.

Pollmcher, J. and Figge, M. T. Agent-based model of human alveoli predicts chemotactic signaling by epithelial cells during early Aspergillus fumigatus infection. *PloS One*, 9 (10):e111630, 2014. ISSN 1932-6203. doi: 10.1371/journal.pone.0111630.

Powrie, F., Leach, M. W., Mauze, S., Caddle, L. B., and Coffman, R. L. Phenotypically distinct subsets of CD4+ T cells induce or protect from chronic intestinal inflammation in C. B-17 scid mice. *International Immunology*, 5(11):1461–1471, November 1993. ISSN 0953-8178.

Powrie, F. Immune regulation in the intestine: a balancing act between effector and regulatory T cell responses. *Annals of the New York Academy of Sciences*, 1029:132–141, December 2004. ISSN 0077-8923. doi: 10.1196/annals.1309.030.

Pulendran, B. and Artis, D. New paradigms in type 2 immunity. *Science (New York, N.Y.)*, 337(6093):431–435, July 2012. ISSN 1095-9203. doi: 10.1126/science.1221064.

Randolph, G. J., Angeli, V., and Swartz, M. A. Dendritic-cell trafficking to lymph nodes through lymphatic vessels. *Nature Reviews Immunology*, 5(8):617–628, August 2005. ISSN 1474-1733. doi: 10.1038/nri1670.

Ratanamahatana, C. A. and Keogh, E. Everything you know about dynamic time warping is wrong. In *Third Workshop on Mining Temporal and Sequential Data*, 2004.

Read, M., Timmis, J., Jon, Andrews, P. S., and Kumar, V. A Domain Model of Experimental Autoimmune Encephalomyelitis. *In 2nd Workshop on Complex Systems Modelling and Simulation*, pages 9–44, 2009.

Read, M., Andrews, P. S., Timmis, J., and Kumar, V. Techniques for Grounding Agent-Based Simulations in the Real Domain : a case study in Experimental Autoimmune Encephalomyelitis. *Mathematical and Computer Modelling of Dynamical Systems*, 18 (1):67–86, 2012.

Read, M. N. *Statistical and Modelling Techniques to Build Confidence in the Investigation of Immunology through Agent-Based Simulation*. Thesis, University of York, September 2011.

Rescigno, M. Dendritic cells and the complexity of microbial infection. *Trends in Microbiology*, 10(9):425–431, September 2002. ISSN 0966-842X. doi: 10.1016/S0966-842X(02)02425-3.

Reynolds, J. M., Martinez, G. J., Nallaparaju, K. C., Chang, S. H., Wang, Y.-H., and Dong, C. Regulation of intestinal inflammation and barrier function by IL-17c. *Journal of immunology (Baltimore, Md. : 1950)*, 189(9):4226–4230, November 2012. ISSN 0022-1767. doi: 10.4049/jimmunol.1103014.

Riggs, T., Walts, A., Perry, N., Bickle, L., Lynch, J. N., Myers, A., Flynn, J., Linderman, J. J., Miller, M. J., and Kirschner, D. E. A comparison of random vs. chemotaxis-driven contacts of T cells with dendritic cells during repertoire scanning. *Journal of Theoretical Biology*, 250(4):732–751, February 2008. ISSN 0022-5193. doi: 10.1016/j.jtbi.2007.10.015.

Riol-Blanco, L., Snchez-Snchez, N., Torres, A., Tejedor, A., Narumiya, S., Corb, A. L., Snchez-Mateos, P., and Rodrguez-Fernndez, J. L. The chemokine receptor CCR7 activates in dendritic cells two signaling modules that independently regulate chemotaxis and migratory speed. *Journal of Immunology (Baltimore, Md.: 1950)*, 174(7):4070–4080, April 2005. ISSN 0022-1767.

Rivera, J., Proia, R. L., and Olivera, A. The alliance of sphingosine-1-phosphate and its receptors in immunity. *Nature Reviews. Immunology*, 8(10):753–763, October 2008. ISSN 1474-1741. doi: 10.1038/nri2400.

Robinson, S. *Simulation: The Practice of Model Development and Use*. Palgrave Macmillan, Houndmills, Basingstoke, Hampshire, UK ; New York, NY, 2nd edition edition edition, September 2014. ISBN 978-1-137-32802-1.

Ryan, C. and Menter, A. Ponesimod–a future oral therapy for psoriasis? *Lancet (London, England)*, 384(9959):2006–2008, December 2014. ISSN 1474-547X. doi: 10.1016/S0140-6736(14)61039-4.

Sadlack, B., Merz, H., Schorle, H., Schimpl, A., Feller, A. C., and Horak, I. Ulcerative colitis-like disease in mice with a disrupted interleukin-2 gene. *Cell*, 75(2):253–261, October 1993. ISSN 0092-8674.

Saltelli, A. and Bollardo, R. An alternative way to compute Fourier amplitude sensitivity test (FAST). *Comput. Stat. Data Anal.*, 26(4):445–460, 1998.

Sanjabi, S., Zenewicz, L. A., Kamanaka, M., and Flavell, R. A. Anti-inflammatory and pro-inflammatory roles of TGF-beta, IL-10, and IL-22 in immunity and autoimmunity. *Current Opinion in Pharmacology*, 9(4):447–453, August 2009. ISSN 1471-4973. doi: 10.1016/j.coph.2009.04.008.

Sartor, R. B. and Mazmanian, S. K. Intestinal Microbes in Inflammatory Bowel Diseases. *The American Journal of Gastroenterology Supplements*, 1(1):15–21, July 2012. ISSN 1948-9498. doi: 10.1038/ajgsup.2012.4.

Schreinemachers, P. and Berger, T. An agent-based simulation model of humanenvironment interactions in agricultural systems. *Environmental Modelling & Software*, 26(7): 845–859, July 2011. ISSN 1364-8152. doi: 10.1016/j.envsoft.2011.02.004.

Schroder, K., Hertzog, P. J., Ravasi, T., and Hume, D. A. Interferon-: an overview of signals, mechanisms and functions. *Journal of Leukocyte Biology*, 75(2):163–189, February 2004. ISSN 0741-5400, 1938-3673. doi: 10.1189/jlb.0603252.

Schulz, E. G., Mariani, L., Radbruch, A., and Hfer, T. Sequential polarization and imprinting of type 1 T helper lymphocytes by interferon-gamma and interleukin-12. *Immunity*, 30(5):673–683, May 2009. ISSN 1097-4180. doi: 10.1016/j.immuni.2009.03.013.

Schulzke, J.-D., Bojarski, C., Zeissig, S., Heller, F., Gitter, A. H., and Fromm, M. Disrupted barrier function through epithelial cell apoptosis. *Annals of the New York Academy of Sciences*, 1072:288–299, August 2006. ISSN 0077-8923. doi: 10.1196/annals.1326.027.

Schwartz, R. H. T cell anergy. *Annual Review of Immunology*, 21:305–334, 2003. ISSN 0732-0582. doi: 10.1146/annurev.immunol.21.120601.141110.

Seksik, P., Rigottier-Gois, L., Gramet, G., Sutren, M., Pochart, P., Marteau, P., Jian, R., and Dor, J. Alterations of the dominant faecal bacterial groups in patients with Crohn's disease of the colon. *Gut*, 52(2):237–242, February 2003. ISSN 0017-5749.

Sellon, R. K., Tonkonogy, S., Schultz, M., Dieleman, L. A., Grenther, W., Balish, E., Rennick, D. M., and Sartor, R. B. Resident enteric bacteria are necessary for development of spontaneous colitis and immune system activation in interleukin-10-deficient mice. *Infection and Immunity*, 66(11):5224–5231, November 1998. ISSN 0019-9567.

Shanno, D. F. Conditioning of quasi-Newton methods for function minimization. *Mathematics of Computation*, 24(111):647–656, 1970. ISSN 0025-5718, 1088-6842. doi: 10.1090/S0025-5718-1970-0274029-X.

Silva, M. J. B., Carneiro, M. B. H., dos Anjos Pultz, B., Pereira Silva, D., Lopes, M. E. d. M., and dos Santos, L. M. The multifaceted role of commensal microbiota in homeostasis and gastrointestinal diseases. *Journal of Immunology Research*, 2015:321241, 2015. ISSN 2314-7156. doi: 10.1155/2015/321241.

Stein, J. V., Rot, A., Luo, Y., Narasimhaswamy, M., Nakano, H., Gunn, M. D., Matsuzawa, A., Quackenbush, E. J., Dorf, M. E., and Andrian, U. H. v. The Cc Chemokine Thymus-Derived Chemotactic Agent 4 (Tca-4, Secondary Lymphoid Tissue Chemokine, 6ckine, Exodus-2) Triggers Lymphocyte FunctionAssociated Antigen 1Mediated Arrest of Rolling T Lymphocytes in Peripheral Lymph Node High Endothelial Venules. *The Journal of Experimental Medicine*, 191(1):61–76, January 2000. ISSN 0022-1007, 1540-9538. doi: 10.1084/jem.191.1.61.

Sterzenbach, T., Lee, S. K., Brenneke, B., Goetz, F. v., Schauer, D. B., Fox, J. G., Suerbaum, S., and Josenhans, C. Inhibitory Effect of Enterohepatic Helicobacter hepaticus on Innate Immune Responses of Mouse Intestinal Epithelial Cells. *Infection and Immunity*, 75(6):2717–2728, June 2007. ISSN 0019-9567, 1098-5522. doi: 10.1128/IAI.01935-06.

Stirk, E. R., Lythe, G., van den Berg, H. A., and Molina-Pars, C. Stochastic competitive exclusion in the maintenance of the nave T cell repertoire. *Journal of Theoretical Biology*, 265(3):396–410, August 2010. ISSN 0022-5193. doi: 10.1016/j.jtbi.2010.05.004.

Stritesky, G. L., Yeh, N., and Kaplan, M. H. IL-23 promotes maintenance but not commitment to the Th17 lineage. *Journal of immunology (Baltimore, Md. : 1950)*, 181(9): 5948–5955, November 2008. ISSN 0022-1767.

Strober, W., Fuss, I. J., and Blumberg, R. S. The Immunology of Mucosal Models of Inflammation. *Annual Review of Immunology*, 20(1):495–549, 2002. doi: 10.1146/annurev.immunol.20.100301.064816.

Suerbaum, S., Josenhans, C., Sterzenbach, T., Drescher, B., Brandt, P., Bell, M., Droge, M., Fartmann, B., Fischer, H.-P., Ge, Z., Horster, A., Holland, R., Klein, K., Konig, J., Macko, L., Mendz, G. L., Nyakatura, G., Schauer, D. B., Shen, Z., Weber, J.,

Frosch, M., and Fox, J. G. The complete genome sequence of the carcinogenic bacterium Helicobacter hepaticus. *Proceedings of the National Academy of Sciences of the United States of America*, 100(13):7901–7906, June 2003. ISSN 0027-8424. doi: 10.1073/pnas.1332093100.

Swat, M., Moodie, S., Wimalaratne, S., Kristensen, N., Lavielle, M., Mari, A., Magni, P., Smith, M., Bizzotto, R., Pasotti, L., Mezzalana, E., Comets, E., Sarr, C., Terranova, N., Blaudez, E., Chan, P., Chard, J., Chatel, K., Chenel, M., Edwards, D., Franklin, C., Giorgino, T., Glont, M., Girard, P., Grenon, P., Harling, K., Hooker, A., Kaye, R., Keizer, R., Kloft, C., Kok, J., Kokash, N., Laibe, C., Laveille, C., Lestini, G., Mentr, F., Munafo, A., Nordgren, R., Nyberg, H., Parra-Guillen, Z., Plan, E., Ribba, B., Smith, G., Trocniz, I., Yvon, F., Milligan, P., Harnisch, L., Karlsson, M., Hermjakob, H., and Le Novre, N. Pharmacometrics Markup Language (PharmML): Opening New Perspectives for Model Exchange in Drug Development. *CPT: Pharmacometrics & Systems Pharmacology*, 4(6):316–319, June 2015. ISSN 2163-8306. doi: 10.1002/psp4.57.

Sykes, D. A., Riddy, D. M., Stamp, C., Bradley, M. E., McGuiness, N., Sattikar, A., Guerini, D., Rodrigues, I., Glaenzel, A., Dowling, M. R., Mullershausen, F., and Charlton, S. J. Investigating the molecular mechanisms through which FTY720-P causes persistent S1p1 receptor internalization. *British Journal of Pharmacology*, 171(21): 4797–4807, November 2014. ISSN 0007-1188. doi: 10.1111/bph.12620.

Tada, Y., Asahina, A., Fujita, H., Mitsui, H., Torii, H., Watanabe, T., and Tamaki, K. Differential effects of LPS and TGF- on the production of IL-6 and IL-12 by Langerhans cells, splenic dendritic cells, and macrophages. *Cytokine*, 25(4):155–161, February 2004. ISSN 1043-4666. doi: 10.1016/j.cyto.2003.11.006.

Takizawa, H., Nakamura, K., Tabira, A., Chikahara, Y., Matsui, T., Hiroi, N., and Funahashi, A. LibSBMLSim: a reference implementation of fully functional SBML simulator. *Bioinformatics*, 29(11):1474–1476, June 2013. ISSN 1367-4803, 1460-2059. doi: 10.1093/bioinformatics/btt157.

Tisue, S. and Wilensky, U. NetLogo: A simple environment for modeling complexity. In *ResearchGate*, pages 16–21, January 2004.

Tokarski, C., Hummert, S., Mech, F., Figge, M. T., Germerodt, S., Schroeter, A., and Schuster, S. Agent-based modeling approach of immune defense against spores of opportunistic human pathogenic fungi. *Microbial Immunology*, 3:129, 2012. doi: 10.3389/fmicb.2012.00129.

Twycross, J., Band, L. R., Bennett, M. J., King, J. R., and Krasnogor, N. Stochastic and deterministic multiscale models for systems biology: an auxin-transport case study. *BMC Systems Biology*, 4(1):1–11, March 2010. ISSN 1752-0509. doi: 10.1186/1752-0509-4-34.

Waage, A., Brandtzaeg, P., Halstensen, A., Kierulf, P., and Espevik, T. The complex pattern of cytokines in serum from patients with meningococcal septic shock. Association between interleukin 6, interleukin 1, and fatal outcome. *The Journal of Experimental Medicine*, 169(1):333–338, January 1989. ISSN 0022-1007, 1540-9538. doi: 10.1084/jem.169.1.333.

Warnock, R. A., Campbell, J. J., Dorf, M. E., Matsuzawa, A., McEvoy, L. M., and Butcher, E. C. The role of chemokines in the microenvironmental control of T versus B cell arrest in Peyer's patch high endothelial venules. *The Journal of Experimental Medicine*, 191(1):77–88, January 2000. ISSN 0022-1007.

Warrington, R., Watson, W., Kim, H. L., and Antonetti, F. R. An introduction to immunology and immunopathology. *Allergy, Asthma, and Clinical Immunology: Official Journal of the Canadian Society of Allergy and Clinical Immunology*, 7 Suppl 1:S1, 2011. ISSN 1710-1492. doi: 10.1186/1710-1492-7-S1-S1.

Watson, J. D. and Crick, F. H. Molecular structure of nucleic acids; a structure for deoxyribose nucleic acid. *Nature*, 171(4356):737–738, April 1953. ISSN 0028-0836.

Wei, L., Laurence, A., Elias, K. M., and OShea, J. J. IL-21 IS PRODUCED BY TH17 CELLS AND DRIVES IL-17 PRODUCTION IN A STAT3-DEPENDENT MANNER. *The Journal of biological chemistry*, 282(48):34605–34610, November 2007. ISSN 0021-9258. doi: 10.1074/jbc.M705100200.

Wei, S. H., Rosen, H., Matheu, M. P., Sanna, M. G., Wang, S.-K., Jo, E., Wong, C.-H., Parker, I., and Cahalan, M. D. Sphingosine 1-phosphate type 1 receptor agonism

inhibits transendothelial migration of medullary T cells to lymphatic sinuses. *Nature Immunology*, 6(12):1228–1235, December 2005. ISSN 1529-2908. doi: 10.1038/ni1269.

Wendelsdorf, K., Bassaganya-Riera, J., Hontecillas, R., and Eubank, S. Model of colonic inflammation: immune modulatory mechanisms in inflammatory bowel disease. *Journal of Theoretical Biology*, 264(4):1225–1239, June 2010. ISSN 1095-8541. doi: 10.1016/j.jtbi.2010.03.027.

Wendelsdorf, K. V., Alam, M., Bassaganya-Riera, J., Bisset, K., Eubank, S., Hontecillas, R., Hoops, S., and Marathe, M. ENteric Immunity SImulator: a tool for in silico study of gastroenteric infections. *IEEE transactions on nanobioscience*, 11(3):273–288, September 2012. ISSN 1558-2639. doi: 10.1109/TNB.2012.2211891.

Westera, L., Drylewicz, J., Braber, I. d., Mugwagwa, T., Maas, I. v. d., Kwast, L., Volman, T., Weg-Schrijver, E. H. R. v. d., Bartha, I., Spierenburg, G., Gaiser, K., Ackermans, M. T., Asquith, B., Boer, R. J. d., Tesselaar, K., and Borghans, J. A. M. Closing the gap between T-cell life span estimates from stable isotope-labeling studies in mice and humans. *Blood*, 122(13):2205–2212, September 2013. ISSN 0006-4971, 1528-0020. doi: 10.1182/blood-2013-03-488411.

Williams, R. A., Timmis, J., and Qwarnstrom, E. E. Computational Models of the NF-KB Signalling Pathway. *Computation*, 2(4):131–158, September 2014. doi: 10.3390/computation2040131.

Wirtz, S., Galle, P. R., and Neurath, M. F. Efficient gene delivery to the inflamed colon by local administration of recombinant adenoviruses with normal or modified fibre structure. *Gut*, 44(6):800–807, June 1999. ISSN 0017-5749.

Wolfram Research, Inc. Mathematica, 2016.

Wooley, J. C. *Catalyzing Inquiry at the Interface of Computing and Biology*. The National Academies Collection: Reports funded by National Institutes of Health. National Academies Press (US), Washington (DC), 2005. ISBN 0-309-09612-X.

Xavier, R. J. and Podolsky, D. K. Unravelling the pathogenesis of inflammatory bowel disease. *Nature*, 448(7152):427–434, July 2007. ISSN 0028-0836. doi: 10.1038/nature06005.

Xie, Z. and Kulasiri, D. Modelling of circadian rhythms in Drosophila incorporating the interlocked PER/TIM and VRI/PDP1 feedback loops. *Journal of Theoretical Biology*, 245(2):290–304, March 2007. ISSN 0022-5193. doi: 10.1016/j.jtbi.2006.10.028.

Yan, F., John, S. K., Wilson, G., Jones, D. S., Washington, M. K., and Polk, D. B. Kinase suppressor of Ras-1 protects intestinal epithelium from cytokine-mediated apoptosis during inflammation. *Journal of Clinical Investigation*, 114(9):1272–1280, November 2004. ISSN 0021-9738. doi: 10.1172/JCI200421022.

Yang, I., Eibach, D., Kops, F., Brenneke, B., Woltemate, S., Schulze, J., Bleich, A., Gruber, A. D., Muthupalani, S., Fox, J. G., Josenhans, C., and Suerbaum, S. Intestinal Microbiota Composition of Interleukin-10 Deficient C57bl/6j Mice and Susceptibility to Helicobacter hepaticus-Induced Colitis. *PLoS ONE*, 8(8), August 2013. ISSN 1932-6203. doi: 10.1371/journal.pone.0070783.

Yates, A., Callard, R., and Stark, J. Combining cytokine signalling with T-bet and GATA-3 regulation in Th1 and Th2 differentiation: a model for cellular decision-making. *Journal of Theoretical Biology*, 231(2):181–196, November 2004. ISSN 0022-5193. doi: 10.1016/j.jtbi.2004.06.013.

Zenewicz, L. A., Antov, A., and Flavell, R. A. CD4 T-cell differentiation and inflammatory bowel disease. *Trends in Molecular Medicine*, 15(5):199–207, May 2009. ISSN 1471-4914. doi: 10.1016/j.molmed.2009.03.002.

Zhang, F., Angermann, B. R., and Meier-Schellersheim, M. The Simmune Modeler visual interface for creating signaling networks based on bi-molecular interactions. *Bioinformatics*, 29(9):1229–1230, May 2013. ISSN 1367-4803. doi: 10.1093/bioinformatics/btt134.

Zheng, H., Jin, B., Henrickson, S. E., Perelson, A. S., von Andrian, U. H., and Chakraborty, A. K. How Antigen Quantity and Quality Determine T-Cell Decisions in Lymphoid Tissue. *Molecular and Cellular Biology*, 28(12):4040–4051, June 2008. ISSN 0270-7306. doi: 10.1128/MCB.00136-08.

Ziraldo, C., Mi, Q., An, G., and Vodovotz, Y. Computational Modeling of Inflammation

and Wound Healing. *Advances in Wound Care*, 2(9):527–537, November 2013. ISSN 2162-1918. doi: 10.1089/wound.2012.0416.

Zolotarevsky, Y., Hecht, G., Koutsouris, A., Gonzalez, D. E., Quan, C., Tom, J., Mrsny, R. J., and Turner, J. R. A membrane-permeant peptide that inhibits MLC kinase restores barrier function in in vitro models of intestinal disease. *Gastroenterology*, 123 (1):163–172, July 2002. ISSN 0016-5085.